

DISSERTATION

CMOS-COMPATIBLE ON-CHIP OPTICAL INTERCONNECTS

Submitted by

Robert Elliott Pownall

Department of Electrical & Computer Engineering

In partial fulfillment of the requirements

For the Degree of Doctor of Philosophy

Colorado State University

Fort Collins, Colorado

Fall 2009

UMI Number: 3401013

All rights reserved

**INFORMATION TO ALL USERS**

The quality of this reproduction is dependent upon the quality of the copy submitted.

In the unlikely event that the author did not send a complete manuscript and there are missing pages, these will be noted. Also, if material had to be removed, a note will indicate the deletion.



UMI 3401013

Copyright 2010 by ProQuest LLC.

All rights reserved. This edition of the work is protected against unauthorized copying under Title 17, United States Code.



ProQuest LLC  
789 East Eisenhower Parkway  
P.O. Box 1346  
Ann Arbor, MI 48106-1346

Copyright by Robert Elliott Pownall 2009

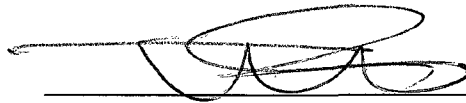
All Rights Reserved

COLORADO STATE UNIVERSITY

November 4, 2009

WE HEREBY RECOMMEND THAT THE DISSERTATION PREPARED UNDER OUR SUPERVISION BY ROBERT ELLIOTT POWNALL ENTITLED CMOS-COMPATIBLE ON-CHIP OPTICAL INTERCONNECTS BE ACCEPTED AS FULFILLING IN PART REQUIREMENTS FOR THE DEGREE OF DOCTOR OF PHILOSOPHY.

Committee on Graduate work



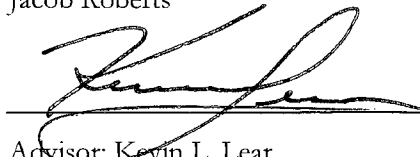
Tom Chen



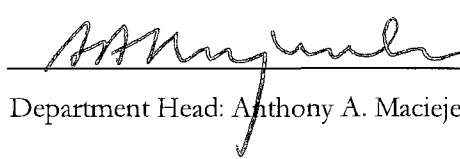
Steven C. Reising



Jacob Roberts



Advisor: Kevin L. Lear



Department Head: Anthony A. Maciejewski

# *ABSTRACT OF DISSERTATION*

## CMOS-COMPATIBLE ON-CHIP OPTICAL INTERCONNECTS

The increase in complexity of integrated circuits (ICs) over the past five decades has resulted in increasing demands on the interconnect layers. In the past decade, the ability of conventional “electrical signal down a metal wire” interconnect to keep up with the increasing demands placed on interconnect has come more and more into question. To meet the increasing demands on interconnect and to get around the limitation of conventional “metal wire” interconnect, various forms of optical interconnect have been proposed.

In the Optoelectronics Research Group at Colorado State University, we have conceived, developed and investigated a proposal to place a nanoscale fiber optic network on an integrated circuit. In contrast to other proposals which use materials and processing which are arguably not part of a standard CMOS process and thus raise equipment compatibility or contamination concerns, our proposal uses materials that exist in any reasonably standard CMOS process. This compatibility greatly reduces barriers to adoption. Waveguide cores are made from silicon nitride (a standard dielectric film), while the waveguide cladding is made of various types of silicon dioxide (another standard dielectric film). Photodetectors in the system are made from polysilicon, a standard gate material. Two generations of optical interconnect test chips were fabricated in a standard CMOS process at a commercial fabrication facility with a few minor variations to meet the needs of the test chip.

Following fabrication of each generation of the optical interconnect test chip, the devices on the test chip were characterized for both DC and AC performance. The waveguide loss, which was expected to be between 0.5 dB/cm and 2 dB/cm, was found to be much

higher than expected, approximately 8.5 dB/cm. This value was essentially independent of waveguide width from 0.5  $\mu\text{m}$  to 8  $\mu\text{m}$ . This high waveguide loss was attributed to an unexpected absorption mechanism in the phosphosilicate glass (PSG) form of silicon dioxide which made up part of the lower cladding.

Detector dark current was extremely low, typically 5 nA or less at a 5 V bias for all device sizes. Dark current was found to follow the hyperbolic sine I-V curve that is characteristic of undoped polysilicon due to thermionic emission over the polysilicon grain boundaries. First generation DC responsivity was measured as high as 0.35 A/W at 654 nm, while second generation DC responsivity measured as high as 1.3 A/W at 690 nm. The higher responsivity observed on second generation material is attributed to the additional thermal processing seen by second generation material. Responsivity increased at smaller contact spacing, however no sign of saturation in responsivity was observed at the smallest contact spacing in this work, 2.14  $\mu\text{m}$ . This suggests that devices with even smaller contact spacing should have even higher responsivity. The dependence of responsivity  $\mathfrak{R} = \mathfrak{R}_0 \left( 1 + \frac{K\mu\tau V}{S^2} \right)$  on voltage V and contact spacing S, suggested that the detectors worked as photoconductors rather than photodiodes.  $\mu$  is the carrier mobility,  $\tau$  is the carrier lifetime, and K depends on the ratio of bulk recombination to contact recombination. Further suggesting a photoconductive, rather than photodiode, principle behind the response was the fact that the photocurrent in the symmetric detector structure increased with voltage, showing no signs of saturation all the way to device breakdown.

AC testing of second generation devices measured pulses with full-width half-max (FWHM) as low as 0.89 ns and 10% - 90% rise times as low as 0.39 ns. The values are

equipment-limited, as we were unable to generate Gaussian optical pulses with FWHM much less than 600 ps. In addition, the transimpedance amplifier (TIA) used to convert the photocurrent signal into a voltage had a 1 GHz bandwidth, which limits the measurable rise time. The shape of the detector photocurrent response to a Gaussian optical input indicated that more than one recombination mechanism was present. An extremely good fit to the data was found by combining a bulk recombination process that dominated at lower optical power levels with a contact recombination process that became dominant at higher optical power levels.

DC responsivity and AC pulse width were both affected by a photoconductive gain process. This process allowed more than one carrier to be counted in the external circuit for every absorbed photon, resulting in quantum efficiencies as high as 234%. However, the same photoconductive gain process effectively allowed carriers to live longer than the transit time between the contacts, causing an exponential decay process to be observed in the AC pulse response and increasing the FWHM of the output pulses. The gain process is due to barrier lowering at the Schottky contacts, enhanced by capture of photogenerated charges in states physically near the contacts.

The detectors and waveguides studied in this work were part of an optical interconnect system. The second generation test chip included a 0.83 cm, 16-node optical clock distribution H-tree, with TIAs and phase comparators at the end nodes of the H-tree. In related work, this H-tree was used to distribute an optical clock signal across the test die, thus validating the concepts behind this proposal. Link budget analysis indicated that measured performance did not meet design goals, with 390  $\mu\text{W}$  of optical power being required at the input to the optical H-tree instead of the 26  $\mu\text{W}$  in the design goals. This was largely due to unexpectedly high

splitter and waveguide losses. If losses in these two areas could be reduced to values typically seen in the literature while still maintaining the high measured responsivity values, then the design goal of  $1\mu\text{A}$  of photocurrent from the detectors at the ends of the optical H-tree could be generated with  $48\mu\text{W}$  of optical power entering the optical H-tree.

Robert Elliott Pownall  
Department of Electrical and Computer Engineering  
Colorado State University  
Fort Collins, CO 80523  
Fall 2009

## ACKNOWLEDGMENTS

In a dissertation, it is somewhat traditional to acknowledge those who have helped you make your way through the trials and tribulations of the Ph.D process. Who am I to ignore tradition?

I'd first like to thank the Electrical Engineering faculty at Purdue University, where I received my BSEE and MSEE degrees, for giving me a solid background in the fundamentals of Electrical Engineering. What I learned there has stood the test of time and has carried me through the rest of my professional and academic career.

At Colorado State University, I'd like to thank Dr. Gary Robinson, emeritus professor of Electrical Engineering. Dr. Robinson was my first contact with the CSU ECE department; through his ECE 570 "Compound Semiconductor Devices and Materials" course. It was with his encouragement that I embarked on the Ph.D program at CSU.

I would also like to thank my advisor, Dr. Kevin Lear, for taking me on when my initial route to a Ph.D was blocked. You kept prodding and pushing me to make it through. In addition to Dr. Lear, I would like to thank the other grad students of Optoelectronics Group, both past and present. I would particularly like to single out Guangwei Yuan, who mentored me when I first came in to the group.

Outside of academia, I'd like to thank my former co-workers in the semiconductor division of Agilent Technologies, now Avago Technologies. I'd particularly like to single out, in alphabetical order, Duane Fasen, Ron Kee, Brad Lewis, Jay Meyer, Phil Nikkel, Mark Urfer and Andy Weilert. When I needed some information or other resource, you got it for me.

I'd like to close with thanking my family. My "furry family" – my cats Misty, Phoebe and Sarah – you were always there when I needed some love, affection and cheering up. Misty, I'm sorry you missed seeing me finish by less than a month. I'll always miss you. My grandparents – Ira and Edna Pownall – without your financial support, I'm not sure I would have been able to make it through. My parents – Bob and Jean Pownall – you were always there when I needed you, believing in me when sometimes I had my doubts. Thank you.

Robert Elliott Pownall

November 5, 2009

Fort Collins, CO 80523

*Table of Contents*

Chapter 1: Introduction and Motivation for On-chip Optical Interconnects..... page 1

Chapter 2: Background of optical waveguides and polysilicon detectors.....page 10

Chapter 3: Design and Fabrication of optical waveguides and polysilicon detectors.....page 54

Chapter 4: DC Testing and Characterization of Optical Waveguides and Polysilicon Detectors  
.....page 79

Chapter 5: AC Testing and Characterization of Polysilicon Detectors.....page 110

Chapter 6: Achievements, Conclusions and Future Work.....page 130

Appendix A: Derivation of the Detector Impulse Response, plus the System DC and AC  
Response.....page 135

Appendix B: First Generation Test Chip Documentation.....page 149

Appendix C: Second Generation Test Chip Documentation.....page 153

Appendix D: Process Flows for the First and Second-Generation Optical Test Chips  
.....page 212

Appendix E: Die Edge Polishing Procedure.....page 216

Appendix F: First and Second Generation Die Numbering Scheme.....page 220

Appendix G: Measurement Instructions.....page 223

Appendix H: LabVIEW Screen Captures.....page 238

INTRODUCTION AND MOTIVATION FOR ON-CHIP OPTICAL INTERCONNECTS

1 Trends in Integrated Circuits

Since the invention of the transistor at Bell Labs in 1947, the invention of the integrated circuit (IC) at Texas Instruments (TI) in 1959 and the development of the microprocessor (largely at TI, Motorola and Intel) in the mid 1970s, two trends have been prominent in IC and microprocessor design. First, as shown in Figure 1, the trend in ICs has been to physically larger die sizes, approaching 2 centimeters by 2 centimeters in recent designs. Second, the trend in transistor design has been to physically smaller dimensions, with minimum feature sizes going from tens or hundreds of microns in the 1960s to 45 nanometers or less in current-day leading-edge production processes, as shown in Figure 2. As a result of these two trends, IC designers have been able to crowd more and more transistors on a die, with recent leading edge microprocessor designs approaching a billion or more transistors each. However, for a microprocessor, or any IC design, to work correctly, input signals must be brought, intact, to appropriate points in the design. In synchronous logic circuits, such as microprocessors and semiconductor memory, one of the most important input signals is the clock.

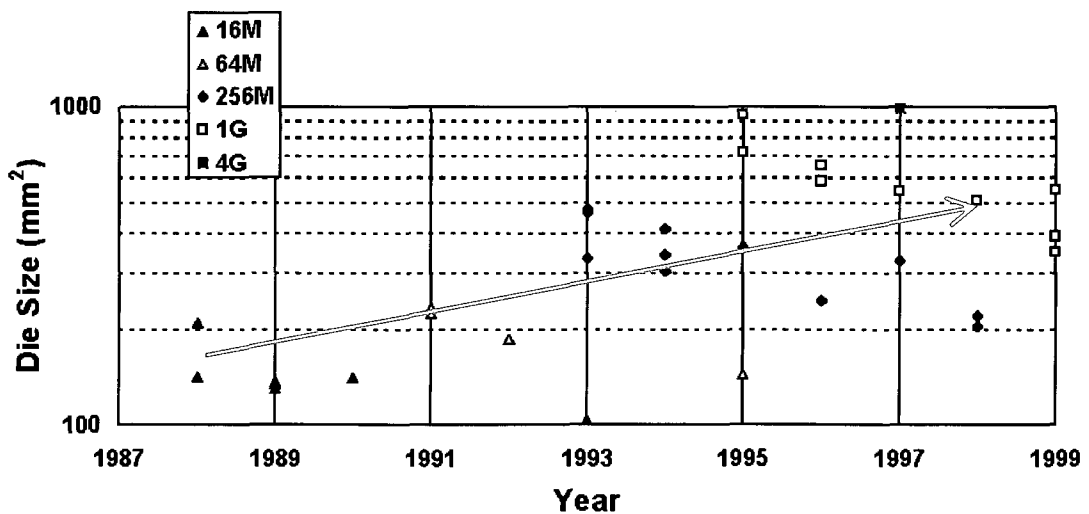


Figure 1: DRAM die size vs. year, 1988 to 1999, reproduced from [1]

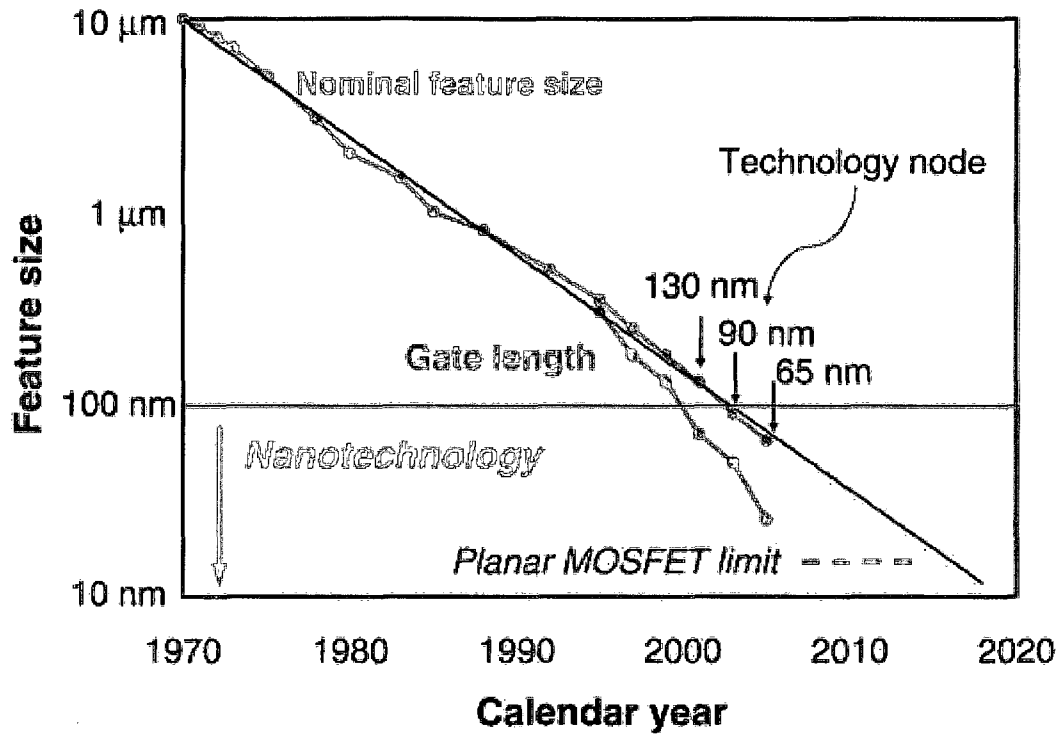


Figure 2: Logic technology node and transistor gate length versus calendar year, reproduced from [2]

## 2 Implications of these trends

As integrated circuit die sizes become larger and larger (i.e. Trend 1), the distance clock signals must travel also grows larger. Assuming that the number of transistors on a die grows linearly with the die area, Rent's Rule [3] implies that the interconnect length will grow at a rate between  $(\text{die area})^{0.5}$  and  $(\text{die area})^{0.6}$ . Since a growth rate exactly proportional to  $(\text{die area})^{0.5}$  implies growth at the rate of the die size dimensions, Rent's Rule implies the interconnect length grows at least as fast as the increase in die size dimensions, but slower than the increase in die size area. [4] With longer distances (i.e. increased global interconnect length) comes longer signal propagation times, even for clock signals moving at an appreciable fraction of the speed of light. With current microprocessor designs running at clock frequencies in the multiple GHz range, picoseconds, let alone nanoseconds, matter, as shown in Figure 3.

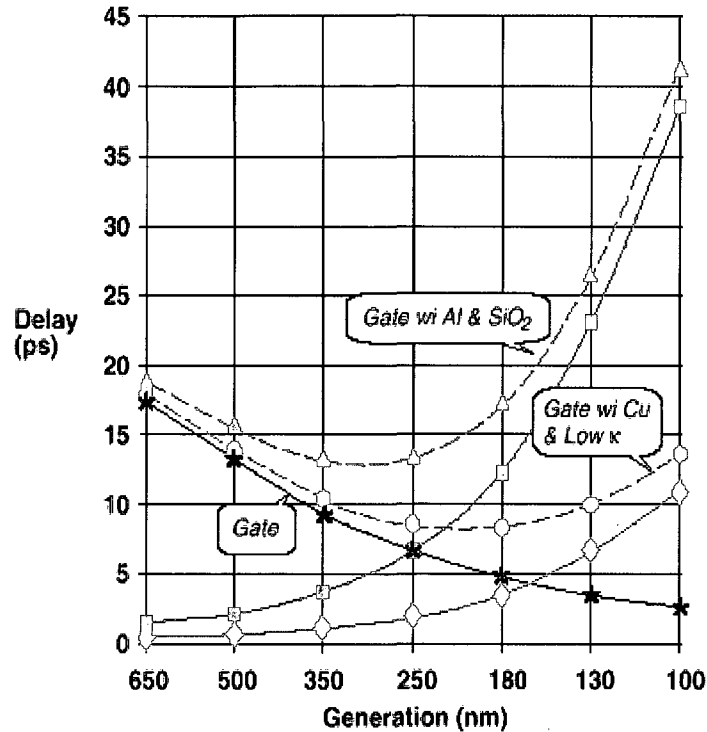


Figure 3: Gate and interconnect delay vs. process generation, reproduced from [5]

Even more significant than the increased signal propagation times due to increased global interconnect length is increased signal dispersion. The metal lines on the die act as waveguides, somewhat similar to stripline or microstrip in a microwave circuit. [6] As the electric field in the waveguide is propagating in a hybrid TM-TE mode<sup>1</sup>, the signal velocity will depend on the frequency. Since the clock is a square wave, it contains signal components ranging in frequency (in theory) up to infinity. (However, as shown in Chapter 2, for a square wave only frequencies up to about 10 times the fundamental square wave frequency are important.) The result of different signal velocity with frequency is a distortion (“smearing out”) of the square wave clock signal. If the signal becomes sufficiently distorted, then accurate clocking can no longer be assured.

<sup>1</sup> Since the dielectric surrounding the metal lines is not radially symmetric, the line cannot support a TEM wave. Indeed, for the top levels of metal, the ones most commonly used for clock, the electric field will extend into the air above the die. If the line propagated a TEM wave, then the phase velocity of the TEM wave in the dielectric would be  $c/n$ , while in the air the TEM phase velocity would be  $c$ . As a result, a phase match at the dielectric-air boundary would be impossible.

As transistor dimensions shrink (i.e. Trend 2), the cross-sectional area of the wires carrying clock signals shrinks, increasing the resistance of the wire. In addition, the distance between wires carrying clock signals and other wires shrinks, both laterally and vertically. This results in increased capacitance between clock wires and the rest of the circuit. This combination of increased resistance,  $R$ , and increased capacitance,  $C$ , results in increased RC time constant delays.

## 2.1 Increases in clock skew, signal latency and clock jitter

The combination of these two factors (increased global interconnect length and increased RC time constant delays) results in increases in clock skew, defined as the difference in arrival times between the source of the clock and various clock-using nodes on the integrated circuit.

[7]

Increased global interconnect length is also leading to problems with signal latency, defined as the delay between when a clock signal enters the clock distribution path and when the signal reaches its destination at the end of the path. If there was only one entrance and one end in the clock distribution network, then there would be no problem with signal latency. However, a typical clock distribution path has a number of endpoints. In the commonly-used H-tree clock distribution network, the number of endpoints is equal to the size of the tree. (i.e. A 16-node H-tree has 16 endpoints.)

Even here, if the signal propagation velocity down the metal lines of the H-tree was identical throughout the H-tree, there would be no problem. As noted above, the metal lines on the die act as waveguides. As a result, the propagation velocity is highly dependent on the surrounding materials and structure geometries, as well as the distance and shape of the ground reference plane. Exacerbating this effect is process variation across the die. Intra-die process variation also impacts the transistors used for repeaters in the H-tree. As such, identical propagation velocity throughout the H-tree cannot be assured, so differing amounts of signal latency through the H-tree is almost inevitable.

A related problem is an increase in clock jitter, defined as the variation of the leading and trailing edges of the clock signal with respect to an ideal reference clock signal. The

capacitance between metal lines depends on the voltage difference between the lines. (i.e. Two metal lines which are at the same potential have no capacitance between them.) As geometries shrink, so that metal lines become closer together and interact more, it becomes more likely that the capacitance between the lines will vary. This variation will be hard to simulate and model. This variation in capacitance results in quasi-random variation in the RC delay associated with the line, and thus in quasi-random time delays associated with any clock signal traveling down the line.

The effects of increased signal latency and increased global interconnect length on each microprocessor generation, resulting in worsening clock skew, timing delay and jitter, as well as factors such as power consumption and area, are driving the investigation of alternate interconnect technologies for on-chip use.

### **3 Solutions to the problems of increased clock skew, signal latency and clock jitter**

Due to the increases in clock skew, signal latency and clock jitter discussed above, researchers in both industry and academia are investigating alternate interconnect technologies for clock distribution. By “alternate”, this work means interconnect technologies which are not based on existing “send a signal down a metal wire” methods.

#### **3.1 Non-optical alternate interconnect technologies**

Two of the alternate interconnect technologies that have been investigated for clock distribution are three-dimensional (3-D) techniques and RF techniques. 3-D interconnect involves the use of more than one silicon chip substrate, typically wafer bonded together, to give smaller die sizes by using vertical interconnects as well as lateral interconnects. RF clock distribution could bypass the interconnect problem entirely, by broadcasting the clock signal from a central source, with each chip receiving the clock signal using an on-chip antenna made from metal wiring, as shown in Figure 4 and Figure 5. [8]

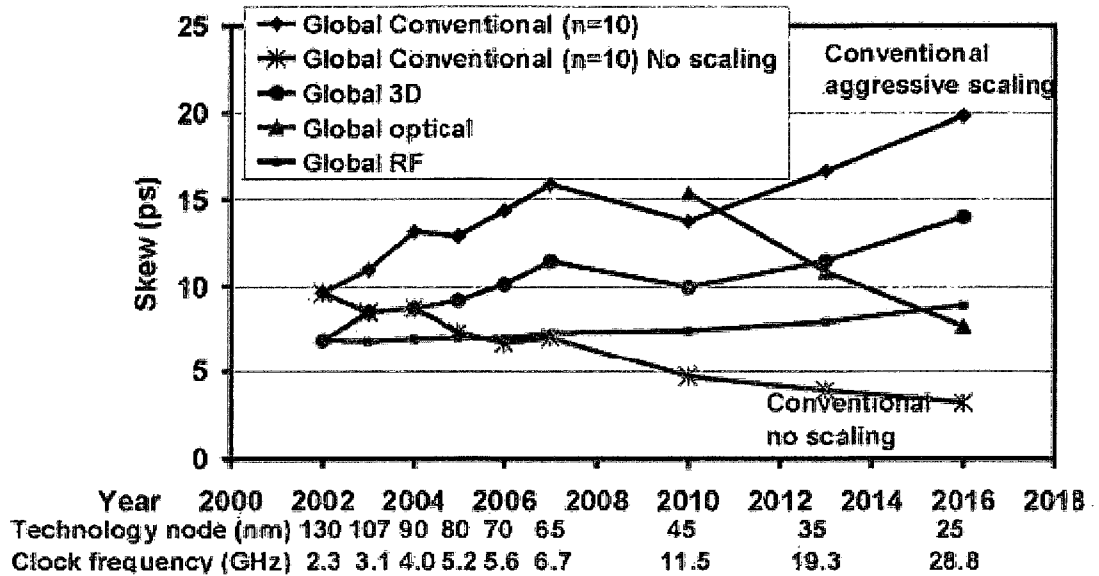


Figure 4: Global clock skew vs. year and process technology, reproduced from [8]

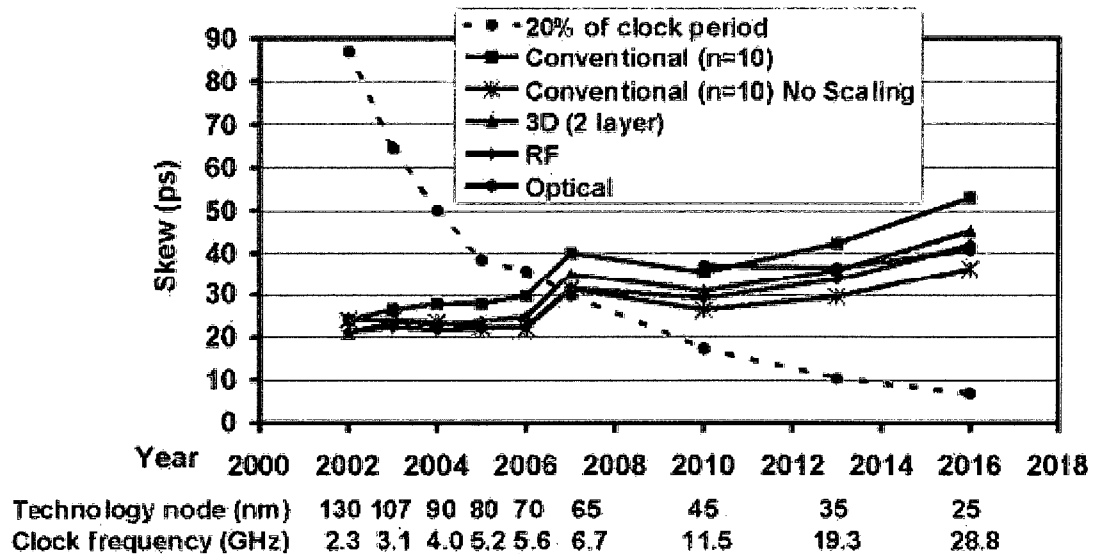


Figure 5: Total clock skew versus technology node for different clock distribution alternatives, reproduced from [8]

### 3.2 Optical alternate interconnect technologies

A third alternate interconnect technology for clock distribution is optical interconnect, the possibility of which was well known by the early 1990s. [9] Optical interconnect technology

can either be free-space or on-chip. As free-space optical interconnects are targeted for chip-to-chip applications [10, 11], this work investigated on-chip optical interconnects.

#### **4 Advantages of on-chip optical interconnect technologies**

On-chip optical interconnects offer several advantages, when compared to conventional electrical interconnects: [12]

- Higher signal propagation velocity (on the order of  $c/2$ ) when compared to electrical interconnects, which have signal propagation velocity on the order of  $c/6$ . [10]
- Elimination of RC time delays, leading to higher bandwidths
- Elimination of cross-talk and electro-magnetic interference (EMI)
- Improved clock skew and jitter performance
- Lower power dissipation

Since power dissipation is becoming at least as big an issue as global interconnect skew / delay in modern integrated circuit designs, this last point is especially significant. Current estimates are that 30% to 50% of total chip power consumption goes to global interconnect. [13]

#### **5 Existing optical interconnect technologies and their disadvantages**

One disadvantage shared by most of the proposed optical interconnect techniques is the use of processing techniques or materials which are not part of a standard CMOS process flow. (e.g. Optical waveguides of SU-8 epoxy-based photoresist or other polymers [14-16].) Other proposed techniques use valuable silicon real estate for their detectors. [17] Since existing electrical interconnect techniques have none of these drawbacks and are, for now, performing adequately, the above disadvantages are strong disincentives for the adoption of optical interconnect technologies by large-scale CMOS wafer fabrication facilities.

#### **6 Advantages of the proposed on-chip optical interconnect technology**

The on-chip optical interconnect technique investigated here uses waveguides with silicon nitride cores and tetra-ethyl ortho-silicate (TEOS) based silicon dioxide cladding, as well as

photodetectors made out of polysilicon. These are materials which exist in any standard CMOS process, and so involve no non-standard processing. In addition, the polysilicon detectors can be placed at any point in the back-half of the process, and so take up no valuable silicon area. (Placement after first-level metal deposition may require a low-temperature polysilicon deposition technique.) Since light is guided to the detectors with optical waveguides, there is no need to keep the area above the detector clear for normal incidence light. The use of standard materials and processing techniques in the work described in this research lowers the barriers to potential adoption of this technique.<sup>2</sup>

## **7 Executive summary of the operating principles behind the proposed on-chip optical interconnect technology**

As noted earlier, light is guided to the detectors by use of optical waveguides based on the principle of total internal reflection. At the detectors, light is leaky-mode coupled to the polysilicon photodetector by means of the evanescent field extending from the lower-index silicon nitride waveguide. Since the light couples to the detector for the entire path length of the waveguide as it crosses the detector, the fraction of power absorbed in the detector is much higher than with vertical incidence photodetectors, lowering the amount of optical power which must be delivered to the detector for a given photocurrent. In the polysilicon, photons generate electron-hole pairs, which lead to a photocurrent when a bias voltage is applied. A transimpedance amplifier is used to convert the photocurrent to a voltage. To reproduce a clock signal, the optical source is square-wave modulated, resulting a square-wave modulated photocurrent, then a square-wave modulated voltage.

### **References:**

- [1] Anonymous, "ISSCC 1999 - Memory," 1999.

---

<sup>2</sup> Luxtera, Inc, of Carlsbad, CA ([www.luxtera.com](http://www.luxtera.com)), is promoting optical interconnect technology (so-called CMOS Photonics™) that is an interesting hybrid of CMOS-compatible and not-so-CMOS-compatible technology. Basically, Luxtera's technology uses silicon waveguides carrying near-IR laser light and uses silicon-germanium photodetectors to convert the light back into a voltage. From one standpoint, Luxtera's technology is CMOS-compatible. It is, after all, being made in co-operation with Freescale Semiconductor, at one of Freescale's large CMOS wafer fabs. From another standpoint, Luxtera's technology is not-so-CMOS-compatible. It requires a wafer fab which is both capable of working with germanium and familiar with working with germanium. While not rare, experience in SiGe technology is at least somewhat uncommon. However, if a fab already has SiGe technology, or if the fab owners / managers want to get into SiGe technology, to access the higher performance of SiGe, then access to Luxtera's technology might prove to be a factor to sway the argument.

- [2] S. E. Thompson and S. Parthasarathy, "Moore's law: the future of Si microelectronics," in *Materials Today*, vol. 9, 2006, pp. 20-25.
- [3] B. S. Landman and R. L. Russo, "Pin Versus Block Relationship for Partitions of Logic Graphs," *IEEE Trans. Comp.*, vol. C 20, pp. 1469-1479, 1971.
- [4] P. Christie and D. Stroobandt, "The interpretation and application of Rent's rule," *IEEE Trans. VLSI Systems*, vol. 8, pp. 639-648, 2000.
- [5] T. W. Chen, "Class notes from CSU EE660 - Advanced Topics in VLSI," 2006.
- [6] D. M. Pozar, *Microwave Engineering*, 3rd ed. Hoboken, NJ: John Wiley & Sons, 2005.
- [7] A. Agarwal, V. Zolotov, and D. T. Blaauw, "Statistical clock skew analysis considering intradie-process variations," *IEEE Trans. CAD Int. Circ. Sys.*, vol. 23, pp. 1231-1242, 2004.
- [8] K. N. Chen, M. J. Kobrinsky, B. C. Barnett, and R. Reif, "Comparisons of conventional, 3-D, optical, and RF interconnects for on-chip clock distribution," *IEEE Trans. Electron Devices*, vol. 51, pp. 233-239, 2004.
- [9] U. Hilleringmann and K. Goser, "Optoelectronic System Integration on Silicon: Waveguides, Photodetectors, and VLSI CMOS Circuits on One Chip," *IEEE Trans. Electron Devices*, vol. 42, pp. 841-846, 1995.
- [10] D. A. B. Miller, "Rationale and challenges for optical interconnects to electronic chips," *Proc. IEEE*, vol. 88, pp. 728-749, 2000.
- [11] H. S. Hinton, T. J. Cloonan, F. B. McCormick, A. L. Lentine, and F. A. P. Tooley, "Free-Space Digital Optical-Systems," *Proc. IEEE*, vol. 82, pp. 1632-1649, 1994.
- [12] B. Ackland, B. Razavi, and L. West, "A Comparison of Electrical and Optical Clock Networks in Nanometer Technologies," in *IEEE Custom Integrated Circuits Conference*, 2005.
- [13] K. Bergman, "Silicon Photonic On-Chip Optical Interconnection Networks (Invited)," LEOS 2007, Orlando, FL.
- [14] C. Buchal, M. Loken, M. Siegert, A. Roelofs, L. Kappius, and S. Mantl, "Ultrafast Si-based MSM mesa photodetectors with optical waveguide connection," *Materials Science in Semiconductor Processing*, vol. 3, pp. 399-403, 2000.
- [15] M. Siegert, M. Loken, C. Glingener, and C. Buchal, "Efficient optical coupling between a polymeric waveguide and an ultrafast silicon MSM photodiode," *IEEE J. Sel. Top. Quant. Elect.*, vol. 4, pp. 970-974, 1998.
- [16] M. Nathan, O. Levy, I. Goldfarb, and A. Ruzin, "Monolithic coupling of a SU8 waveguide to a silicon photodiode," *J. Appl. Phys.*, vol. 94, pp. 7932-7934, 2003.
- [17] M. Yang, K. Rim, D. L. Rogers, J. D. Schaub, J. J. Welser, D. M. Kuchta, et al., "A high-speed, high-sensitivity silicon lateral trench photodetector," *IEEE Electron Dev. Lett.*, vol. 23, pp. 395-397, 2002.

## BACKGROUND OF OPTICAL WAVEGUIDES AND POLYSILICON DETECTORS AND THEIR CHARACTERIZATION

### **1 Introduction**

This chapter will provide background on the theory and practice of optical waveguides, with Section 2 covering Snell's Law and the concept of total internal reflection, Section 3 discussing evanescent fields, Section 4 discussing radiation modes and Section 5 discussing optical coupling via evanescent fields and radiation modes. In addition, the theory behind the polysilicon detectors used in the on-chip optical interconnects will be discussed in Section 6, including the concepts of photoconductivity and photoconductive gain. Section 7 is a discussion of Schottky contacts. DC characterization of optical waveguides and polysilicon detectors will be discussed in Sections 8. Section 9 will discuss some of the theory behind AC characterization of the detectors. Finally, a review of the literature of on-chip optical interconnects and related topics will be presented in Section 10.

It should be noted that this chapter is devoted to knowledge which existed prior to the start of the research discussed in this work. In some cases, this knowledge proved to be irrelevant or inapplicable to the structures and devices studied in this work. Those cases will be noted when the appropriate background material is discussed.

### **2 Snell's Law**

The concept of an optical waveguide is implied by Snell's Law, discovered by Willebrord Snellius in 1621. In its most basic form, Snell's Law can be stated as  $n_1 \sin \theta_1 = n_2 \sin \theta_2$ , where  $n_1$  and  $n_2$  are the indices of refraction of medium 1 and medium 2, respectively, while  $\theta_1$  and  $\theta_2$  are the angles between a propagating ray and the normal to the interface between the two materials, as shown in Figure 1. (As with almost any relationship having to do with electromagnetism, Snell's Law can be derived from Maxwell's Equations and the appropriate boundary conditions. For example, see [1], pp. 302 – 304.)

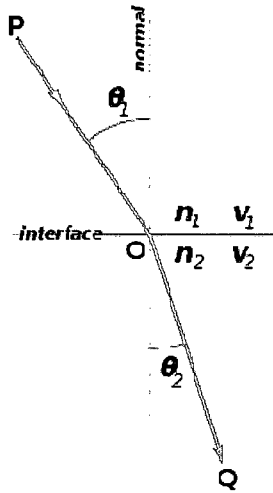


Figure 1: An example of refraction at an interface, with  $n_2 > n_1$ . From Snell's Law,  $\theta_2$  must be less than  $\theta_1$ . (Illustration adapted from [http://en.wikipedia.org/wiki/Snell%27s\\_law](http://en.wikipedia.org/wiki/Snell%27s_law))

As a concrete example, if material 1 is an optically dense medium, such as water ( $n=1.33$ ), while material 2 is an optically less dense medium, such as air ( $n=1.00$ ), then it is obvious that for some  $\theta_1$ ,  $\sin\theta_2$  must be equal to 1 for Snell's Law to be satisfied. The  $\theta_1$  for which  $\sin\theta_2$  must be 1 is called the critical angle,  $\theta_c$ . For any  $\theta_1$  greater than  $\theta_c$ ,  $\sin\theta_2$  would have to be greater than 1 to satisfy Snell's Law. As this is impossible for any real angle  $\theta_2$ , the implication is that for any angle of incidence in medium 1 greater than  $\theta_c$ , there can be no refracted ray in medium 2. The ray is, instead, reflected from the interface and undergoes total internal reflection.

This is the principle behind optical waveguides – containing optical power, by means of total internal reflection, inside an optically dense medium (the core) that is surrounded by an optically less dense medium (the cladding).

### 3 Evanescent Fields

The optical power is not completely contained within the core of a dielectric waveguide, even in the case of total internal reflection. If the optical power was completely contained within the core of the dielectric waveguide, then the electrical field would be discontinuous at the boundary between the two media. Since this is a non-physical situation, an evanescent field exists outside of the waveguide core. This evanescent field decays exponentially, over a distance on the order of a wavelength. Since in a typical situation the

cladding surrounding the core has a thickness of many wavelengths, the power in the evanescent field has decayed to zero by the time the field reaches the edge of the cladding, Thus no energy can be transferred from the waveguide core to another system by the evanescent field under typical conditions. An alternate way of looking at Snell's Law and total internal reflection provides perhaps more physical insight into the mechanism behind the creation of the evanescently propagating field. As noted above, if  $\theta_1$  is greater than  $\theta_c$ ,  $\sin\theta_2$  must be greater than one for Snell's Law to be satisfied. From a basic trigonometric

relationship,  $\cos\theta_2 = \sqrt{1 - \sin^2\theta_2} = \sqrt{1 - \left(\frac{n_1}{n_2}\sin\theta_1\right)^2} = i\sqrt{\left(\frac{n_1}{n_2}\sin\theta_1\right)^2 - 1}$ , where the

second equality follows from Snell's Law and last equality follows from the assumption that  $\sin\theta_2 \left( = \frac{n_1}{n_2}\sin\theta_1 \right)$  is greater than 1. Since  $\cos\theta_2$  is an imaginary quantity,  $\theta_2$  must be an imaginary angle. The implications of an imaginary  $\theta_2$  (i.e.  $\sin\theta_2 > 1$ ) are discussed below.

The propagation of a periodic wave can be expressed as  $e^{i\mathbf{k}\cdot\mathbf{x}}$ , where  $\mathbf{k}$  is the propagation constant  $\left( = \frac{2\pi}{\lambda} \right)$  and  $\mathbf{x}$  is the propagation vector. Considering the quantity  $\mathbf{k}\cdot\mathbf{x}$  for the refracted wave in medium 2, with the z-direction normal to the interface between mediums

1 and 2 and the x-direction parallel, we have  $e^{i\mathbf{k}\cdot\mathbf{x}} = e^{ik(x\sin\theta_2 + z\cos\theta_2)} = e^{ikx\sin\theta_2} e^{-kz\sqrt{\left(\frac{n_1}{n_2}\sin\theta_2\right)^2 - 1}}$ .

Thus for  $\theta_1 > \theta_c$  (i.e.  $\sin\theta_2 > 1$ ), we have propagation only in the x-direction (parallel to the interface), since  $e^{ikx\sin\theta_2} = e^{ikx} e^{\sin\theta_2} = C_1 e^{ikx} = C_1 \cos(kx)$ . (By convention, the imaginary part of  $e^{ikx}$  has been suppressed, since we are discussing real quantities.) In the z-direction

(perpendicular to the interface), we have  $e^{-kz\sqrt{\left(\frac{n_1}{n_2}\sin\theta_2\right)^2 - 1}} = e^{-\alpha kz}$ , or exponential attenuation.

[1]

It may be of interest to note that the existence of an evanescent field outside the core is related to the Goos-Hänchen effect, the lateral shift of an incoming ray when undergoing total internal reflection.

#### **4 Radiation modes**

In addition to the evanescent fields described above, a dielectric slab waveguide also supports radiation modes. These radiation modes are additional solutions to Maxwell's equations which satisfy the boundary conditions outside the waveguide. Since the existence of a discrete solution to Maxwell's equations in a given direction depends on the existence of boundaries on both sides in that direction<sup>3</sup> and there is only one boundary on the outside of the waveguide (i.e. the external surface of the waveguide), there exists a continuum of radiation modes.

A very crude analogy may be made between the existence of bound modes inside a dielectric slab waveguide as well as the existence radiation modes outside and the existence of bound modes inside a metal waveguide and the existence of radiation modes of an antenna. Just as the bound modes inside a metallic waveguide are normally of primary interest, the bound modes inside an optical dielectric slab waveguide are normally of primary interest. Similarly, just as an antenna can radiate electrical power independent of whether the antenna elements are solid or hollow<sup>4</sup>, an optical dielectric slab waveguide can radiate optical power whether it is solid or hollow.

#### **5 Optical coupling by means of Evanescent Fields, Leaky Modes and Radiation Modes**

As noted above, under typical situations, zero net energy is transferred by the evanescent field. However if a "non-typical" situation is arranged, the evanescent field is a means by which energy can be coupled out of the optical waveguide to another medium. Specifically, if a third material with an index of refraction higher than the cladding is placed within a few ( $<3$ ) wavelengths of the core, the evanescent wave can transmit power

---

<sup>3</sup> Consider, for example, the discrete solutions of a particle's wavefunction in an infinite two-dimensional square well. Or, more pertinently, the bound modes contained inside a dielectric slab waveguide.

<sup>4</sup> I know experimentally that antennas can receive electrical power independent of whether the antenna elements are solid or hollow, as I have built and used receiving antennas of both types. And by symmetry, if an antenna can receive electrical power, it can transmit electrical power. Note that I make no claims about relative efficiency of solid versus hollow elements, nor about their relative receive and transmit patterns, only that they both work.

from the cladding into this third material, by means of evanescent field coupling. For example, if the third material is the core of a second optical waveguide identical to the first, power will couple into the second waveguide's core. This is the principle behind optical N x M couplers and optical directional couplers.[2, 3]

Closely related to evanescent coupling is leaky-mode coupling. Leaky-mode coupling exists when there is a (partially) guided wave and the index of refraction of the waveguide core is less than the index of refraction of the substrate or cladding. The original theoretical and experimental investigation of this phenomenon in dielectric slab waveguides was performed by Hall & Yeh [4], and the theory was extended by Haus & Miller. [5] Hall & Yeh derived a leaky-mode attenuation constant of

$$\alpha \approx \frac{n^2}{16 \sqrt{\frac{\epsilon_{\text{substrate}}}{\epsilon_{\text{core}}} - 1}} \frac{\lambda^2}{a^3},$$

where the mode order  $n = 1, 2, 3, \dots$  and the thickness of the

slab waveguide is  $2a$ . Other symbols have their conventional meaning. The attenuation

constant derived by Haus & Miller was nearly identical:  $\alpha \approx \frac{n^2}{16 \epsilon_{\text{core}} \sqrt{\frac{\epsilon_{\text{substrate}}}{\epsilon_{\text{core}}} - 1}} \frac{\lambda^2}{a^3}$ . Note

that the attenuation constant increases rapidly as the wavelength increases and as the thickness of the dielectric slab waveguide decreases. Haus & Miller's derivation provides better physical insight to the leaky-mode coupling process, through analogies to Fabry-Perot resonators.

Radiation modes can also transfer power from one material (e.g. the waveguide core) to another (e.g. the detector), by effectively "broadcasting" the power out of the waveguide. It should be noted that Benech & Khalil [6] derived essentially the same attenuation constant result as Haus & Miller by treating the problem not as a leaky mode but as a group of radiation modes around a central mode which satisfied the transverse resonance of the dielectric slab waveguide.

## 6 Photoconduction and Production of Photogenerated Electron-Hole Pairs

If optical power is coupled from the waveguide core to a semiconductor with a band gap energy less than the energy of the photons, then the photons will produce electron-hole pairs (EHP) in the semiconductor. In this situation, the semiconductor can be considered as a detector of the power in the optical waveguide core, with a quantum efficiency which may or may not be equal to 1.<sup>5</sup>

Probably the two most common types of semiconductor photodetectors are photodiodes and photoconductors. In a photodiode, it is possible to have photocurrent flow with no externally applied voltage bias, due to the built-in internal electric field which exists in all diodes, including photodiodes. A photoconductor requires an external voltage bias to generate a photocurrent. The rest of this section will discuss photogenerated EHP in photoconductors, as the detectors in this work behaved like photoconductors.

In a photoconductor, photogenerated EHP will increase the electron and hole concentrations above the equilibrium value, resulting in a decrease in the resistivity of the material or equivalently, an increase in the conductivity. The change in conductivity  $\sigma$  is given by  $\Delta\sigma = q(\Delta n\mu_n + \Delta p\mu_p)$ , where  $q$  is the charge on an electron,  $\Delta n$  and  $\Delta p$  are the excess electron and hole concentrations, respectively, and  $\mu_n$  and  $\mu_p$  are the electron and hole mobilities, respectively<sup>6</sup>. If a bias voltage is applied across the photoconductor, then a photocurrent will be generated which can be detected and measured<sup>7</sup>

### 6.1 Continuity equations for holes and electrons

Before going further, it is worth writing down and briefly discussing the continuity equations for holes and electrons in the material.

---

<sup>5</sup> If each incident photon generates, on average, less than one collected EHP, the quantum efficiency is less than 1. If each incident photon generates, on average, more than one collected EHP, the quantum efficiency is greater than 1. If each incident photon generates exactly one EHP, the quantum efficiency is 1.

<sup>6</sup> This assumes that the change in carrier concentration does not affect the mobility.

<sup>7</sup> Much of the rest of this section is adapted from R.H. Bube, "Photoelectronic Properties of Semiconductors", Cambridge University Press 1992

The continuity equation for electrons is

$$\frac{\partial n}{\partial t} = G - \sum_j [n\beta_j(N_j - n_j)] + \sum_j \left\{ n_j N_c \beta_j \exp\left[-\left(\frac{E_c - E_j}{kT}\right)\right] \right\} + \frac{\nabla \cdot \mathbf{J}_n}{q}$$

The first term on the right,  $G$ , is the photoexcitation rate of electrons (and therefore holes) per unit volume per second. (e.g.  $\text{m}^{-3} \text{s}^{-1}$ )

The second term on the right represents the capture of free electrons by defects.  $n$  is the free electron concentration (equals  $n_0$ , the dark electron concentration, plus  $\Delta n$ , the photogenerated electron concentration),  $\beta_j$  is the capture coefficient ( $\text{m}^3/\text{s}$ ) for free electrons of the  $j^{\text{th}}$  type of defect,  $N_j$  is the total density of the  $j^{\text{th}}$  type of defect and  $n_j$  is the density of the electron-filled  $j^{\text{th}}$  type of defect. (i.e. A defect that already has an electron can't capture another electron.)

The third term on the right represents thermal promotion of trapped electrons to the conduction band.  $n_j$ ,  $N_j$  and  $\beta_j$  are as before,  $E_c$  is the conduction band edge energy level,  $E_j$  is the energy level of the  $j^{\text{th}}$  defect (so  $E_c - E_j$  is the energy required to promote the electron from the trap to the conduction band, leaving behind an unfilled positively ionized trap), and  $kT$  is the thermal energy.

The fourth term on the right, involving the divergence of the electron current density, represents the flow of electrons into (positive  $\mathbf{J}_n$ ) or out of (negative  $\mathbf{J}_n$ ) the volume in question.

The hole continuity equation is almost identical to the electron continuity equation:

$$\frac{\partial p}{\partial t} = G - \sum_j (p\beta_j n_j) + \sum_j \left\{ (N_j - n_j) N_v \beta_j \exp\left[-\left(\frac{E_j - E_v}{kT}\right)\right] \right\} + \frac{\nabla \cdot \mathbf{J}_p}{q}$$

The first term on the right again represents the photogeneration rate of electrons and holes.

Here, the second term on the right represents the capture of free holes by defects.  $p$  is the free hole concentration (equals  $p_0$ , the dark hole concentration, plus  $\Delta p$ , the photogenerated hole concentration),  $\beta_j$  is the capture coefficient ( $\text{m}^3/\text{s}$ ) for free holes of the  $j^{\text{th}}$  defect and  $n_j$  is the density of the electron-filled  $j^{\text{th}}$  defect. (i.e. A defect which lacks an electron to recombine with a captured hole won't remove any captured holes from the system.)

The third term on the right represents thermal promotion of trapped holes to the valence band.  $n_j$ ,  $N_j$  and  $\beta_j$  are as before,  $E_v$  is the valence band edge energy level,  $E_j$  is the energy level of the  $j^{\text{th}}$  defect (so  $E_j - E_v$  is the energy required to promote the hole from the valence band to the defect), and  $kT$  is the thermal energy.

The fourth term on the right, involving the divergence of the hole current density, represents the flow of holes into (positive  $J_p$ ) or out of (negative  $J_p$ ) the volume in question

## 6.2 Recombination centers versus traps

I am distinguishing between recombination centers, which have roughly equal capture cross-sections for holes and electrons, and traps, which have a higher capture cross-section for one carrier than the other. Recombination centers capture a carrier and hold on to it long enough that it has a chance to recombine with a carrier of the opposite type. Traps capture carriers and then release them before they can recombine with carriers of the opposite type. Recombination centers are most effective if they have energy levels near mid-gap, making it hard for a carrier to exit with just thermal energy. Traps are most effective if they have energy levels near band edges, so carriers caught in a trap are relatively easily excited from the trap to a band or vice-versa. Note that the terms “recombination center” and “trap” indicate tendencies for the defects, not definite behavior. A recombination center is mostly likely to capture two carriers of opposite and cause them to recombine, but it has some probability of releasing the captured carrier before it can recombine and thus act in a trap-like manner. Similarly, a trap is mostly likely to release a captured carrier, but it has some probability of capturing a carrier of the opposite sign, leading to recombination.

Note that a trapping (and by implication, detrapping) mechanism is different from a recombination mechanism. A trapping/detrapping mechanism captures and releases carriers at random intervals. A recombination mechanism removes carriers from the system, effectively terminating the associated current.

Further, note that if a recombination center has a time constant much longer than other times that are characteristic of the system, it may share some characteristics of a trap in terms of electrostatics. For example, if a recombination center has a lifetime in the ns range, but other characteristic times of the system are in the ps range, then from an electrostatics point of view there is little difference between the filled recombination center and a filled trap.

### **6.3 Existence of photoconductive gain<sup>8</sup>**

While it is obvious that every absorbed photon will generate, in theory, one electron-hole pair (EHP), it is not so obvious that under certain circumstances, it is possible for an absorbed photon to effectively result in more than one EHP, at least as observed by the external circuit. This is known as photoconductive gain. [7] As a result of photoconductive gain, the measured photocurrent can be higher than would be expected based on a “one collected EHP per photon” assumption.

This section is devoted to a discussion of standard photoconductive gain theory. As is discussed in Section 7.1, photoconductive gain greater than 1, as it was understood at the start of this research, required ohmic contacts. [7 - 9] When gain greater than 1 was observed in the detector response, the initial belief was that we were observing standard photoconductive gain, and that the device contacts were somehow, contrary to expectations, acting as ohmic contacts. Instead, we were observing a lesser-known photoconductive gain process that occurs in devices with Schottky contacts. Accordingly, much of this section is irrelevant in the understanding of the devices in this work. However, it is included to aid in the overall understanding of photoconductive behavior.

---

<sup>8</sup> Much of this section is adapted from R.H. Bube, “Photoelectronic Properties of Semiconductors”, Cambridge University Press, 1992.

The process of photoconductive gain in a homogeneous material may be understood qualitatively as follows.

Consider a photon which is incident on a photoconductor, and assume the photon has energy  $h\nu > E_g$ , so that it can be absorbed in the material. Further assume that the internal quantum efficiency is 1, so that each incident photon generates an electron-hole pair. (This last assumption is not critical, but it does simplify the analysis.) Further, assume that a bias voltage is applied across the photoconductor, so that the electron-hole pairs drift apart, each with some unspecified velocity. Finally, define the photoconductive gain as the number of charge carriers which pass between the contacts for each absorbed photon.

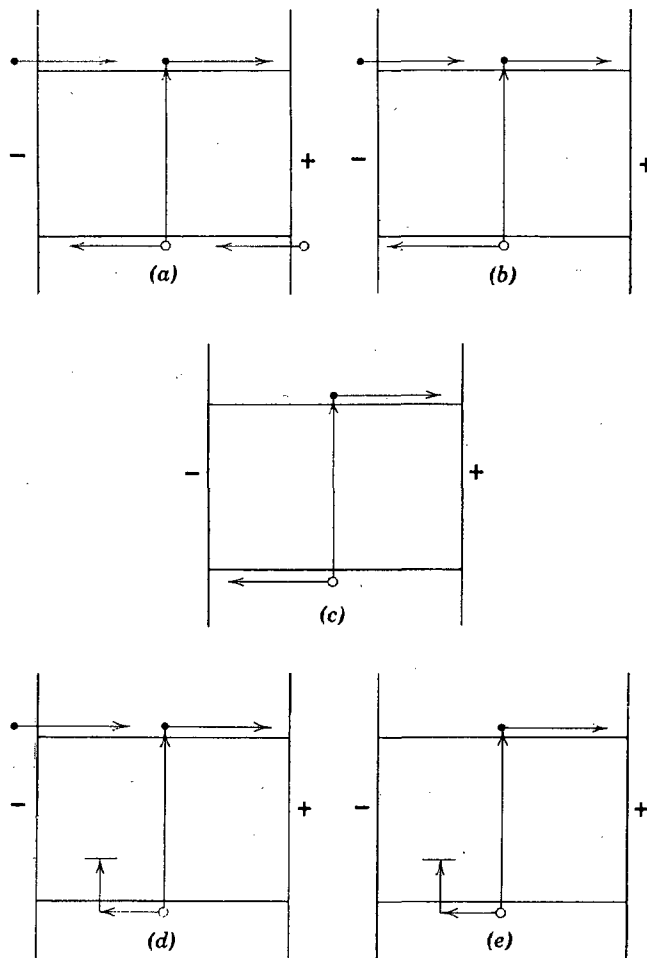


Figure 2: The five basic types of photoconductivity in a homogeneous semiconductor. The + and - signs indicate the direction of the applied external bias voltage. (Copied from Bube, "Photoconductivity of Solids", Krieger, 1978)

Figure 2 shows the five basic types of photoconductivity existing in a homogeneous semiconductor, depending on the behavior of the contacts and the importance of the capture of photogenerated electrons or holes. Each type of photoconductivity can be investigated for the possibility of gain. Scenario designations below correspond to the illustrations in Figure 2.

Scenario (a): Both electrons and holes are mobile and contacts are ohmic for both types of carriers.

This scenario has an implicit assumption that there are no traps or recombination centers. In this scenario, photogenerated EHPs separate into free electrons and holes and move through the material. When they leave the material through a contact, they are replaced until they recombine with each other. Since the gain for each carrier type can also be expressed as the ratio of the free lifetime of the charge carrier to the transit time for the carrier, the gain in this

scenario is given by  $G = \frac{\tau_n}{\tau_{trn}} + \frac{\tau_p}{\tau_{trp}} = (\tau_n \mu_n + \tau_p \mu_p) \frac{V}{S^2}$ , where  $\tau_{n,p}$  is the free lifetime of the

electron or hole,  $\tau_{trn,p}$  is the transit time for the electron or hole,  $\mu_{n,p}$  is the mobility of the carrier,  $V$  is the applied bias voltage and  $S$  is the spacing between the contacts.

Scenario (b): Both carriers are mobile but only the contact for electrons is ohmic.

Note that scenario (a) is similar to scenario (b). As in scenario (a), the gain can be expressed as the electron gain plus the hole gain. However, in this case the effective free hole lifetime is the hole transit time, since the hole is not replaced when it leaves through the contact. Due to charge neutrality, the effective free lifetime for an electron is also the hole transit time, since once the hole leaves the material there is no need to replace the electron. In this scenario, the

gain is given by  $G = \frac{\tau_n}{\tau_{trn}} + \frac{\tau_p}{\tau_{trp}} = \frac{\tau_{trp}}{\tau_{trn}} + \frac{\tau_{trp}}{\tau_{trp}} = 1 + \frac{\mu_n}{\mu_p}$ .

Scenario (c): Both carriers are mobile but neither contact is ohmic.

Note that scenario (c) is similar to scenario (b) in the same sense that scenario (b) is similar to scenario (a). Once again the gain can be expressed as the electron gain plus the hole gain. In this scenario, the free lifetime for each type of carrier is its transit time, so the gain is 1. Note

that this scenario is characterized by the occurrence of saturation of photocurrent, which occurs when the applied voltage bias creates a field strong enough to separate the carriers before they can recombine with each other.

Scenario (d): Only one type of carrier is mobile, and contacts are ohmic for only that carrier type.

For concreteness, assume that electrons are the mobile carriers. When the EHP is generated by the absorption of a photon of sufficient energy, the hole is captured nearly immediately by a trap caused by a defect in the semiconductor, so it can be considered immobile. When the photogenerated electron leaves through one contact, it is replaced at the other contact. This continues until the free electron recombines with the trapped hole. Since the hole is immobile, gain comes only from the electron gain, and is given by  $G = \frac{\tau_n}{\tau_{trn}} = \frac{\tau_n \mu_n V}{S^2}$ . Scenario (d) is the typical situation found in homogeneous photoconductors with gain  $> 1$ .

Scenario (e): Only one type of carrier is mobile and both contacts are non-ohmic.

Figure 2e shows this scenario in the case where the hole is trapped and the electron is mobile. Under this scenario, the material polarizes as the trapped charge opposes the field from the applied external voltage bias. As a result, the initial photocurrent decays with time so no steady photocurrent is observed. This behavior was observed by some of the early researchers in the field of photoconductivity.

## 7 Schottky contacts

Metal-to-semiconductor contacts can be grouped into two broad categories – ohmic or Schottky. Ohmic contacts are non-rectifying, and thus do not block injection of holes or electrons in either direction across the metal-semiconductor interface when under an applied bias. Ohmic contacts are essentially pn diodes where one side is degenerately doped. As a result, the depletion region is extremely narrow, allowing carriers to tunnel through it easily. Schottky contacts are rectifying, and can block the injection of holes or electrons when a reverse voltage bias is applied. As is well-known, Schottky contacts are majority-carrier devices. [10]

As the contacts on the devices in this work were metal on undoped polycrystalline silicon, they were expected to be Schottky contacts. The remaining discussion will focus on this type of contact.

### **7.1 Schottky contacts and their impact on device response**

In reading the known relevant literature at the start of this research, it became clear that the nature of the contacts – blocking versus ohmic – was key in determining the existence and nature of a photoconductive gain process. Specifically, the known literature by well-known and long-standing authorities in the field of photoconductivity stated that a photoconductive gain process could only occur in devices with ohmic contacts[7-9]. As a result, the existence of a photoconductive gain process in the samples, with Schottky contacts, came as somewhat of a surprise. Since this chapter is devoted to knowledge which existed prior to the start of research discussed in this work, the mechanism by which photoconductive gain exists in a photoconductor with contacts which were designed to Schottky (i.e. blocking) contacts will be deferred to a later section on experimental results. It should be noted that once experimental results made the concept of photoconductive gain in materials with Schottky contacts a viable one, literature searches turned up several examples. [11-15] In this context, Clarke’s First Law is applicable: “Whenever a distinguished but elderly scientist states that something is possible, he is almost certainly right. When he states that something is impossible, he is very probably wrong.”

### **7.2 Schottky contacts and their impact on device speed**

pn diodes have both majority and minority carrier current flow. As a result of the minority carrier injection, minority carrier storage exists while the pn junction is forward biased. If the bias is changed from forward to reverse, the minority carriers must be swept out of the junction region. This recovery time limits the speed of pn diode like structure. [16]

Since Schottky contacts are majority-carrier devices, they have no analog to minority-carrier storage, and no need to sweep out minority carriers. The recovery time of a Schottky contact is limited only by the RC delays of the structure. [16]

The capacitance of a reverse-biased Schottky contact is given by

$$\frac{C}{A} = \sqrt{\frac{q\epsilon_s N_D}{2}} / \sqrt{V_{d0} - V_r - \frac{kT}{q}},$$

where  $C$  is the capacitance,  $A$  is the area,  $q$  is the charge on an electron,  $\epsilon_s$  is the dielectric constant of the semiconductor,  $N_D$  is the dopant concentration in the semiconductor,  $V_{d0}$  is potential difference across the depletion region at zero bias,  $V_r$  is the reverse bias,  $k$  is Boltzmann's constant and  $T$  is the absolute temperature. [16]

The above Schottky capacitance equation is also valid in forward bias. Since a Schottky diode has essentially no minority carrier storage, it will have no diffusion capacitance. Because of this, the forward-bias capacitance of a Schottky diode is just the capacitance of the depletion region, as in reverse bias. [16]

Figure 3 below shows curves of the capacitance of the reverse-biased Schottky contact for various reverse biases, plotted against doping concentration. Note that increased reverse bias decreases the capacitance, by making the depletion region wider. Similarly, higher doping concentrations increase the capacitance by making the depletion region smaller.

Note that the lowest plotted doping concentration is  $1.5 \times 10^{10} \text{ cm}^{-3}$ , which is the intrinsic carrier concentration in silicon, while the highest plotted doping concentration is  $10^{14} \text{ cm}^{-3}$ , which is at least at order of magnitude higher than is plausible for the doping concentration in the undoped, or at least not intentionally doped polysilicon used for the photodetectors in this work.  $5 \mu\text{m}^2$  is used for the area of the Schottky capacitance, based on SEM photos of the Schottky contact regions. While this area assumes a  $10 \mu\text{m}$  long detector, that length is typical of the detectors used in this study. The message to be taken away from this plot is that the contact capacitance of the detectors in this work is very small, much less than a femtofarad. It should, however, be noted that while the Schottky capacitance scales linearly with detector length, the photocurrent scales sublinearly with detector length, due to the exponential nature of the light absorption along the length of the detector.

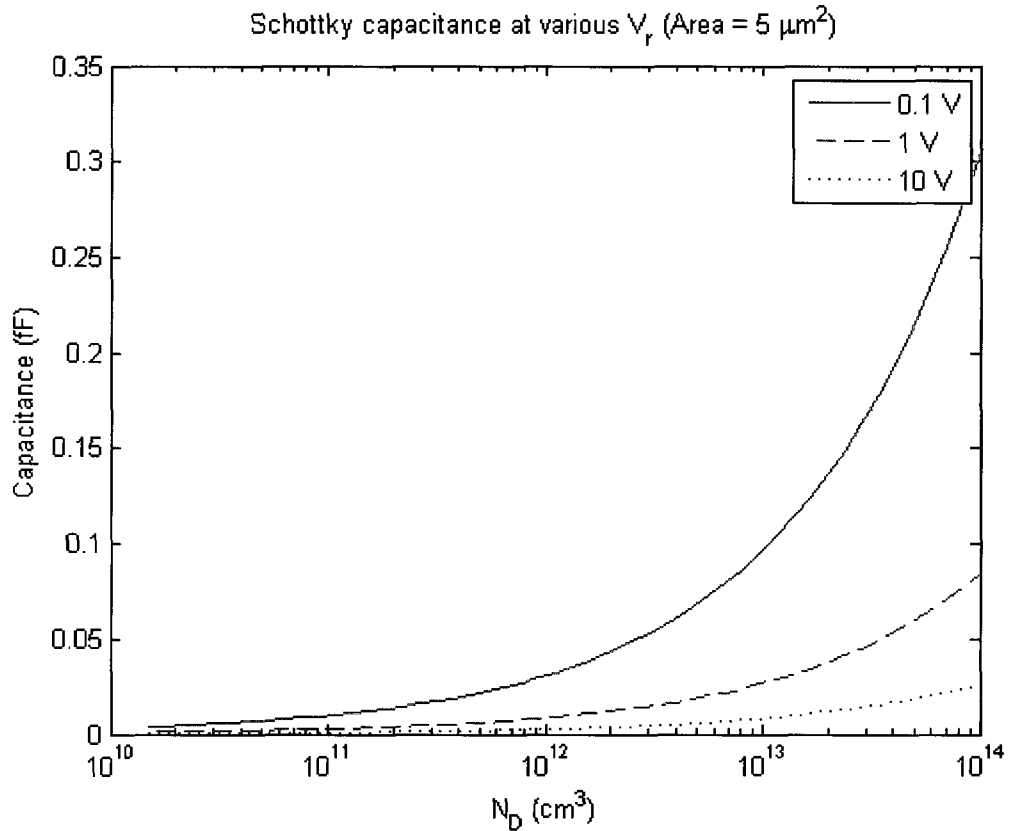


Figure 3 Reverse-bias Schottky capacitance vs. doping level at various bias voltages

From Figure 3, the worst-case capacitance is on the order of 0.3 fF. From the definition of capacitance (i.e.  $C = \frac{q}{V}$ ), to charge this capacitance to 1V would require 0.3 fC of charge. (1 V is an arbitrarily chosen value, but easy to scale.) This amount of charge would be provided by a  $1 \mu\text{A}$  photocurrent (well on the low side of typical  $10 \mu\text{m}$  long detector at reasonable bias voltages) in just 0.3 nsec. Note that RC time constants do not apply here, as the capacitance is being charged by a current source (the photocurrent), not by a source with a finite impedance. Also note that this 0.3 nsec time estimate is very much a worst-case scenario, as it assumes both an unrealistically small bias voltage and an unrealistically high semiconductor doping level.

This charging time indicates that the time to charge the zero-biased Schottky capacitance to a point where it would be forward biased is probably less than frequency-limiting delays in the system. This is an assumption which will have to be verified later, by experimental results.

Note that if the voltage across the Schottky contact is constant, then the capacitance isn't important. (If there is no  $\Delta V$ , then there is no  $\Delta q$ , no matter what the  $C$  is.) However, since in operation, the current through Schottky contact will be varying from nanoamp-level dark current to microamp-level photocurrent, and since the bias voltage across the detector structure should remain constant, assuming a constant voltage across the Schottky contact does not seem prudent. Any change across the Schottky contact should be small, though, due to the Schottky diode nature of the contact. This is analogous to the way the voltage drop across a forward-biased silicon diode is around 0.65 V over a wide range of currents.

However, since the Schottky capacitance is very small, the RC delay associated with the contacts will also be very small. In a 50  $\Omega$  system (typical of high-frequency applications), worst-case RC will be on the order of 15 fsec, implying a single-pole -3 dB frequency on the order of 10 THz. While unrealistically high – at the very least, the system will not have a single-pole response, nor has the impact of the transimpedance amplifier (TIA) used to convert the photocurrent into a voltage been considered – this value does give some idea why Schottky contacts are often used in high-frequency applications. In addition, it suggests that RC-related delays associated with the contacts may not be the limiting factor in terms of device speed.

Factors which are more likely to be limiting factors in terms of device speed are RC time constants not associated with the contacts, carrier transit times and carrier recombination lifetimes. RC time constants not associated with the contacts could come from interconnect between the detectors and the rest of the signal recovery circuitry (e.g. the TIAs). Carrier transit times may limit the performance, as mobility in polysilicon (the photodetector material) is an order of magnitude lower than in single-crystal silicon. Since absorption of photons causes the photodetector to generate an “ON” signal by creating EHPs, long carrier recombination lifetimes would slow the performance of the photodetectors, by limiting how quickly the “OFF” signal could come. Note that while long carrier lifetimes make for slow

detectors, long carrier lifetimes enhance the photoconductive gain of the device, as will be discussed later. In other words, there is a gain-bandwidth tradeoff.

## **8 DC Characterization**

### **8.1 DC Characterization of Waveguides**

As will be discussed in Chapter 3, one of the major design goals for optical waveguides is maximizing power transfer to the detector. A sub-goal of this goal was minimizing bulk and surface scattering losses in the waveguide. However, in order to minimize waveguide losses, one must first be able to measure waveguide losses.

Several methods of characterizing waveguide loss are discussed in the literature. These systems generally fall into one of two categories: systems which work by measuring how scattered power and thus guided power varies along the length of the waveguide and systems based on measuring insertion loss. In the first category are systems which rely on expensive near-field scanning apparatus [17-19], multiple high-precision stages, possibly with specialty optical fibers [20], or cameras-based techniques which require careful calibration of the imaging array and (if used) the imaging microscope objective for accurate results [21, 22] In the second category are systems which rely on time-consuming and destructive cut-back techniques. [23]

For this work, a fiber scanning system to measure waveguide loss was developed. The system measures the light scattered out of the waveguide and thus falls into the first category.

Development of the fiber scanning waveguide loss system and the results from the system will be discussed in Chapter 4.

### **8.2 DC Characteristics of Polysilicon Photodetectors**

DC characterization of the polysilicon photodetectors involves measuring the detector's dark current and the detector's photocurrent. The theoretical expectations for dark current are discussed first, in Section 8.2.1, with the photocurrent discussed in Section 8.2.2.

### 8.2.1 Dark current

If I've learned anything while going through the Ph.D process, it's that if a technical problem doesn't make sense, then I'm looking at it from the wrong direction – I need to take a step back and come at it from a different angle. Nowhere was this truer than in understanding the device physics behind the detectors. I spent a great deal of time trying to understand the devices by looking at the Schottky contacts and by trying to explain the photocurrent results first, and then the dark current results. Instead, I should have been looking at the undoped polysilicon regions and I should have been trying to explain the dark current results, then the photocurrent results.

Kamins [24] appears to be the first person to recognize the importance of traps, and therefore energy barriers, at the grain boundaries in polycrystalline silicon in reducing carrier mobility. The basic mechanism is modulation of the materials resistivity by the barrier height, with decreasing mobility at lower doping concentrations being attributed to the effects of high resistivity space-charge regions that surround the grain boundaries in polycrystalline material. Similarly, Seto [25] appears to be the first to develop a comprehensive and consistent theory of carrier transport in polysilicon. He also pointed out that under typical polysilicon conditions, thermionic emission over the potential barrier between grains would dominate field emission (tunneling) through the barrier. Baccarani, et al [26] showed that a  $\delta$ -function energy distribution of the trap states, peaked at mid-gap, best explained experimental results. Korsh and Muller [27] took the idea of thermionic emission of majority carriers over the inter-grain barriers and derived a hyperbolic sine (sinh) relationship between voltage and current:

$I = AJ = 2K \sinh\left(\frac{V_a}{\xi}\right)$ , where  $A$  is the area perpendicular to current flow,

$K = AA^*T^2 \exp\left(\frac{-qV_{BO}}{kT}\right)$  and  $\xi = \frac{2kTN}{q}$ . Here,  $A^*$  is the modified Richardson's constant

( $\approx 110 \text{ A/cm}^2\text{-K}^2$ ),  $T$  is the absolute temperature in Kelvin,  $V_{BO}$  is the barrier height at zero bias voltage,  $V_a$  is the applied bias voltage and  $N$  is the number of grain boundaries between the contacts.

Since the hyperbolic sine function is not as common as the regular sine function, its overall form may not be as familiar as the sine. For that reason, plots of  $\sinh(x)$  vs.  $x$ , for various ranges of  $x$ , are shown below, in Figure 4 through Figure 7. In Chapter 4, it will be shown that a  $\sinh$  curve closely fits observed dark current results. Note the nearly linear nature of the  $\sinh(x)$  function for small ranges of  $x$ , as shown in Figure 7, implying that the polysilicon resistors are very nearly ohmic for small voltages.

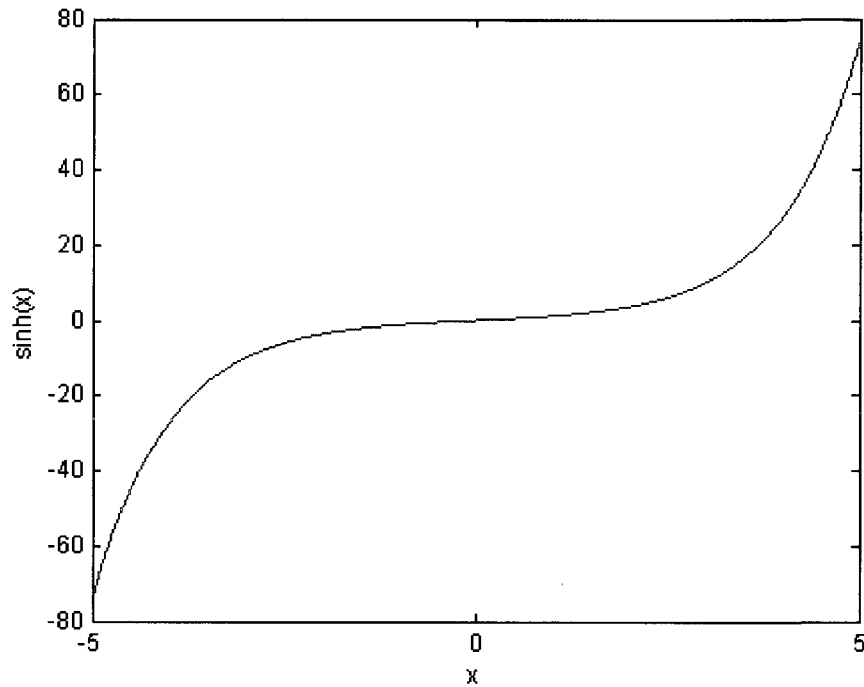


Figure 4:  $\sinh(x)$  vs.  $x$ ,  $x = -5$  to  $+5$

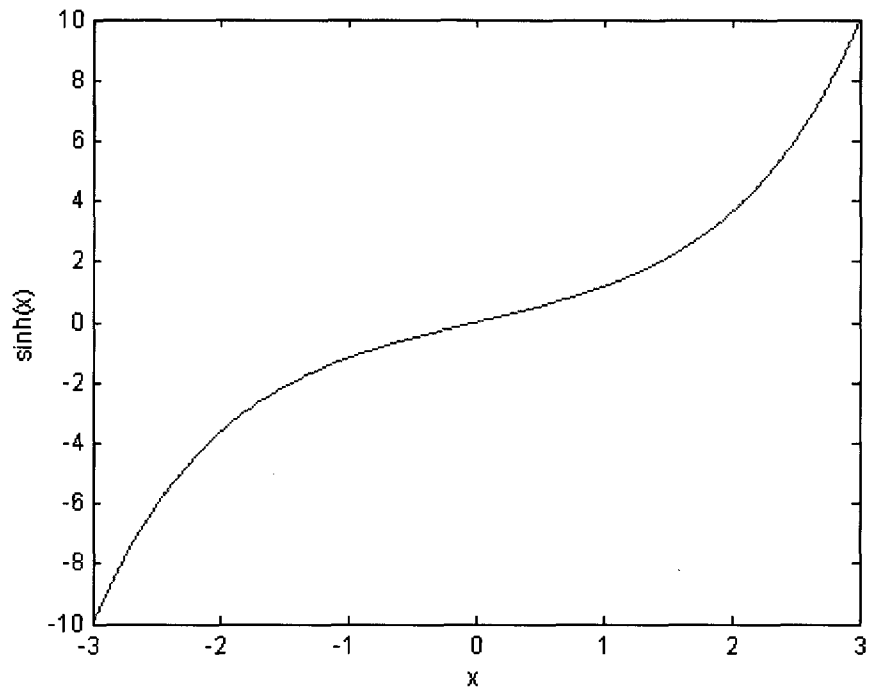


Figure 5:  $\sinh(x)$  vs.  $x$ ,  $x = -3$  to  $+3$

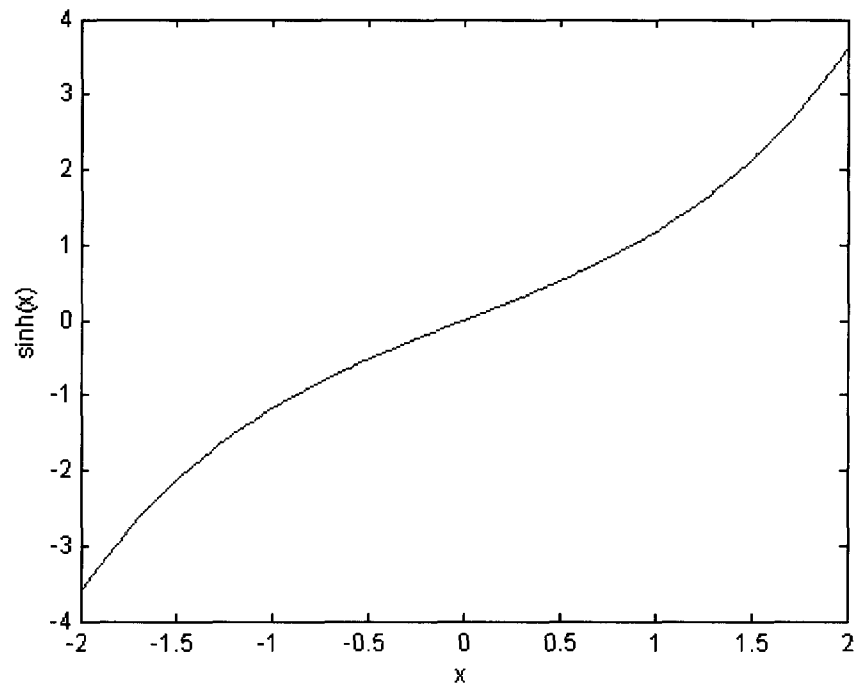


Figure 6:  $\sinh(x)$  vs.  $x$ ,  $x = -2$  to  $+2$

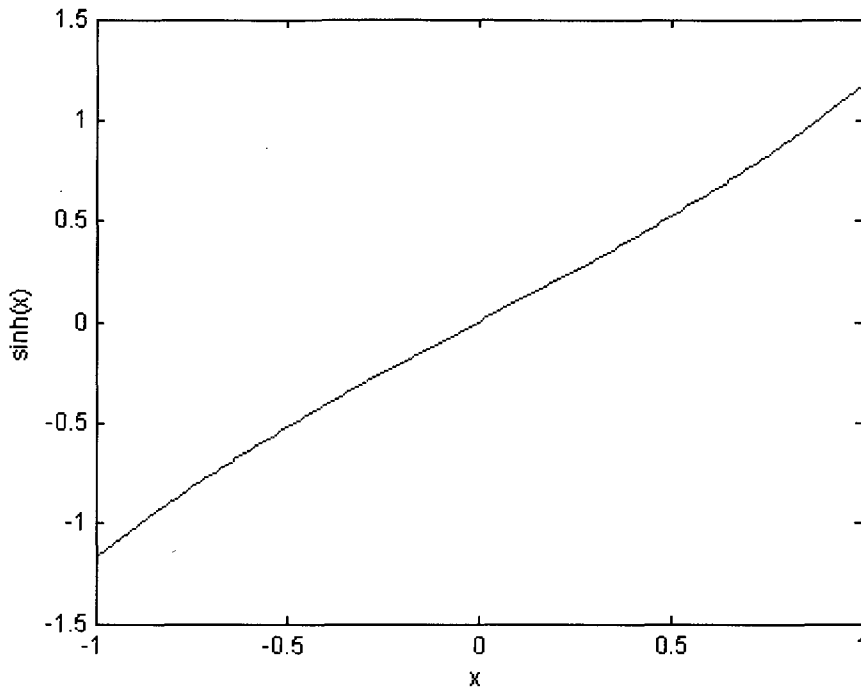


Figure 7:  $\sinh(x)$  vs.  $x$ ,  $x = -1$  to  $+1$

Several modifications to the basic theory of conductance and current flow in polysilicon, as outlined in [24, 25, 27], have been proposed. However, they are largely extensions of existing theory to large grain size polysilicon [28], cases where tunneling through the intergrain potential barrier is significant [29], high-temperature processing of the polysilicon along with differing polysilicon dopant species [30], or cases when the I-V results do not fit a sinh curve [31].

### 8.2.2 DC Photocurrent

The DC photocurrent arises from the interaction between the grain boundaries in the polysilicon and the photoconductive nature of the detectors. There are three possible models for looking at barriers and photoconductivity behavior.[7] First, photoexcitation serves to increase the free carrier density in the intergrain regions. This is essentially a standard photoconductivity problem, not a barrier problem. Second, photoexcitation increases the free carriers density in the in the grains. This will, of course, result in an increase in the free carrier density in the intergrain region as well. In the literature, this second scenario is often referred to as a “numbers” model. In the third model, the effect of photoexcitation is to reduce the

barrier height between grains, through trap-filling. This scenario is often referred to as the “mobility modulation” model.

If the polysilicon region was uniformly illuminated, it would be hard to distinguish between these three models from exterior measurements. Indeed, both a numbers model and a mobility-modulation model may be present at the same time in a given material.

This also proves to be the case with the non-uniformly illuminated photodetectors of this work. (The illumination is non-uniform because photons were leaky-mode coupled into the polysilicon from a waveguide structure that might cover as little as a quarter of the polysilicon region.) The observed data could be equally well explained by either the numbers model or the modulation model, with the carriers drifting from where they are generated under the waveguide to intergrain regions outside the waveguide region.

The photoconductive gain mechanism observed in the detectors has already been discussed, in Section 6.3.

### *8.2.3 DC responsivity*

DC characterization of the polysilicon photodetectors involves measuring the photodetector’s responsivity, or the photocurrent out of the photodetector per unit optical power into the photodetector.

In performing the DC characterization and reporting the results, specifying the test conditions is even more critical than is usually the case. For photodiodes, the test conditions found in the literature typically specify a 0 V applied bias, relying on the internal built-in field of the photodiode to generate the photocurrent. While non-zero bias voltages are sometimes used when reporting photodiode responsivity, the de-facto “0 V bias voltage” convention provides a common reference point.

In contrast, since a photoconductor requires an external voltage bias, a decision must be made about whether to hold constant the applied bias voltage or the applied electric field for all devices to be tested. Holding the bias voltage constant has the advantage that the chosen bias voltage can be one which is readily available in the target system application. However, using a

constant bias voltage typically gives a measurement advantage to smaller devices, due to the higher resulting electric fields. Holding the applied electric field constant eliminates one confounding variable, but does not reflect how the real world typically operates.

In this work, the bias voltage was generally held constant at 10 V for all devices. 10 V was chosen to be compatible with previous work done on similar devices by the Optoelectronics Research Group at Colorado State.

Since the responsivity is the photocurrent out per unit optical power, knowing the input optical power is critical. The initial proposal for determining the input optical power was to use a fiber scanning system, similar to that used to measure the waveguide loss, to scan across the waveguide leading to the photodetector. A measurement of the optical power scattered out of this waveguide, in combination with knowledge of the waveguide loss characteristics, could be used to determine the optical power reaching the detector.

This initial proposal proved to be impractical for several reasons. Possibly the two most important were that that A) the proposed system required blind placement of the sensing fiber to an accuracy of 10  $\mu\text{m}$  or better and B) the proposed system was expected to detect pW or at most nW signals scattered out of the waveguide leading to the photodetector while simultaneously keeping out any of the  $\mu\text{W}$  to mW levels signals coming from the input optical fiber which was at most 20  $\mu\text{m}$  away.

Development of the system to measure the photodetector's responsivity and the results from the system will be discussed in Chapter 4.

## **9 AC Characterization of Polysilicon Photodetectors**

### **9.1 Theoretical limits on AC performance**

#### *9.1.1 Carrier transit time effects on bandwidth*

Possibly the most obvious factor affecting the detector's response speed is the transit time of carriers across the detector.

Considering the detector as a switch, it is self-evident that the switch cannot be turned on or off significantly faster than it is possible to get carriers through the switch. Thus, for a transit time  $T$ , the maximum frequency response of the switch will be on the order of  $1/T$ .

### *9.1.2 RC time constant effects on bandwidth*

The effect of the capacitance of the Schottky contacts on the speed of the detectors has been discussed in Section 7.2. As discussed there, the capacitance of the contacts is so small, for any reasonable contact structure, that RC delays associated with the contacts are unlikely to be the limiting factor.

As an optical system, RC delays do not apply to the optical waveguides used to bring the energy in the clock signal to the detectors.

RC delays associated with the transimpedance amplifier used to convert the photocurrent to a voltage signal are beyond the scope of this work, as are RC delays associated with the local clock distribution network used to route the clock signal from the TIA to the points of direct use. They are, however, discussed in a companion work. [32, 33]

### *9.1.3 Carrier lifetime effects on bandwidth*

In addition to RC delays and transit-time limitation discussed above, carrier lifetimes also will limit the speed of the detector.

Just as a switch cannot be turned on or off significantly faster than carriers can get through the switch, a switch that relies on photo-generated electron-hole pairs (as do the detectors in this work) cannot be turned on or off significantly faster than the electrons and holes can recombine. (If the electrons and holes haven't recombined, current is still flowing through the circuit, so the switch has not turned off.)

Consider the carrier lifetime. To a first approximation, the hole and electron traps can conceptually be considered as current sources connected to an ideal photoconductor (i.e. light-dependent resistor) by switches that open and close at random, with the random switching representing the carrier lifetime.

The presence of a trapping mechanism will slow down the response of the detector, as the random discharge of electrons and holes from traps will “smear out” the on-to-off response, while the random charging of traps will have a similar effect on the off-to-on response. Note that a trapping (and by implication, detrapping) mechanism is different from a recombination mechanism. As discussed earlier, a trapping/detrapping mechanism captures and releases carriers at random intervals. While a recombination mechanism removes carriers from the system, effectively terminating the associated current. A practical example of this is the use of gold doping in the base of BJTs, to create recombination centers, thus reducing minority carrier lifetimes and increasing device switching speed.

The major problem with this approach was deciding how to model the random nature of the charge/discharge trap lifetime. After trying several models, a negative exponential lifetime distribution appeared to both provide physically-meaningful result and to fit the experimental results. In addition, a negative exponential distribution is common among decay processes.

Now that this introductory discussion is over, we can proceed to calculate the theoretical bandwidth.

Consider the current established by a photon flux that is sufficiently high that we can consider the generated EHPs statistically. The current due to each EHP will be a pulse which persists from time  $t = 0$  (when the incident photon creates the EHP) to time  $t = \tau_{n,p}$  (when the EHP recombines). The magnitude of the current due to a single EHP will be  $q(v_{n,p}/S)(1 + \tau_{n,p}\mu_{n,p}V/S^2)$ , where  $q$  is the charge on an electron,  $v_{n,p}$  is the carrier velocity,  $S$  is the spacing between contacts and  $\tau_{n,p}\mu_{n,p}V/S^2$  is the photoconductive gain discussed earlier. (Note that  $v_{n,p} = \mu_{n,p}E = \mu_{n,p}V/S$ , where  $E$  is the electric field. Note also that the  $q(v_{n,p}/S)$  term could be written simply as  $I_{ph,0}$ , the photocurrent without photoconductive gain from a single EHP. Note also that I am assuming behavior identical to that of classical photoconductive gain Scenarios (c) and (d). These are the most common scenarios seen in the literature and were believed to be those observed experimentally. However, as shown in Appendix A, the correct equation multiplies  $\mu\tau$  by a factor representing the ratio of bulk to contact recombination.

If, instead of a single EHP, we talk about the average photocurrent from an ensemble of EHPs, we have  $I_{ph} = nI_{ph,0} \left( 1 + \frac{\bar{\tau}_{n,p} \mu_{n,p} V}{S^2} \right)$ , where  $n$  is the number of EHPs and  $\bar{\tau}_{n,p}$  is the average lifetime.

Assume the lifetimes have a negative exponential distribution (as is common for decay processes) with mean  $\bar{\tau}_{n,p}$ . Then  $P(\tau) = \frac{1}{\bar{\tau}_{n,p}} \exp\left(-\frac{\tau}{\bar{\tau}_{n,p}}\right)$  where  $P(\tau)$  is the probability of a lifetime value  $\tau$ . (The  $\frac{1}{\bar{\tau}_{n,p}}$  term is so that the integral of the probability function over all  $\tau$  equals 1.)

Since the photocurrent pulse from a single EHP is  $I_{ph} = I_{ph,0} \left( 1 + \frac{\tau_{n,p} \mu_{n,p} V}{S^2} \right)$ , and will have a duration of  $\tau_{n,p}$ , the expected photocurrent from a single EHP will be  $I_{ph} = I_{ph,0} \left( 1 + \frac{\tau_{n,p} \mu_{n,p} V}{S^2} \right) P(\tau_{n,p}) = I_{ph,0} \left( 1 + \frac{\tau_{n,p} \mu_{n,p} V}{S^2} \right) \frac{1}{\bar{\tau}_{n,p}} \exp\left(-\frac{\tau_{n,p}}{\bar{\tau}_{n,p}}\right)$  (It is necessary to talk about an expected value of photocurrent from a single EHP. With only one EHP, the concept of an average value doesn't really make sense.)

Since this is a time-dependent process (i.e.  $I_{ph} = 0$  before the EHP is generated, then  $I_{ph}$  is represented by the above equation for  $0 < t < \tau_{n,p}$ , then  $I_{ph}$  again is 0 for  $t > \tau_{n,p}$ ), it is possible to do a Fourier transform and convert from the time domain to the frequency domain. (Note that the  $I_{ph}$  equation above has an implicit time-dependence, due to the pulse duration.)

Resorting to a table of Fourier transforms to determine the transform of a negative exponential, we have:

$$\begin{aligned}
I_{ph}(\omega) &= I_{ph,o} \left( \delta(\omega) + \frac{\bar{\tau}_{n,p} \mu_{n,p} V}{S^2} \frac{1}{\bar{\tau}_{n,p} j\omega \bar{\tau}_{n,p} + 1} \right) \\
&= I_{ph,o} \left( \delta(\omega) + \frac{\bar{\tau}_{n,p} \mu_{n,p} V}{S^2} \frac{1}{j\omega \bar{\tau}_{n,p} + 1} \right) \\
&= I_{ph,o} \left( \delta(\omega) + \bar{G} \frac{1}{j\omega \bar{\tau}_{n,p} + 1} \right)
\end{aligned}$$

If we concern ourselves only with the magnitude of the response, we have

$$\left| I_{ph}(\omega) \right| = I_{ph,o} \left( \delta(\omega) + \bar{G} \frac{1}{\omega \bar{\tau}_{n,p} + 1} \right).$$

Note that this is approximately the form of a standard single-pole frequency response equation. If the DC frequency  $\delta(\omega)$  term is ignored, the equation matches the single-pole frequency response equation exactly. Note also the intuitive result that good high-frequency response requires carrier lifetimes which are short. Short carrier lifetimes, though, hurt the gain.

For the negative exponential lifetime distribution and ignoring the delta-function term, the

half-power bandwidth is where  $\left( \frac{1}{\omega \bar{\tau}_{n,p} + 1} \right)^2 = \frac{1}{2}$ , or  $\frac{1}{\omega \bar{\tau}_{n,p} + 1} = \frac{1}{\sqrt{2}} = 0.707$ . Solving for  $\omega$

yields  $\omega|_{\text{half-power}} = BW = \frac{\sqrt{2}-1}{\tau_{n,p}}$ . This leads to a gain-bandwidth product of

$$GBW = \frac{\mu_{n,p} \tau_{n,p} V}{S^2} \frac{\sqrt{2}-1}{\tau_{n,p}} = \frac{8\mu_{n,p} V (\sqrt{2}-1)}{S^2} = 3.3137 \frac{\mu_{n,p} V}{S^2}.$$

Note that these are all material, device or operating condition parameters.

### 9.1.3.1 Bandwidth assuming a Gaussian lifetime model

The other major lifetime model which was considered was that of a Gaussian distribution, instead of a negative exponential distribution. It is interesting to go through the frequency response calculations for this case, if for no other reason than the fact that as the standard

deviation of a Gaussian lifetime distribution tends to zero, the distribution tends to approach that of a single lifetime model.

Assume the lifetimes have a Gaussian distribution with mean  $\bar{\tau}_{n,p}$  and standard deviation  $\sigma_{n,p}$ ,

so  $P(\tau) = \frac{1}{\sigma_{n,p} \sqrt{\pi}} \exp\left[-\frac{(\tau - \bar{\tau}_{n,p})^2}{\sigma_{n,p}^2}\right]$ , where  $P(\tau)$  is the probability of a lifetime value  $\tau$ .

The  $\frac{1}{\sigma_{n,p} \sqrt{\pi}}$  term is so that the integral of the probability function over all  $\tau$  equals 1. Also

assume, for now, that  $\bar{\tau}_{n,p} \geq 4\sigma_{n,p}$ , so that there is essentially no probability of an EHP having a non-physical lifetime  $\tau < 0$ . (The fact that a non-physical lifetime is even mathematically possible when using a Gaussian lifetime model was one of the attractions of the negative exponential lifetime model.)

Since the photocurrent pulse from a single EHP is  $I_{ph} = I_{ph,0} \left( \frac{\tau_{n,p} \mu_{n,p} V}{S^2} \right)$ , and will have a

duration of  $\tau_{n,p}$ , the expected photocurrent from a single EHP will be

$$I_{ph} = I_{ph,0} \left( \frac{\tau_{n,p} \mu_{n,p} V}{S^2} \right) P(\tau_{n,p}) = I_{ph,0} \left( \frac{\tau_{n,p} \mu_{n,p} V}{S^2} \right) \frac{1}{\sigma_{n,p} \sqrt{\pi}} \exp\left[-\frac{(\tau_{n,p} - \bar{\tau}_{n,p})^2}{\sigma_{n,p}^2}\right]$$

As noted

elsewhere, we have to talk about an expected value of photocurrent from a single EHP. With only one EHP, the concept of an average value doesn't really make sense.

Since this is a time-dependent process (i.e.  $I_{ph} = 0$  before the EHP is generated, then  $I_{ph}$  is represented by the above equation for  $0 < t < \tau_{n,p}$ , then  $I_{ph}$  again is 0 for  $t > \tau_{n,p}$ ), we should be able to do a Fourier transform and convert from the time domain to the frequency domain. Note that the  $I_{ph}$  equation above has an implicit time-dependence, due to the pulse duration.

As is well-known, the Fourier transform of a Gaussian is also a Gaussian and the Fourier transform of a constant is a delta function. Since the pulse duration,  $\tau_{n,p}$ , is assumed to be a Gaussian as described above, we have:

$$\begin{aligned}
I_{ph}(\omega) &= I_{ph,0} \left( \delta(\omega) + \frac{\mu_{n,p} V}{S^2} \frac{\bar{\tau}_{n,p}}{\sigma_{n,p} \sqrt{\pi}} \exp(-j\bar{\tau}_{n,p}\omega) \sqrt{\pi} \sigma_{n,p} \exp \left[ - \left( \frac{\omega \sigma_{n,p}}{2} \right)^2 \right] \right) \\
&= I_{ph,0} \left( \delta(\omega) + \frac{\mu_{n,p} V}{S^2} \bar{\tau}_{n,p} \exp(-j\bar{\tau}_{n,p}\omega) \exp \left[ - \left( \frac{\omega \sigma_{n,p}}{2} \right)^2 \right] \right) \\
&= I_{ph,0} \left( \delta(\omega) + \bar{G} \exp(-j\bar{\tau}_{n,p}\omega) \exp \left[ - \left( \frac{\omega \sigma_{n,p}}{2} \right)^2 \right] \right)
\end{aligned}$$

where  $\bar{G}$  is the photoconductive gain term.

If (as assumed above),  $\tau_{n,p} = 4\sigma_{n,p}$ , we have

$$I_{ph}(\omega) = I_{ph,0} \left( \delta(\omega) + \bar{G} \exp(-j\bar{\tau}_{n,p}\omega) \exp \left[ - \left( \frac{\omega \tau_{n,p}}{8} \right)^2 \right] \right) \quad \text{Note that this means that the}$$

photoconductive gain term is frequency dependent. (Not surprising, since it's the trap/lifetime dependent term.)

The  $\exp(-j\bar{\tau}_{n,p}\omega)$  term represents a frequency-dependent phase factor. Since this term is multiplying other terms, it's easiest to deal with it in polar form, with magnitude 1 and angle  $-\bar{\tau}_{n,p}\omega$  (i.e.  $1 \angle -\bar{\tau}_{n,p}\omega$ ). In fact, it's even easier just to ignore the phase dependence entirely, at

least for now, leading to  $|I_{ph}(\omega)| = I_{ph,0} \left( \bar{G} \exp \left[ - \left( \frac{\omega \tau_{n,p}}{8} \right)^2 \right] \right)$ , under the assumption that the

DC frequency  $\delta(\omega)$  term can be ignored. (Again, this assumes  $\tau_{n,p} = 4\sigma_{n,p}$ . If  $\tau_{n,p} = 3\sigma_{n,p}$ , then the denominator in the exponential becomes 6. If  $\tau_{n,p} = 5\sigma_{n,p}$ , then the denominator in the exponential becomes 10.)

If the delta-function term is ignored, the half-power bandwidth is

where  $\left( \exp \left[ - \left( \frac{\omega \tau_{n,p}}{8} \right)^2 \right] \right)^2 = \frac{1}{2}$ , or  $\exp \left[ - \left( \frac{\omega \tau_{n,p}}{8} \right)^2 \right] = \frac{1}{\sqrt{2}} = 0.707$ . Solving for  $\omega$ , we

find  $\omega|_{\text{half-power}} = BW = \frac{8\sqrt{\ln(\sqrt{2})}}{\tau_{n,p}}$ . Since the low-frequency gain is  $G = \frac{\mu_{n,p}\tau_{n,p}V}{S^2}$ , the gain-

bandwidth product (assuming a Gaussian lifetime) is

$$GBW = \frac{\mu_{n,p}\tau_{n,p}V}{S^2} \frac{8\sqrt{\ln(\sqrt{2})}}{\tau_{n,p}} = \frac{8\mu_{n,p}V\sqrt{\ln(\sqrt{2})}}{S^2} = 4.7096 \frac{\mu_{n,p}V}{S^2},$$

all of which are material,

device or operating condition parameters. If  $\sigma=3\tau$ ,  $GBW = 3.5322 \frac{\mu_{n,p}V}{S^2}$ . If  $\sigma=5\tau$ ,

$$GBW = 5.8871 \frac{\mu_{n,p}V}{S^2}.$$

Note that the GBW product for the negative exponential lifetime distribution above is very close to the GBW product for a Gaussian distribution with  $\sigma=3\tau$ .

### 9.1.3.2 Predicted frequency response

A  $\mu\tau$  value of  $1.79 \mu\text{m}^2/\text{V}$  at a bias voltage of 10 V was derived for first-generation material by

fitting the theoretically expected  $I_{ph} = I_{phl} \left( 1 + \frac{\mu_n \tau_n V}{S^2} \right)$  curve to experimental data. [34]<sup>9</sup> A

lower bound on  $\tau$  can be obtained by assuming  $\mu_n = 1360 \text{ cm}^2/\text{V-s}$ , the single-crystal value,

leading to  $\tau = 13.2 \text{ ps}$ . A more realistic value for  $\tau$  can be obtained by using a mobility value

of  $1.9 \text{ cm}^2/\text{V-s}$  found in the literature for undoped polysilicon deposited under conditions

similar to the undoped polysilicon of this work's detectors. [35] This leads to  $\tau = 9.42 \text{ ns}$ .

Plots of the theoretical frequency response for the negative exponential and Gaussian lifetime

models, and for the single-crystal and literature polysilicon mobility values are shown in Figure

8 through Figure 11. Note that the Gaussian model approaches a single-lifetime model as the

$\sigma/\tau$  ratio goes down.

---

<sup>9</sup> As noted in Appendix A, this theoretical equation overlooked a K factor which multiplies  $\mu\tau$  and which represents the ratio of bulk to contact recombination.

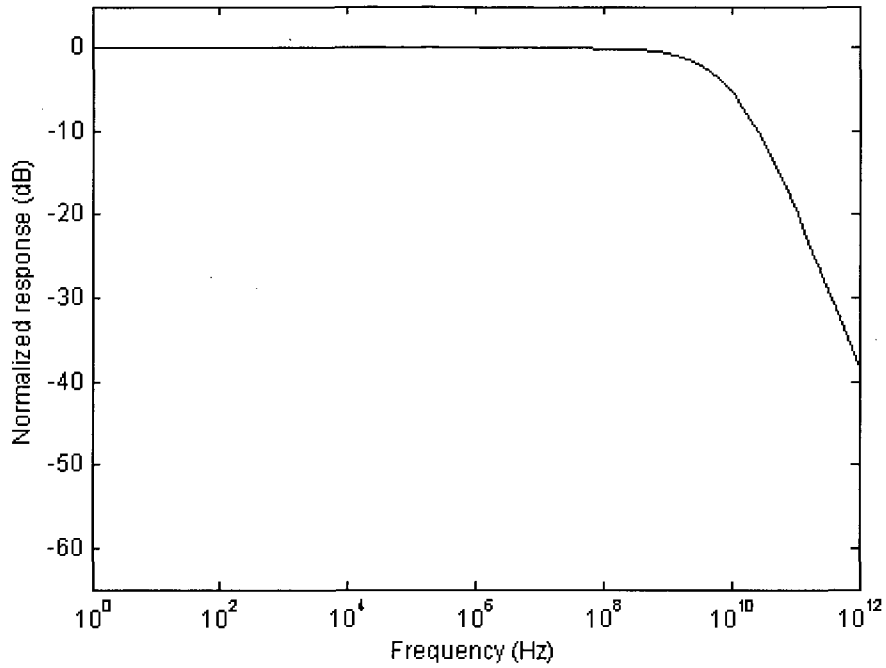


Figure 8: Theoretical frequency response for the negative exponential lifetime model, assuming single-crystal mobility of  $1360 \text{ cm}^2/\text{V}\cdot\text{s}$ . -3dB frequency is 5.0 GHz.

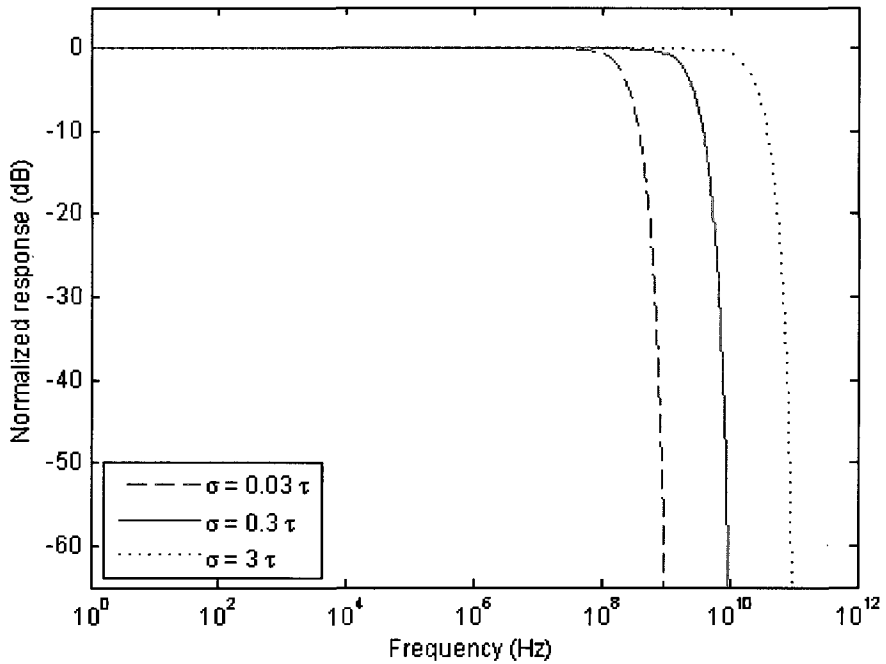


Figure 9: Theoretical frequency response for the Gaussian lifetime model, assuming single-crystal mobility of  $1360 \text{ cm}^2/\text{V}\cdot\text{s}$ . -3dB frequencies are 210 MHz for  $\sigma = 0.03\tau$ , 2.1 GHz for  $\sigma = 0.3\tau$ , and 21 GHz for  $\sigma = 3\tau$ .

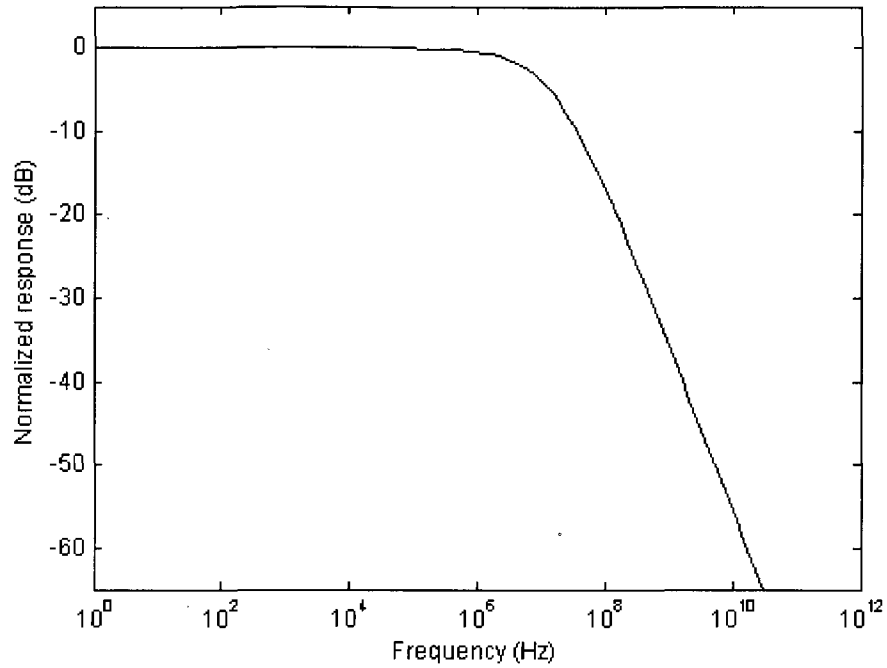


Figure 10: Theoretical frequency response for the negative exponential lifetime model, assuming a mobility of  $1.9 \text{ cm}^2/\text{V-s}$ , from the literature. -3dB frequency is 6.9 MHz.

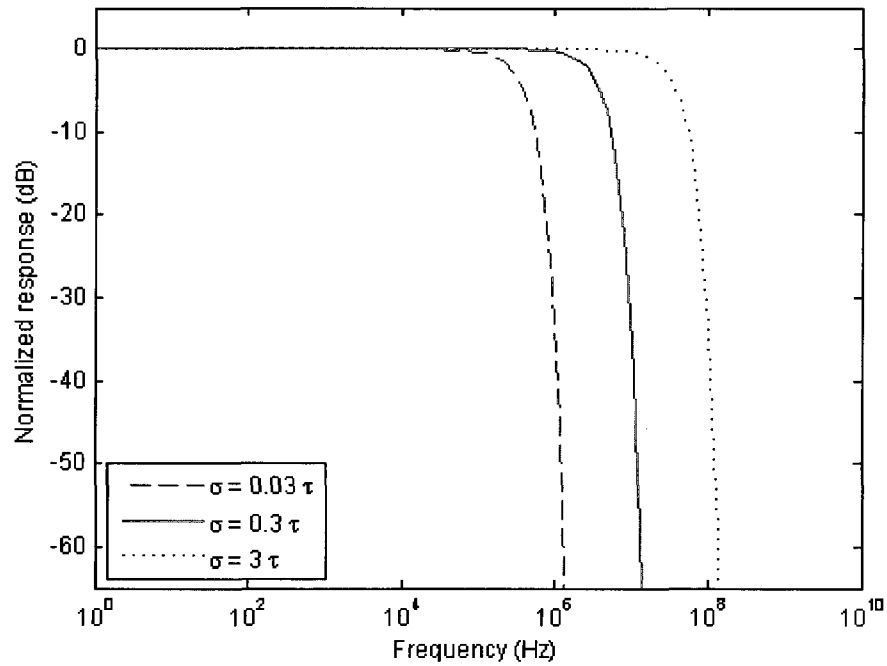


Figure 11: Theoretical frequency response for the Gaussian lifetime model, assuming a mobility of  $1.9 \text{ cm}^2/\text{V-s}$ , from the literature. -3dB frequencies are 290 kHz for  $\sigma = 0.03\tau$ , 2.9 MHz for  $\sigma = 0.3\tau$ , and 29 MHz for  $\sigma = 3\tau$ .

### 9.1.3.3 *Experimental evidence in favor of either the negative exponential or Gaussian models*

As noted earlier, the possibility of a non-physical negative lifetime when using a Gaussian lifetime distribution was one of the attractions of the negative exponential lifetime model. However, as will be discussed in Chapter 5, I was not able to obtain experimental data at a high-enough frequency to provide convincing proof of in favor of either the negative exponential model, the Gaussian lifetime model, or the single-lifetime model (the small variance limit of the Gaussian lifetime model.)

Obtaining higher frequency experimental data is an item in the “Future Work” section. From the slope of the frequency response at high frequencies, it will be possible to determine whether a negative exponential or Gaussian lifetime model fits the data better.

With a value for  $\mu$  from the literature, and the extracted value for  $\tau$  using this  $\mu$ , it is worth noting that for a field strength of  $5 \times 10^4$  V/cm (e.g. 10 V across a 2  $\mu\text{m}$  contact spacing detector), carriers will travel 8.95  $\mu\text{m}$  before recombining, on average. Since photoconductive gain depends on carriers living long enough to transit the detector at least once before recombining, the numbers are internally consistent. (i.e. Photoconductive gain would be significant for a 2  $\mu\text{m}$  contact spacing detector, but not for a 10  $\mu\text{m}$  contact spacing detector. At 10 V, carrier lifetime and transit time would match for a 4.23  $\mu\text{m}$  contact spacing device.)

## 9.2 **General concepts related to characterization of AC performance**

When considering the AC characterization of any system, it is important to keep in mind the purpose of the system. For example, when considering the AC response of an audio or RF amplifier, one is primarily interested in the magnitude of the gain of the amplifier and linearity (“flatness”) of the gain response with frequency.

For detectors to be used in an on-chip optical interconnect application, one needs to keep in mind that the input of the detector will be a square-wave-modulated optical signal, representing the clock signal of the integrated circuit, and that the output of the detector should accurately reproduce this square wave in an electrical signal. In such an application, the primary parameters of interest are the rise and fall times of the modulated signal. If the rise

time or fall time of the detector's output is too slow, then the detector will not be able to be modulated as quickly as necessary to keep up with the optical input.

Characterization of the AC response of the polysilicon detectors – the speed of the detectors – can be done in either the time domain or the frequency domain. This characterization will be discussed in the next two sections, with frequency domain characterization first.

### 9.3 Frequency-domain characterization of AC performance

Frequency domain characterization of the detector relies on the Fourier decomposition of the desired square wave output. Figure 12 shows the construction of the approximation of a square wave by summing its fundamental frequency and first eight harmonics. Note that the Fourier decomposition of a square wave contains only odd harmonics.

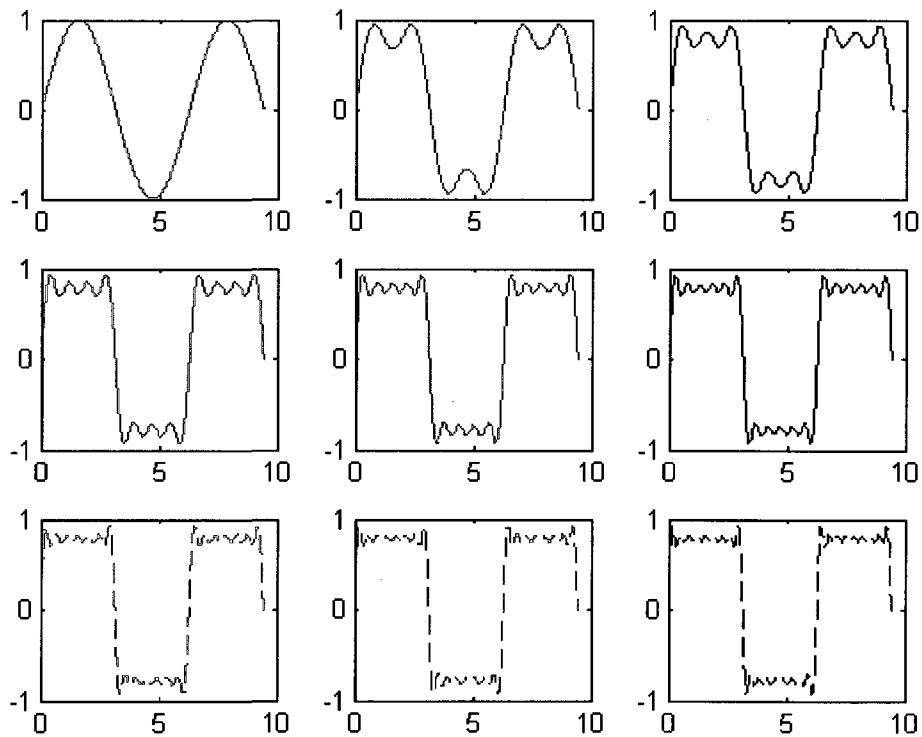


Figure 12: Construction of a square wave from its fundamental frequency and harmonics as discussed in the text.

The fundamental alone is in the upper left corner of Figure 12. As the plots move from left to right and from top to bottom, an additional odd harmonic is added. (i.e. The plot in the center row, right-most column contains the fundamental and the first five odd harmonics.)

While how many harmonics need to be added to obtain an adequate square wave depends on the definition of “adequate”, it is obvious that all but the least demanding applications will require at least the first two odd harmonics (i.e. the fundamental plus the third and fifth harmonics), while more than the first five odd harmonics will only be required if the application is particularly demanding.

Therefore, to accurately reproduce an integrated circuit square-wave clock signal, the detectors should have a frequency response extending to at least five times the frequency of the clock signal, but probably won’t need a response more than 11 times the frequency of the clock signal.

As an unrelated note, the overshoot seen near the high-to-low and low-to high discontinuities of the plots in Figure 12 is known as the Gibbs phenomenon, and is a characteristic of the Fourier series at discontinuities. [36] The Gibbs phenomenon is especially noticeable on the plots with higher numbers of harmonics, and cannot be removed by adding more harmonics.

#### **9.4 Time-domain characterization of AC performance**

Time domain characterization of the detectors’ speed is straightforward. Namely, pulse the laser diode on-and-off, and then observe the resulting photocurrent on an oscilloscope display.

This could be done using a sinusoidal input to the input optical source (a laser diode), but it is much more practical to drive the input optical source with a square wave or an impulse. (With a sine wave, the source would only be on during the portion of the waveform above threshold, and the output of the source would vary with the magnitude of the sine wave during the “above threshold” portion. With a square wave input, once the amplitude of the square wave is above threshold, the source output is as constant as the driving square wave.)

In either case, the rise and fall times of the detector can be observed directly on an oscilloscope of sufficient speed. If an impulse is used, then the resulting full-width half-max

(FWHM) of the output photocurrent pulse can be observed. From the pulse's FWHM, information about the frequency response of the detector can be deduced. If a square wave is used, then the rise and fall times can be read directly off the oscilloscope trace.

## 10 Literature review of optical interconnects<sup>10</sup>

The mid-1980s to the early 1990s was the period where basic concepts in the field of on-chip optical interconnect were being established. Goodman, et al published the first paper to bring the possibility of optical interconnects to a widespread audience. [37] Their 1984 paper highlighted many of the future challenges and opportunities in the field, such as interconnect-delay-limited circuits, the advantages of optical methods for global clock distribution, and possible optical interconnect technologies and components. In 1986, Bowers and Burrus published the first results from waveguide-based photodetectors. [38] Their structure was an InGaAsP PIN waveguide device, and they reported an equipment-limited FWHM impulse response at 4 V bias of 34 ps, a packaging-limited -3dB frequency of 28 GHz, a quantum efficiency of 35 % at 4 V bias and an effective absorption coefficient of  $2.3 \mu\text{m}^{-1}$ . Hilleringmann and Gosser published several seminal papers in the field of optical interconnections, starting in 1991. [39-41] These papers (some written with co-authors) described the development of monolithically integrated electrooptical systems of waveguides, photodetectors and VLSI CMOS circuitry. Uncertainties in the amount of coupled optical power prevented determination of quantum efficiency and absorption coefficients. 1 MHz frequencies were measured.

During the late 1990s, novel detector and waveguide structures and materials were increasingly investigated. In 1996, Diaz, et al [42] published results on resonant-cavity photodiodes which were compatible with standard silicon processing. They reported quantum efficiencies of 44% and bandwidths in excess of 1.4 GHz. In 1997, this work was extended by Bean, et al [43], to bandwidths of 10 GHz, along with improved dark current. Also in 1997, Maiello, et al [44] reported some early results on amorphous silicon waveguide photodetectors and oxidized porous silicon waveguides which were buried in the silicon substrate. Optical interconnects were obviously becoming an area of increased

---

<sup>10</sup> A tabular summary of key results from the waveguide interconnect papers discussed in this section is at the end of this section.

research interest by 1997, as in that year Moreno & Calderer [45] published work on lateral photodetectors using an ARROW (Anti-Resonant Radiative Optical Waveguide) structure to couple optical power from the waveguide to the amorphous silicon PIN photodetector. The authors reported waveguide loss results as low as 0.3 dB/cm and detector coupling greater than 100 dB/cm. However, the authors obtained this high value by growing the PIN photodiode on top of an indium tin oxide (ITO) electrode layer. In addition to requiring the use of amorphous silicon in the PIN photodiode, ITO is not commonly used in standard integrated circuit processing. In 1998, Benaissa, et al [46] reported results from a ARROW structure compatible with standard integrated circuit processing. The authors report waveguide loss around 1 dB/cm and leaky-wave attenuation to the detector generally around 10 dB/cm, but as high as 180 dB/cm in some situations for one of the three detector structures they studied. The authors attributed this high value to their processing resulting in a thin second cladding underneath the first cladding (presumably enhancing the ARROW effect) as well as core mismatch / misalignment at the ARROW waveguide / detector boundary exciting higher order modes with higher attenuation coefficients. System quantum efficiency (from laser source to detector) was estimated to be between 0.5 to 2%, while responsivity was around 0.01 A/W at a reverse bias of 1V.

Towards the end of the 1990s, concern for compatibility with CMOS processing began to be more prominent. In 1998, Siegert, et al [47] published results from a polymeric waveguide structure coupled to a metal-semiconductor-metal (MSM) silicon mesa photodetector sandwiched between a  $\text{CoSi}_2$  bottom electrode and a transparent Cr top electrode. They reported quantum efficiencies around 35% when light is laterally coupled to the detector by polymer waveguide. Normal incidence excitation of the detectors resulted in 3.5 psec full-width half-max (FWHM) pulses at room temperature. It is debatable, however, just how compatible polymeric waveguides, even the heat-resistant polymeric waveguides used in the author's work, are with conventional CMOS processing.<sup>11</sup> In 1999, MacDonald, et al [48] reported achieving a -3 dB bandwidth of 750MHz and a responsivity of 0.13 A/W at 680 nm and 12 V bias on interdigitated normal

---

<sup>11</sup>  $\text{CoSi}_2$  and Cr, however, are quite compatible with standard CMOS processing. For example, both Intel and Freescale use  $\text{CoSi}_2$  to obtain low-resistance source/drain regions.

incident MSM photodetectors which were fabricated on polysilicon. Internal quantum efficiency was a reasonably good 54%, while external quantum efficiency was 19%. Unfortunately, dark current was a relatively high 1.1  $\mu\text{A}$ . Processing was compatible with standard CMOS, however the 12 V bias requirement would require some special circuitry such as an on-chip switching power supply. Similar supplies, however, are already in use in DRAM chips. Buchal, et al [49] in 2000 extended the work reported in Siegert, et al [47], achieving quantum efficiencies of 4.6% at 800 nm (quite low) and FWHM pulse widths of 3.2 psec from normal incidence 1250 nm light. As in the earlier work, the devices used polymer waveguides and silicon-mesa MSM photodetectors, so the same concerns about compatibility of polymeric waveguides with standard integrated circuit processing applies. Also in 2000, Miller published an excellent review of the current status of work on on-chip optical interconnects. [50] While focused mainly on board-level interconnects, Cho, et al's 2002 paper [51] presented a number of interesting concepts, using benzocyclobutane polymer waveguides and embedded thin-film InGaAs photodiodes to achieve responsivity of 0.38 A/W at 5 V bias (wavelength not specified), as well as FWHM pulse widths of 16.73 psec. While several interesting concepts were developed in the paper, the use of polymer waveguides and embedded thin-film detectors largely eliminates the use of the techniques presented in the paper for on-chip optical interconnects in a standard CMOS process. In contrast, DeVries, et al's paper of the same year [52] (which appears to be an extension of MacDonald's 1999 work [48]) uses standard CMOS techniques to create normal incidence MSM with a -3 dB bandwidth of 1.5 GHz. Unfortunately, responsivity is a very low 0.008 A/W at a wavelength of 980 nm and a 4 V bias. The reported absorption coefficient is  $2.5 \times 10^3 \text{ cm}^{-1}$ . Also in 2002, El Kurdi, et al [53] reported on photodetectors made of Ge/Si self-assembled islands embedded in rib waveguides constructed from silicon-on-insulator wafers. While a novel concept, the responsivity of 0.025 A/W at 1300 nm and 0.00025 A/W at 1550 nm at 0 V bias were too low to be of interest for on-chip optical interconnect applications. Another interesting paper from 2002 is Yang, et al [54], where the authors used VLSI-compatible processing to create a trench structure photodetector which decoupled carrier transit distance from light absorption depth. The authors report a -6 dB bandwidth of 1.6 GHz at a 3 V bias and 845 nm, and a responsivity of 0.47 A/W. This responsivity value corresponds to an external quantum efficiency of

68%. One major drawback of this technology is that the detectors must be placed in the silicon substrate, thus taking up valuable silicon real estate. In addition, since the detectors use vertically incident light, the space above the trench must be kept clear of metal lines and other circuitry, so that vertically incident light can reach the trench. This is a significant restriction on circuit layout. In 2003, Jokerst, et al [55] published a very interesting review paper on integrating optical interconnections into board, package and chip-level systems, highlighting the existing challenges and existing techniques being used to meet them. Nathan, et al paper [56], also in 2003, presented results on coupling light from SU8 polymer waveguides to silicon pn diodes in monolithically integrated structures. Reported responsivity values of 0.33 A/W at 633 nm and 0.2V reverse bias is quite good. Reported waveguide attenuation was quite high, between 1.9 and 2.9 dB/mm. This high value was attributed to large sidewall roughness of the waveguide. Since this technique shares the problems of other polymer waveguides, in terms of integration into standard CMOS processing, this high waveguide loss probably means this technique is not a promising candidate for on-chip optical interconnects.

Given all the work going into on-chip optical interconnects, it is not surprising that people began publishing theoretical analyses of and comparisons between various types of alternative interconnect technologies. Chen, et al's 2004 paper [57] provides a useful comparison between conventional, 3-D, optical and RF interconnect technologies for on-chip clock distribution. One of their main conclusions is that most of the clock skew and power consumption are associated with local, not global, clock distribution. Since most alternative clock distribution techniques are focused on global clock distribution, they claim that they have no significant advantage over conventional (i.e. metal lines) clock distribution. In any technology associated with integrated circuits, people are interested in what Intel thinks and is doing. Accordingly, Kobrinsky, et al's 2004 review paper on on-chip optical interconnects make for interesting reading. [58] Cassan, et al, 2005 paper [59] is a theoretical analysis and comparison of electrical and optical global clock distribution, in terms of pulse spreading, clock skew and jitter, temperature sensitivity and power consumption, and provides an interesting contrast to Chen, et al's 2004 paper mentioned above.

In addition to the work discussed above, which is directly related to on-chip optical interconnects, work was taking place in the area of board-level optical interconnects, with at least some relevance to on-chip optical interconnects. Seo, et al's paper in 2005 [60] appears to be somewhat of an extension of Cho's 2002 work mentioned earlier. In it, the authors use polyimide polymer waveguides on a Si-SiO<sub>2</sub> substrate to couple light to InGaAs MSM photodetectors which are fabricated and characterized separately, then bonded to the Si substrate. Responsivity for the photodetectors is reported as 0.38 A/W at 1300 nm (bias voltage was not specified), while waveguide propagation loss is reported as 0.58 dB/cm (0.058 dB/mm) at 1300 nm. While this may be a promising technique for board-level interconnects, the complexity of flip-chip bonding photodetectors to a die makes this a likely candidate for on-chip optical interconnect applications.

Table 1: Summary of DC results from optical interconnect-related papers. WG loss and detector attenuation are in dB/cm. Responsivity values in **bold-face** are calculated from wavelength and quantum efficiency, and assume that the Q.E. is an external value.

Lead Author	Year	$\lambda_{\text{WG}}$ (nm)	WG core	WG cladding	WG loss	$\lambda_{\text{Det}}$ (nm)	Detector material	Q.E. $\eta$ (%)	Atten.	R (A/W)
Bowers	1986		InGaAsP	InP		1060	InGaAsP	35		<b>0.30</b>
Hilleringman	1995	633	SiON	SiO <sub>2</sub> rib	<0.5		Si			
Diaz	1996					660	poly-Si	44		<b>0.23</b>
Bean	1997					650	poly-Si	40		<b>0.21</b>
Moreno	1997	650	SiO <sub>2</sub>	SiN <sub>x</sub>	<0.3	<b>650</b>	$\alpha$ -Si		>100	
Benaissa	1998	633	SiO <sub>2</sub>	SiN <sub>x</sub>	1	633	Si	2	180	.01
Siegert	1998		polymer	SiO <sub>2,air</sub>		800	Si	35		<b>0.23</b>
MacDonald	1999					860	poly-Si	19		0.13
Buchal	2000	800	polymer	SiO <sub>2,air</sub>	3.85	800	epi-Si	4.6		0.036
Cho	2002	1300	polymer	SiO <sub>2</sub>	0.36	?	InGaAs			0.38
DeVries	2002					980	poly-Si			0.008
El kurdi	2002		Si	SiO <sub>2,air</sub>		1300	Ge/Si	2.35		0.025
Yang	2002					845	poly-Si	68		0.47
Nathan	2003	633	polymer	SiO <sub>2,air</sub>	29	633	Si		30	0.33
Seo	2005	1300	polymer	SiO <sub>2,air</sub>	0.58	1300	InGaAs			0.38
this work, 1 <sup>st</sup>	2006	654	SiN <sub>x</sub>	SiO <sub>2</sub>	17	654	poly-Si			0.35
this work, 2 <sup>nd</sup>	2007	654	SiN <sub>x</sub>	SiO <sub>2</sub>	8.5	654	poly-Si			0.7

Table 2: Summary of AC results from optical interconnect-related papers. Some authors use different wavelengths for detector AC and DC characteristics.  $f_{3dB}$  values in **bold-face** are calculated from the FWHM and assume a Gaussian pulse, so  $f_{3dB} = 0.44/t_{FWHM}$ .

Lead Author	Year	$\lambda_{AC}$ (nm)	Detector material	$f_{3dB}$ (GHz)	FWHM (ps)	$\lambda_{Det}$ (nm)	R (A/W)
Bowers	1986	1060	InGaAsP	28	34	1060	<b>0.30</b>
Hilleringman	1995	532	Si	0.001			
Diaz	1996	790	poly-Si	1.4		660	<b>0.23</b>
Bean	1997	790	poly-Si	10		650	<b>0.21</b>
Moreno	1997		$\alpha$ -Si			650	
Benaissa	1998		Si			633	.01
Siegert	1998	?	Si	<b>126</b>	3.5	800	<b>0.23</b>
MacDonald	1999	850	poly-Si	0.75	~250	860	0.13
Buchal	2000	1250	epi-Si	<b>137</b>	3.2	800	0.036
Cho	2002	1550	InGaAs	<b>26</b>	16.73	?	0.38
DeVries	200	850	poly-Si	1.5		980	0.008
El kurdi	2002		Ge/Si			1300	0.025
Yang	2002	845	poly-Si	1.5		845	0.47
Nathan	2003		Si			633	0.33
Seo	2005		InGaAs			1300	0.38
this work, 1 <sup>st</sup>	2006		poly-Si			654	0.35
this work, 2 <sup>nd</sup>	2007		poly-Si			654	0.7

## References

- [1] J. D. Jackson, *Classical Electrodynamics*, 3rd ed. Hoboken, NJ: John Wiley & Sons, 1999.
- [2] G. Keiser, *Optical Fiber Communications*, 3rd ed. New York, New York: McGraw-Hill, 2000.
- [3] H. G. Unger, *Planar Optical Waveguides and Fibres*. Oxford, UK: Clarendon Press, 1977.
- [4] D. B. Hall and C. Yeh, "Leaky waves in a heteroepitaxial film," *J. Appl. Phys.*, vol. 44, pp. 2271-2274, 1973.
- [5] H. A. Haus and D. A. B. Miller, "Attenuation of Cutoff Modes and Leaky Modes of Dielectric Slab Structures," *IEEE J. Quant. Elect.*, vol. 22, pp. 310-318, 1986.
- [6] P. Benech and D. Khalil, "Rigorous Spectral-Analysis of Leaky Structures - Application to the Prism Coupling Problem," *Optics Communications*, vol. 118, pp. 220-226, 1995.
- [7] R. H. Bube, *Photoelectronic Properties of Semiconductors*. New York, NY: Cambridge University Press, 1992.
- [8] R. H. Bube, *Photoconductivity of Solids*, 2nd ed. Huntington, New York: Krieger, 1978.
- [9] A. Rose, *Concepts in Photoconductivity and Allied Problems*, 2nd ed. Huntington, NY: Krieger, 1978.
- [10] B. G. Streetman and S. Banerjee, *Solid State Electronic Devices*, 5th ed. Upper Saddle River, NJ: Prentice-Hall, 2000.

- [11] R. R. Mehta and B. S. Sharma, "Photoconductive Gain Greater Than Unity in CdSe Films with Schottky Barriers at Contacts," *J. Appl. Phys.*, vol. 44, pp. 325-328, 1973.
- [12] S. F. Soares, "Photoconductive Gain in a Schottky-Barrier Photodiode," *Jpn. J. Appl. Phys. Pt. 1*, vol. 31, pp. 210-216, 1992.
- [13] F. A. Rubinelli, J. Y. Hou, and S. J. Fonash, "Bias-Voltage-Dependent and Bias-Light-Dependent High Photocurrent Gains in Amorphous-Silicon Schottky Barriers," *J. Appl. Phys.*, vol. 73, pp. 2548-2554, 1993.
- [14] M. Klingenstein, J. Kuhl, J. Rosenzweig, C. Moglestue, A. Hulsmann, J. Schneider, et al., "Photocurrent Gain Mechanisms in Metal-Semiconductor-Metal Photodetectors," *Sol. St. Elect.*, vol. 37, pp. 333-340, 1994.
- [15] J. Burm and L. F. Eastman, "Low-Frequency Gain in MSM Photodiodes Due to Charge Accumulation and Image Force Lowering," *IEEE Phot. Tech. Lett.*, vol. 8, pp. 113-115, 1996.
- [16] E. H. Roderick and R. H. Williams, *Metal-Semiconductor Contacts*, 2nd ed. vol. 19. Oxford, U.K.: Clarendon Press, 1988.
- [17] G. Yuan, R. Pownall, P. Nikkel, C. Thangaraj, T. W. Chen, and K. L. Lear, "Characterization of CMOS compatible, waveguide coupled leaky-mode photodetectors," *IEEE Phot. Tech. Lett.*, vol. 18, pp. 1657 - 1659, 2006.
- [18] B. Cluzel, E. Picard, T. Charvolin, E. Hadji, L. Lalouat, F. de Fornel, et al., "Near-field spectroscopy of low-loss waveguide integrated microcavities," *Appl. Phys. Lett.*, vol. 88, p. 051112, 2006.
- [19] R. Wuest, D. Erni, P. Strasser, F. Robin, H. Jackel, B. C. Buchler, et al., "A "standing-wave meter" to measure dispersion and loss of photonic-crystal waveguides," *Appl. Phys. Lett.*, vol. 87, p. 261110, 2005.
- [20] Y. B. Lin, J. Cardenas, S. Kim, and G. P. Nordin, "Reduced loss through improved fabrication for single air interface bends in polymer waveguides," *Optics Express*, vol. 14, pp. 12803-12813, 2006.
- [21] N. Daldosso, M. Melchiorri, F. Riboli, M. Girandini, G. Pucker, M. Crivellari, et al., "Comparison among various Si<sub>3</sub>N<sub>4</sub> waveguide geometries grown within a CMOS fabrication pilot line," *Journal of Lightwave Technology*, vol. 22, pp. 1734-1740, 2004.
- [22] I. Fatadin, D. Ives, and M. Wicks, "Accurate magnified near-field measurement of optical waveguides using a calibrated CCD camera," *Journal of Lightwave Technology*, vol. 24, pp. 5067-5074, 2006.
- [23] N. Daldosso, M. Melchiorri, F. Riboli, F. Sbrana, L. Pavesi, G. Pucker, et al., "Fabrication and optical characterization of thin two-dimensional Si<sub>3</sub>N<sub>4</sub> waveguides," *Materials Science in Semiconductor Processing*, vol. 7, pp. 453-458, 2004.
- [24] T. I. Kamins, "Hall Mobility in Chemically Deposited Polycrystalline Silicon," *J. Appl. Phys.*, vol. 42, pp. 4357-4365, 1971.
- [25] J. Y. W. Seto, "The Electrical Properties of Polycrystalline Silicon Films," *J. Appl. Phys.*, vol. 46, pp. 5247-5254, 1975.
- [26] G. Baccarani, B. Ricco, and G. Spadini, "Transport Properties of Polycrystalline Silicon Films," *J. Appl. Phys.*, vol. 49, pp. 5565-5570, 1978.
- [27] G. J. Korsh and R. S. Muller, "Conduction Properties of Lightly Doped, Polycrystalline Silicon," *Sol. St. Elect.*, vol. 21, pp. 1045-1051, 1978.
- [28] N. C. C. Lu, L. Gerzberg, C. Y. Lu, and J. D. Meindl, "Modeling and Optimization of Monolithic Polycrystalline Silicon Resistors," *IEEE Trans. Electron Devices*, vol. 28, pp. 818-830, 1981.

- [29] N. C. C. Lu, L. Gerzberg, C. Y. Lu, and J. D. Meindl, "A New Conduction Model for Polycrystalline Silicon Films," *IEEE Electron Dev. Lett.*, vol. 2, pp. 95-98, 1981.
- [30] M. M. Mandurah, K. C. Saraswat, and T. I. Kamins, "A Model for Conduction in Polycrystalline Silicon - .1. Theory," *IEEE Trans. Electron Devices*, vol. 28, pp. 1163-1171, 1981.
- [31] M. Rodder, "Modeling of Nonhyperbolic Sine I-V Characteristics in Poly-Si Resistors," *IEEE Electron Dev. Lett.*, vol. 13, pp. 74-76, 1992.
- [32] C. Thangaraj, "Truly CMOS compatible wave-guide based on-chip optical clock distribution and recovery," Master's thesis, Department of Electrical and Computer Engineering, Colorado State University, Fort Collins, Colorado, 2005.
- [33] C. Thangaraj, "Placeholder for Charles' PhD dissertation," PhD dissertation, Electrical & Computer Engineering, Colorado State University, Fort Collins, CO, 2008.
- [34] R. Pownall, G. Yuan, T. W. Chen, P. Nikkel, and K. L. Lear, "Geometry dependence of CMOS-compatible, polysilicon, leaky-mode photodetectors," *IEEE Phot. Tech. Lett.*, vol. 19, pp. 513-515, 2007.
- [35] C. Shu, B. B. Hu, X. C. Zhang, P. Mei, and E. S. Yang, "Picosecond Photoconductive Response of Polycrystalline Silicon Thin-Films," *Appl. Phys. Lett.*, vol. 57, pp. 64-66, 1990.
- [36] G. B. Arfken and H. J. Weber, *Mathematical Methods for Physicists*, 5th ed. San Diego: Harcourt Academic Press, 2001.
- [37] J. W. Goodman, F. J. Leonberger, S. Y. Kung, and R. A. Athale, "Optical Interconnections for VLSI Systems," *Proc. IEEE*, vol. 72, pp. 850-866, 1984.
- [38] J. E. Bowers and C. A. Burrus, "High-Speed Zero-Bias Wave-Guide Photodetectors," *Electron. Lett.*, vol. 22, pp. 905-906, 1986.
- [39] U. Hilleringmann, K. Knospe, C. Heite, K. Schumacher, and K. Goser, "A Silicon Based Technology for Monolithic Integration of Wave-Guides and VLSI CMOS Circuits," *Microel. Eng.*, vol. 15, pp. 289-292, 1991.
- [40] U. Hilleringmann and K. Goser, "Results of Monolithic Integration of Optical Wave-Guides, Photodiodes and CMOS Circuits on Silicon," *Microel. Eng.*, vol. 19, pp. 211-214, 1992.
- [41] U. Hilleringmann and K. Goser, "Optoelectronic System Integration on Silicon: Waveguides, Photodetectors, and VLSI CMOS Circuits on One Chip," *IEEE Trans. Electron Devices*, vol. 42, pp. 841-846, 1995.
- [42] D. C. Diaz, C. L. Schow, J. M. Qi, J. C. Campbell, J. C. Bean, and L. J. Peticolas, "Si/SiO<sub>2</sub>: Resonant cavity photodetector," *Appl. Phys. Lett.*, vol. 69, pp. 2798-2800, 1996.
- [43] J. C. Bean, J. M. Qi, C. L. Schow, R. Li, H. Nie, J. Schaub, et al., "High-speed polysilicon resonant-cavity photodiode with SiO<sub>2</sub>-Si Bragg reflectors," *IEEE Phot. Tech. Lett.*, vol. 9, pp. 806-808, 1997.
- [44] G. Maiello, M. Balucani, V. Bondarenko, G. De Cesare, S. La Monica, G. Masini, et al., "Amorphous silicon photodetectors for silicon based optical waveguides," *Solid State Phenomena*, vol. 54, pp. 45-49, 1997.
- [45] M. Moreno and J. Calderer, "Lateral photodetectors on ARROW structures for optical interconnections," *Optics Communications*, vol. 140, pp. 27-31, 1997.
- [46] K. Benaissa, A. Nathan, S. T. Chu, and W. Huang, "IC compatible optical coupling techniques for integration of ARROW with photodetector," *Journal of Lightwave Technology*, vol. 16, pp. 1423-1432, 1998.

- [47] M. Siegert, M. Loken, C. Glingener, and C. Buchal, "Efficient optical coupling between a polymeric waveguide and an ultrafast silicon MSM photodiode," *IEEE J. Sel. Top. Quant. Elect.*, vol. 4, pp. 970-974, 1998.
- [48] R. P. MacDonald, N. G. Tarr, B. A. Syrett, S. A. Boothroyd, and J. Chrostowski, "MSM photodetector fabricated on polycrystalline silicon," *IEEE Phot. Tech. Lett.*, vol. 11, pp. 108-110, 1999.
- [49] C. Buchal, M. Loken, M. Siegert, A. Roelofs, L. Kappius, and S. Mantl, "Ultrafast Si-based MSM mesa photodetectors with optical waveguide connection," *Materials Science in Semiconductor Processing*, vol. 3, pp. 399-403, 2000.
- [50] D. A. B. Miller, "Rationale and challenges for optical interconnects to electronic chips," *Proc. IEEE*, vol. 88, pp. 728-749, 2000.
- [51] S. Y. Cho, S. W. Seo, M. A. Brooke, and N. M. Jokerst, "Integrated detectors for embedded optical interconnections on electrical boards, modules, and integrated circuits," *IEEE J. Sel. Top. Quant. Elect.*, vol. 8, pp. 1427-1434, 2002.
- [52] A. M. DeVries, N. G. Tarr, P. Cheben, P. D. Grant, S. Janz, and D. X. Xu, "Submicron, high speed complementary metal-oxide semiconductor compatible metal-semiconductor-metal photodetector," *J. Vac. Sci. Technol. A*, vol. 20, pp. 1079-1081, 2002.
- [53] M. El kurdi, P. Boucaud, S. Sauvage, G. Fishman, O. Kermarrec, Y. Campidelli, et al., "Silicon-on-insulator waveguide photodetector with Ge/Si self-assembled islands," *J. Appl. Phys.*, vol. 92, pp. 1858-1861, 2002.
- [54] M. Yang, K. Rim, D. L. Rogers, J. D. Schaub, J. J. Welsler, D. M. Kuchta, et al., "A high-speed, high-sensitivity silicon lateral trench photodetector," *IEEE Electron Dev. Lett.*, vol. 23, pp. 395-397, 2002.
- [55] N. M. Jokerst, M. A. Brooke, S. Y. Cho, S. Wilkinson, M. Vrazel, S. Fike, et al., "The heterogeneous integration of optical interconnections into integrated microsystems," *IEEE J. Sel. Top. Quant. Elect.*, vol. 9, pp. 350-360, 2003.
- [56] M. Nathan, O. Levy, I. Goldfarb, and A. Ruzin, "Monolithic coupling of a SU8 waveguide to a silicon photodiode," *J. Appl. Phys.*, vol. 94, pp. 7932-7934, 2003.
- [57] K. N. Chen, M. J. Kobrinsky, B. C. Barnett, and R. Reif, "Comparisons of conventional, 3-D, optical, and RF interconnects for on-chip clock distribution," *IEEE Trans. Electron Devices*, vol. 51, pp. 233-239, 2004.
- [58] M. J. Kobrinsky, B. A. Block, J.-F. Zheng, B. C. Barnett, E. Mohammed, M. Reshotko, et al., "On-Chip Optical Interconnects," *Intel Tech. J.*, vol. 8, pp. 129 - 141, 2004.
- [59] E. Cassan, D. Marris, M. Rouviere, L. Vivien, and S. Laval, "Comparison between electrical and optical global clock distributions for CMOS integrated circuits," *Optical Engineering*, vol. 44, pp. 105402-01 - 105402-10, 2005.
- [60] S. W. Seo, S. Y. Cho, and N. M. Jokerst, "A thin-film laser, polymer waveguide, and thin-film photodetector cointegrated onto a silicon substrate," *IEEE Phot. Tech. Lett.*, vol. 17, pp. 2197-2199, 2005.

## DESIGN AND FABRICATION OF OPTICAL WAVEGUIDES AND POLYSILICON DETECTORS

### 1 Introduction

The goal of this research was to develop an optical interconnect technology that was fully compatible with existing standard CMOS processes. That meant using only industry-standard design tools, only industry-standard geometries, and only industry-standard materials and processing. This chapter will first discuss the design of the optical waveguides, in Section 2, while Section 3 will discuss the design of the polysilicon detectors. Section 4 will discuss fabrication of the waveguides and detectors. Section 5 will discuss how samples were prepared prior to DC and AC measurements. Section 6 will discuss physical analysis of the sample, as a complement to the DC and AC electrical analysis discussed in Chapters 4 and 5, respectively.

### 2 Design of optical waveguides

#### 2.1 Design goals

The major design goal for the optical waveguides was maximizing power transfer to the detector, which will convert the optical signal into an electrical signal.<sup>12</sup> In broad terms, maximizing the power transferred to the detector involves maximizing the power coupled from the source to the waveguide leading to the detector, and minimizing the waveguide loss. Specific steps to accomplish this involve:

- A waveguide with a large cross-sectional area to maximize the optical power transfer from the optical source to the waveguide and to minimize the effect of surface-roughness-induced scattering. A waveguide larger than that required to capture all the optical power from the source would be inefficient, however.

---

<sup>12</sup> Maintaining signal integrity (i.e. maintaining the waveform integrity) would have been a design objective for the waveguide if the waveguide lengths had been long enough for signal dispersion to be a factor. Over the centimeter-scale distances of on-chip waveguide, however, there is not enough distance for modal dispersion and other factors to significantly affect the shape of the waveform. The addition of noise is not an issue in a passive device such as a waveguide, and optical waveguides, unlike electrical waveguides, are not subject to crosstalk or electromagnetic interference.

- Minimizing waveguide loss due to bulk scattering.
- Minimizing waveguide loss due to surface scattering
- Minimizing waveguide loss due to bulk material absorption.
- Minimizing waveguide loss due to scattering at splits and branches in the waveguide.
- Minimizing bending losses in the waveguide.

The reasons behind the various factors involved in maximizing power transfer to the detector are discussed in more detail below.

### *2.1.1 Maximizing power transfer to the detector*

As mentioned above, maximizing the power transferred to the detector involves several considerations.

To maximize power transfer from the input source to the waveguide leading to the detector, good matching of the waveguide dimensions to the mode-field diameter of the input fiber is desired. Given the nature of integrated circuit processing, where film thicknesses are typically tens of nanometers to a micron but linewidths are essentially unrestricted, this “mode-field matching” goal implies a waveguide with a width equal to that of the core of the input fiber. The waveguide height will probably be limited to a few hundred nanometers, due to the need to be compatible with other film thicknesses and processing requirements. This process of transferring power from the input source to the waveguide is somewhat analogous to transferring an optical signal from a large-diameter multimode fiber to a second large-diameter multimode fiber, as compared to transferring the signal from a multimode fiber to a single-mode fiber. If the area of the source is much larger than the area of the waveguide, then either power will be lost in the transfer or lensing / focusing systems will be required. (And even with lenses, power may be lost, due to the NA of the waveguide and the resolution limit of the lenses.) If the waveguide is larger than the source, then the beam will be expanded, almost certainly unnecessarily. (The process of shrinking the beam again will add complexity, expense and almost certainly loss of optical power.) As single-mode visible wavelength optical fibers

have a core diameter on the order of  $4\ \mu\text{m}$  (area of around  $12.5\ \mu\text{m}^2$ ), while the largest on-chip optical waveguides used in this research had dimensions of  $0.3\ \mu\text{m}$  high by  $30\ \mu\text{m}$  wide (area of  $9\ \mu\text{m}^2$ ) and typical waveguides had dimensions of  $0.5\ \mu\text{m}$  wide by  $0.3\ \mu\text{m}$  high (area of  $0.15\ \mu\text{m}^2$ ), the assumption of “source larger than on-chip waveguide” is reasonable.

In addition to the issue of coupling optical power from the source into the waveguide, there are also the issues of light scattering out of the waveguide and light being absorbed in the waveguide. The two main scattering mechanisms are surface roughness, caused by the photolithographic and etch processes used to define the waveguide, and bulk scattering, discussed below.

The effect of surface roughness can be minimized by making the cross-sectional area of the waveguide relatively large. This helps in two ways. First, the obvious way that the ratio of the waveguide perimeter to the waveguide cross-sectional area decreases as the area increases. Second, as the waveguide width, and therefore area, increases, the size of the evanescent tail decreases, resulting in less power at the surface of the waveguide to be scattered. (Note that the amount of power which reaches the detector depends on the evanescent tail extending from the vertical axis of the waveguide. Changing the width of the detector won't affect this, except near the waveguide corners.)

Bulk scattering, due to nonuniformities (e.g. defects, inclusions, particles, localized areas of lower or higher refractive index, et cetera) can also reduce the power delivered to the detector. However, bulk scattering is determined by the deposition conditions, and is therefore outside the control of the waveguide designer. If bulk scattering is found to be a significant factor, it could, however, be minimized through careful design of the deposition process and equipment.

Material absorption is dealt with by choosing a waveguide core material (silicon nitride,  $\text{SiN}_x$ ) that has zero absorption at the wavelength of interest.<sup>13</sup>

---

<sup>13</sup> 654 nm for Sharp GH06510B2A laser diodes and 685 nm for Hitachi HL6738MG laser diodes.

Waveguide splits are required in any kind of waveguide distribution geometry. An example of a typical waveguide split is shown in Figure 1.

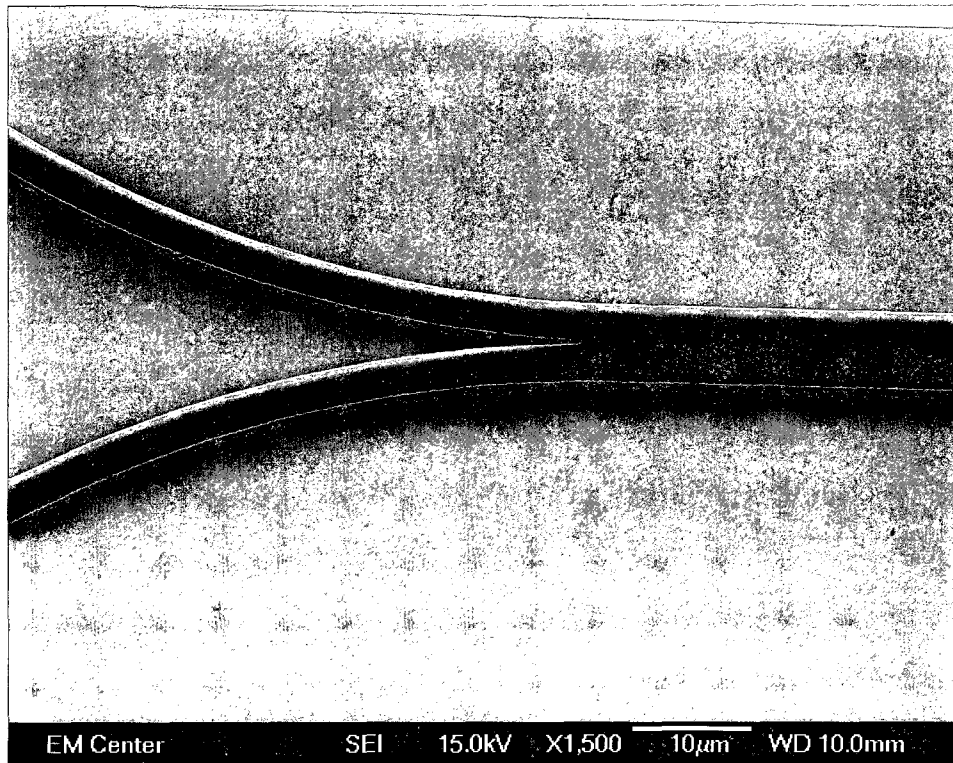


Figure 1: First split in the large H-tree clock distribution circuit (Second-generation die)

However, splits will reduce power delivered to the detector as a result of excess loss at the split. NSOM measurements [1] showed that a nominal 3 dB splitter (e.g. A waveguide of width  $N$  coming in and with two waveguides each of width  $N/2$  going out, each carrying half the input optical power) can lose as much as 4 dB at the split.

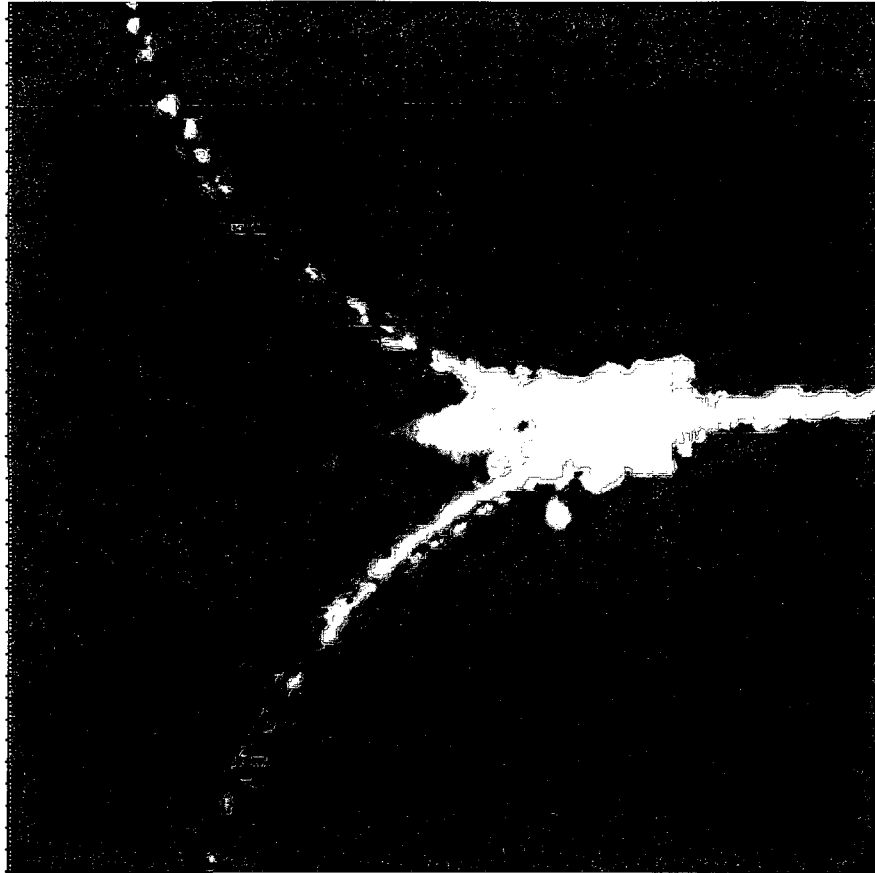


Figure 2: NSOM image of waveguide split. The bright spot surrounding the split is due to optical power scattered out of the waveguide at the split. This power scattered out of the waveguide at the split results in excess loss at the split [1]

As is well known from fiber optic waveguides, bends in the waveguide can also reduce the power delivered to the waveguide, due to an increased evanescent tail on the outside of the bend, relative to a straight waveguide. [2]

All of these effects – waveguide cross-sectional area that is well matched to the mode field diameter of the input source, as well as minimizing waveguide surface roughness, waveguide bulk scattering, excess loss at splits, and waveguide bending loss – must be taken into account when designing the optical waveguides if maximum power transfer to the detector is to be obtained.

### **3 Design of polysilicon detectors**

#### **3.1 Design goals**

The two major design goals for the detector were:

1. Maximize speed of the detector
2. Maximize the responsivity of the detector (i.e. Maximize the photocurrent out for a given optical power in.)

Since this research is targeted toward on-chip optical interconnects, specifically clock circuitry, and modern integrated circuits are clocked in the one to four GHz range, the detectors must be capable of response in the one to four GHz range as well. Maximizing the response of the detector will allow lower-power sources to be used while still generating sufficient response from the detector.

##### *3.1.1 Detector geometry*

Figure 3 and Figure 4 are SEM images of the detectors. Note that the images are of different detectors.

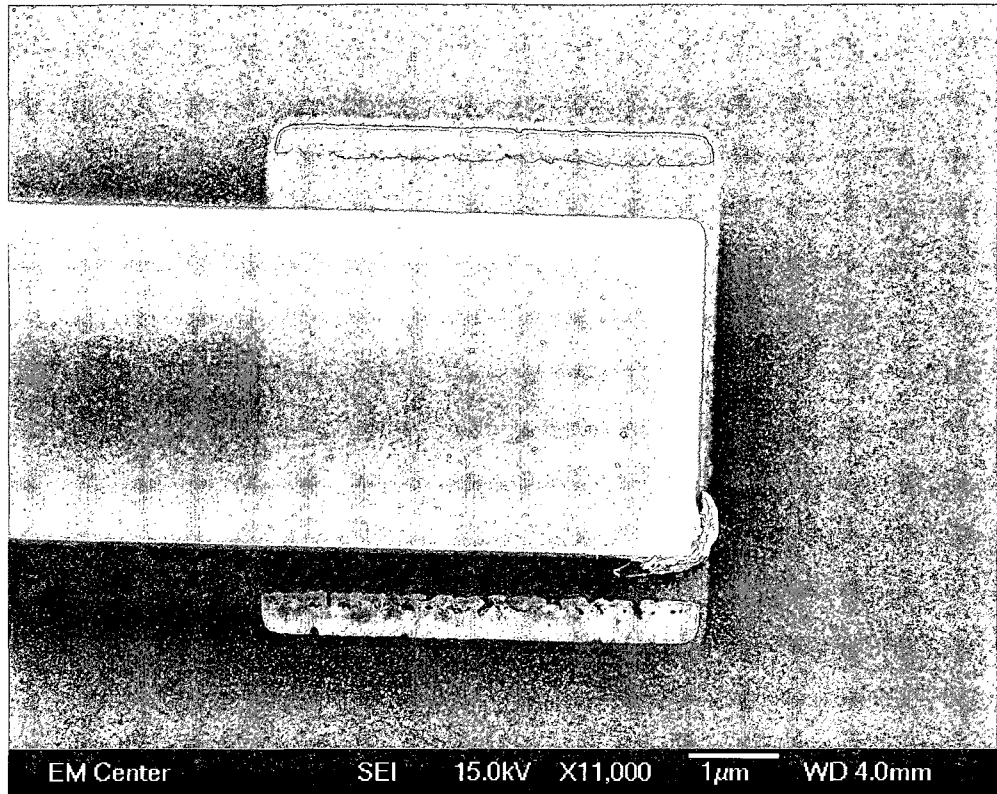


Figure 3: Waveguide on top of a polysilicon detector. Rough regions at the top and bottom of the detector are silicided regions.

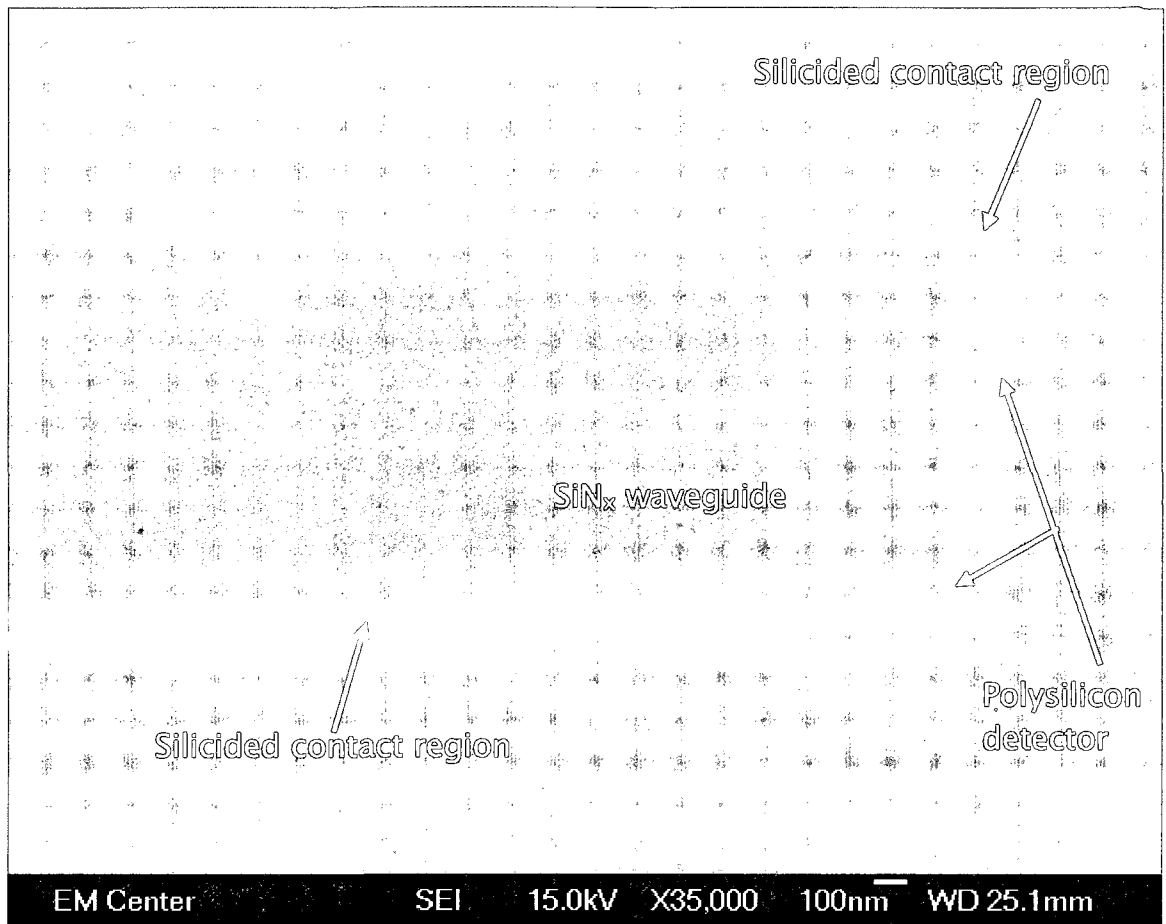
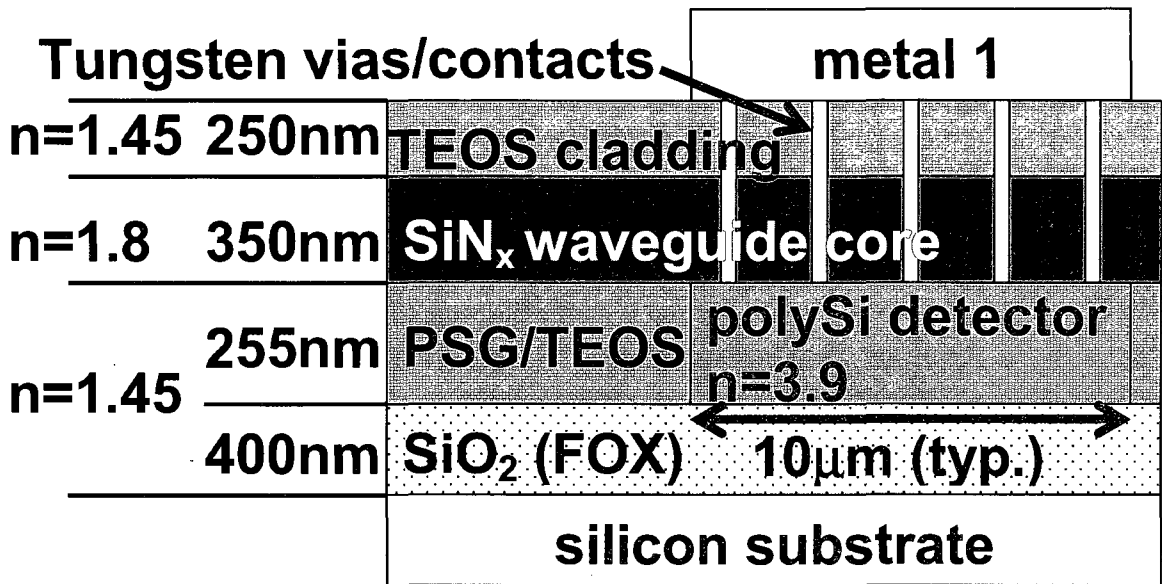
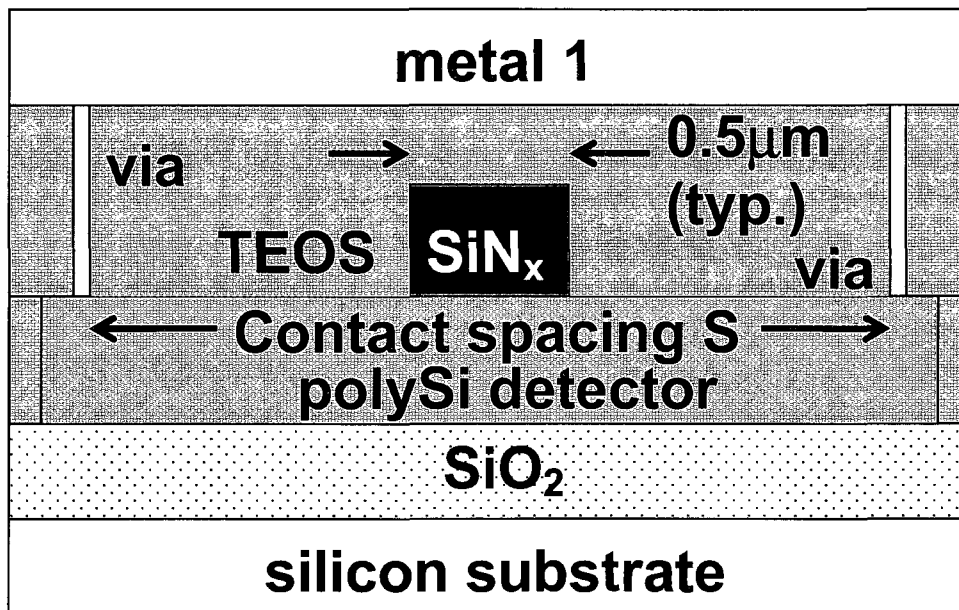


Figure 4: Oblique view of waveguide and detector

The design variables for the detectors were the contact spacing  $S$ , the detector length  $L$  and the waveguide width  $W$ . Figure 5 shows side-view and end-view cross-section illustrations of the detector structure, indicating the definitions of  $S$ ,  $L$  and  $W$ . Note that Figure 5a is a merged side view, showing both the contacts, which are at the edge of the device, and the waveguide core, which run through the middle of the device. The end view of Figure 5b more clearly shows the separation between the waveguide core and the contacts. Figure 6 is an isometric projection cross-section of the device, giving a third perspective of the detector structure.



(a)



(b)

Figure 5: (a) Side and (b) end views of waveguide and detector structure, showing typical contact spacing  $S$ , waveguide width  $W$  and detector length  $L$ . For clarity, the low-pressure chemical vapor deposition (LPCVD) silicon nitride “spacers” on the sides of the polysilicon have been omitted.

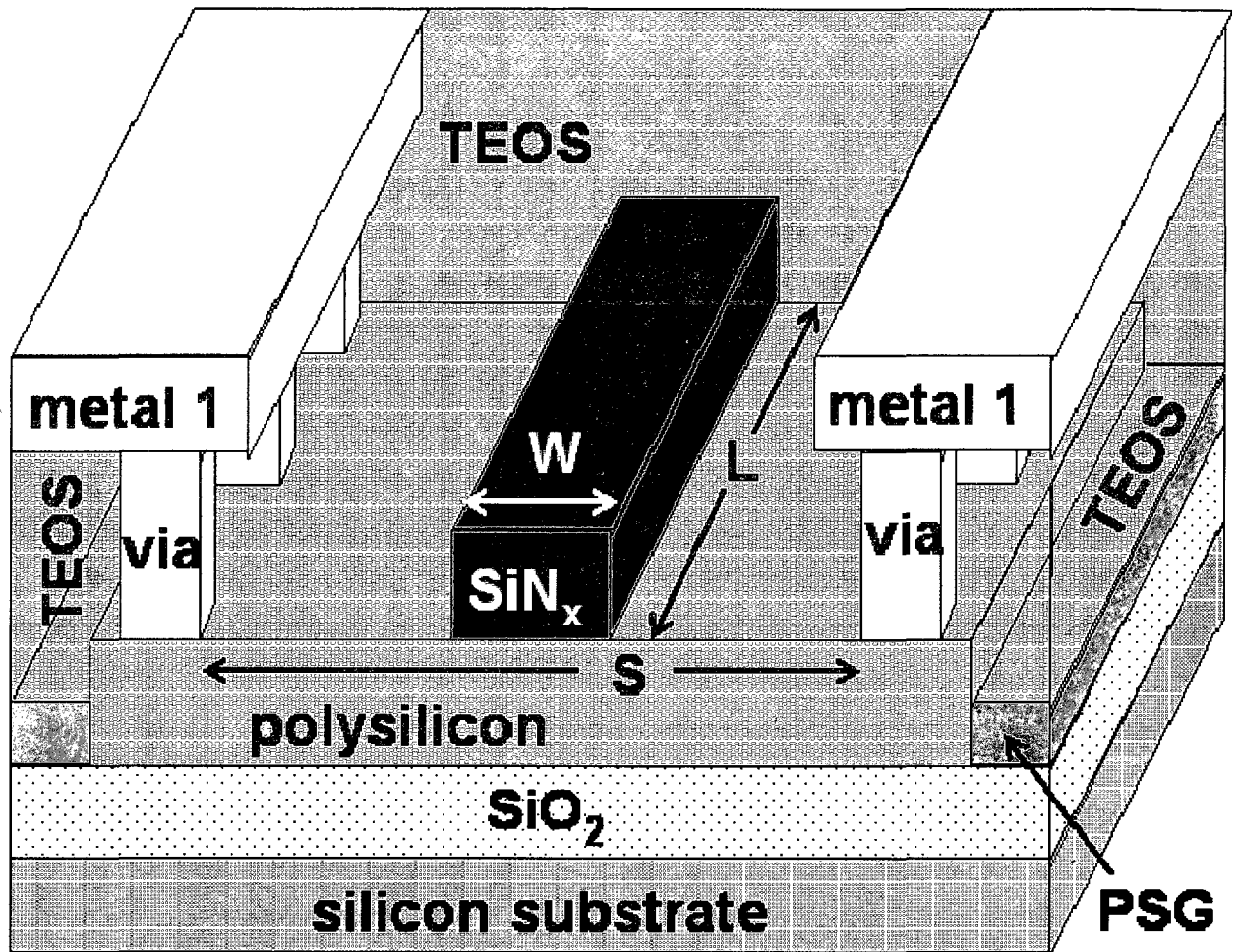


Figure 6: Isometric projection cross-section of the detector and waveguide. TEOS and PSG are types of  $\text{SiO}_2$  and form the cladding layers around the  $\text{SiN}_x$  waveguide core. For clarity, the LPCVD silicon nitride spacers on the sides of the polysilicon have been omitted.

There were two generations of optical interconnect chip designs. Both generations of test chips contained detectors placed around the perimeter of the die, with waveguides leading from the edge of the die to the detectors, and detectors in the H-tree. (For brevity, the detectors around the edge of die are referred to as “edge-coupled waveguide detectors”.) The first generation test chip is documented in Appendix B, while the second generation is documented in Appendix C. On the first generation design, shown in Figure 7, the contact spacing varied in somewhat logarithmic steps from  $1.14 \mu\text{m}$  to  $30.14 \mu\text{m}$ . Detector length was limited to two values:  $5 \mu\text{m}$  and  $10 \mu\text{m}$ . This 2:1 ratio allowed for analytic extraction of the absorption coefficient of the polysilicon detector, as described in Chapter 4. Detectors with a

variety of waveguide widths – from 0.5  $\mu\text{m}$  to 30  $\mu\text{m}$  - were fabricated. Half (13 out of 26) of the first-generation edge-coupled detectors, however, had a single-mode 0.5  $\mu\text{m}$  wide waveguide. On the second-generation design, shown in Figure 8, contact spacing varied from 0.68  $\mu\text{m}$  to 4.64  $\mu\text{m}$ , again in a somewhat logarithmic fashion. (Two edge-coupled detectors had asymmetrically spaced contacts – 1  $\mu\text{m}$  on one side of the waveguide and 10  $\mu\text{m}$  on the other side of the waveguide. This was done to investigate the effect of asymmetrically placed contacts.) With one exception, detector length on the edge-coupled devices was again limited to the two values of 5  $\mu\text{m}$  and 10  $\mu\text{m}$ . The one exception was a 40  $\mu\text{m}$  long detector, to investigate the impact of extremely long detectors. Waveguide widths varied from 0.5  $\mu\text{m}$  to 4  $\mu\text{m}$ . Most of the devices (14 out of 19) had 0.5  $\mu\text{m}$  single-mode waveguides. Table 1 through Table 4 list the various values of the detector geometry variables.

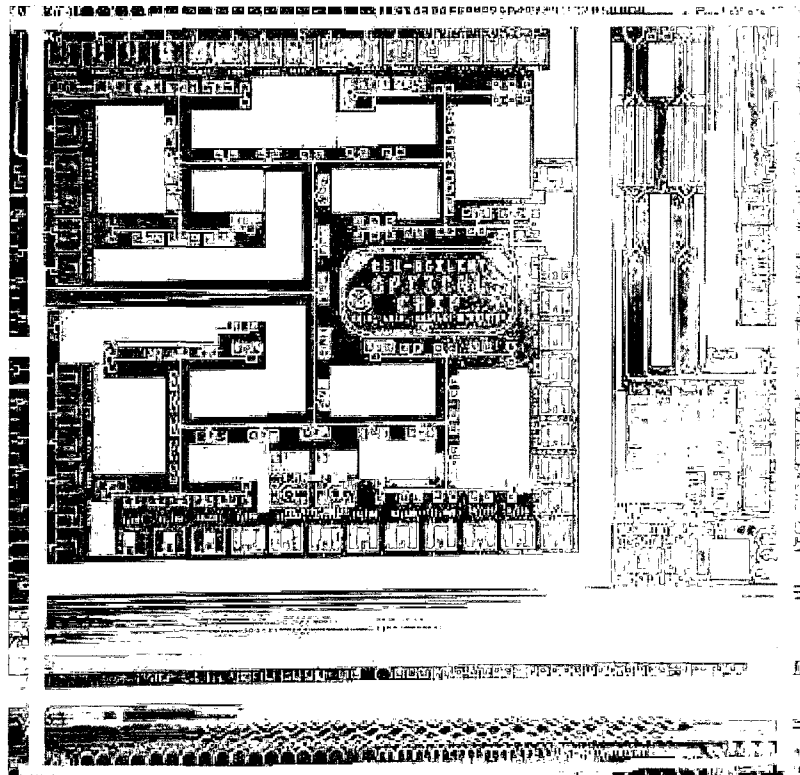


Figure 7: Microphotograph of a first-generation die, courtesy of Aspen Technologies

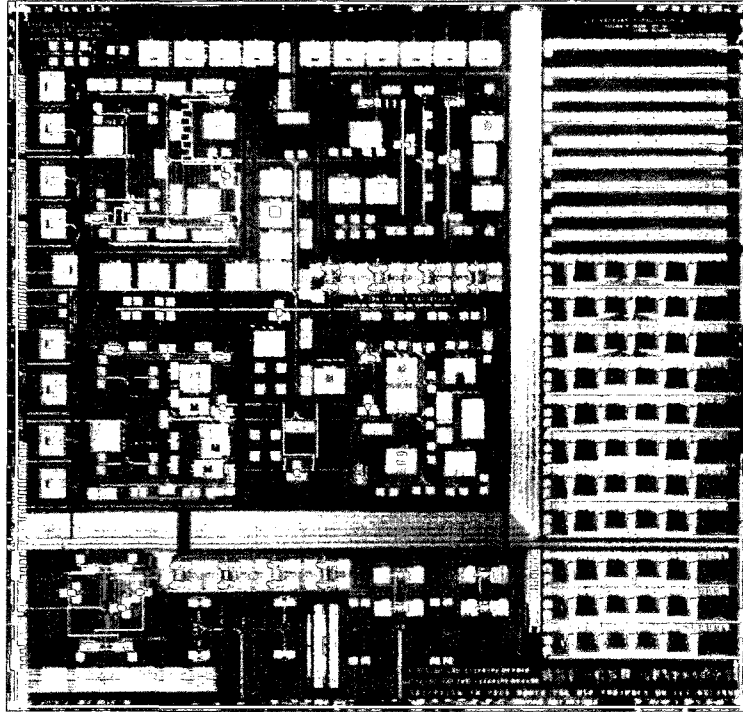


Figure 8: Microphotograph of a second-generation die, courtesy of Aspen Technologies

Table 1: 1<sup>st</sup> generation edge-coupled detector geometry variables. Values are artwork dimensions. Not all combinations are available. Contact spacing is edge-to-edge, not center-to-center. See Appendix B for details.

WG width $W$ ( $\mu\text{m}$ )	0.5, 1.5, 2.5, 3.5, 4.5, 5.5, 9.5, 24.5, 29.5
Detector length $L$ ( $\mu\text{m}$ )	5, 10
Contact spacing $S$ ( $\mu\text{m}$ )	2.14, 3.14, 4.14, 5.14, 6.14, 10.14, 25.14, 30.14

Table 2: 1<sup>st</sup> generation H-tree detector geometry variables. Values are artwork dimensions. The 1<sup>st</sup> generation H-tree had only one detector layout. Contact spacing is edge-to-edge, not center-to-center.

WG width $W$ ( $\mu\text{m}$ )	0.5
Detector length $L$ ( $\mu\text{m}$ )	10
Contact spacing $S$ ( $\mu\text{m}$ )	1.14

Table 3: 2<sup>nd</sup> generation edge-coupled detector geometry variables. Values are artwork dimensions. Not all combinations are available. Contact spacing is edge-to-edge, not center-to-center. See Appendix C for details.

WG width $W$ ( $\mu\text{m}$ )	0.5, 2, 4
Detector length $L$ ( $\mu\text{m}$ )	5, 10, 40
Contact spacing $S$ ( $\mu\text{m}$ )	0.68, 0.8, 0.9, 1.6, 2.14, 2.64, 4.14, 4.64 (Two asymmetric devices: 11.5, 15)

Table 4: 2nd generation H-tree detector geometry variables. Values are artwork dimensions. Not all combinations are available. Contact spacing is edge-to-edge, not center-to-center. See Appendix C for details.

WG width $W$ ( $\mu\text{m}$ )	0.25, 0.5, 2
Detector length $L$ ( $\mu\text{m}$ )	2, 3, 4, 5, 50
Contact spacing $S$ ( $\mu\text{m}$ )	0.89, 1.14, 1.64, 2.97, 3.44

Figure 9 through Figure 11 are microphotographs of some selected second-generation devices<sup>14</sup>. The first-generation devices look essentially like the device of Figure 9, with modifications for different waveguide widths, detector lengths and contact spacings, as appropriate. The only visible differences between first-generation and second-generation devices are that first-generation devices had much longer metal traces running from the device pads to the devices ( $\sim 200\mu\text{m}$  versus  $\sim 15\mu\text{m}$ ) and that about half of the second-generation devices had large U-shaped bends in the waveguides, so that the detector was placed “behind” the pad with the waveguide coming in “from the back”. (The waveguide bend is not visible at the scale of these microphotographs.) The U-bend was included to try to eliminate the possibility of light from the source reaching the detector directly, rather than through the waveguide. An example of a second-generation U-bend, leading to the 0.4,10,4.14 device, is shown in Figure 12. More documentation about the U-bends and the devices to which they lead is in Appendix C.

---

<sup>14</sup> In the triple of numbers describing the edge-coupled waveguide devices, the first number is the waveguide width in  $\mu\text{m}$ , the second number is the detector length in  $\mu\text{m}$  and the third number is the contact-edge-to-contact-edge spacing, again in  $\mu\text{m}$ . For the asymmetric contact spacing devices, the third value is in parenthesis, and represents the contact-edge-to-waveguide spacing on each side of the waveguide. Thus, the 0.5,10,(1,10) device has a contact-edge-to-contact-edge spacing of  $11.5\mu\text{m}$ .

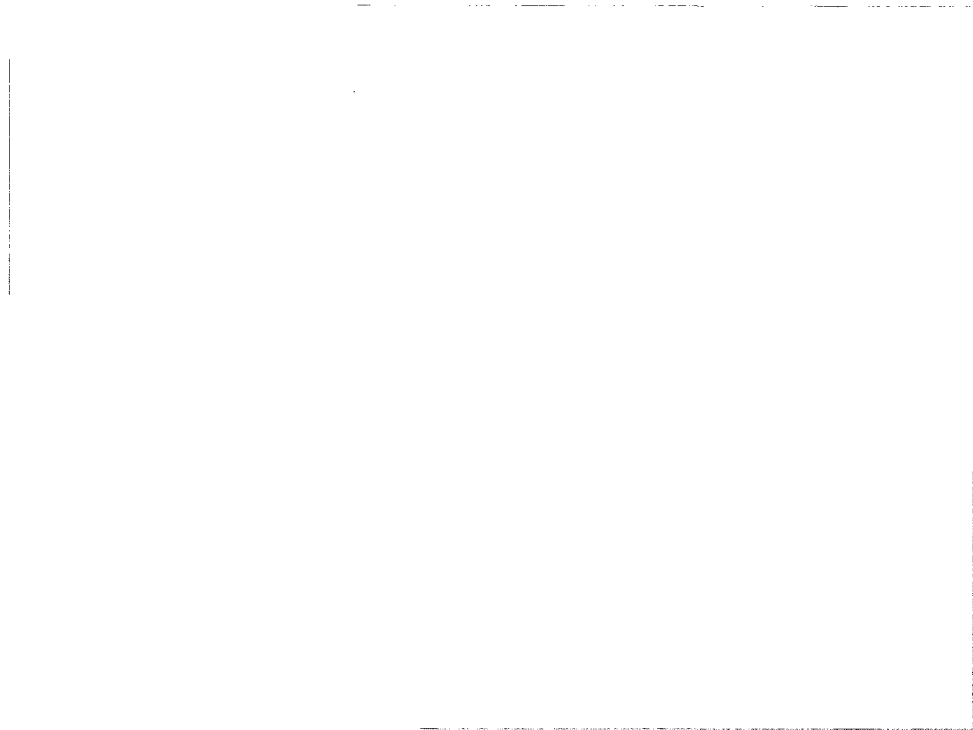


Figure 9: 2<sup>nd</sup>-generation 0.5,10,1.6 device (Original image is 160x, this is 120x.)

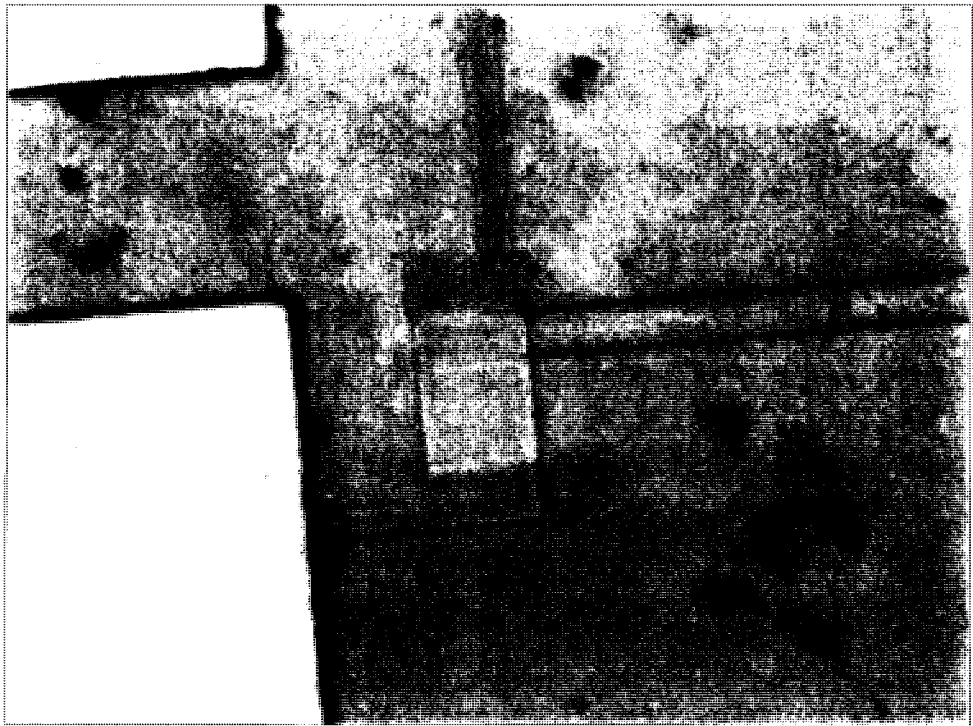


Figure 10: 2<sup>nd</sup>-generation 4,10,[1,10] asymmetric device (Original image is 160x, this is 120x.)

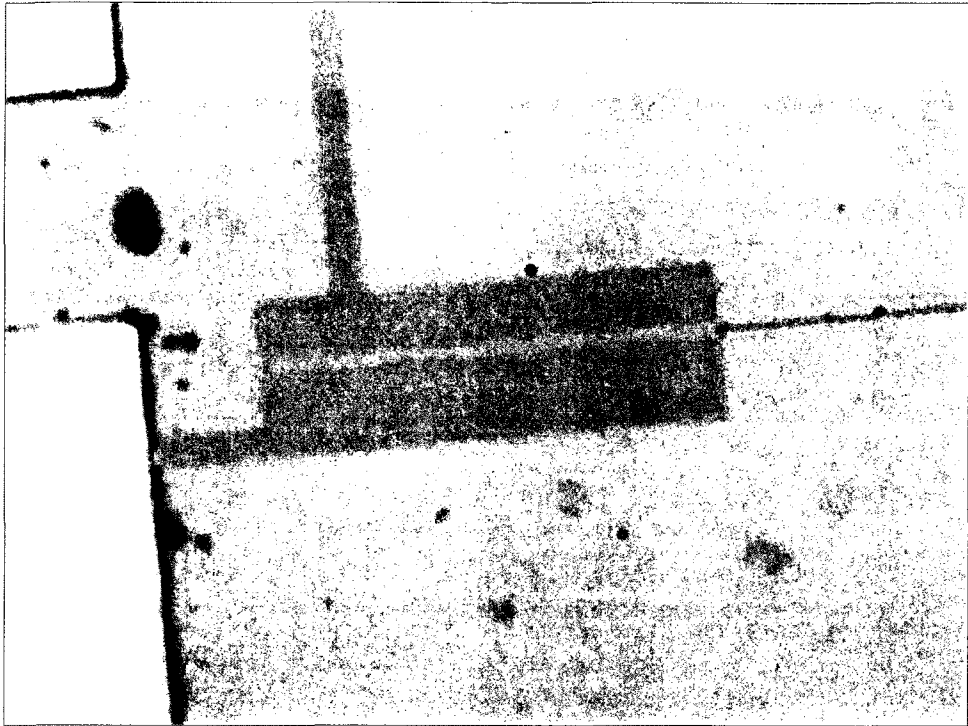


Figure 11: 2nd-generation 0.5,40,2.6 device (Original image is 160x, this is 120x.)

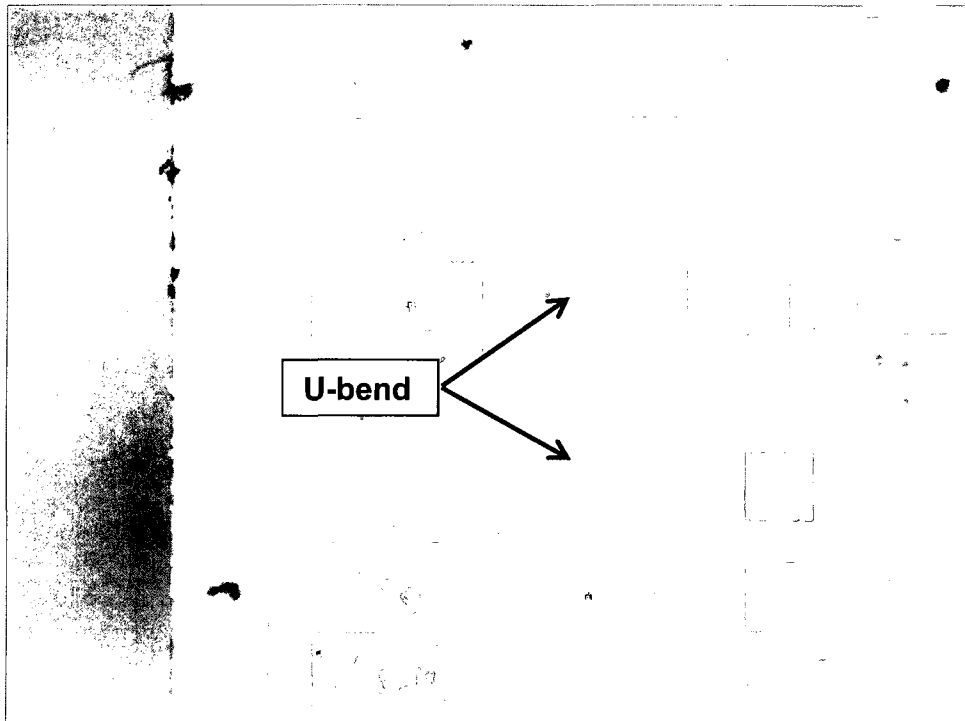


Figure 12: U-bend waveguide, leading to the 0.5,10,4.14 second-generation device

Unfortunately, on the second generation wafers, all of the edge-coupled detectors with contact spacing less than 2.14  $\mu\text{m}$  were unusable. Some of the 2.14  $\mu\text{m}$  devices were also unusable. As will be discussed in Chapter 4, dark currents were in excess of 100  $\mu\text{A}$  at 0.1 V bias for the smallest contact spacing, indicating the devices were shorted. Typical dark current values are on the order of 100 picoamps at 0.1 V bias.

### 3.1.2 Maximizing detector speed

As discussed in Chapter 2, detectors should be designed to have a short transit time. As the transit time is a function of the contact spacing  $S$  and the carrier velocity  $v$ , and the carrier velocity is outside the control of the detector designer, the detectors should be designed for small contact spacing. (The carrier velocity in a polysilicon detector is a function of the polysilicon grain size and the electric field strength, which in turn is a function of the bias voltage and the contact spacing. While the contact spacing is determined by the detector designer, the polysilicon grain size is determined by the process designer and the maximum bias voltage is determined by the overall system designer.)

As discussed in Chapter 2, if the electron-hole pair (EHP) lifetimes follow a negative exponential distribution, the corresponding frequency response of the photocurrent is

$$|I_{ph}(\omega)| = I_{ph,0} \left( \delta(\omega) + \bar{G} \frac{1}{\omega \bar{\tau}_{n,p} + 1} \right),$$

where  $I_{ph,0}$  is the photocurrent at very low bias voltages (i.e. without any photoconductive gain mechanism),  $\bar{G}$  is the photoconductive gain and  $\bar{\tau}$  is the average carrier lifetime. Therefore, for high-speed devices, a short carrier lifetime is desired.

### 3.1.3 Maximizing detector current responsivity

There are several factors which the device or detector designer can easily control in order to maximize the detector's responsivity (i.e. current out for optical power in).

First, make the detector long. The longer the detector, the more evanescent coupling will occur. However, since the power which is evanescently coupled out of the waveguide and into the detector at one point is no longer available in the waveguide for later points, it is possible to reach a point of diminishing returns. For example, if 90% of the power in the waveguide is

absorbed in the first 10  $\mu\text{m}$  that the waveguide crosses the detector, then doubling the detector length to 20  $\mu\text{m}$  would only result in an increase in absorbed power, from 90% to 99% - a 10% (9 percentage point) increase in absorbed power for a doubling of length.

Second, make the contact spacing as small as possible, consistent with the waveguide width and design rules for the process. For a given bias voltage, this will produce the maximum electric field in the detector, resulting in the most efficient separation of photogenerated electrons and holes. In addition, as discussed in Chapter 2, smaller contact spacing results in higher photoconductive gain, with the gain inversely proportional to the square of the contact spacing. (As discussed in Section 3.1.2 of this chapter, small contact spacing also helps device speed.)

Third, minimize the vertical distance between the waveguide and the detector. This will provide the strongest evanescent coupling between the waveguide and the detector. (Strictly speaking, this factor is under the control of the process designer, not the detector designer.)

Fourth, design the detector to have gain – more than one counted electron for every absorbed photon. In other words, design the detector to have a photoconductive gain process similar to those discussed in Chapter 2. However, as noted in Chapter 2, photoconductive gain is proportional to carrier lifetime. Thus, for high gain and the corresponding improved responsivity, a long lifetime is desired. However, as noted in Section 3.1.2, a short lifetime is desired for high speed. This trade-off in carrier lifetime between high responsivity and high speed is similar to the well-known gain-bandwidth tradeoff in amplifiers.

#### *3.1.4 Summary*

In summary, the design of the polysilicon photodetectors must take into account the twin goals of high speed and high responsivity. Some factors help both (e.g. small contact spacings and high bias voltages), some are irrelevant to one or the other (e.g. long detector length – remember that the detector length is perpendicular to the direction of photocurrent flow), and some are opposing (e.g. carrier lifetimes should be short for high speed, but long for high gain and thus high responsivity). The nature of the Schottky contacts is critical in both goals.

### 3.1.5 Acknowledgements

I want to acknowledge the contribution of Matheen Raza [3] and Charles Thangaraj [4] in designing the first-generation test chip. In addition, I want to acknowledge Charles Thangaraj and Tej Balijepalli for their work designing the second-generation test chip.

## 4 Fabrication of optical waveguides and polysilicon photodetectors

Since, as mentioned at the start of this chapter, the goal of this research was to develop an optical interconnect technology compatible with standard CMOS processing, the processing of samples was essentially the same as that of a standard CMOS process. For that reason, only the steps unique to fabricating the optical waveguides and the polysilicon detectors will be discussed. For details of general CMOS fabrication, one can consult any number of books. [5-7] All thicknesses and refractive index values listed here and shown in the figures are nominal values.

It should be noted here that there were two wafer fabrication runs, using two different chip designs. The first run focused solely on the optical waveguides and polysilicon photodetectors. It omitted MOSFET formation and stopped after the first metal deposition. The second run was a full process flow, including MOSFET formation, through second metal deposition, with the addition of the cladding and core layer depositions for the optical waveguide. (Since the polysilicon detectors were based on the polysilicon MOSFET gate layer, no special deposition was required to create them.) The processing discussion below is for the first generation material. As noted earlier, the second generation material included the processing necessary to make MOSFET, which was done before the optical interconnect processing. The second generation material also included the processing necessary to have two levels of metal, which was done after the optical interconnect processing. First and second generation process flows are listed in Appendix D.

As part of the design process, artwork is created to define the photomasks that will be used to create the waveguides and detectors on the wafers, as well as all of the MOSFETs, metal lines and other structures on the die. As part of the artwork, regions are defined which will prevent the polysilicon areas that are to become photodetectors from being doped with impurities or from being “silicided”. (i.e. Converted into titanium silicide through a high-temperature

reaction with titanium that has been deposited onto polysilicon.) Thus, the polysilicon photodetectors were formed from the 255 nm,  $n=3.85$  MOSFET polysilicon gate deposition<sup>15</sup>, but without the dopants<sup>16</sup> and titanium silicide formation<sup>17</sup> that the MOSFET gates received.

The lower cladding of the optical waveguide was a nominal 440 nm,  $n=1.45$  deposited silicon dioxide ( $\text{SiO}_2$ ) film. The silicon dioxide is formed by the decomposition of tetra-ethyl ortho-silicate (TEOS) vapor at high temperatures and low pressures, and is a standard recipe in the process, used for inter-metal dielectrics. [8] Only the deposition time, and thus thickness, has been modified. Below the lower cladding was a 200 nm,  $n = 1.45$  phosphosilicate glass (PSG) layer – silicon dioxide doped with phosphorous. This layer turned out to play an unexpectedly important role in the waveguide loss mechanisms, to be discussed in Chapter 4.

After the TEOS deposition, the lower (PSG plus TEOS) cladding is chem-mechanically polished (CMP) to provide a smooth, planar surface for subsequent film depositions and photolithographic patterning. Again, this is a standard recipe in the process.

The waveguide core is a nominal 350 nm,  $n = 1.8$  deposited silicon nitride ( $\text{SiN}_x$ ) film. The silicon nitride is formed by the reaction of silane ( $\text{SiH}_4$ ) and ammonia ( $\text{NH}_3$ ) at low pressures with an electrical plasma providing the energy required to make the reaction occur. (i.e. The silicon nitride layer is a plasma-enhanced chemical vapor deposition, or PECVD.) Stoichiometric silicon nitride is  $\text{Si}_3\text{N}_4$ , however the deposited film is non-stoichiometric, leading to the “ $\text{SiN}_x$ ” designation. The silicon nitride is another standard recipe in the process, used as passivation layer. It has been modified only in terms of thickness from existing recipes. It should be noted that PECVD silicon nitride is slightly less dense, both physically and optically, than thermally-deposited silicon nitride.

---

<sup>15</sup> Nominal deposition conditions are: temperature: 620 C; pressure: 200 mtorr; silane ( $\text{SiH}_4$ ) flow: 100 sccm at top of vertical reactor, 160 sccm at bottom of vertical reactor, giving a nominal deposition rate of 0.1 nm/minute.

<sup>16</sup> While the polysilicon used for the photodetectors was not intentionally doped, it may have been inadvertently doped due to tails from the source/drain implants or the polysilicon doping implant extending through the implant blocking layers, or as a result of boron outdiffusion from the back of the adjacent p-type wafer during the poly deposition step. Any inadvertent doping would be at a very low level, if present at all.

<sup>17</sup> While the artwork contained a silicided block layer over the entire polysilicon detector region, Figure 3 shows that the contact regions to the polysilicon were, in fact, silicided.

The use of polysilicon as the detector layer provides a material with a refractive index higher than silicon nitride, permitting the desired leaky-mode coupling from the nitride waveguide core to the detector, while maintaining mechanical and thermal compatibility with the other films in the structure.

Following the waveguide creation step, an  $n=1.45$  TEOS layer was deposited and thinned, by CMP, to a nominal thickness of 280 nm over the waveguide nitride. This top cladding TEOS layer is identical to the TEOS in the bottom cladding except for thickness. The as-deposited thickness of the top cladding TEOS is 1200 nm, versus 440 nm for the bottom cladding TEOS. As noted, the top cladding TEOS is thinned to a nominal 280 nm by CMP. This TEOS is part of the standard CMOS process flow, as an intermetal dielectric.

After the top cladding deposition, the standard CMOS process resumes, with definition of the contacts and first level metal.

The contacts are plugged with tungsten. The metal stack consisted of a 10 nm Ti layer, then a 390 nm Al/0.5% Cu layer, with a 35 nm TiN layer on top.

## **5 Sample preparation**

Once processing and initial electrical testing (for process-control reasons) was finished at Agilent/Avago, the wafers were sent to Aspen Technologies in Colorado Springs, CO for dicing. (i.e. Sawing the wafers into individual die.) Following dicing, selected die were edge polished to an optical-quality finish, to allow end-fire coupling to the waveguide.

Polishing was done in-house at CSU, using a Buehler Eco-Met polisher, and at Agilent/Avago, using an Allied Multi-Prep polisher. In both cases, polishing was done using a variety of Allied polishing papers. Prior to starting polishing, a cover-slip was attached to the patterned side of the die sample, using CrystalBond. At CSU, polishing started with 30  $\mu\text{m}$  grit papers, to quickly remove the cover slip, the bulk of the excess material on the die and get close to the entrance of the waveguide, and proceeded through 10  $\mu\text{m}$ , 5  $\mu\text{m}$ , 1  $\mu\text{m}$  and finer grits, down to 0.1  $\mu\text{m}$  grit paper. At Agilent/Avago, polishing started with grinding down the cover slip until close to the die edge. Polishing then switched to the MultiPrep with 15  $\mu\text{m}$  grit paper,

until very close to the waveguide entrance. At that point, polishing switched to a 1  $\mu\text{m}$  grit paper. Once the polishing had gotten into the waveguide, polishing switched to Buehler Masterpolish 2 polishing liquid for the final polish. Information about the polishing procedure is in Appendix E.

To allow for identification of the die used to make any given measurement, a die numbering scheme was developed and used on both first and second generation wafers. This information allowed tracking back if, for example, results from some die were found to be good while other results from other die were found to be poor. This might be caused by a center to edge or top to bottom differences in wafer processing. Knowing the die number potentially allowed discovery of differences in measured results were connected to die location on the wafer. As it turned out, though, wafer to wafer differences swamped within-wafer differences. The principle, though, is sound. Information on the die numbering scheme is in Appendix F.

## **6 Physical analysis of samples**

In addition to the DC and AC analysis of the samples, discussed in Chapters 4 and 5 respectively, physical analysis was also performed on the samples. The specific techniques were polysilicon grain size measurement using atomic force microscopy (AFM), polysilicon surface roughness and scanning electron microscopy (SEM) cross-sections. Of these three techniques, the polysilicon grain size measurements were the most interesting, due to the insights they provided into contact behavior, as will be discussed in Chapter 4. AFM polysilicon grain size measurement results are shown in Figure 13, Figure 14 and Figure 15. (AFM measurements are courtesy of Avago Technologies, Fort Collins, CO.). These results are from first-generation material. Second-generation material should have similar or somewhat larger grain size. While the polysilicon was deposited under identical conditions (leading to identical grain size), the additional processing received by the second-generation material resulted in an additional thermal history for the second generation material, compared to the first generation material. While the exact effect of the additional thermal processing on grain size is unknown (unlike the first generation material, no second generation samples were pulled after polysilicon deposition), the additional thermal history would not make the grain size smaller, and might well make the grain size larger.

Two factors stand out most prominently in the AFM results. First, the generally small size of the grains (minimum grain size are  $3.815 \text{ nm}^2$ ,  $3.815 \text{ nm}^2$  and  $3.815 \text{ nm}^2$  in samples 1, 2 and 3, respectively, with mean grain size of  $12438 \text{ nm}^2$ ,  $1495.4 \text{ nm}^2$  and  $6252.3 \text{ nm}^2$ ). Second, the large standard deviation in the grain size ( $24065 \text{ nm}^2$ ,  $1900.7 \text{ nm}^2$  and  $8677.0 \text{ nm}^2$  in samples 1, 2 and 3, respectively).

The small grain sizes imply many grain boundaries, with the possibility of enhanced carrier diffusion along the boundaries. [9] Smaller grain size will also result in more grain boundaries between the contacts, which will affect both the dark current [10] and the photocurrent. [9]. The large standard deviation implies a wide variation in grain sizes.

Finally, the maximum grain size is of interest, due to relevance for the behavior of the devices as contact spacing shrinks. The maximum grain size is  $96702 \text{ nm}^2$ ,  $6298 \text{ nm}^2$  and  $27538 \text{ nm}^2$ , for samples #1, #2 and #3 respectively. The large grain size from sample #1 may be a measurement artifact, as the sample image appears to show three adjacent grains which apparently are being treated as one. This impression is reinforced by the fact that a histogram of the grain sizes in sample #1 indicates that the  $96702 \text{ nm}^2$  grain is several times larger than the next largest grain size in the sample.

While the grains are irregular in shape, an idea of their linear dimensions may be obtained by treating the grains as circles. Under that assumption, the smallest grains are circles with diameter  $2.2 \text{ nm}$ , while the largest grains are circles with diameter  $351 \text{ nm}$ ,  $89.6 \text{ nm}$  and  $187 \text{ nm}$ , for samples 1, 2 and 3 respectively. (Remember that the largest grain from sample 1 may be three grains combined, so that its “radius” value may not be an accurate reflection of even the assumed condition. If the true largest grain size for sample #1 is on the order of one-third the indicated maximum grain size, then the true radius for sample #1 is on the order of  $202 \text{ nm}$ .)

Since potential barriers exist at the grain boundaries between grains and are significant barriers to current flow [11], as contact spacing becomes comparable or even smaller than grain size, then the detectors will tend to behave as single-crystal devices. If the contacts to the detectors

are ohmic or leaky Schottky contacts, then the dark current will be limited largely by the resistance of the quasi-single-crystal silicon of the grain.

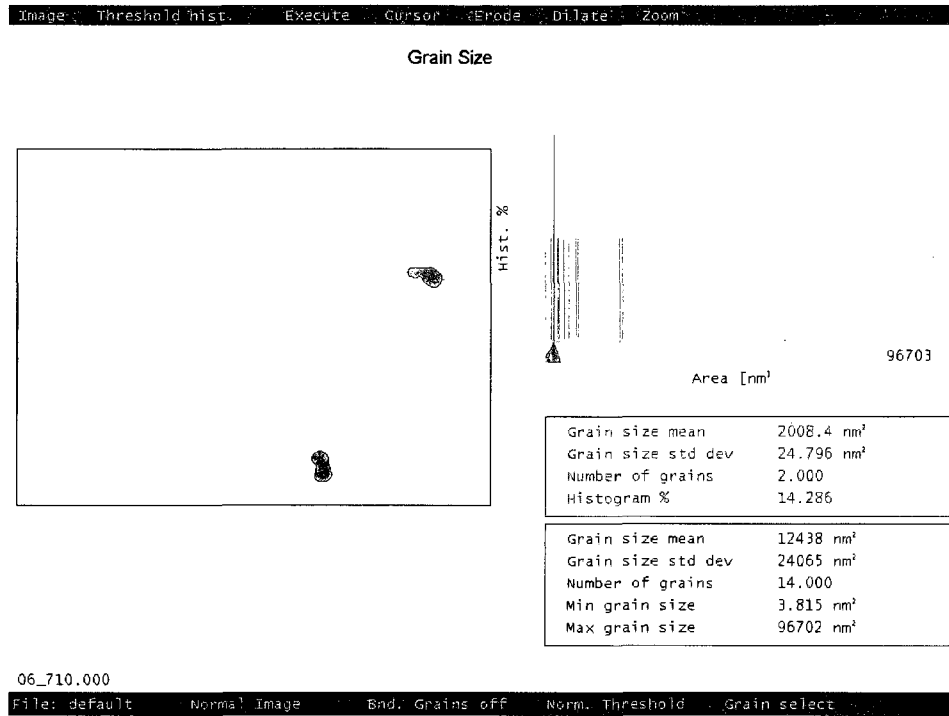


Figure 13: Polysilicon grain size, region 1, 1  $\mu\text{m}$  scan

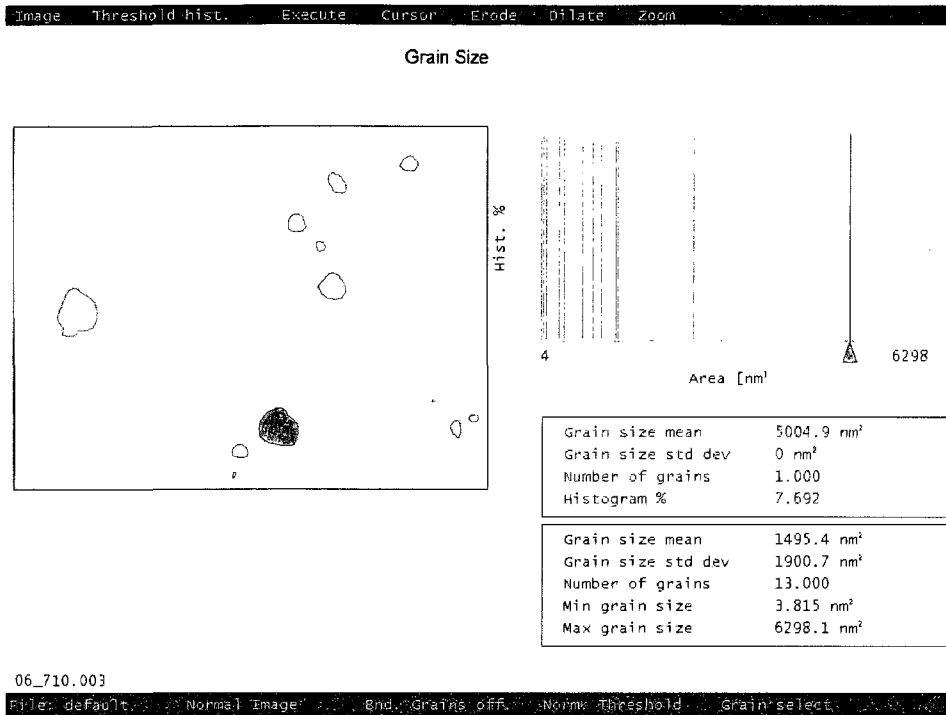


Figure 14: Polysilicon grain size, region 2, 1  $\mu\text{m}$  scan

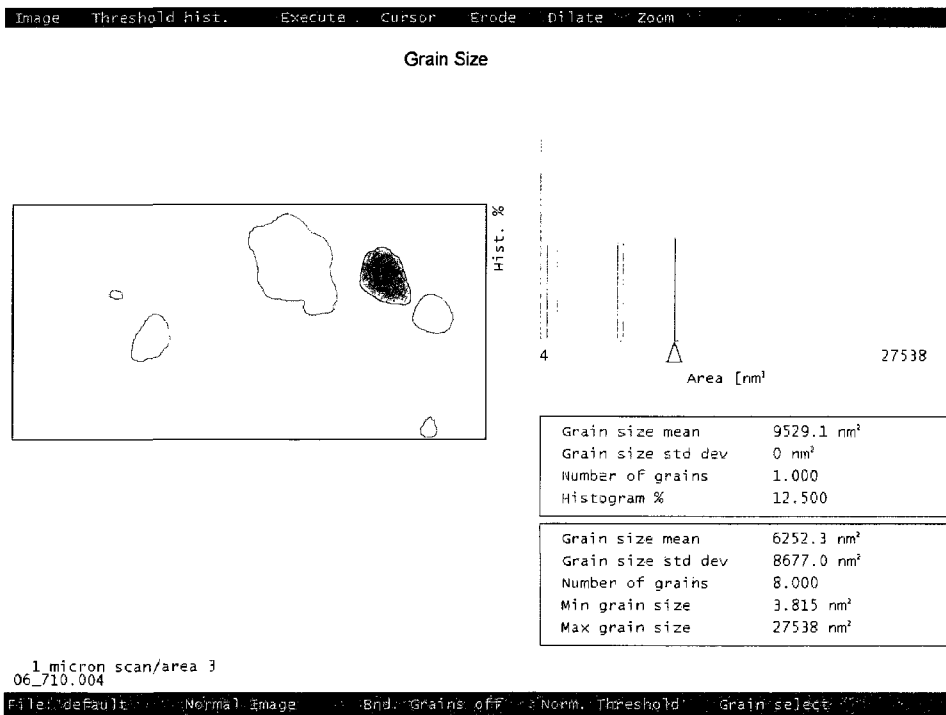


Figure 15: Polysilicon grain size, region 3, 1  $\mu\text{m}$  scan

## References

- [1] G. W. Yuan, "Characterization of integrated waveguide devices," PhD Dissertation, Electrical & Computer Engineering, Colorado State University, Fort Collins, CO, 2007.
- [2] G. Keiser, *Optical Fiber Communications*, 3rd ed. New York, New York: McGraw-Hill, 2000.
- [3] A. M. Raza, "A Truly CMOS Compatible Waveguide Coupled Photodiode for On-Chip Optical Interconnects," Master's thesis, Department of Electrical and Computer Engineering, Colorado State University, Fort Collins, Colorado, 2005.
- [4] C. Thangaraj, "Truly CMOS compatible wave-guide based on-chip optical clock distribution and recovery," Master's thesis, Department of Electrical and Computer Engineering, Colorado State University, Fort Collins, Colorado, 2005.
- [5] S. Wolf, *Silicon Processing for the VLSI Era - The Submicron MOSFET* vol. 3. Sunset Beach, CA: Lattice Press, 1995.
- [6] B. G. Streetman and S. Banerjee, *Solid State Electronic Devices*, 5th ed. Upper Saddle River, NJ: Prentice-Hall, 2000.
- [7] S. K. Ghandi, *VLSI Fabrication Principles: Silicon and Gallium Arsenide*, 1st ed. New York, NY: Wiley-Interscience, 1983.
- [8] I. Time Domain CVD, "TEOS/Oxygen Thermal CVD."
- [9] H. C. Card and E. S. Yang, "Electronic Processes at Grain-Boundaries in Polycrystalline Semiconductors under Optical Illumination," *IEEE Trans. Electron Devices*, vol. 24, pp. 397-402, 1977.
- [10] G. J. Korsh and R. S. Muller, "Conduction Properties of Lightly Doped, Polycrystalline Silicon," *Sol. St. Elect.*, vol. 21, pp. 1045-1051, 1978.
- [11] J. Y. W. Seto, "The Electrical Properties of Polycrystalline Silicon Films," *J. Appl. Phys.*, vol. 46, pp. 5247-5254, 1975.

## DC TESTING AND CHARACTERIZATION OF OPTICAL WAVEGUIDES AND POLYSILICON DETECTORS

### **1 Introduction**

As noted in the previous chapter, the optical waveguides and the polysilicon detectors have design goals which can be characterized as primarily AC or primarily DC. The primarily AC design goal is maximizing the speed of the polysilicon detector. The primarily DC design goals are twofold. One goal is maximizing power transfer through the waveguide to the detector. A second goal is maximizing the response of the polysilicon detector for a unit optical power in.

This chapter will discuss the testing and characterization related to the DC design goals. Testing and characterization of the AC design goals will be discussed in the next chapter.

Section 2 will discuss DC testing and characterization of the waveguides, while Section 3 will discuss the polysilicon detectors. Section 4 will describe the current understanding of the device physics behind the detector, with the exception of the photoconductive gain mechanism discussed in Chapter 2.

### **2 DC Testing and Characterization of the Optical Waveguides**

As discussed in Chapter 2, in order to maximize optical power transfer from the source to the detector, waveguide loss must be minimized. In order to understand the loss mechanisms, and in order to know how much optical power is reaching the detectors, the waveguide loss must be measured. This section will discuss a fiber scanning system which was developed to measure waveguide loss.

#### **2.1 Fiber scanning system hardware**

The fiber scanning system used in this research detects the light scattered up out of the waveguide, similar to the camera method. It consists of a 1 m long, 62.5  $\mu\text{m}$  core diameter, multimode patch cord, a sensitive photodetector (Hamamatsu S8745-01 silicon photodiode/TIA combination), three micropositioners (Zaber T-LA28A) and an XYZ stage

(OptoSigma 65mm x 65mm base, 25mm travel, p/n 122-0470). The output of the photodetector is measured by a Keithley 2400 SourceMeter operating in voltmeter mode. The photodetector was not originally connectorized, so an adaptor port (Fiber Plus International custom threaded detector port) was used to mate the photodetector with the connector on the patch cord. Figure 1 shows a block diagram of the scanning apparatus, while Figure 2 and Figure 3 are photos of the scanning apparatus.

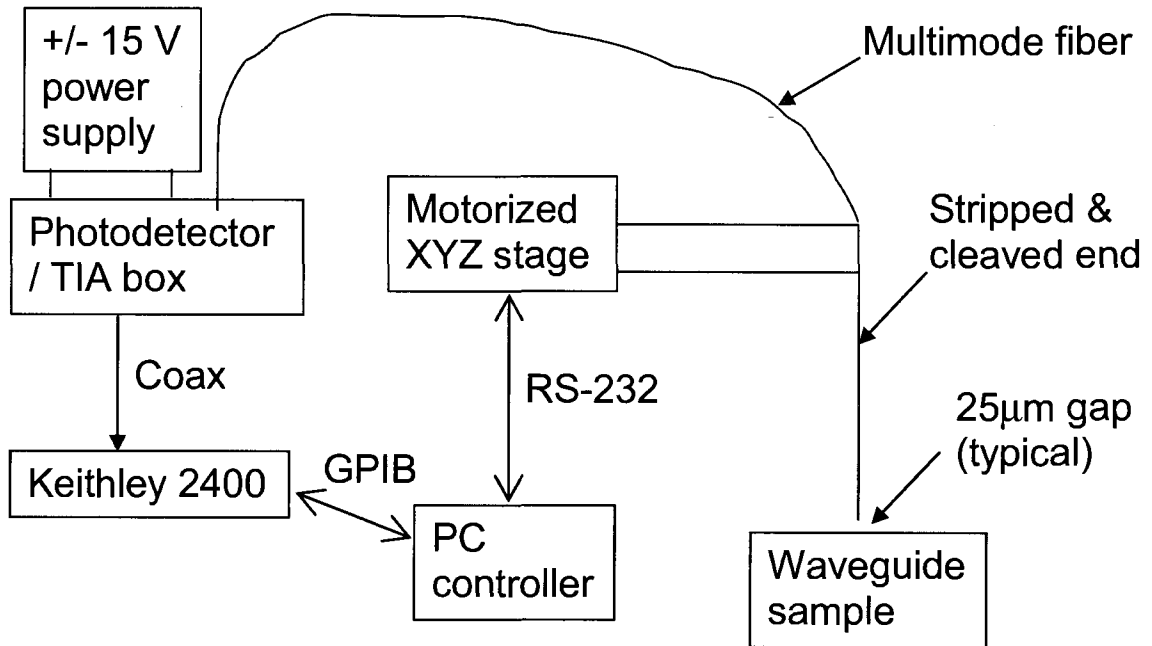


Figure 1: Block diagram of the fiber scanning system

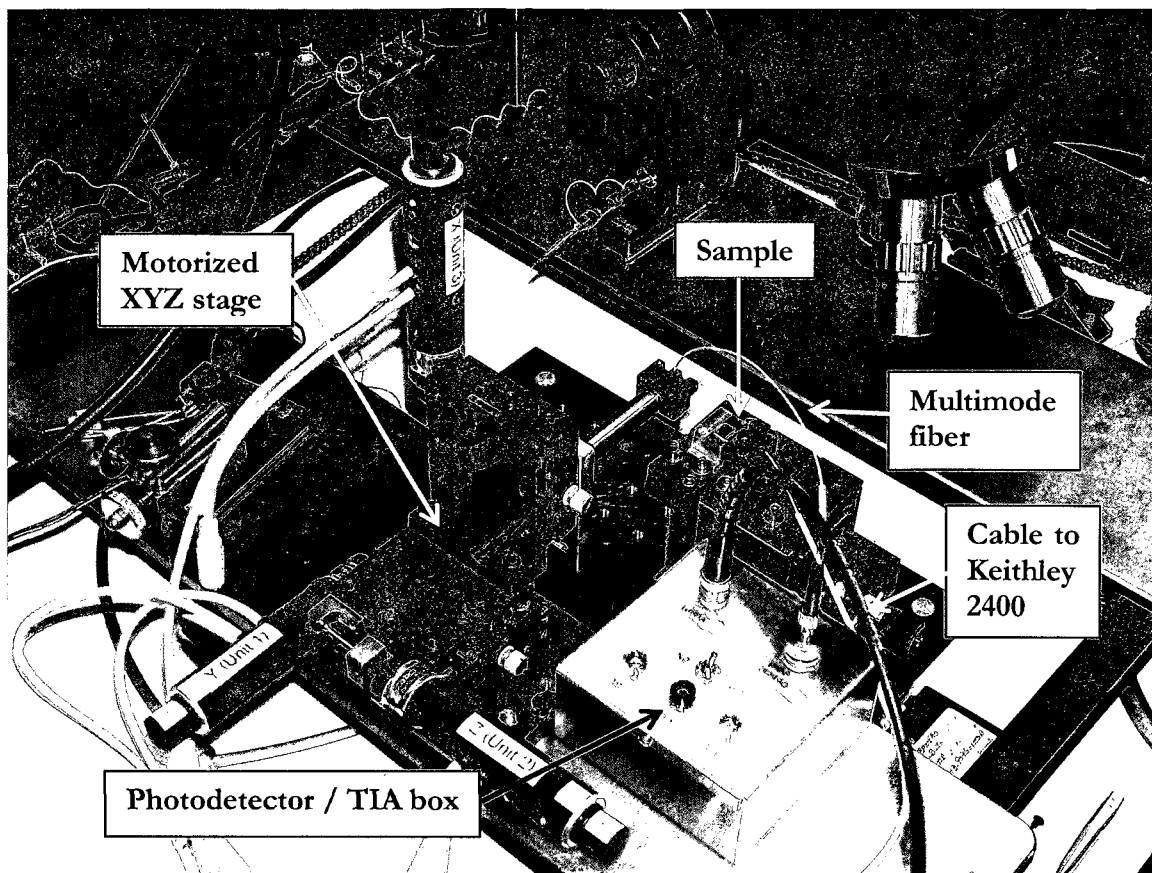


Figure 2: Overhead view of the fiber scanning apparatus. For clarity, the power supply cables to the photodetector / TIA box have been disconnected.

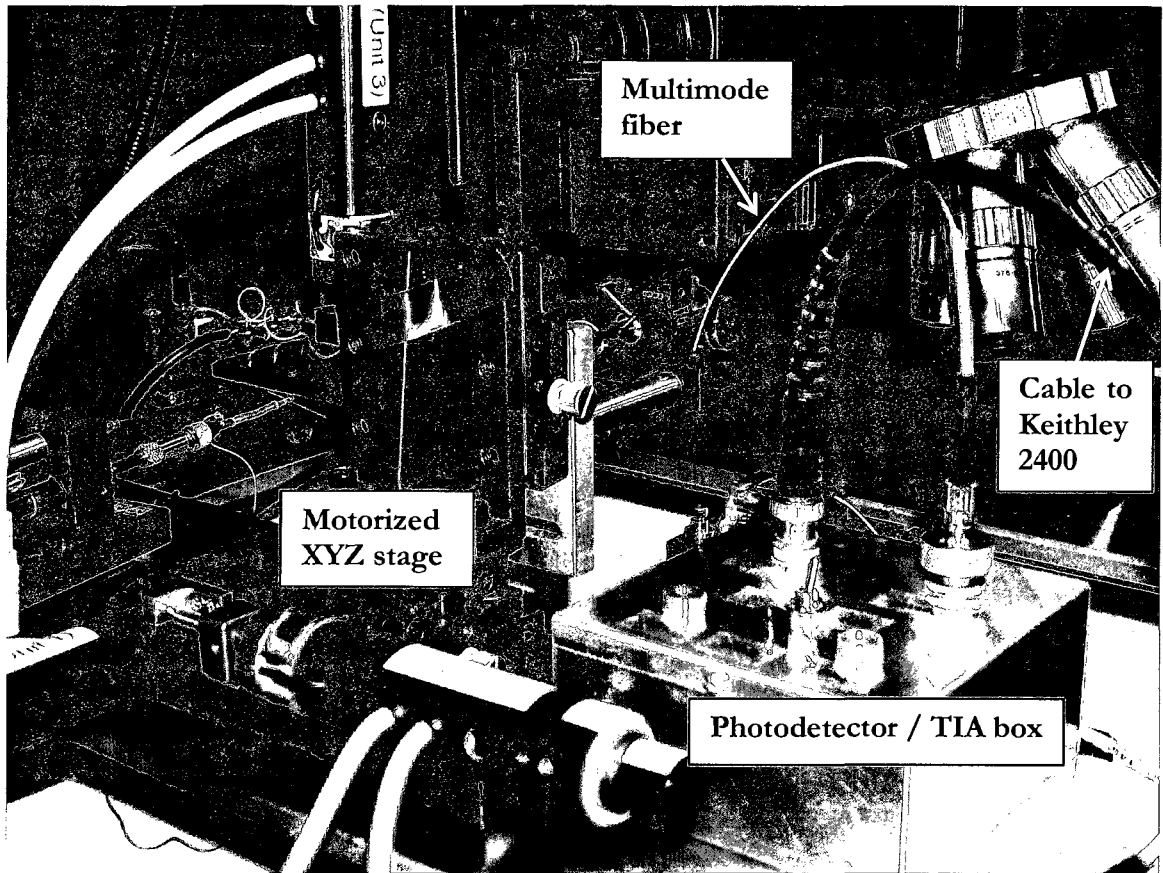


Figure 3: Slight elevation view of the fiber scanning apparatus. For clarity, the power supply cables to the photodetector / TIA box have been disconnected.

The hardware is controlled by a LabVIEW program written around LabVIEW device drivers supplied by Zaber and Keithley. The LabVIEW program will be discussed in the next section.

As mentioned above, the system collects light in a manner similar to camera-based systems depicted in the literature. However, in contrast to camera systems, which are generally limited to visible or near-infrared wavelengths, the fiber scanning system used in this work can be customized to work at any wavelength for which a suitable single-element detector can be found. In addition, camera-based systems need to assure response linearity across the field of view. By using a single detector, the fiber scanning system used in this work eliminates this problem.

Camera pixels often possess relatively low quantum efficiencies, much lower than available from commercial single-element photodiodes. This frequently limits the sensitivity of camera-based systems unless excessively long integration times are used. In contrast, the system used in this research regularly detects optical signals in the picowatt range. Camera-based systems can suffer from quantization error and dark current, especially at low light levels. The quantization error of this system is limited only by the voltmeter used in the system. Dark current in the system is low enough (equivalent to 0.5 pW) that picowatt-level signals can be reliably observed, as mentioned earlier. The specific photodetector used for the results reported in this work is not suitable for observing optical signals above 32 Hz. (Since the fiber scanning system is performing DC waveguide loss characterization, this is not a significant problem for this application.)

It should be noted that the system's sensitivity to picowatt-level signals allows the system to be used with either moderate loss waveguides with very low launched power (the application in this research) or very low loss waveguides with moderate launched power.

Each micropositioner controls the position of one axis of the XYZ stage, replacing the manual micrometers which came with stage. One axis (X) is used to maintain a constant height above the waveguide while the other two axes control the motion across the waveguide (typically Y) and along the length of the waveguide (typically Z).

Standard optical bench hardware was used to attach a post-mountable fiber clamp (ThorLabs T711-250) to the vertical axis stage, with the axis of the clamp in the vertical direction.

The multi-mode patch cord was cut in half. The free end was stripped to a length of 40 to 50 mm by removing the outer jacket, buffer and inner jacket. To eliminate light entering the fiber by any means other than through the fiber tip, the stripped fiber was painted black. The fiber tip was then cleaved to obtain a good optical finish. The stripped end of the fiber was then placed in the fiber clamp, with approximately 30 mm of the stripped fiber below the fiber clamp. Despite concerns about vibration, no vibration-related problems have been observed in practice. If vibrations are a problem, standard anti-vibration precautions (e.g. floating the table) can be taken.

The photodetector and associated circuitry were installed in a box. Inputs to the box are two banana jacks, for the +15 V and -15 V supplies required by the photodetector, a double-pole, single-throw on/off switch, and the adaptor port for the sensing fiber. Output is a BNC connector for the photodetector's output. The circuit used was the example circuit provided on the photodetector's datasheet, with the addition of ferrite cores on the +15 V and -15 V leads at the photodetector, for EMI suppression.

The sensing fiber collects light scattered up out of the optical waveguide and transmits it to the photodetector, which converts it to a voltage. The assumption is made that the optical power scattered up out of the waveguide is a constant fraction of the optical power in the waveguide.

Care is required to ensure that light from the source which is not coupled into the optical waveguide is not scattered from surface of the sample. Uncoupled scattered light from surface defects could lead to a false value of the intrinsic waveguide scatter and thus waveguide loss. This problem is easily avoided by the use of a physical light block near the input of the waveguide, such as a small piece of opaque paper temporarily attached to the sample.

## **2.2 Fiber scanning system software**

As mentioned above, Keithley meter and the Zaber micropositioners which drive the XYZ stage are controlled by a LabVIEW program which combines Keithley and Zaber-supplied device drivers with in-house written code. In general terms, the LabVIEW program commands the micropositioners to scan the sensing fiber across the waveguide to be measured a user-specified number of times, typically three. Following this, the LabVIEW program commands the micropositioners to move the sensing fiber to a new position along the waveguide. Once the sensing fiber is in the new position, the "scan across the waveguide" step is repeated. This "move to a new location on the waveguide and scan across it" procedure is repeated for a user-specified distance along the waveguide.

The LabVIEW program was written to command the micropositioners to move in absolute amounts (e.g. move to 17280  $\mu\text{m}$ ). Tests were performed using movements in relative amounts (e.g. move 10  $\mu\text{m}$  forward from the current position), but it was found that absolute movements had better position repeatability. This is because an arbitrary amount, whether an

absolute movement or a relative movement, may not be exactly expressible as an integer multiple of the stage resolution –  $0.0992\ \mu\text{m}$  for the units used in this system. When making absolute moves, the micropositioner will take the stage to within one stage resolution of the desired location. When making relative moves, the position errors tend to add. (e.g. If the first movement is short by, for example, half the stage resolution, all subsequent motions will also be short by the same amount. If the stage takes, say, 30 steps to get to its desired final position, the final position will be off by 30 times half the stage resolution.)

The starting position for the scan at each step down the waveguide is adjusted to place the peak of the scan at the previous step in the center of the scan. This reduces the scan length required to characterize the waveguide, by eliminating the need to have the scan length large enough to compensate for any misalignment of the sensing fiber to the waveguide. By reducing the scan length, the measurement time is reduced. (The initial starting position is established by a single relatively long scan (typically 1 mm) whose sole purpose is to locate the peak. Once the location of the peak has been found, the starting position is set so that the peak will be half-way through the relatively short scan (typically  $200\ \mu\text{m}$ ) used to for the measurements which will characterize the waveguide.)

### **2.3 Fiber scanning system experimental procedure**

When preparing to scan a waveguide, care was taken to arrange the scan start and stop positions so that the vertical axis is either unchanging or moving down (being pushed by the micropositioner) while scanning, to avoid any problems caused by the lack of force exerted by the vertical stage's internal spring when near the stage's fully retracted position. Note that this was a problem only for the vertical axis stage, not for either of the horizontal axis stages. Since the problem only exists near the vertical axis stage's fully retracted position, and the scan typically takes place with the vertical axis stage near the middle of its travel, ensuring the scan moves down was done largely to eliminate one possible source of error.

The vertical axis height change down the waveguide is found by commanding the vertical axis micropositioner to lower the multimode sensing fiber until it just touches the surface of the sample at one end of the region to be scanned, then repeating this procedure at the other end of the region to be scanned. Touching is determined by carefully observing the fiber to see

where it begins to flex. This is one reason why a long length of fiber is stripped – the sideways flexing is easier to see when a long length of stripped fiber is involved. The vertical axis height change is found by calculating the difference between the “just touching” height at the two ends of the region to be scanned. This vertical axis height change is one of the inputs to the LabVIEW program which runs the fiber scanning system. With practice, a vertical position repeatability of 2  $\mu\text{m}$  or better was obtained.

The scanning process is divided into two parts – a “fast” scan across the width of the waveguide and a “slow” scan along the length of the waveguide. The LabVIEW program allows the user to specify which horizontal stage will be the fast scan axis; the other horizontal stage is assigned the slow axis scan. The program also allows the user to specify, for both horizontal scan axes, the total scan length, the number of steps and the delay between steps. Finally, the user can specify how many passes across the waveguide and down the waveguide are to be performed. Typical values used are three passes across the waveguide and one pass down the waveguide. (The three passes across the waveguide allow for averaging and thus signal-to-noise improvement and anomalous spike identification.)

Maintaining the sensing fiber at a constant height above the waveguide, from the start of the scan to the end of the scan is important. If the sensing fiber’s height above the waveguide varies, the amount of optical power collected by the sensing fiber will also vary. This height-induced variation will cause errors in waveguide loss calculations.

The LabVIEW program also allows the user to specify the height change between the start and end of the scan along the length of the waveguide. This total height change is divided by the number of steps along the length of the waveguide, giving a “vertical axis height change per slow axis step”. This procedure assumes there is no topography involved with the waveguide, but as this is commonly the case, it is not a severe restriction. In addition, height change across the width of the waveguide is ignored. However, since waveguide widths are commonly on the order of a few microns or less, while the length of the waveguide is typically a few millimeters, this is again not a severe restriction.

In theory, if the waveguide is a constant width, the full-width half-max (FWHM) of the peak could be used to keep the sensing fiber at a constant height above the waveguide. This would be done by adjusting the height of the sensing fiber to keep the FWHM constant. However, to date attempts to use the FWHM have proved less satisfactory than the fiber-touch technique described above.

#### 2.4 Fiber scanning system experimental results

Figure 4 and Figure 5 show experimental results obtained with the system. These results are from three passes across the waveguide at a position approximately 2 mm from the input of the waveguide. When the average peak value from these results is combined with results from other positions along the waveguide, the waveguide loss is easily determined. Figure 6 shows the full-width half-max (FWHM) of the detector peak down the waveguide.

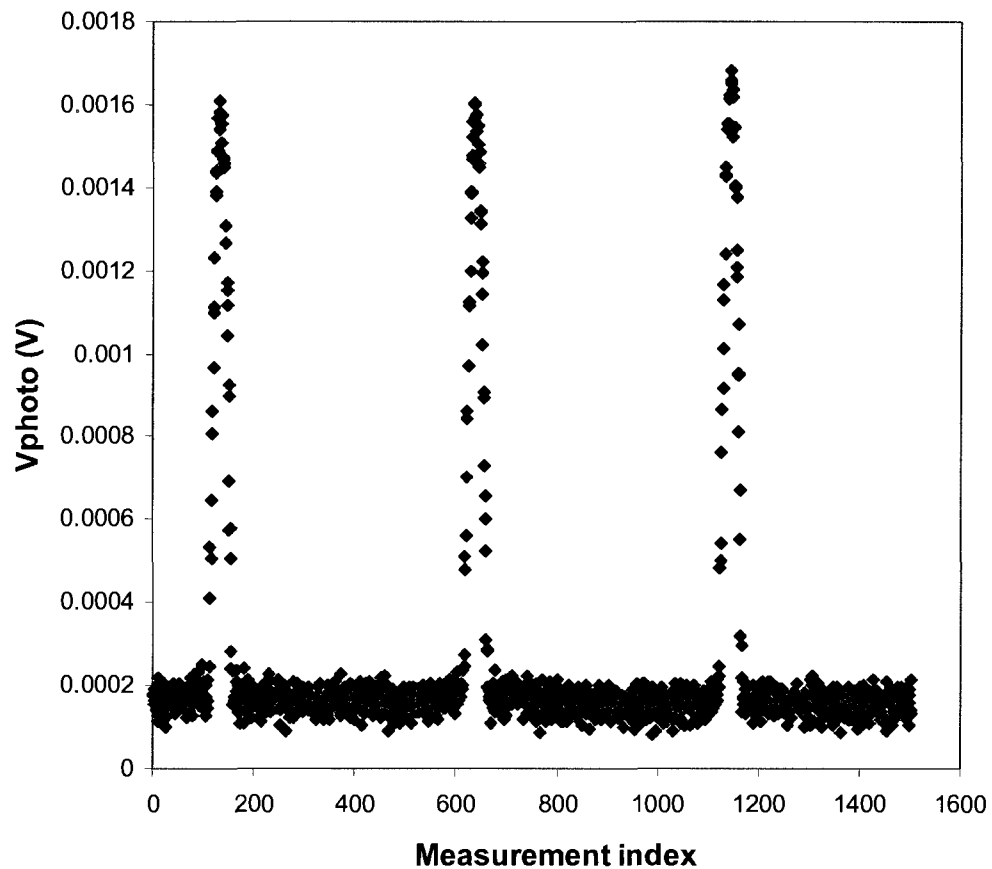


Figure 4: Results from the pass furthest from the waveguide input, clearly showing the three passes and a good contrast ratio

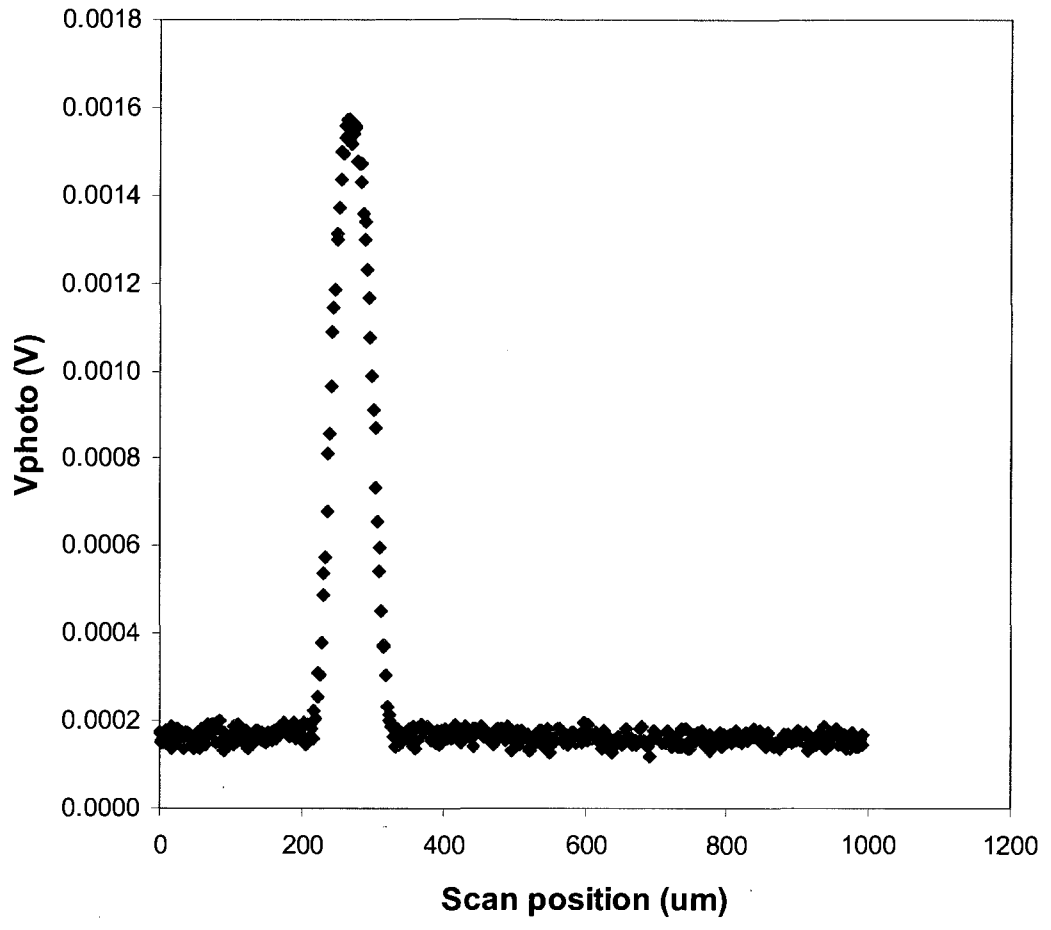


Figure 5: Average of three passes. Max  $V_{\text{photo}} = 0.001573$  V, FWHM = 67  $\mu\text{m}$

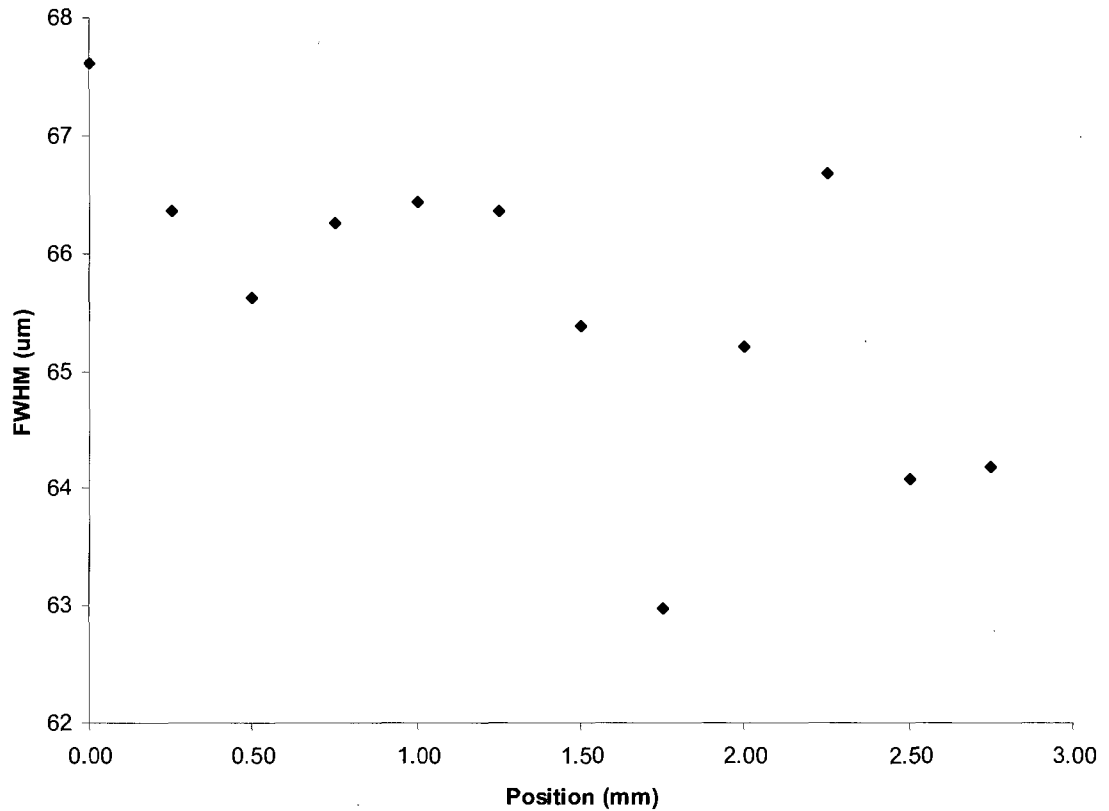


Figure 6: FWHM of detector response vs. position down waveguide

### 2.5 Anomalously high waveguide loss and its cause

An unexpected waveguide loss mechanism made its existence known during waveguide loss testing. The first sign of this loss mechanism was when waveguide loss measurements showed that the loss was both much higher than expected and almost independent of waveguide width, as shown in Figure 7 below. Note that the waveguide loss results are even more uniform than they might appear, as the points “109, O10, try #1” and “167, I8, try #1” are both at width = 0.5, loss = 8.8dB/cm.

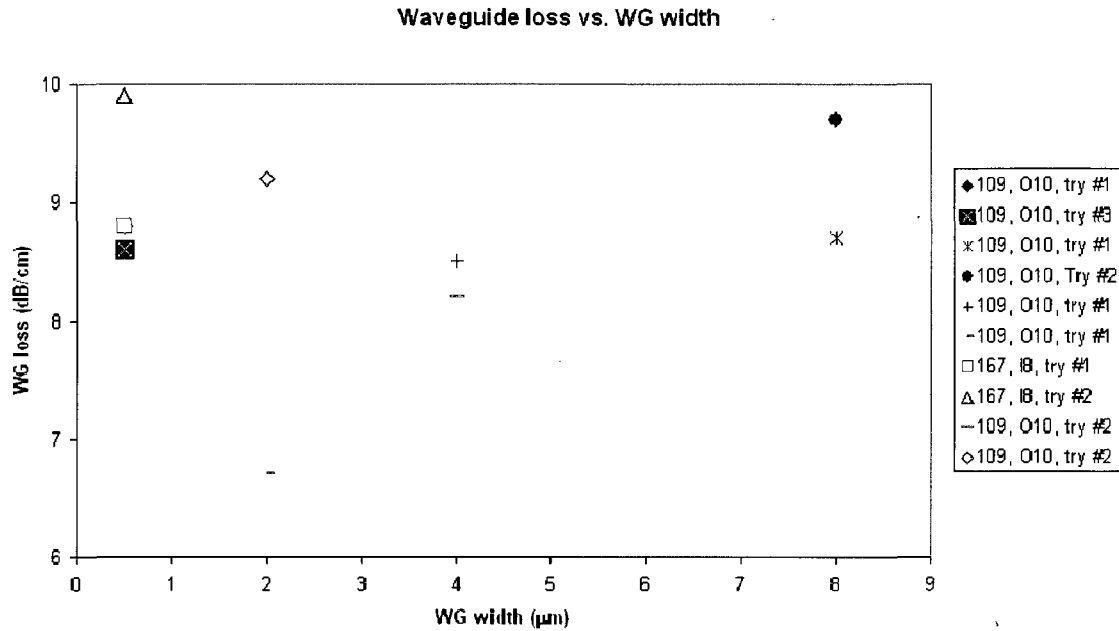


Figure 7: Waveguide loss vs. waveguide width

Investigations uncovered the fact that the phosphosilicate glass (PSG) which forms part of the lower cladding of the waveguide has a very low, but non-zero, absorption coefficient, or equivalently, the imaginary part of the index of refraction, with  $n_i = 0.0015$ . [3] As a result, evanescent coupling and radiation mode coupling from the waveguide core to the PSG layer, similar to the desired coupling between the waveguide and the polysilicon detectors, caused optical power to flow from the waveguide into the PSG film. While the unexpected and undesired coupling from the waveguide to the PSG film is much lower than the desired coupling to the polysilicon detectors, the waveguide runs are also much longer than the polysilicon detectors – a few millimeters versus a few microns.

RSoft simulations of the waveguide structure, summarized in Figure 8 below, confirmed the proposed mechanism for the high observed waveguide loss.

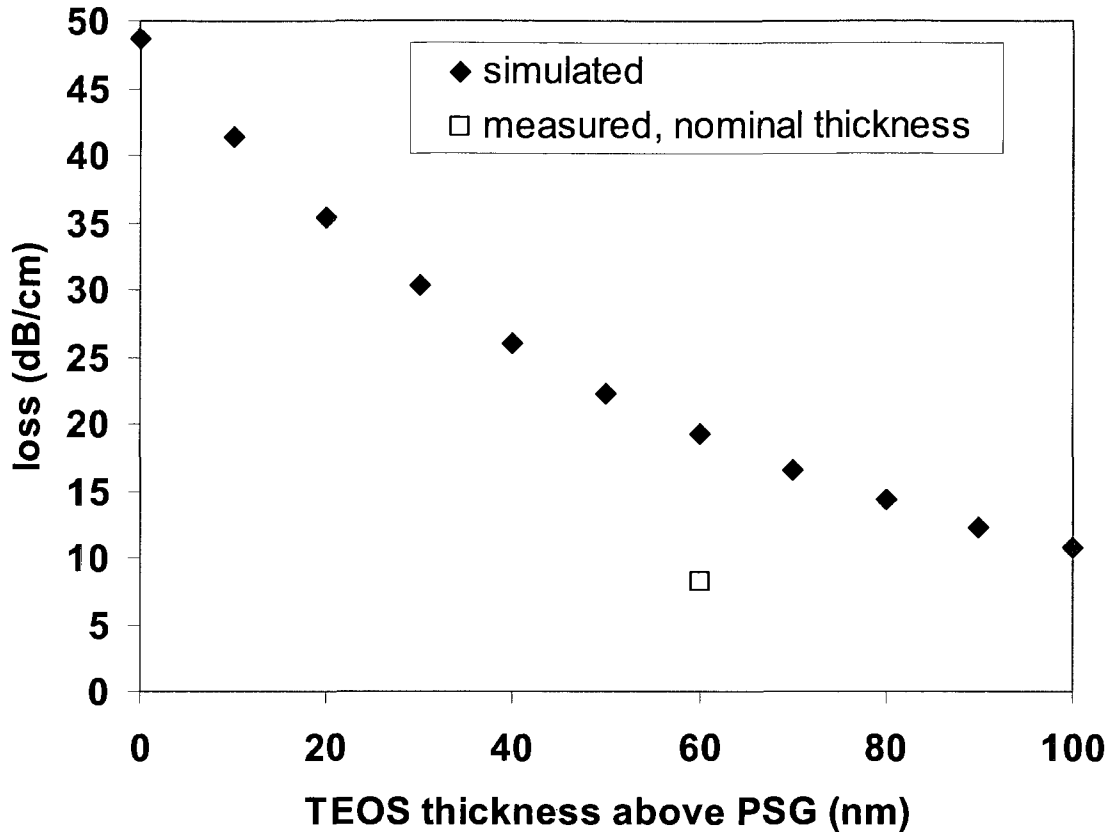


Figure 8: Simulated waveguide loss for varying TEOS thicknesses over PSG. Since the TEOS layer is between the  $\text{SiN}_x$  waveguide core and the PSG layer, thicker TEOS layers reduce the evanescent coupling between the waveguide core and the PSG and thus reduce the optical power absorbed in the PSG.

This unexpected waveguide loss mechanism could be ameliorated in several ways: The lower cladding is a tetra-ethyl orthosilicate (TEOS)-based silicon dioxide layer on top of the PSG layer. If PSG layer is made thinner, since the TEOS layer is chem-mechanically polished (CMP) down to the top surface of the polysilicon, the TEOS layer will be thicker, to compensate for the thinner PSG layer underneath it. As a result, the evanescent overlap will decrease. Alternatively, if the polysilicon is made thicker, the TEOS will become thicker. Since the wafer fabrication process is such that the PSG thickness is fixed at a nominal 195 nm, and since (as mentioned above) the top of the TEOS layer is CMP'd down to the top surface of the polysilicon layer, if the polysilicon is thicker, the TEOS will be thicker. This concept is shown in Figure 9 below. Finally, it might be possible to adjust the deposition

conditions of the PSG layer to reduce its absorption coefficient without interfering with its role in the standard CMOS process.

On implication of the near-independence of waveguide loss on waveguide width shown in Figure 7 is that sidewall losses are not very important compared to other loss mechanisms.

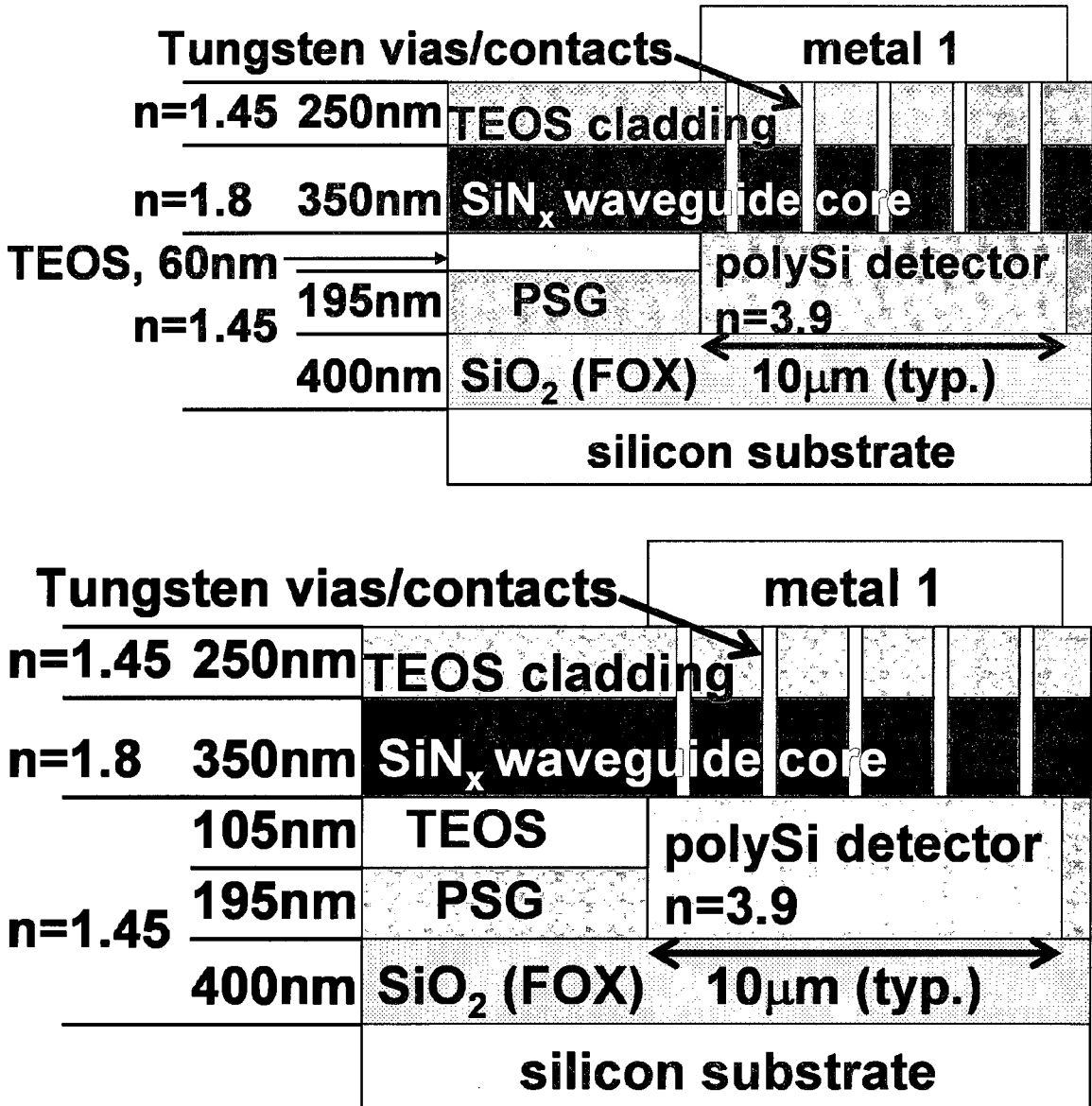


Figure 9: Detector side views, with standard 255 nm poly (top) and modified 300 nm poly (bottom), showing increased TEOS thickness. For clarity, the LPCVD silicon nitride “spacers” on the sides of the polysilicon have been omitted.

### **3 DC testing and characterization of the polysilicon detectors**

As noted in the previous chapter, one of the major design goals for the polysilicon detectors is maximizing the photocurrent response for a unit optical power input. This is known as the responsivity of the detector, and is expressed in Amperes/Watt. A related design goal is minimizing the dark current. If the dark current is not low, it will be difficult to get adequate photocurrent / dark current contrast ratios at low optical signal intensities.

Detector responsivity was measured largely using the edge-coupled waveguide photodetectors. However, one first-generation H-tree detector, with 1.14  $\mu\text{m}$  contact spacing, was also measured. This was done to probe the smallest contact spacing device on the first-generation test chip.

Sample preparation is discussed in Chapter 3 and Appendix E. First and second generation test chips and detectors are discussed in Chapter 3, Appendix B and Appendix C. While discussed in Chapter 3, it is worth repeating that first generation detector length was limited to 5  $\mu\text{m}$  and 10  $\mu\text{m}$ , with the 2:1 ratio allowing analytical extraction of the absorption coefficient of the polysilicon detector. Similarly, it is worth repeating that on the second generation test chip, all edge-coupled waveguide devices with contact spacing smaller than 2.14  $\mu\text{m}$  were unusable, with signs of shorting. Even 2.14  $\mu\text{m}$  contact spacing devices were unusable on some die. Dark current were in excess of 100  $\mu\text{A}$  at 0.1 V bias. Typical dark currents are on the order of 100 picoamps at 0.1 V bias. Oddly, most H-tree detectors were not dead, despite most devices having contact spacing of 1.14  $\mu\text{m}$  or smaller. A mask problem is suspected, as the design artwork conforms to all of the process design rules and the fabrication appears correct.

#### **3.1 Experimental procedure for measuring detector responsivity**

As noted in Chapter 3, following fabrication and sawing of the wafers, individual die were edge-polished to an optical quality finish, to allow end-fire coupling to the waveguide.

Following polishing, DC characteristics of photodetectors with varying contact spacing and length values on the same die were measured using an HP 4145 Semiconductor Parametric Analyzer. The sample was electrically probed with needle probes while light from a  $\lambda = 654$

nm laser diode (for first-generation devices) or  $\lambda = 690$  nm laser diode (for second generation devices)<sup>18</sup> was coupled to the waveguide via a 4 $\mu$ m core diameter, 0.11 NA (numerical aperture) visible single mode fiber with a cleaved end close to the polished chip facet. The fiber was actively aligned to the waveguide by initially biasing the photodetector under test at +5 V and maximizing the photocurrent. The bias voltage was swept from -20 V to +20 V for first generation devices while measuring the photocurrent using a 267 ms integration time. Dark current for each photodetector was measured over the same bias range. Second generation devices tended to break down around 13 V, so the voltage sweep for second generation devices was from -10 V to +10 V.

While the reported measurements were made using needle probes, later responsivity measurements were made using a Cascade Microtech ACP-GSG-125 high-speed probe. While overkill for DC responsivity measurements, sample probing was simplified by using the Cascade probe. In addition, use of the Cascade probe simplified switching between DC measurements and AC measurements. No difference was seen in the responsivity results between the two types of probes.

Input optical power was estimated by coupling light into a 0.5  $\mu$ m waveguide that crossed the die without being coupled to an on-chip detector. Scattered intensity was measured by scanning a 62.5  $\mu$ m core diameter fiber 25  $\mu$ m above the surface of the waveguide and fit to determine waveguide loss. Based on the loss as well as the output power of the waveguide, the typical power in the waveguide immediately prior to the photodetector was estimated to be  $P_{inc} = 5.3 \mu$ W

### 3.2 Detector responsivity experimental results

The multiple of two in detector lengths (5  $\mu$ m, 10  $\mu$ m), combined with the standard exponential absorption model, results in a quadratic equation that can be solved to find the

$$\text{effective absorption rate, } \alpha_{eff} = \frac{1}{L} \ln \left( \frac{2\rho}{1 - \sqrt{1 - 4\rho(1-\rho)/(1-f)}} \right).$$

---

<sup>18</sup> The 645 nm laser diode was a Sharp G06510B2A. The 690 nm laser diode was a Hitachi HL6738MG. The only reason for the switch between first and second generation devices is that we became aware of the higher power and higher bandwidth

Using  $f=0.355$  from [4] ( $f$  is the fraction of the incident power that is directly coupled from the waveguide into guided modes of the polysilicon),  $L=5\ \mu\text{m}$  (the short detector length) and  $\rho=0.81$  as the average ratio of photocurrent of  $5\ \mu\text{m}$  and  $10\ \mu\text{m}$  long detectors for the  $2.6\ \mu\text{m}$  and  $5.6\ \mu\text{m}$  contact spacings, the calculated effective absorption coefficient is  $0.63\ \text{dB}/\mu\text{m}$ , in good agreement with the value of  $0.67\ \text{dB}/\mu\text{m}$  from [4].

The dependence of photocurrent on contact spacing and applied voltage indicated that photoconductive gain was significant at E-fields above  $10\ \text{kV}/\text{cm}$ . As expected, reducing the contact spacing increased the responsivity for both  $5\ \mu\text{m}$  and  $10\ \mu\text{m}$  long detectors as shown for a fixed bias of  $+10\ \text{V}$  in Figure 10 below. Other bias voltages had similar trends. No saturation of gain as a function of contact spacing was observed at the smallest contact spacing, indicating that yet smaller contact spacings will result in higher effective responsivity. The observed behavior is consistent with the known behavior of primary and secondary photocurrent resulting from a photoconductive gain process which is proportional to the ratio of carrier recombination lifetimes to transit time between the electrodes of the device [5].

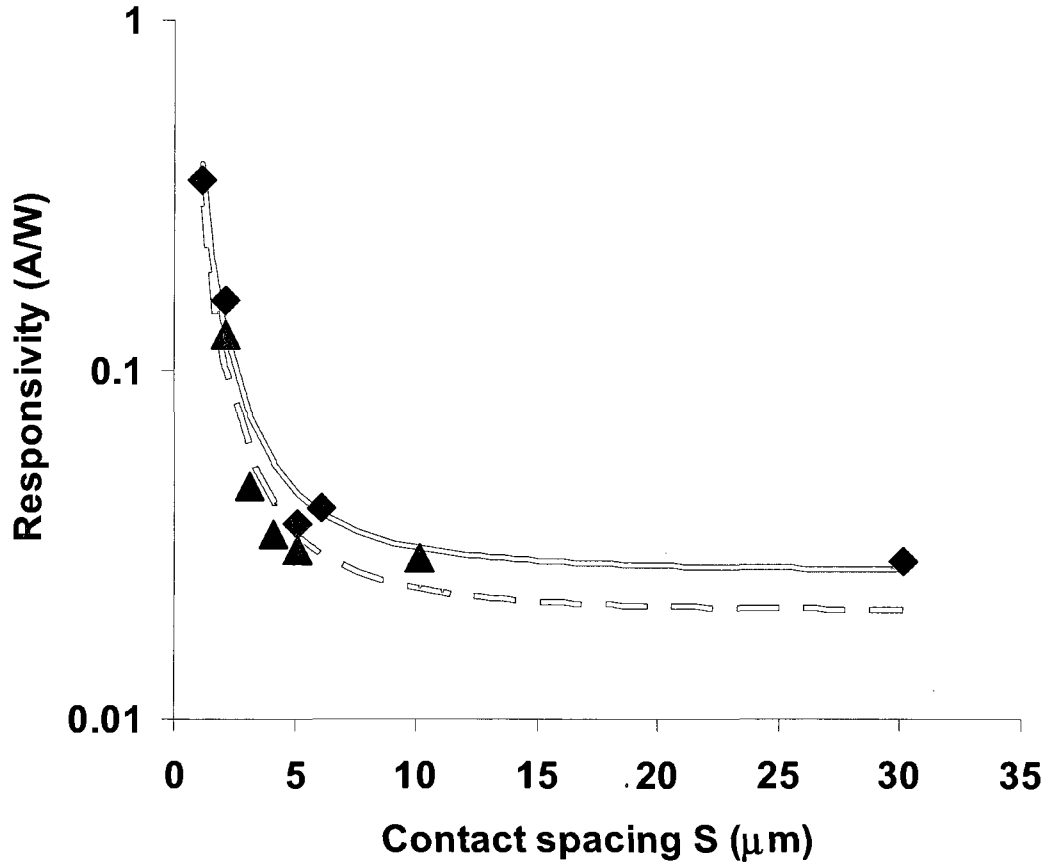


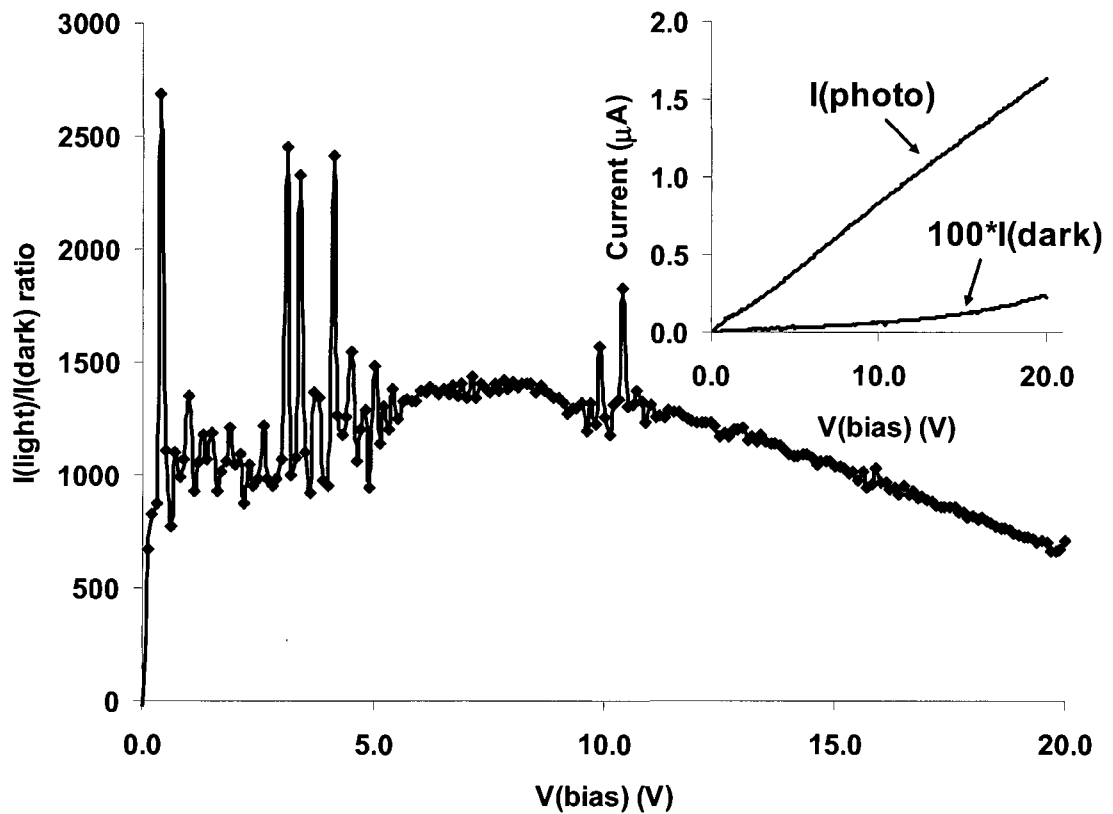
Figure 10: Experimental data for 10  $\mu\text{m}$  devices (diamonds) and fit to theory. (solid line). 5  $\mu\text{m}$  devices (triangles, dashed line) are also shown.  $V_{\text{bias}}$  is 10 V.

The primary photocurrent is given by  $I_1 = \eta_c [q\lambda/hc] P_{\text{opt}}$ , where  $\eta_c$  is the primary carrier collection efficiency and  $P_{\text{opt}}$  is the incident optical power. The primary photocurrent is largely independent of the applied field, as long as the field strength is sufficient to separate the photogenerated holes and electrons before they can recombine with each other. The photocurrent response shown in Fig. 5 for devices with 6  $\mu\text{m}$  contact spacing or greater is mostly due to primary photocurrent.

The total photocurrent was assumed to be given by the sum of primary and secondary photocurrent. [5], [6]  $I_{ph} = I_1 (1 + \tau(\mu_n + \mu_p)V/S^2)$ , where  $\mu_n$  and  $\mu_p$  are the carrier

mobilities,  $\tau$  is the lifetime, and  $S$  is the contact spacing. This matches the observed behavior in Figure 10 above. For the 10  $\mu\text{m}$  long devices and  $P_{\text{inc}} = 5.3 \mu\text{W}$ , an  $I_1$  of 0.139  $\mu\text{A}$  ( $R_1 = 0.026 \text{ A/W}$ ) and a  $\tau(\mu_n + \mu_p)$  of 1.79  $\mu\text{m}^2/\text{V}$  at  $V=10 \text{ V}$  fits the data well.<sup>19</sup> With the same  $\tau(\mu_n + \mu_p)$ , the 5  $\mu\text{m}$   $I_1$  is 0.106  $\mu\text{A}$  ( $R_1 = 0.0200 \text{ A/W}$ ). As shown in Figure 10, and as expected from the detector length and contact spacing results, the 0.5  $\mu\text{m}$  wide waveguide, 10  $\mu\text{m}$  long detector and 2.6  $\mu\text{m}$  contact spacing device had the highest responsivity, at 0.16  $\text{A/W}$  at 10V. Earlier work [4], which examined only 10  $\mu\text{m}$  long, 1.14  $\mu\text{m}$  contact spacing detectors in a clock-distribution H-tree, reported a responsivity of 0.35  $\text{A/W}$  at 10 V.

Figure 11, below, shows that the  $I_{\text{ph}}$  to dark current ratio, which is important for noise and signal detection threshold considerations, is above 500 and generally above 1000.



<sup>19</sup> Note, however, that the correct photocurrent fitting equation has a K factor multiplying the  $\mu\tau$  values, as discussed in Appendix A, "DC response from impulse response". As a result, the extracted  $\mu\tau$  value is incorrect.

Figure 11: Photocurrent to dark current ratio for a 0.5  $\mu\text{m}$  waveguide, 10  $\mu\text{m}$  detector, 2.6  $\mu\text{m}$  contact spacing device. Inset shows I-V characteristics for the same device. Noise spikes are due to quantization noise when measuring dark current.

### 3.3 Asymmetric device results

The asymmetric device results, shown in Figure 12, from the second-generation wafers were interesting. As noted in Chapter 3, there were two devices with asymmetrically-placed contacts. One device had a 0.5  $\mu\text{m}$  wide waveguide; the other had a 4  $\mu\text{m}$  wide waveguide. Both devices had 10  $\mu\text{m}$  long detectors, and both devices had contact-edge-to-waveguide-edge distances of 1  $\mu\text{m}$  on one side of the waveguide and 10  $\mu\text{m}$  on the other side of the waveguide. When doing voltages sweeps, the results did not appear to depend on which contact was held fixed at 0 V and which contact had the swept voltage applied. Comparing asymmetric device results to symmetric device results proved difficult. The most similar symmetric device to the 0.5,10,(1,10) asymmetric device was the 0.5,10,2.14 device. (This assessment is based on the waveguide-center-to-closest-contact-edge distance of 1.07  $\mu\text{m}$  on the 0.5,10,2.14 device and 1.25  $\mu\text{m}$  on the 0.5,10,(1,10) device.) The most similar symmetric device to the 4,10,(1,10) asymmetric device was the 4,10,4.64 device. (This assessment is based on the waveguide-center-to-closest-contact-edge distance of 2.32  $\mu\text{m}$  on the 4,10,4.64 device and 3  $\mu\text{m}$  on the 4,10,(1,10) device. While the distances are not very close, there was only one symmetric 4,10,X device on the second-generation die.) Unfortunately, the 0.5,10,2.14 symmetric device was one of the devices which appeared to be shorted on almost all of the tested die. The only consistently working 0.5,10,X symmetric device was the 0.5,10,4.14 device, and it was felt that this was too different from the 0.5,10,(1,10) device to allow useful comparisons. For the 4,10,(1,10) device, the maximum photocurrent at 10 V bias was 0.79  $\mu\text{A}$ . Under the same illumination and bias conditions, the 4,10,4.64 device had a maximum photocurrent of 20.9  $\mu\text{A}$ , or 26 times higher. This tends to indicate that the waveguide-edge-to-closest-contact-spacing distance is not very important. As both the transit time and the electric field depend on the contact-edge-to-contact-edge spacing, this is not surprising, in retrospect. In essence, it appears that the exact location of the waveguide between the contacts (i.e. the location of the photogenerated EHP in the polysilicon detector) is not

particularly important, at least for DC results. Note that Figure 12 is for 0.5,10,X devices, not 4,10,X devices. Also note that while the 4,10,4.64 device had a photocurrent 26 times that of the asymmetric 4,10,(1,10) device, the 0.5,10,4.14 device has a photocurrent only about twice that of the asymmetric 0.5,10,(1,10) device. This may indicate that the optical power delivered by the 4  $\mu\text{m}$  wide waveguide is enough greater than that delivered by the 0.5  $\mu\text{m}$  wide waveguide that the generation of EHPs in the 4  $\mu\text{m}$  waveguide device does a better job of lowering the polysilicon grain boundaries.[7] The hump in the 0.5,10,2.14 device's I-V curve may be connected with the problems seen with that device being shorted on most tested die.

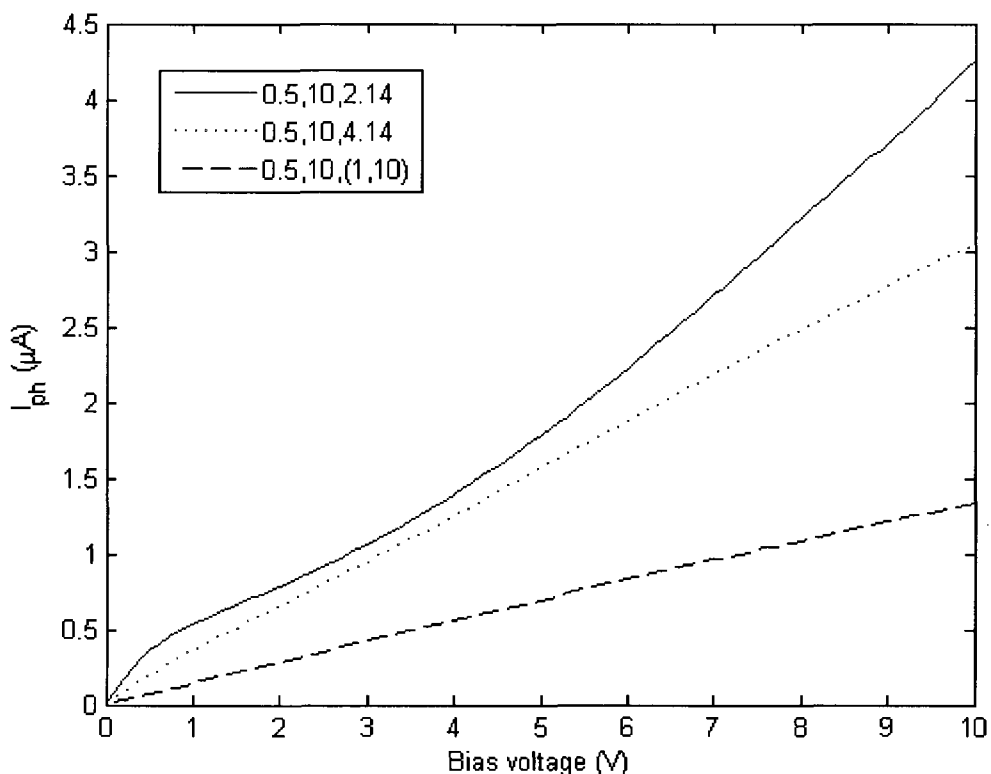


Figure 12: Second-generation I-V comparison of asymmetric device with two related symmetric devices

### 3.4 Experimental procedure for measuring detector dark current

Dark current was measured using the same devices as were used for responsivity measurements. The typical procedure was to measure the dark current and then to measure the photocurrent. As with the responsivity measurements, an HP 4145 Semiconductor Parametric Analyzer was used to measure the current, with the detector bias voltage swept

from -20 V to +20 V for first-generation devices and -10 V to +10 V for second generation devices. Dark current was measured using a 267 ms integration time, as mentioned above. As with the responsivity measurements, initial measurements were made using needle probes, while later measurements were made using a Cascade Microtech ACP-GSG-125 probe. (As mentioned above, use of the Cascade probe simplified both probing the sample and switching between DC and AC measurements.) To ensure that no light reached the detector during the dark current measurements, the input laser diode, the microscope light and the room lights were all turned off and an opaque black cloth was draped over the test system.

### 3.5 Detector dark current experimental results

A key piece of data in understanding the physics behind the detectors, as discussed in Section 4, was provided by the dark current results. Figure 13 through Figure 17 show typical first- and second-generation  $I_{\text{dark}}$  results. Note the exponential nature of I-V relationship. In particular, note that there is no sign of the dark current reaching a saturation value. Figure 17 also shows the fit of the data to a hyperbolic sine (sinh) curve. The significance of this will be discussed later.

While the exponential growth could be a sign of Schottky diode breakdown, that seemed unlikely to me. Breakdowns tend to result in an abrupt increase in current, not the relatively gradual increase seen here. In addition, only part of the bias voltage will be dropped across the Schottky junction. Finally, there should be a diode reverse leakage region before breakdown occurs. As noted above, there is no sign of a reverse leakage limited current in the I-V plots. (With back-to-back Schottky contacts, one of them had to be reverse-biased when doing an I-V sweep in the dark, and should therefore limit the overall current.)

The Schottky diode's I-V characteristic is  $I = I_S \left[ \exp\left(\frac{qV_A}{kT}\right) - 1 \right]$ , where

$I_S = AA^*T^2 \exp\left(\frac{\Phi_B}{kT}\right)$ , A is the cross-sectional current flow area of the diode, A\* is modified

Richardson's constant, T is the absolute temperature,  $\Phi_B$  potential height of the Schottky barrier and k is Boltzmann's constant. [1] This is the same basic form as the ideal diode

equation. However, as noted above, and as seen in the plots, there is no sign of reverse-biased Schottky current in the dark current I-V plots.

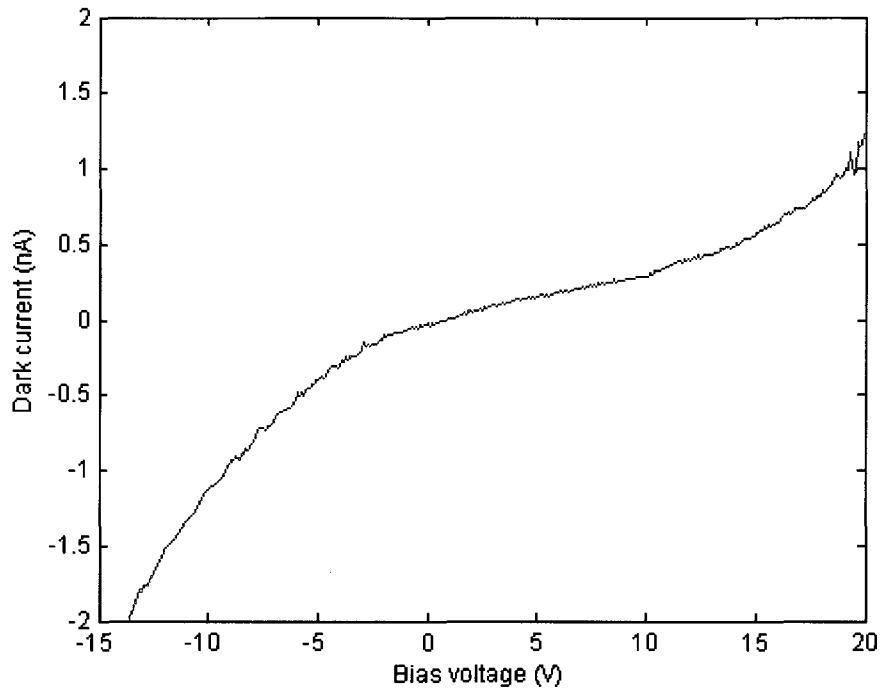


Figure 13: 1<sup>st</sup>-gen  $I_{\text{dark}}$ , wafer 6598A0388SEE0, die G8, device 0.5,5,2.6

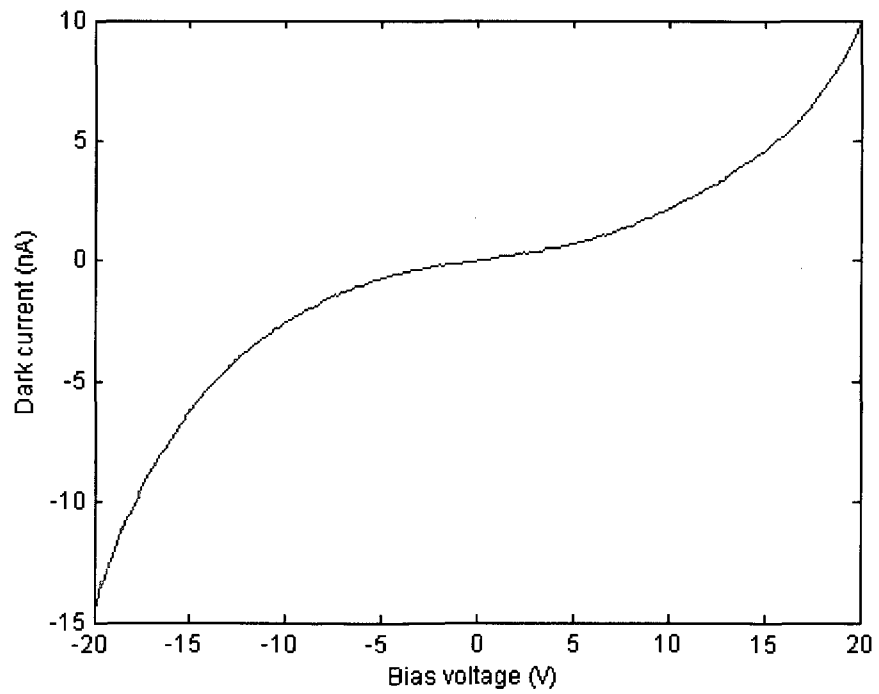


Figure 14: 1<sup>st</sup>-gen  $I_{\text{dark}}$ , wafer 6598A0388SEE0, die G8, device 0.5,10,3.6

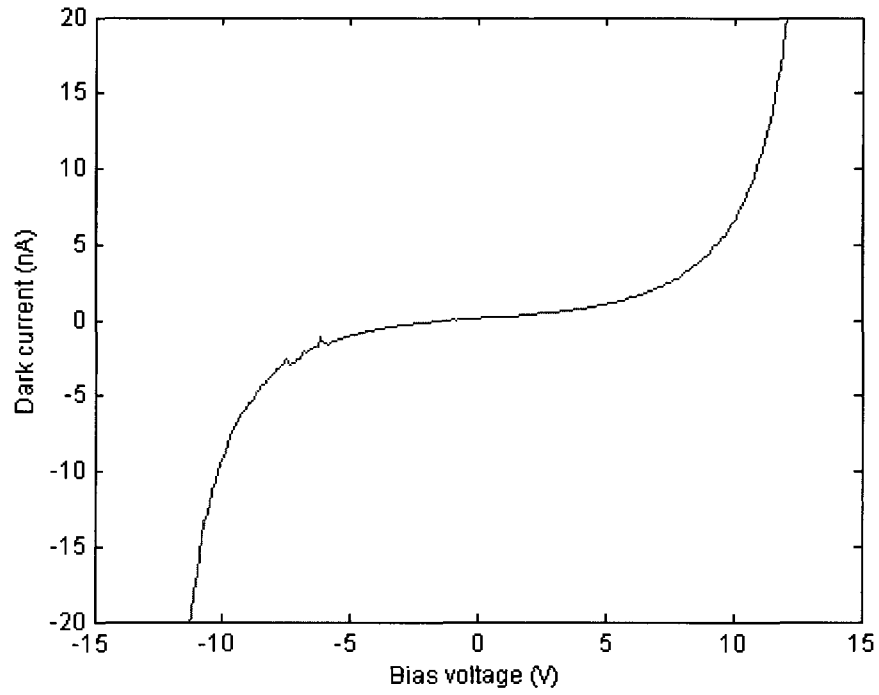


Figure 15: 2<sup>nd</sup>-gen  $I_{\text{dark}}$  wafer 1269P109SEA7, die I07, device 0.5,10,2.14

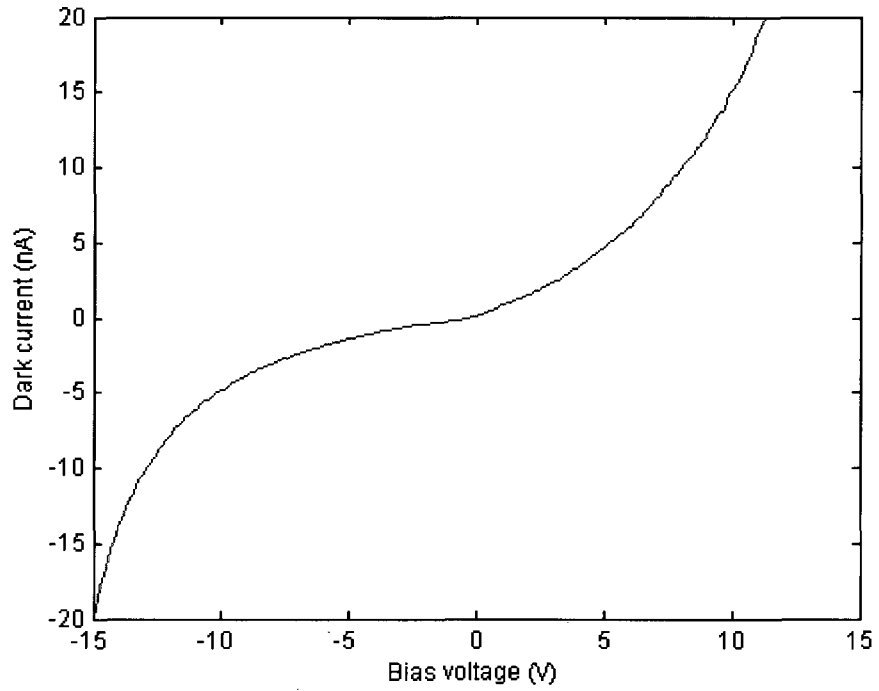


Figure 16: 2<sup>nd</sup>-gen  $I_{\text{dark}}$  wafer 1269P109SEA7, die I07, device 2,5,2.64

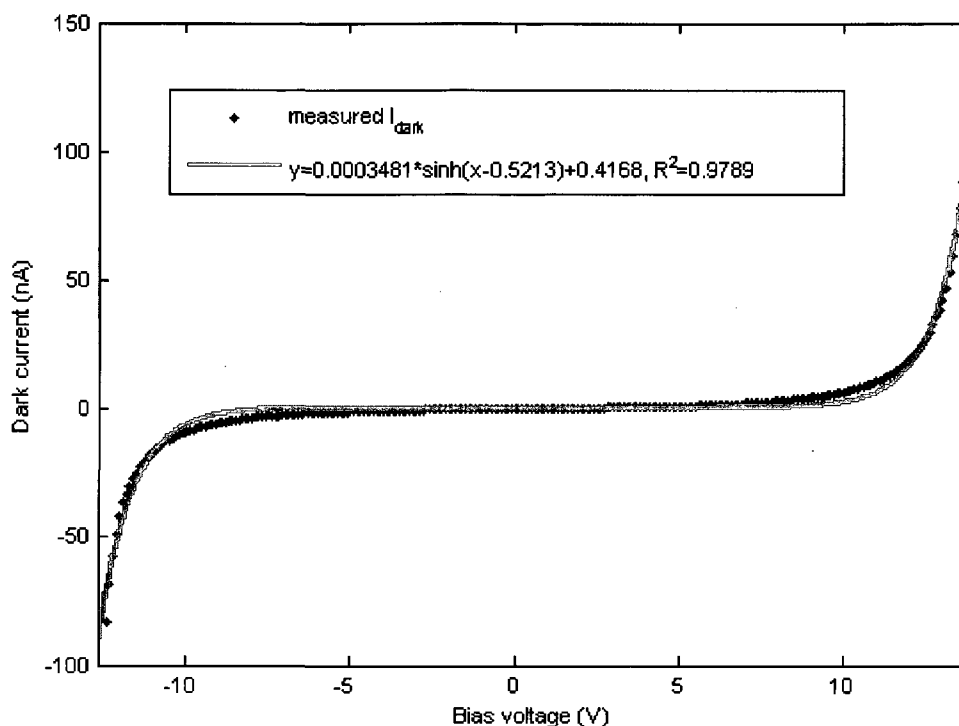


Figure 17:2<sup>nd</sup>-gen  $I_{\text{dark}}$  wafer 1269P109SEA7, die I07, device 2,5,2.64

The primary significance of the dark current results was to start me questioning some of the assumptions I was making about the photodetectors. Specifically, that the undoped polysilicon resistivity was on the order of tens to hundreds of thousands of  $\Omega$  per square and that the mechanism behind current flow in polysilicon was similar to that in single crystal silicon.. Once I began questioning these assumptions, things rapidly fell into place.<sup>20</sup>

## 4 Device physics behind the detector

### 4.1 Dark current

As discussed in Chapter 2, a hyperbolic sine dependence of current on voltage was expected, based on theoretical concerns. As shown in Figure 17, the expected sinh I-V dependence was experimentally observed. This confirmed that thermionic emission over grain boundaries, the principle behind the sinh I-V dependence, was the primary mechanism for dark current in the photodetectors studied in this work. One final puzzle remained, that of explaining the very

<sup>20</sup> American humorist Josh Billings had a saying which seems applicable: "I honestly believe that it is better to know nothing than to know what ain't so."

low (nanoamp-level) dark currents observed in the photodetectors. Prior to beginning this research, I believed (based on extrapolations from previous experience in the semiconductor industry) that undoped polysilicon resistors would have values in the range of tens of  $k\Omega$  to hundreds of  $k\Omega$  per square.<sup>21</sup> Instead, as Mahan, et al showed, [8] undoped polysilicon, deposited under conditions similar to the polysilicon in this work, can be used to create resistors in the range of a few  $G\Omega$  per square to a few tens of  $G\Omega$  per square at room temperature when measured in the dark. With this realization, the existence of nanoamp-level dark currents comes as no surprise. Since the detector structures all have at least a quarter of a square of undoped polysilicon between the contacts, there is no need to appeal to reverse-biased Schottky diode leakage currents to explain the observed nanoamp dark current levels. The resistance of the undoped polysilicon is all that is required.<sup>22</sup>

## 4.2 DC Photocurrent results

The observed photocurrent results from the detectors studied in this work are the result of the photoconductive process discussed in Chapter 2. The photocurrent is enhanced by a photoconductive gain process, also discussed in Chapter 2. The photoconductive nature of the devices is confirmed through two factors. First, the  $(1 + \mu\tau V/S^2)$  dependence of current on voltage. Second, the failure of the photocurrent to saturate before device breakdown. If the photodetectors were behaving as photodiodes, a I-V dependence on contact spacing would be different and the photocurrent would saturate at the reverse leakage current value.

## 4.3 Temperature results

As the on-chip environment in which the detectors will be used will not be at room temperature, and may be at a temperature exceeding 200 C, determining the temperature dependence of the detectors' dark current and photocurrent was of interest. To this end, a

---

<sup>21</sup> Another example of where "...it is better to know nothing than to know what ain't so."

<sup>22</sup> One reason one might want gigaohm-level polysilicon resistors is to serve as load resistors in 4T SRAM cells. However, 4T SRAM cells (and therefore the need for extremely high value load resistors) were technologically obsolete by the time of the 4M SRAM generation in the early 1990s. They were replaced by 6T SRAM cells due to the 6T cell's lower leakage and better process margin as geometries shrank. A second reason gigaohm-level polysilicon resistors might be desired would be for use in analog circuit designs, possibly as feedback resistors.

first-generation die was placed on a thermoelectric heater/cooler stage, which was then placed under a microscope objective. The photodetector region of the experimental structure was illuminated using white light from the microscope. Needle probes were used to contact the die and probe the detector being tested as the die was ramped from 15 C to 55 C using the thermoelectric stage. An HP 4145A semiconductor parametric analyzer was used to bias the detector and record the photocurrent. Figure 18 shows the photoconductivity results (i.e. conductance when illuminated) while Figure 19 shows the dark conductivity results. For the photoconductivity results, anomalous results were measured at 15 C. As the dark conductivity 15 C data fits the same line as the other temperatures, condensation seems unlikely as the cause of the anomalous results.

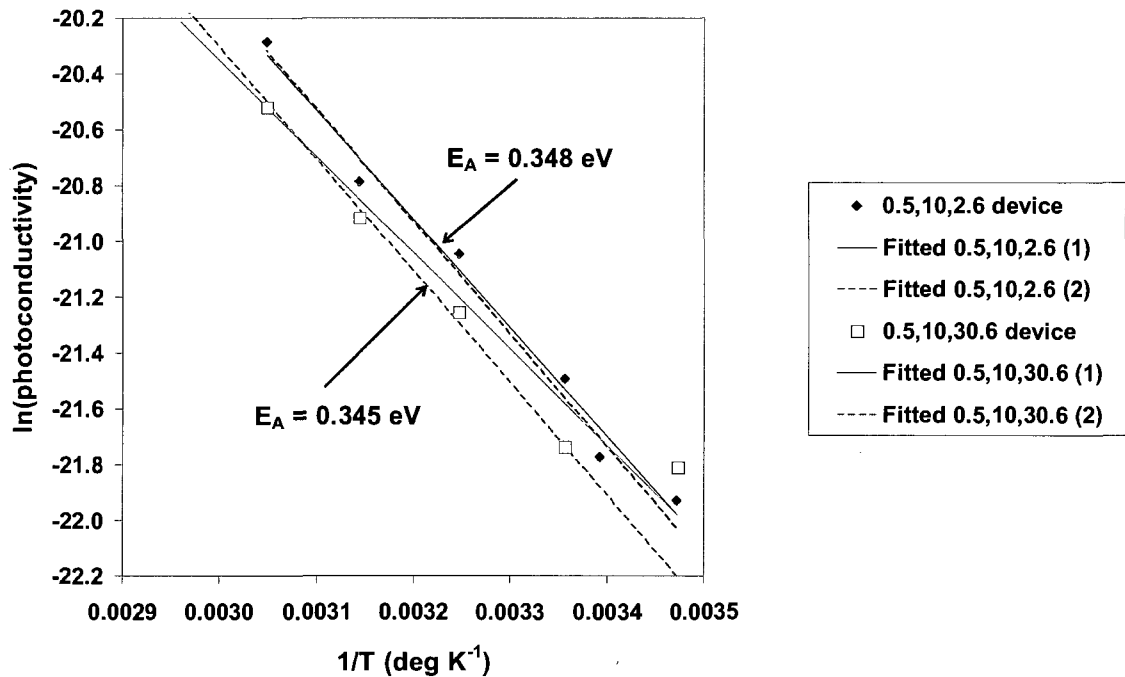


Figure 18:  $\ln(\text{photoconductivity})$  vs.  $1/T$  for two first-generation devices. “Fit 1” is a line fitted to all data. “Fit 2” ignores anomalous 15 C data.

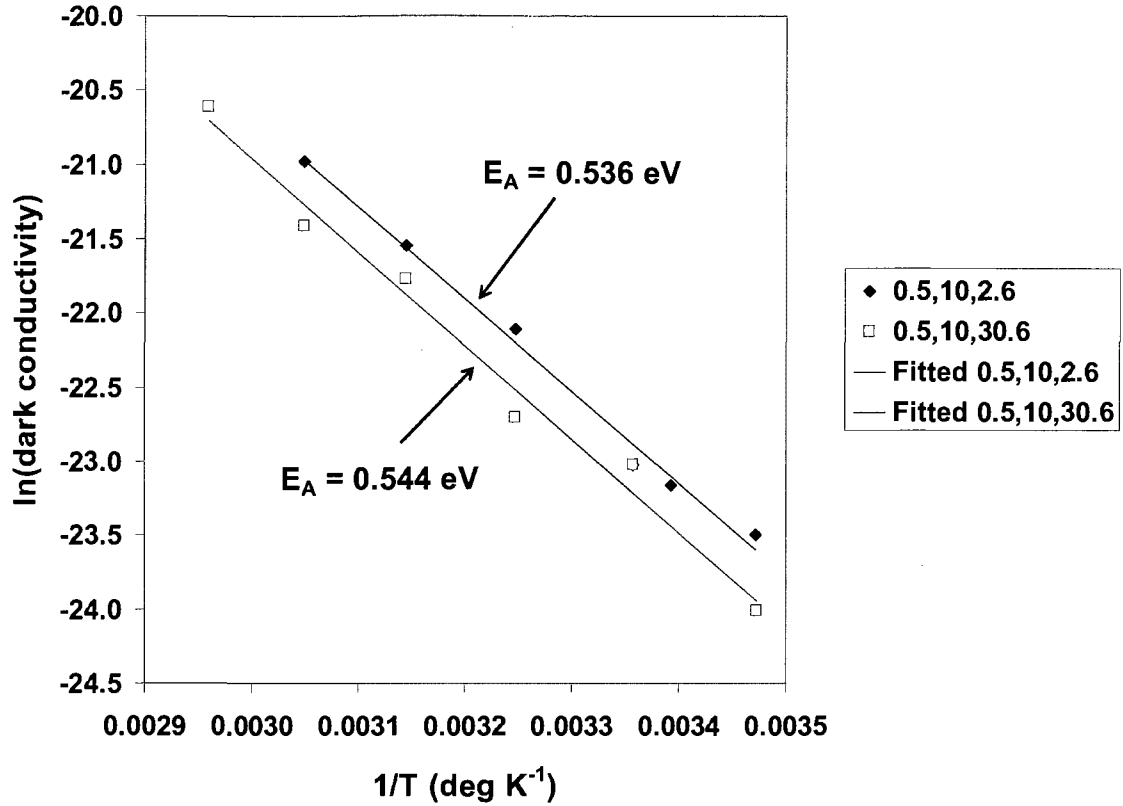


Figure 19:  $\ln(\text{dark conductivity})$  vs.  $1/T$  for the same devices as Figure 18 and under the same test conditions.

The measured photoconductivity activation energies of  $\sim 0.35$  eV are higher than those reported elsewhere [9], and may be explained by a relatively high defect level, as our polysilicon films is optimized for purposes other than photoconductance. The measured dark conductivity activation energies of  $\sim 0.54$  eV is typical of results reported elsewhere [9, 10], and suggests that recombination is dominated by defects near mid-gap, as expected.

The photocurrent and dark current activation energies, when considered together, indicate that in the intended purpose of on-chip optical interconnect, a significant degradation in the photocurrent-to-dark current contrast ratio will not be observed.

#### 4.4 Impact of the second-generation U-bend waveguides

As discussed in Chapter 3, many second generation edge-coupled waveguide detectors used a U-bend waveguide leading from the edge of the die to the detector. The idea behind the U-bend was to eliminate any possibility of light reading the detector other than through the waveguide. The U-bend was very successful in this, as shown in Figure 20. As can be seen, by the time the input fiber is even 10  $\mu\text{m}$  away from the optimum alignment point for the waveguide, the photocurrent has dropped to background levels. Since the U-bends have radii of curvature of 100  $\mu\text{m}$ , only negligible amounts of optical power will reach the detector other than through the waveguide.

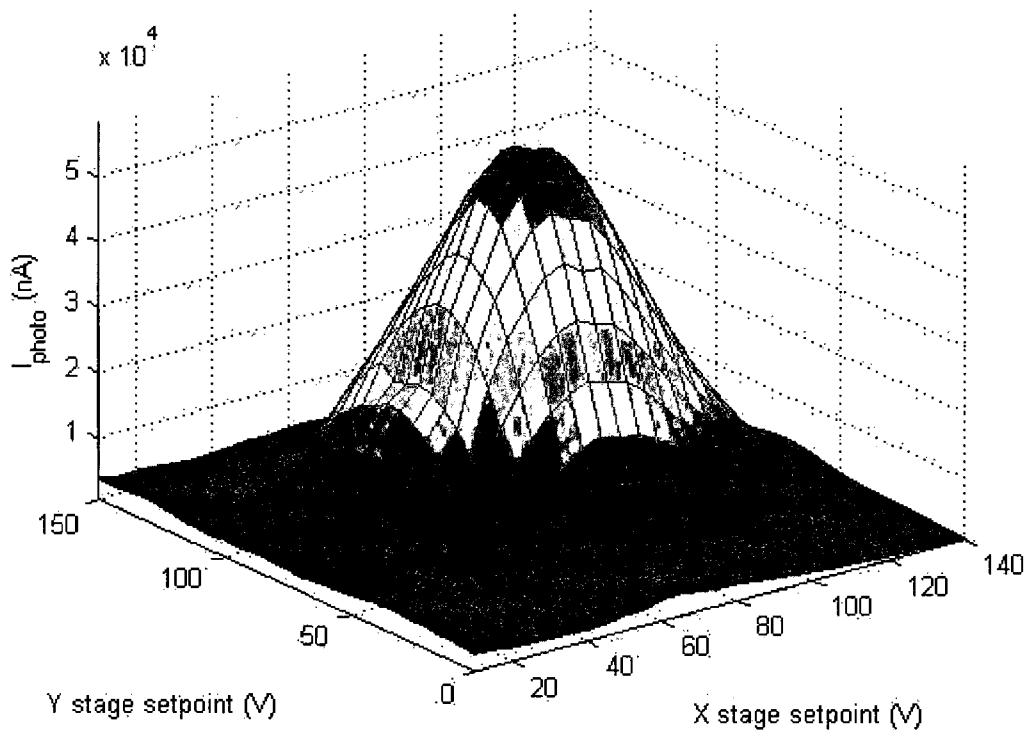


Figure 20:  $I_{\text{photo}}$  vs. Y stage and X stage setpoints. 1V = 100 nm

## 5 Contact structures – Are they Schottky or ohmic?

As noted in Chapter 3, the contacts were designed to be metal<sup>23</sup> contacting undoped, unsilicided polysilicon. As such, the contacts were expected to be Schottky contacts, just as metal contacts on lightly-doped single-crystal silicon are Schottky contacts.[1, 11, 12] In reality, though, the contacts were silicided, as shown in Figure 3 of Chapter 3. The silicidation of the contacts won't affect the Schottky nature of the contacts, though. In essence, it just extends the metal filling the contact hole a little further down.

Initially, it was hard to explain the observed photoconductive gain mechanism if the contacts were Schottky in nature, and therefore blocking. It was easy to explain if the contacts were ohmic. The only question was "How could contacts to undoped silicon be ohmic?"

However, as discussed in Chapter 2, further reading of the literature showed that several researchers [13-16] had reported a photoconductive gain mechanism in material with Schottky contacts. The mechanism was image-force reduction of the Schottky barrier [1], caused by photogenerated charge. [2] This mechanism will be discussed further in Chapter 5. Reports attributing the behavior to other mechanisms, such as localized conduction paths arising from polysilicon grain boundaries intersecting the metal-silicon junction [17] are probably mistaken.

Thus, it is not necessary to invoke exotic methods to explain ohmic behavior in contacts to undoped polysilicon. The observed behavior can be explained if the contacts are Schottky, as expected.

### References

- [1] R. F. Pierret, *Semiconductor Device Fundamentals*. Reading, MA: Addison-Wesley, 1996.
- [2] P. Panayotatos and H. C. Card, "Recombination Velocity at Grain-Boundaries in Polycrystalline Si under Optical Illumination," *IEEE Electron Dev. Lett.*, vol. 1, pp. 263-266, 1980.
- [3] D. P. Poenar and R. F. Wolffenbuttel, "Optical properties of thin-film silicon-compatible materials," *Applied Optics*, vol. 36, pp. 5122-5128, 1997.
- [4] G. Yuan, R. Pownall, P. Nikkel, C. Thangaraj, T. W. Chen, and K. L. Lear, "Characterization of CMOS compatible, waveguide coupled leaky-mode photodetectors," *IEEE Phot. Tech. Lett.*, vol. 18, pp. 1657 - 1659, 2006.

---

<sup>23</sup> A tungsten plug in the contact hole, then a metal-1 film stack consisting of 10 nm Ti, a 390 nm Al / 0.5% Cu alloy on top of the Ti, then a 35 nm TiN layer on top of the Al / Cu alloy.

- [5] S. Donati, *Photodetectors: Devices, Circuits and Applications*. Upper Saddle River, NJ: Prentice-Hall, 2000.
- [6] R. H. Bube, *Photoconductivity of Solids*, 2nd ed. Huntington, New York: Krieger, 1978.
- [7] H. C. Card and E. S. Yang, "Electronic Processes at Grain-Boundaries in Polycrystalline Semiconductors under Optical Illumination," *IEEE Trans. Electron Devices*, vol. 24, pp. 397-402, 1977.
- [8] J. E. Mahan, D. S. Newman, and M. R. Gulett, "Gigaohm-Range Polycrystalline Silicon Resistors for Microelectronic Applications," *IEEE Trans. Electron Devices*, vol. 30, pp. 45-51, 1983.
- [9] R. Cherfi, G. Farhi, and M. Aoucher, "Thin films hydrogenated silicon deposited by direct current magnetron sputtering at high rate," *Solid State Phenomena*, vol. 67-8, pp. 113-118, 1999.
- [10] A. Poruba, J. Springer, L. Mullerova, A. Beitlerova, M. Vanecek, N. Wyrsh, et al., "Temperature dependence of the optical absorption coefficient of microcrystalline silicon," *Journal of Non-Crystalline Solids*, vol. 338-40, pp. 222-227, 2004.
- [11] B. G. Streetman and S. Banerjee, *Solid State Electronic Devices*, 5th ed. Upper Saddle River, NJ: Prentice-Hall, 2000.
- [12] E. H. Rhoderick and R. H. Williams, *Metal-Semiconductor Contacts*, 2nd ed. vol. 19. Oxford, U.K.: Clarendon Press, 1988.
- [13] S. F. Soares, "Photoconductive Gain in a Schottky-Barrier Photodiode," *Jpn. J. Appl. Phys. Pt. 1*, vol. 31, pp. 210-216, 1992.
- [14] M. Klingenstein, J. Kuhl, J. Rosenzweig, C. Moglestue, A. Hulsmann, J. Schneider, et al., "Photocurrent Gain Mechanisms in Metal-Semiconductor-Metal Photodetectors," *Sol. St. Elect.*, vol. 37, pp. 333-340, 1994.
- [15] J. Burm and L. F. Eastman, "Low-Frequency Gain in MSM Photodiodes Due to Charge Accumulation and Image Force Lowering," *IEEE Phot. Tech. Lett.*, vol. 8, pp. 113-115, 1996.
- [16] R. R. Mehta and B. S. Sharma, "Photoconductive Gain Greater Than Unity in CdSe Films with Schottky Barriers at Contacts," *J. Appl. Phys.*, vol. 44, pp. 325-328, 1973.
- [17] C. Shu, B. B. Hu, X. C. Zhang, P. Mei, and E. S. Yang, "Picosecond Photoconductive Response of Polycrystalline Silicon Thin-Films," *Appl. Phys. Lett.*, vol. 57, pp. 64-66, 1990.

## AC TESTING AND CHARACTERIZATION OF POLYSILICON DETECTORS

### 1 Introduction

As noted in Chapter 3, the polysilicon detectors have two major design goals: one DC and one AC. The DC design goal of maximizing the response of the polysilicon detector for a unit optical power in was discussed in Chapter 4, as was testing and characterization related to this goal. This chapter will discuss the testing and characterization related to the AC design goal of maximizing the speed of the polysilicon detectors.

### 2 AC Testing and Characterization of the Polysilicon Detectors

AC characterization of the polysilicon detectors can be performed in either the frequency domain or the time domain, as discussed earlier, in Chapter 2, Section 9.2 (“General concepts related to characterization of AC performance”). The results of frequency domain characterization will be discussed first, followed by the results of time domain characterization.

#### 2.1 Frequency domain characterization of the polysilicon detectors

A particularly novel method of characterizing the frequency response of a photodetector involves measuring the shot noise spectrum of the photodetector when illuminated by unmodulated incoherent light [1], and uses the close correspondence between the shot noise spectrum and the frequency response of the photodetector. [2, 3] The method has the distinct advantage of not requiring high-gain, high-bandwidth amplifiers. Instead, the measurement is performed using only commonly available spectrum analyzers. The theory behind the technique is as follows [4].

Consider incoherent light from an incoherent source, such as an incandescent light. In addition to describing the light as incoherent, it could also be described as monochromatic light randomly amplitude modulated and phase modulated, with frequency components extending out to the spectral bandwidth of the light. This is true even if the incoherent light is narrow-band. Unless the light has been filtered to be extremely narrow-band, it will contain a

continuous distribution of amplitude and phase modulation components well out into the GHz range.

If one takes this incoherent source, shines it on the photodetector of interest, feeds the output of the photodetector into an RF spectrum analyzer, and integrates over some suitable time, then the way the output of the spectrum analyzer falls off at high frequencies gives the desired amplitude response of the photodetector.

While simple and elegant, there are some problems with this technique. [5]

The main problem is that the frequency response (power or voltage) is not the only parameter of interest for data applications, such as an on-chip optical interconnect. Probably the most common method of judging the high-speed response of an electrical system is the so-called “eye diagram”. Phase problems in the photodetector, which will not show up in a frequency response plot, can wreak havoc on an eye diagram.

For the work reported here, the practical problem with this technique was the signal levels involved. The maximum observed DC photocurrent response was on the order of 10  $\mu\text{A}$ . The shot noise associated with this current level in a 1Hz bandwidth is  $\langle i_{N,shot}^2 \rangle = 2qI_{ph}\Delta f = 2(1.6 \times 10^{-19} \text{ C})(10 \mu\text{A})(1\text{Hz}) = (1.78 \text{ pA})^2$ . In a 50  $\Omega$  system, this is a power of  $1.60 \times 10^{-22} \text{ W}$ , or -188 dBm.

Note that this shot noise level is for the maximum observed DC photocurrent, which was obtained when the source laser diode was lasing. As noted earlier, use of the shot noise technique to determine the frequency response relies on an incoherent source. A laser diode that is lasing does not qualify as an incoherent source.

Generously assuming that the observed photocurrent would only drop by a factor of ten, to 1  $\mu\text{A}$ , if the source is operating below threshold gives a 1Hz bandwidth shot noise current level of 0.565 pA. In a 50  $\Omega$  system, this corresponds to a power of  $1.60 \times 10^{-23} \text{ W}$ , or -198 dBm.

The available spectrum analyzers have sensitivities on the order of -154 dBm in a 1 Hz bandwidth.

For this reason, investigation into using the shot noise technique to determine the frequency response of the detectors was abandoned. There appeared to be no likelihood of getting sufficient power to the detector to raise the shot noise of the detector's photocurrent above the noise floor of the spectrum analyzer.

While a sufficiently broadband, high-gain, gain-calibrated<sup>24</sup> amplifier could be used to boost the shot noise above the noise floor of the amplifier, if such an amplifier is available; it is probably simpler to use it to perform time-domain characterization of the detectors. In addition, note that it would not be sufficient to amplify the shot noise "signal" just to the noise floor of the amplifier. Instead, it would have to be amplified to at least several dB above the noise floor, to provide dynamic range.

While the shot noise technique to determine the frequency response was abandoned, it is worth mentioning a related technique. Baney et al. [6] have described a technique which uses fiber Fabry-Perot (FFP) cavity to optically filter the amplified spontaneous emission (ASE) output of erbium-doped fiber amplifier (EDFA). They showed that reducing the source bandwidth increased the low-frequency relative intensity noise (RIN) of the source, increasing the dynamic range of their system. Feeding the filtered output into a second EDFA boosted the power levels to a point compatible with their spectrum analyzer. The frequency response of their photodiode was obtained by observing the response at the periodic-filtered frequencies coming out of the FFP filter.

## **2.2 Time domain characterization of the polysilicon detectors**

Two basic time-domain techniques exist for characterizing detector speed: autocorrelation techniques and direct waveform observation. Nahman's 1983 article [7], while somewhat outdated, is still a useful introduction to and overview of high-speed time-domain techniques.

### *2.2.1 Correlation techniques*

Several authors have reported correlation-based [8] and auto-correlation-based [9] techniques for determining device speed. While generally compatible with standard CMOS processing,

---

<sup>24</sup>While it would be helpful for the gain to be flat over the entire frequency range of interest, all which is really required is that the gain be known over the entire frequency range of interest.

the techniques require special test structures which were not included in either the first-generation or second-generation designs.

### 2.2.2 Direct observation techniques

For the shot-noise technique of determining the frequency response of the photodetectors, the major problem was the signal levels involved. In a way, that is also the problem for direct-observation time-domain characterization of the detectors as well.

Since all high-speed direct-observation time-domain electrical measurement techniques measure voltage, not current, it is necessary to turn the photocurrent coming out of the detector into a voltage. This is done with a transimpedance amplifier or TIA. Figure 1 shows a basic TIA circuit, implemented with an op-amp.

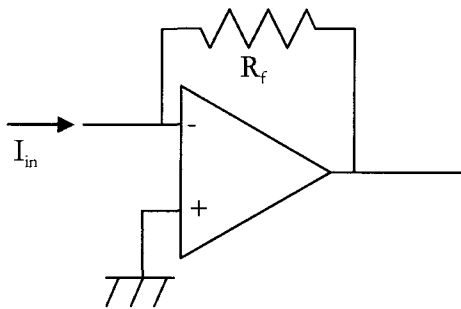


Figure 1: Basic transimpedance amplifier (TIA) circuit

The operation of the basic TIA circuit shown in Figure 1 is easily described.[10] Since the op-amp has a very high gain, there is very little voltage between its + and – terminals. Since the + terminal is at ground, the – terminal is almost at ground, or is at a “virtual ground”. Since the op-amp has a very high to infinite input impedance, all of the input current  $I_{in}$  goes through the feedback resistor,  $R_f$ . Therefore, the voltage drop across  $R_f$  is  $R_f \times I_{in}$ . Since the current is going into the – (inverting) terminal of the op-amp, the output voltage  $V_{out}$  is

$$V_{out} = -(R_f \times I_{in}).$$

To prevent oscillation, a feedback capacitor is usually added in parallel with the feedback resistor. See Figure 2. The addition of the feedback capacitor reduces the effect of the feedback resistor at high frequencies. It also introduces a pole into the transfer function of the circuit, compensating for the inductive nature of the transfer function of an inverting amplifier's gain. Both factors help to reduce oscillation.[11]

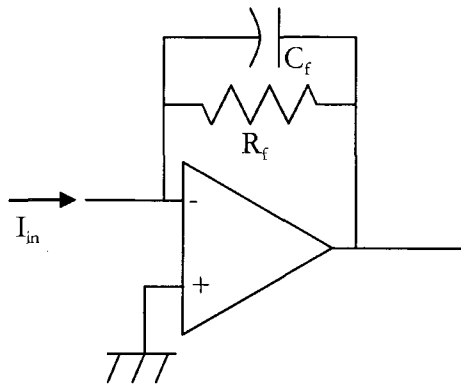


Figure 2: Basic TIA with feedback capacitor

Constructing a high-speed, high-gain TIA is a non-trivial task.<sup>25</sup> It is all too easy to try to construct a TIA and end up with an oscillator, even when using a feedback capacitor. For this reason, the maximum observed square-wave response when using TIAs built in the lab was on the order of 150 kHz, implying a -3 dB frequency response of around 750 kHz to 1.5 MHz. This was obtained with a TIA constructed according to the schematic of Figure 2, using National Semiconductor LF412 op-amp, a 20k $\Omega$  feedback resistor and a 12.5 pF feedback capacitor. While the LF412 is not a particularly high performance op-amp (gain-bandwidth of 3MHz), it was readily available in the lab. Attempts to use higher gain-bandwidth op-amps (e.g. Burr-Brown OPA656, 500 MHz, or OPA657, 1.6 GHz) resulted in output oscillation even with no input. Figure 3 shows the entire AC measurement circuit, including the TIA, the Keithley 2400 SourceMeter used for the detector bias supply, and the oscilloscope. Note that the bias circuit for the detector uses the virtual ground of the op-amp's + input. In the

<sup>25</sup> High gain, on the order of 10,000 V/A, is needed to turn the  $\mu$ A level photocurrents that come out of the photodetectors in this work into the tens of mV signal levels required by an oscilloscope. The reason behind the need for high bandwidth when determining detector speed is obvious.

context of discussing the AC measurement circuits, it is worth noting that an HP 8116A function generator was used to square-wave modulate the source laser diode. An HP 3466A DMM was initially used to monitor the RMS current from the function generator to the laser diode. However, I discovered that the presence of the DMM in the laser diode drive circuit was causing electrical ringing on high/low and low/high transitions in the TIA circuitry. (The ringing was electrical, not optical, in nature – it existed even with the source laser diode unplugged from the input fiber.)

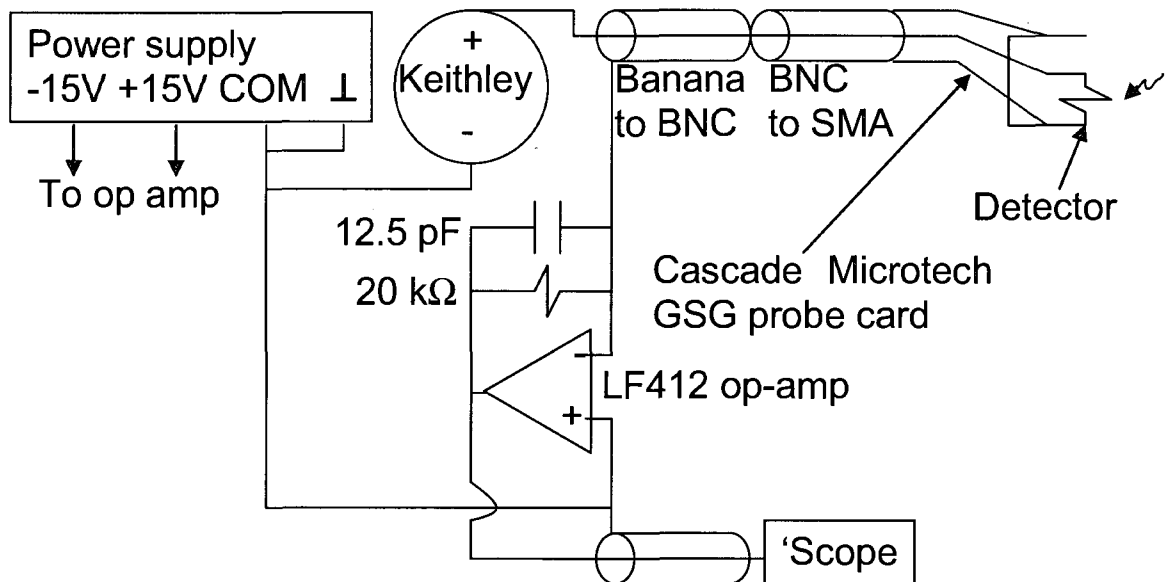


Figure 3: AC measurement circuit schematic, showing TIA with feedback resistor and capacitor.

I wrote a LabVIEW program to transfer data from the HP 54610B oscilloscope used in Figure 3. However, performance of the LF412-based TIA in this system was so poor that an alternate TIA was obviously needed. Accordingly, data from the circuit of Figure 3 will not be reported here. The results indicate only the capabilities of the TIA, not the capabilities of the detector.

A circuit schematic related to Figure 3 is shown in Figure 4. The main difference from Figure 3 is that the circuit of Figure 4 uses a bias tee to decouple the biasing of the detector from the input of the TIA. However, the resulting TIA voltage output with a square-wave modulating

the source laser diode was highly distorted, with an almost sine-wave-like appearance, even at 50 kHz. I suspect the DC block capacitor inside the bias tee is interacting unfavorably with the TIA input.

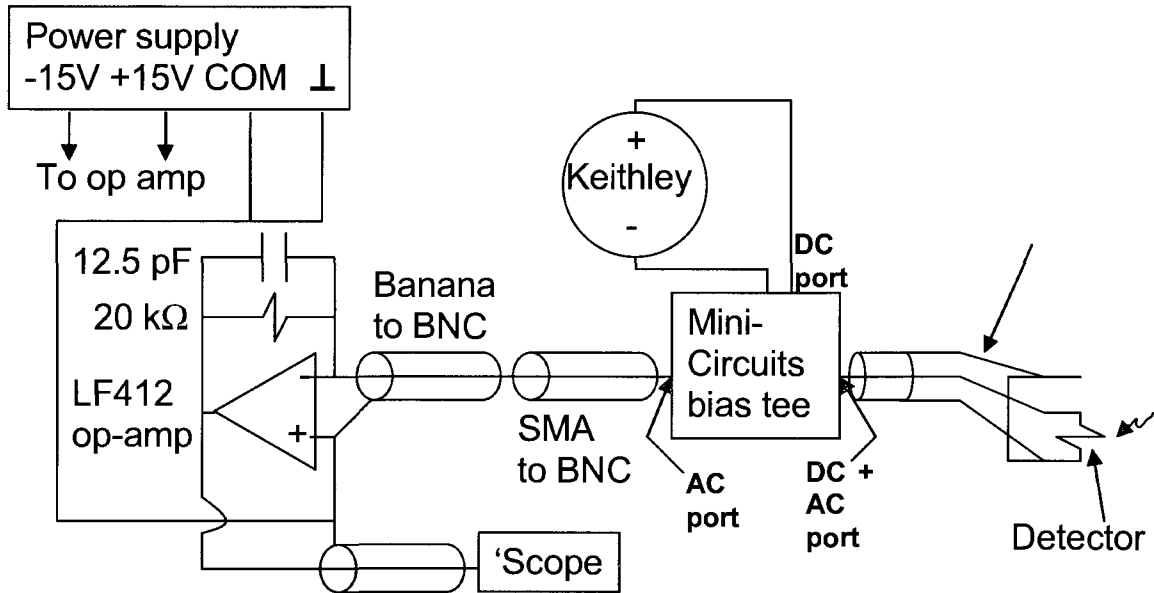


Figure 4: Schematic of second AC measurement circuit, showing bias tee and TIA with feedback resistor and capacitor.

A “brute-force” plan was used to solve the problem with insufficient bandwidth from low-performance TIAs (i.e. ones based on the LF412) and oscillatory output from high-performance TIAs (i.e. ones based on the OPA656). Specifically, a commercial “off the shelf” high-performance amplifier was purchased. The first attempt at this approach involved buying an Analog Modules 313A TIA designed and built to a 1 pF input capacitance spec. Unfortunately, the Analog Modules TIA exhibited an oscillatory output for any input condition other than open-circuited. This included shorting the inputs. The second attempt at the “brute force” approach involved buying a Miteq AM-1646 RF amplifier. In combination with an SMA cable running to the detector, this amplifier effectively served as a TIA. This second approach proved successful and was the basis for all measured results reported in this chapter. In addition, all measured results reported in this chapter are from 2<sup>nd</sup>-generation material.

The circuit used with the Miteq AM-1646 is shown in Figure 5. A Keithley 2400 SourceMeter supplied a DC bias to the detector through a Mini-Circuits ZFBT-4R2GW-FT+ bias tee (0.1 to 4200 MHz bandwidth). A Cascade Microtech ACP40-GSG-125 probe (40 GHz bandwidth) was used to contact the detector structure and brought the modulated photocurrent signal through the bias tee to a Miteq AM-1646 amplifier (bandwidth: 0.3 to 1000 MHz). The resulting signal was measured using an Agilent 86100A oscilloscope (20 GHz bandwidth). The input optical pulse was provided by a Hitachi HL6738MG laser diode (690 nm, 1 GHz bandwidth) which was modulated using an HP 8116A pulse/function generator set to its minimum pulse width of 8 ns and using a 20 MHz repetition rate. The laser diode was coupled into an Oz Optics visible wavelength single-mode fiber. The electrical pulse low voltage level was fixed at 0.0 V, while the high level was adjusted to minimize the optical pulse width through gain switching of the laser diode and was typically between 3.5 V and 3.9 V. A  $47\ \Omega$  resistor was in series with the laser diode, to protect the laser diode by limiting the current and to better match the  $50\ \Omega$  output impedance of the HP 8116A.

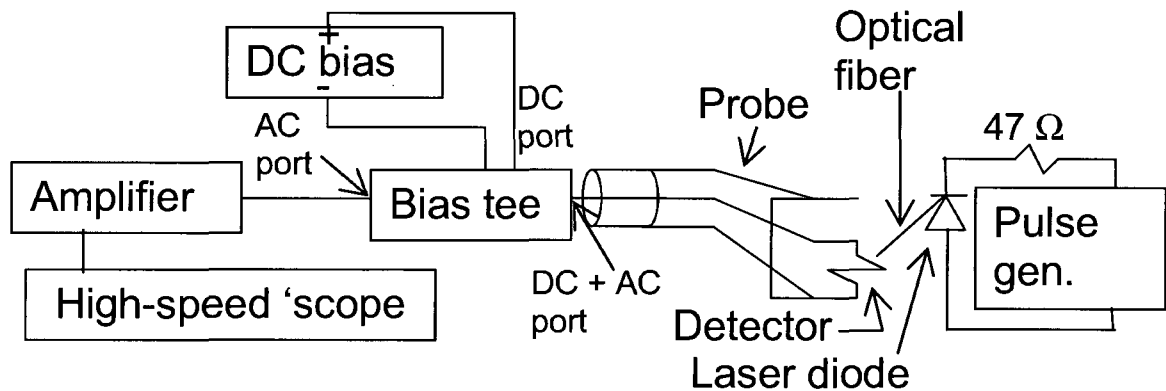


Figure 5: Block diagram of the circuit used for AC measurements reported in this chapter.

As the photodetector material is undoped polysilicon, the I-V characteristics of undoped polysilicon in the dark and when illuminated are of interest. In the absence of light, undoped polysilicon is known to have a hyperbolic sine ( $\sinh$ ) dependence of current on voltage. This is due to thermionic emission over potential barriers at the grain boundaries. [12] Figure 6, which shows DC I-V plots at two different optical power levels, shows an essentially linear dependence of current on voltage. Figure 6 also shows a dark current plot. The “ $P_{\text{opt,max}}$ ”

curve roughly corresponds to a laser diode drive voltage high level of 4.8V, while the “20%  $P_{opt,max}$ ” curve roughly corresponds to a laser diode drive voltage high level of 3.4V. The reason behind the linear photocurrent I-V characteristics will be discussed in the Theory section. The dark current plot begins to show the upsweep that is characteristic of a sinh plot around 11 V.

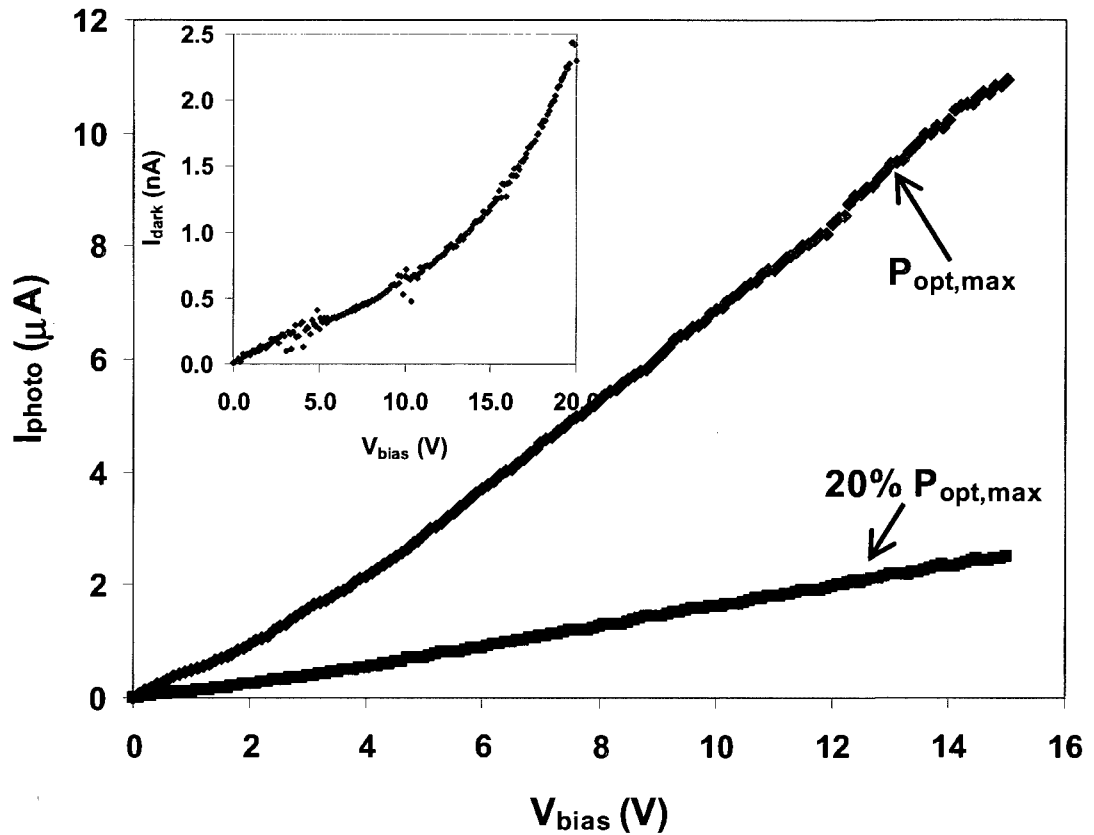


Figure 6: DC I-V plots of detector photocurrent at two different optical power levels. Inset shows the dark current. Note that the dark current y-axis is nA, not  $\mu$ A.

Figure 7 shows a typical pulse response for a 2<sup>nd</sup>-generation detector with waveguide width  $W = 2 \mu\text{m}$ , detector length  $L = 10 \mu\text{m}$  and contact spacing  $S = 2.64 \mu\text{m}$ . FWHM is 1.32 ns, with a 10% - 90% rise time of 0.46 ns. FWHM values as low as 0.81 ns have been measured, as have 10% - 90% rise time as low as 0.39 ns. [13] Note that the actual detector FWHM pulse response performance is almost certainly better than these values; measured performance was limited by the inability to modulate the source laser diode to have Gaussian pulses with

FWHM less than approximately 600 ps. A recombination lifetime of 2.5 ns is extracted from the exponentially decaying tail of the data.

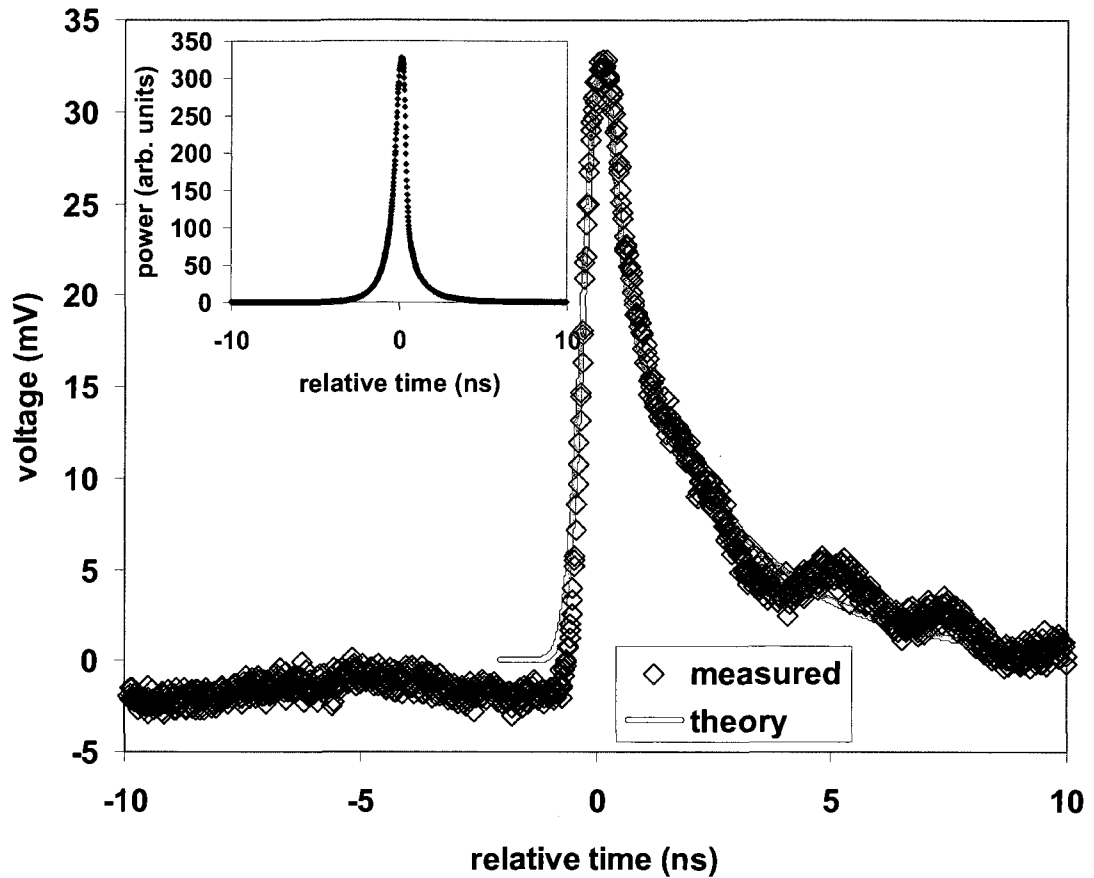


Figure 7: Pulse response from a  $W = 2.0 \mu\text{m}$ ,  $L = 10 \mu\text{m}$ ,  $S = 2.64 \mu\text{m}$  detector at a 10 V bias. FWHM = 1.32 ns. The inset shows the optical pulse. The solid line is theory for an optical input pulse with FWHM of 750 ps, and assumes a polysilicon mobility of  $100 \text{ cm}^2/\text{V}\cdot\text{s}$  and a  $\tau_r$  of 2.5 ns.

The measurement in Figure 7 was taken with a 10 V bias applied to the detector, as were the other measurements reported in this chapter. While this high bias is undesirable in the intended application of on-chip interconnects, it was required due to poor coupling efficiency, on the order of 1%, between the input laser diode source and the waveguide leading to the detector. The 10V applied bias provided significant photoconductive gain, which is linear with applied bias. [14] Increasing the photoconductive gain effect compensates for the poor

coupling efficiency. At the 10 V applied bias, the 2.64  $\mu\text{m}$  contact spacing and the model-fitting mobility of 100  $\text{cm}^2/\text{V}\cdot\text{s}$  [15] should result in a velocity below the polysilicon saturation velocity. [16] The resulting calculated transit time of 69 ps is much less than the 2.5 ns recombination lifetime. As will be discussed later, the photoconductive gain mechanism provides a means for the carriers to effectively live longer than the transit time.

Figure 8 shows the pulse response at two different laser diode drive levels. Of interest is the fact when the laser diode is driven at a higher voltage level (3.80V vs. 3.70V), most of the additional optical power results in an increase in the main peak of the response. The exponentially decaying tail shows little change in its magnitude between the two different drive levels. Indeed, the tails at the two drive levels overlap during much of their decay. This tends to indicate that the processes involved in the exponential decay have reached a limit such that additional photogenerated carriers are not involved with these processes.

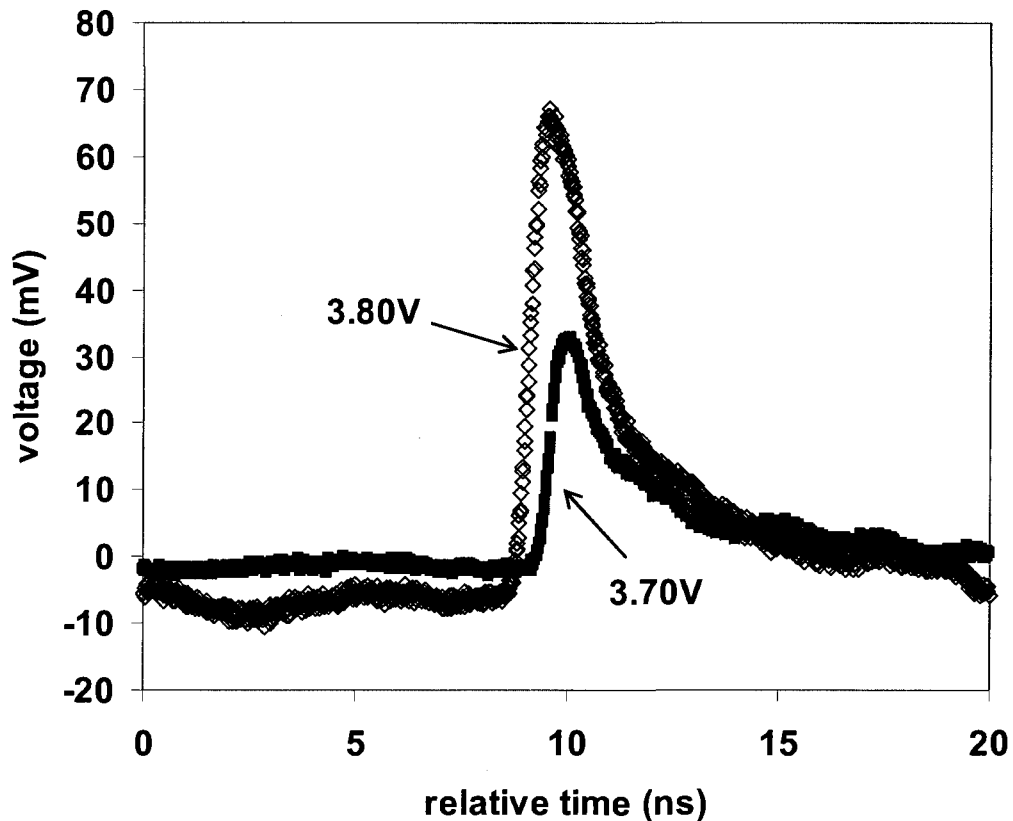


Figure 8: Pulse response at two different laser diode drive levels.  $W = 2.0 \mu\text{m}$ ,  $L = 10 \mu\text{m}$ ,  $S = 2.64 \mu\text{m}$  detector at a 10 V bias.

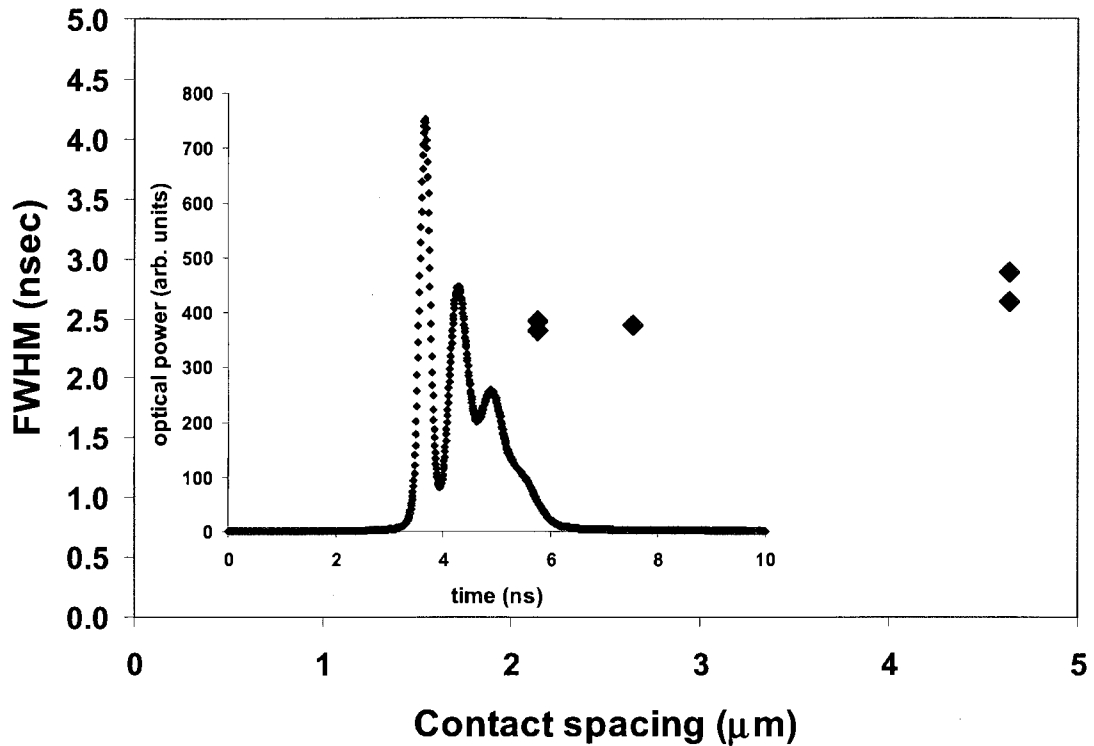


Figure 9: Detector FWHM vs. contact spacing. Inset shows the optical pulse for a laser diode electrical pulse high level of 4.0V.

Figure 9 shows the FWHM of the detector response for a range of contact spacing. The 490 ps variation in the measured FWHM values for a change of more than 2:1 in contact spacing is comparable to the 200 ps variation in optical pulse FWHM repeatability. This indicates that the response is lifetime limited, rather than transit time or RC time constant limited.

Note that the FWHM values in Figure 9 are greater than in Figure 7 because it was necessary to drive the laser diode with a higher voltage, 4.0 V, in order to obtain a measurable response from the larger contact spacing detectors. At these higher drive voltages, gain switching was less effective in reducing the optical pulse width, as shown in the inset of Figure 9.

### 3 Theory

While MSM photodetectors are commonly thought of as photodiodes, the first important key in understanding the behavior of the MSM photodetectors in this work is realizing that they are behaving as photoconductors, not photodiodes. This behavior manifests itself in an I-V

curve which is symmetric about 0 V, with no sign of current saturation up to the point of device breakdown. This I-V behavior is associated with the MSM photodetectors in this work being symmetric devices. In addition, the detectors have no built-in internal field in the region where the carriers are absorbed to sweep the carriers apart and to the electrodes. As photoconductors, the detectors act as resistors which vary with optical power level, not as current sources as is the case with photodiodes. While the responsivity  $\mathfrak{R}$  of a photodetector is usually defined in the context of a photodiode, it also applies to a photoconductor as long as the bias voltage of the photoconductor is also specified.

The second important key in understanding the behavior of the photodetectors is knowing how the photodetectors are made. The body of the photodetector consists of undoped polysilicon. The grain boundaries in the polysilicon provide potential barriers to current flow [12]. The potential barriers arise due to unsatisfied silicon bonds at the grain boundaries. This is conceptually similar to how surface states arise at the silicon-oxide interface in metal-oxide-semiconductor devices. The contacts to the polysilicon consist of a Ti layer on top of the undoped polysilicon, with a TiN seed layer on top of the Ti. A tungsten plug sits on top of the seed layer and fills the entire contact hole, up to the aluminum metal interconnect layer. The process for filling the contact with metal is done under high vacuum and includes an Ar sputter etch before depositing the Ti layer. The sputter etch ensures good electrical contact between the undoped polysilicon and the Ti layer, by eliminating any oxide on top of the polysilicon. The metal contacts to the undoped polysilicon will be Schottky for one type of carrier, not ohmic, as long as the work function of the metal and polysilicon are different and assuming the depletion region in the undoped polysilicon is wide enough that tunneling through the contact barrier is not significant.

At low optical power levels, the existence of potential barriers at the grain boundaries results in current having a sinh dependence with voltage, due to thermionic emission over the grain boundary potential barriers. In the dark, when there is no optical power incident on the detector, a sinh dependence of current on voltage is observed at all bias voltages until the device starts to break down at fields of around  $10^5$  V/cm. At the optical power levels used in this work, the presence of photogenerated carriers causes the height of the barrier to

decrease.[17, 18] As a result, thermionic emission over the boundary is no longer a limiting factor and a sinh I-V dependence is not observed, as shown in Figure 6.

The theory which follows focuses on the interaction between recombination states and holes, and assumes that electrons are removed at the reverse-biased Schottky diode that is one contact. The electron injection occurs through a thermionic emission mechanism that is enhanced by a barrier-lowering mechanism described later. The assumption of electron removal is made partly because of the relative velocities of holes and electrons and partly because the described scenario seems to most simply explain the observed phenomena. However, the roles of holes and electrons could be reversed without fundamentally altering the theoretical explanation.

The Ar sputter etch in the contact-filling process has two effects. The first, desired, effect is to remove any oxide between the Ti layer and the polysilicon. Due to the critical nature of this step, the sputter etch is much longer than is needed to remove the expected amount of oxide, so that even much thicker-than-expected oxide films will be completely removed. As a result, a second, unintentional, effect is to physically damage the surface of the polysilicon. In the commercial CMOS process used to create the samples used in this work, this damage is unimportant, as the silicon is already heavily damaged by the high-dose implants used to dope the polysilicon n-type and p-type for use as the gate electrode in MOS devices. In the intentionally undoped polysilicon used for the photodetectors in this work, the damage is believed to create recombination states over the surface of the polysilicon in the contact area. That is, within the grains rather than at the grain boundaries.

As is well-known, recombination states are most effective when they have roughly equal probabilities of capturing an electron from the conduction band or capturing a hole from the valence band [19]. At the forward-biased contact, the recombination states will primarily capture holes, as holes in the polysilicon will drift towards the forward-biased contact and electrons will drift away, resulting in an accumulation of holes at the forward-biased contact and electrons at the reverse-biased contact. Figure 10 shows the energy band diagram of the detector when illuminated under voltage bias. For clarity, only one polysilicon grain boundary, in the middle of the detector, is shown.

Once a recombination state near the forward-biased contact captures a hole, the state will either be positively charged or neutral, depending on its initial charge state. If neutral, a state at the forward-biased contact is more likely to next capture a hole than an electron, for the reasons noted above, resulting in a positively charged state. This accumulation of positively-charged recombination states will result in image-charge lowering of the Schottky barrier at the

forward-biased contact, according to the equation  $\Delta\Phi_B = q\sqrt{\frac{q|E_s|}{4\pi\epsilon_s\epsilon_0}}$ , where  $\Delta\Phi_B$  is the change in the barrier height  $\Phi_B$ ,  $q$  is the charge on the electron,  $E_s$  is the field at the metal-semiconductor Schottky junction due to the charge accumulation,  $\epsilon_s$  is the relative dielectric constant of silicon and  $\epsilon_0$  is the permittivity of free space. A similar effect, involving electrons, occurs at the reverse-biased contact. This barrier lowering will result in an increased reverse leakage current at the reverse-biased contact, due to an exponential increase in the removal of electrons from the polysilicon into the metal. [20]

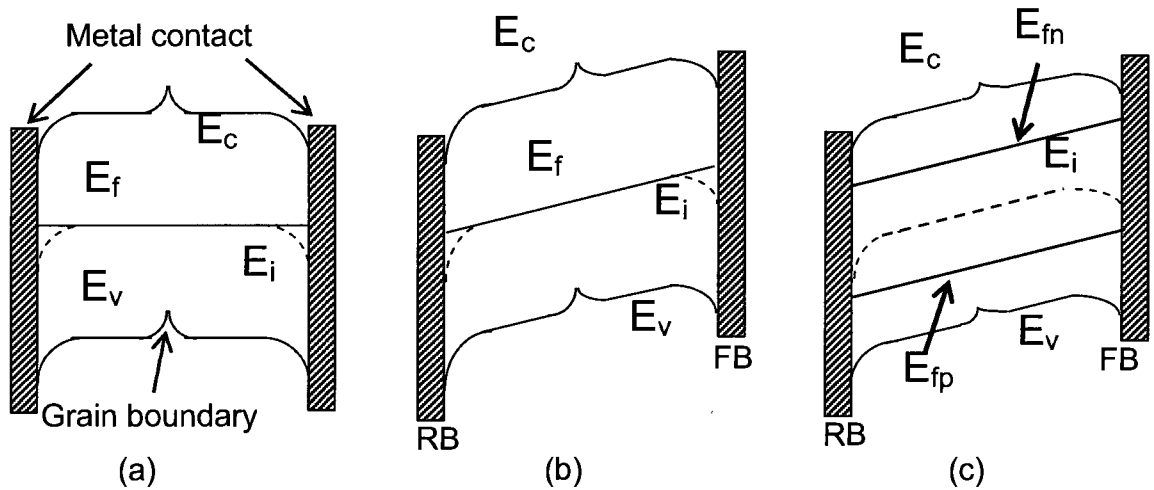


Figure 10: Energy band diagram of the detector under both voltage bias and illumination. (a) is in the dark and with no applied bias. (b) is in the dark but under an applied bias. (c) is illuminated and under an applied bias. In (b) and (c), FB and RB indicate the forward-biased and reversed-biased contacts, respectively. Note that in (c), both the grain boundary height and the contact barrier heights have decreased in magnitude, when compared to (b).

The measured photocurrent from any photoconductor consists of a primary photocurrent and potentially a secondary photocurrent [21]. The primary photocurrent arises directly from the absorbed photon. Any secondary photocurrent comes from a gain process associated with the absorbed photon, and results in injection of carriers at one contact to replace those carriers removed at the other contact. In this way, the effective lifetime of the carrier in the case of a secondary photocurrent is increased over the case where only a primary photocurrent is present. In the case of a photoconductor with Schottky contacts, the gain mechanism is the lowering of the Schottky barriers previously discussed. The lifetime in the case of a primary photocurrent is  $\tau_{life,r1} = \frac{S-x}{v}$ , where S is the contact spacing, x is the location where the

EHP is created and v is the mobile carrier velocity. This equation assumes that the mobile carrier moves from the creation point towards the contact at S, with the other contact at x = 0.

For secondary photoconductivity, the lifetime is  $\tau_{life,r2} = n \frac{S}{v} = n \tau_{transit}$ , where n is the number of times the mobile carrier is injected into the photoconductor from a contact and  $\tau_{transit}$  is the time it takes a carrier to transit between the contacts. Thus, the effective lifetime of a carrier is

$$\tau_{life} = \frac{S-x}{v} + n \tau_{transit}, \text{ where } n \text{ may equal zero.}$$

Photogenerated charges which are being held in traps (prior to detrapping) or in recombination states (prior to recombination) will result in a charge accumulation which enhances the image-force lowering of the Schottky barrier at the contact [22], thus enhancing the gain mechanism. Correspondingly, photogenerated charge which is not in a trap or recombination state will not enhance the gain mechanism. Under the assumption that photogenerated carriers recombine either at recombination states in the bulk or at the contacts, the implication is that the effective lifetime for carriers which recombine in the bulk is

$$\tau_{life,bulk\_recomb} = \frac{S-x}{v} + n \tau_{transit}, \text{ where } n \text{ is a statistical average, while the effective lifetime for}$$

$$\text{carriers which recombine at the contacts is } \tau_{life,cont\_recomb} = \frac{S-x}{v}.$$

Since there are a finite number of sputtering-induced recombination states at the contacts, eventually the contact will reach an equilibrium of occupied states. At that point, image-charge lowering of the Schottky barrier is at a maximum and the reverse leakage current will no longer increase. Note that sputtering-induced recombination states provide a mechanism for barrier lowering across the entire contact region. Grain-boundary recombination states only provide a mechanism for barrier lowering where grain boundaries intersect the contact region. In addition, carriers at recombination states associated with grain boundaries in the bulk are less effective at barrier lowering, due to their greater distance from the contacts.

With the background material given previously and a few pages of algebra, the impulse function in the presence of bulk, grain-boundary and sputtering-induced recombination sites

(“bulk\_recomb” for short) is obtained in Appendix A as 
$$h_{bulk\_recomb}(t) = \frac{\Re e^{-t/\tau_R}}{\tau_{transit}} u(t). \quad (1)$$

where  $\tau_R$  is the recombination time constant,  $u(t)$  is the unit step function and the other terms are as previously defined. In the unit step function,  $t = 0$  is defined as when the electron-hole pair is generated. In the absence of bulk, grain-boundary and sputtering-induced recombination sites, so that carriers only recombine at the contacts, the impulse function is

obtained as in Appendix A as 
$$h_{cont\_recomb}(t) = \frac{\Re}{\tau_{transit}} [u(t) - u(t - \tau_{life,cont\_recomb})]. \quad (2)$$

This second impulse function will only apply at higher optical levels and to the photogenerated carriers in excess of that necessary to keep the recombination sites fully occupied. i.e. If all recombination sites are occupied by electrons, any additional photogenerated electrons are unaffected by the recombination sites until some sites become available through the capture of holes.

Assuming a waveguide of width  $W$  centered between the contacts, integrating the impulse response across the waveguide and then convolving with a Gaussian pulse with pulse energy  $E_{opt}$  and standard deviation  $\sigma$  yields an analytical time-domain recombination response of

$$i_{bulk\_recomb}(t) = \frac{\Re E_{opt}}{2\tau_{transit}} e^{(\sigma^2/2\tau_R^2)} e^{-(t/\tau_R)} \left[ 1 + erf\left(\frac{t}{\sqrt{2}\sigma} - \frac{\sigma}{\sqrt{2}\tau_R}\right) \right]. \quad (3)$$

Once all bulk, grain boundary and sputtering-induced recombination sites are occupied, so that recombination only occurs at the contacts, the response becomes

$$i_{cont\_recomb}(t) = \frac{\mathfrak{R}E_{opt}}{2\tau_{transit}} \left[ erf\left(\frac{t}{\sqrt{2}\sigma}\right) - erf\left(\frac{\left(t - \frac{S+W}{2v}\right)}{\sqrt{2}\sigma}\right) \right]. \quad (4)$$

Figure 11 shows the theoretical pulse response of the detector with the photoconductive gain mechanism in Eqn. 3 turned on and off. All other parameters remain constant. In essence, when a photoconductive gain mechanism is present the carriers effectively live long enough for the recombination tail to be significant. The “with photoconductive gain” plot of Figure 11 is the theory plot of Figure 7. Note that theory and experiment in Figure 7 show excellent agreement.

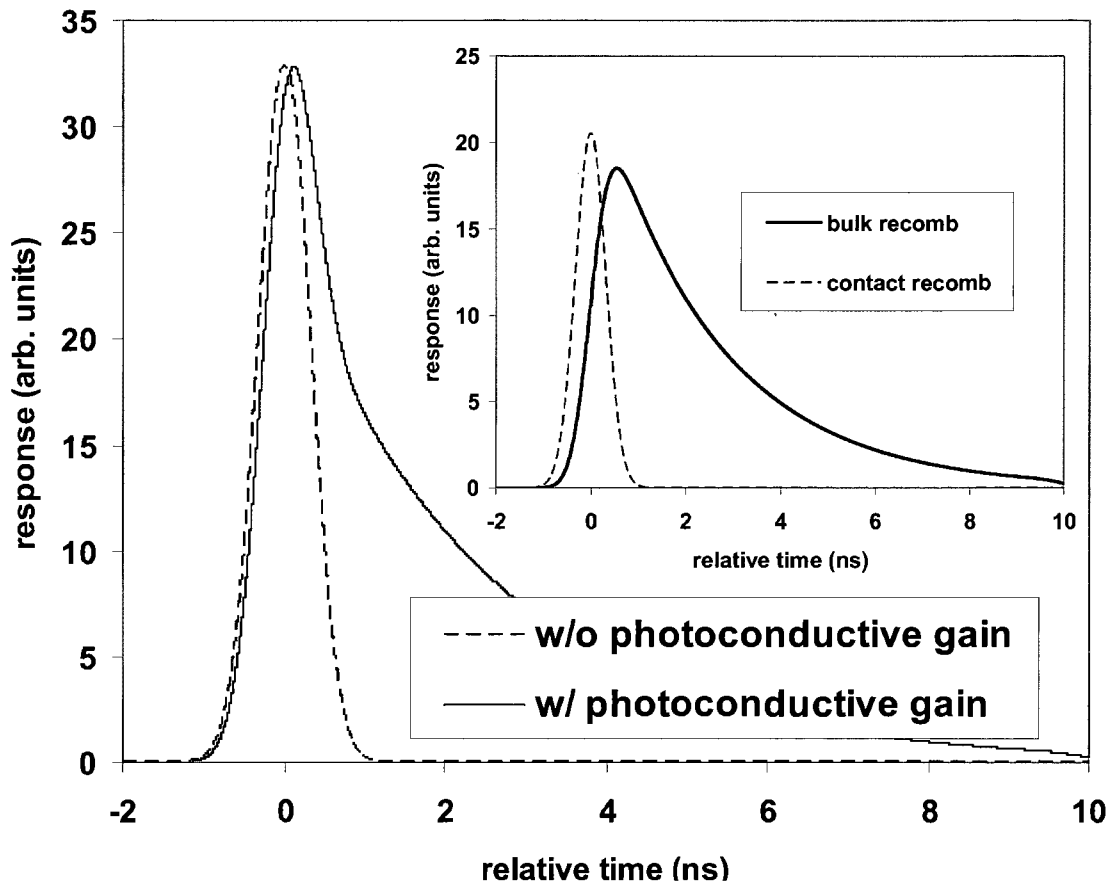


Figure 11: Comparison of theoretical detector response with and without a photoconductive gain mechanism. Responses have been normalized to the same magnitude, to focus on the pulse width. Inset shows the bulk recombination and contact recombination parts of the photoconductive gain response

## References

- [1] L. K. Anderson, "Measurement of the Microwave Modulation Frequency Response of Junction Photodiodes," *Proc. IEEE*, vol. 51, p. 847, 1963.
- [2] T. Andersson, A. R. Johnston, and H. Eklund, "Temporal and frequency response of avalanche photodiodes from noise measurements," *Applied Optics*, vol. 19, pp. 3496-3499, 1980.
- [3] T. Kaneda and H. Takanashi, "The Frequency Response of Germanium Avalanche Photodiodes," *Jpn. J. Appl. Phys. Pt. 1*, vol. 12, pp. 1652-1653, 1973.
- [4] A. E. Siegman, "Private communication," 2007, pp. Response to "References for high-speed (>GHz) testing of photodetectors" posting to sci.optics (Useful response #1).

- [5] P. C. D. Hobbs, "Private communication," 2007, pp. Response to "References for high-speed (>GHz) testing of photodetectors" posting to sci.optics (Useful response #3).
- [6] D. M. Baney, W. V. Sorin, and S. A. Newton, "High-Frequency Photodiode Characterization Using a Filtered Intensity Noise Technique," *IEEE Phot. Tech. Lett.*, vol. 6, pp. 1258-1260, 1994.
- [7] N. S. Nahman, "Picosecond-Domain Waveform Measurement - Status and Future Directions," *IEEE Trans. Instr. Meas.*, vol. 32, pp. 117-124, 1983.
- [8] D. R. Bowman, R. B. Hammond, and R. W. Dutton, "Polycrystalline-Silicon Integrated Photoconductors for Picosecond Pulsing and Gating," *IEEE Electron Dev. Lett.*, vol. 6, pp. 502-504, 1985.
- [9] C. Shu, B. B. Hu, X. C. Zhang, P. Mei, and E. S. Yang, "Picosecond Photoconductive Response of Polycrystalline Silicon Thin-Films," *Appl. Phys. Lett.*, vol. 57, pp. 64-66, 1990.
- [10] B. Pease, "What's All This Transimpedance Amplifier Stuff, Anyway?," in *Electronic Design*, 2001.
- [11] J. Graeme, *Photodiode Amplifiers: Op Amp Solutions*, 1st ed. Boston: McGraw-Hill, 1996.
- [12] G. J. Korsh and R. S. Muller, "Conduction Properties of Lightly Doped, Polycrystalline Silicon," *Sol. St. Elect.*, vol. 21, pp. 1045-1051, 1978.
- [13] R. Pownall, C. Thangaraj, G. Yuan, P. Nikkel, T. W. Chen, and K. L. Lear, "CMOS Optoelectronic Components for Clock Distribution," *Microel. Eng.*, submitted for publication.
- [14] R. Pownall, G. Yuan, T. W. Chen, P. Nikkel, and K. L. Lear, "Geometry dependence of CMOS-compatible, polysilicon, leaky-mode photodetectors," *IEEE Phot. Tech. Lett.*, vol. 19, pp. 513-515, 2007.
- [15] A. K. Ghosh, C. Fishman, and T. Feng, "Theory of the Electrical and Photo-Voltaic Properties of Polycrystalline Silicon," *J. Appl. Phys.*, vol. 51, pp. 446-454, 1980.
- [16] A. Valletta, P. Gaucci, L. Mariucci, and G. Fortunato, "Modelling velocity saturation effects in polysilicon thin-film transistors," *Jpn. J. Appl. Phys. Part 1 - Regul. Pap. Brief Commun. Rev. Pap.*, vol. 45, pp. 4374-4377, 2006.
- [17] P. Panayotatos and H. C. Card, "Recombination Velocity at Grain-Boundaries in Polycrystalline Si under Optical Illumination," *IEEE Electron Dev. Lett.*, vol. 1, pp. 263-266, 1980.
- [18] H. C. Card and E. S. Yang, "Electronic Processes at Grain-Boundaries in Polycrystalline Semiconductors under Optical Illumination," *IEEE Trans. Electron Devices*, vol. 24, pp. 397-402, 1977.
- [19] S. M. Sze, *Physics of Semiconductor Devices*, 2nd ed. New York, NY: Wiley-Interscience, 1981.
- [20] S. F. Soares, "Photoconductive Gain in a Schottky-Barrier Photodiode," *Jpn. J. Appl. Phys. Pt. 1*, vol. 31, pp. 210-216, 1992.
- [21] R. H. Bube, *Photoconductivity of Solids*, 2nd ed. Huntington, New York: Krieger, 1978.
- [22] J. Burm and L. F. Eastman, "Low-Frequency Gain in MSM Photodiodes Due to Charge Accumulation and Image Force Lowering," *IEEE Phot. Tech. Lett.*, vol. 8, pp. 113-115, 1996.

ACHIEVEMENTS, CONCLUSIONS AND SUGGESTIONS FOR FUTURE WORK

**1 Achievements**

Achievements to date from this work are listed below

**1.1 Journal papers**

Lead author on “Geometry Dependence of CMOS-Compatible, Polysilicon, Leaky-Mode Photodetectors”, *IEEE Photonics Technology Letters*, v. 19, no. 7, pp. 513 – 515 (April 1, 2007).

Lead author on “CMOS Optoelectronic Components for Clock Distribution”, accepted for publication in *Microelectronic Engineering*.

Second author on “Fully CMOS-Compatible On-Chip Optical Clock Distribution & Recovery”, accepted for publication in *IEEE Transaction on VLSI Systems*.

Second author on “Characterization of CMOS compatible waveguide-coupled leaky-mode photodetectors”, *IEEE Photonics Technology Letters*, v. 18, n. 13-16, pp. 1657-1659 (Jul-Aug 2006)

Third author on “Amplified spontaneous emission measurements in a diamond anvil cell: A tool to investigate laser diode gain under high pressure”, *Physica Status Solidi B-Basic Research*, v. 241, n. 14, pp. 3420-3426 (Nov. 2004)

**1.2 Conference papers**

“Geometry dependence of Leak-Mode, Waveguide-Coupled, Polysilicon Photodetectors”, paper ThQ4, presented at LEOS 2006, Montreal, Quebec, Canada.

**1.3 Conference posters**

“CMOS-Compatible On-Chip Optical Interconnects”, ISTeC, November 2006, CSU, Fort Collins, CO

“Temperature Dependence of Polysilicon Photodetectors for Integrated Optical Sensors and Electronics Applications”, American Physic Society annual meeting, March 2007, Denver CO

“CMOS-Compatible On-Chip Optical Interconnects”, CPIA Annual Meeting, CU, Boulder, CO, November 2007

#### **1.4 Lab tools**

Developed a fiber-scanning system for determining loss in optical waveguides. Developed an automated system for optimizing input fiber to detector waveguide alignment. Wrote a LabVIEW program to control HP 54600 series oscilloscopes, including downloading trace data to an ASCII file suitable for importation into MATLAB or Excel.

## **2 Conclusions**

The overall objective of this Ph.D research was to investigate and characterize a novel proposal for a nanoscale on-chip optical network for clock distribution. The novel aspect of this proposal was that it was fully compatible with any reasonably standard CMOS process.

From the aspect of demonstrating the basic capabilities and feasibility of the proposal, the work was successful. Responsivities of 1.3 A/W have been demonstrated, sufficient for the application. Measured detector speed is equivalent to a few hundred MHz. While roughly an order of magnitude too slow for the intended application, the measured values were limited by the ability to modulate the source laser diode at the desired speeds. Waveguide loss, at ~8.8 dB/cm, and split loss, at ~4 dB/cm, are both too high. This hurts the ability to deliver sufficient power from the input of the optical clock distribution H-tree network to the end nodes. However, reasonable proposals for lowering these losses have been made and have a good chance of success. Most critically, in related work [1] integration of optical source, waveguides, waveguide splits, detectors and clock recovery circuitry have been demonstrated in a test chip manufacturing in a commercial CMOS process.

## **3 Suggestions for future work**

The future work proposed for this research is listed below.

### **3.1 Improved means of coupling light into the waveguide**

Getting enough light into the waveguides leading to the edge-coupled waveguide detectors and into the optical H-tree waveguides was a constant problem. Some measurements (e.g. bandwidth measurements of the detectors using shot-noise based frequency domain techniques) were unsuccessful due to the inability to couple enough optical power into the waveguides. Developing improved methods of coupling light into the waveguide should be a high priority.

### **3.2 Calculation of the variation of the propagation velocity in waveguide with respect to waveguide dimensional variations**

Calculation of the propagation velocity of signals in the optical waveguides versus dimensional tolerances might yield interesting results and should be pursued.

### **3.3 Higher frequency data**

Obtaining higher frequency data would be useful for two reasons.

First, and most obviously, is to determine the ultimate performance of the photodetectors in this work.

Second, higher frequency data would allow a determination of whether a negative exponential lifetime model, a Gaussian lifetime model, or a single-lifetime model (the small variance limit of the Gaussian model and what is currently being used) best fits the data.

### **3.4 Third generation test chip**

Much was learned going from the first generation to the second generation of test chip. A third generation would allow more learning and experimentation.

Some possibilities for third generation test structures are:

#### *3.4.1 Improved method of determining power to edge detector structures, version 1*

Take input waveguide, split half of it to detector (by means of a large radius bend?) and the other half back to the edge of the die, where the light power in the waveguide can be measured by a commercial detector. (Since the waveguide is a 50/50 splitter, the light detected by the

commercial detector should equal the light incident on the CSU detector, with allowance for any additional loss in the path caused by a slightly longer path to the edge of the die than to the CSU detector.)

#### *3.4.2 Improved method of determining power to edge detector structures, version 2*

Take the input waveguide, bend it in a large radius curve (no split this time) and bring it in to the detector "from the back", so to speak. Then, continue the waveguide across the polysilicon detector and on to the edge of the die. The power leaving the detector can be determined this way. From the power leaving the detector, we should be able to determine the power entering the detector by using some reasonable assumptions about the fraction of power absorbed in the detector.

#### *3.4.3 Vary the contact type to the detector – Ohmic vs. Schottky*

Make some detectors with various kinds of contacts - Schottky (using undoped polysilicon), n-type ohmic and p-type ohmic. (This would require checking to see if the Avago process has both n-type and p-type polysilicon. A possibility might be to implant dope just the contact regions in the poly, so that the main part of the poly is undoped.)

Related to this idea, it might be interesting to have some detectors with ohmic contacts on one side, and Schottky contacts on the other, to look for asymmetries.

#### *3.4.4 Testability concerns*

Before starting the design, think through, very carefully, issues related to testing a die. In particular, think through three-dimensional issues related to bringing light to the die by means of an optical fiber while simultaneously bringing high-speed probes in from the top. And don't overlook the need to use a microscope to align the fiber to the waveguide and to align the probes to pads.

#### *3.4.5 Improved SEM structures*

Better SEM cross-section structures. For SEM cross-sections looking down the waveguide, a structure with a 0.5  $\mu\text{m}$  waveguide and a detector that is 2.6  $\mu\text{m}$  wide and 100  $\mu\text{m}$  long, or longer, would be nice. Just in case it's not obvious, the 0.5  $\mu\text{m}$  dimension of the waveguide

should be parallel to the die edge, while the 100  $\mu\text{m}$  dimension of the detector should be perpendicular to the die edge. Similarly, for SEM cross sections looking across the waveguide, a structure with a 100  $\mu\text{m}$  wide waveguide and a 10  $\mu\text{m}$  long detector would be nice. (Rotate this structure 90 degrees relative to the previous cross-section structure, so that the 100  $\mu\text{m}$  dimension of the waveguide is perpendicular to the edge of the die while the 10  $\mu\text{m}$  dimension of the detector is parallel to the die edge. Note that in both cases, the direction of primary interest is parallel to the die edge, as that's the way the polish is coming, and the direction perpendicular to the die edge is extremely long, so there's no problem with not going far enough or with going too far. If you want a cross-section through a contact, you're either going to need a FIB cut or you're going to have to be very lucky with your polishing.

### References

- [1] C. Thangaraj, R. Pownall, P. Nikkel, G. Yuan, K. L. Lear, and T. W. Chen, "Fully CMOS-Compatible On-Chip Optical Clock Distribution & Recovery," *IEEE Trans. VLSI Systems*, Accepted for publication.

DERIVATION OF THE DETECTOR IMPULSE RESPONSE, PLUS THE SYSTEM  
DC AND AC RESPONSE

The standard method of determining the system response to a signal is to find the impulse response of the system and then convolve the impulse response with the signal of interest. In this appendix, I determine the impulse response of the detectors in this work in the presence of bulk recombination and contact recombination. I then convolve the impulse responses with a DC signal, to determine the DC response, to see how well the theoretical system response matches the observed system response to a DC signal. Following that, I convolve the impulse responses with an AC signal, in the form of Gaussian pulse, to determine the AC response, to see how well the theoretical system response matches the observed system response to an AC signal.

**1 Bulk recombination center impulse response**

The road map I'll follow to determine the impulse response of the detectors in the presence of bulk recombination is to add, step-by-step, factors which affect the impulse response. Each new sub-section will add a new factor. The factors are added in what seems to me to be the most logical and obvious order, coinciding, as much as possible, with the physical order in which events occur. As a sanity check, the units of the impulse response will be tracked.

The driving impulse is a single photon impinging on the detector.

**1.1 Probability of a photon entering the detector**

Taking into account the probability of a photon entering the detector yields an impulse response of  $h(t) = (1 - R)$ , where  $R$  is the power reflectivity (i.e. the Fresnel reflection). The units of the impulse response are dimensionless.

## 1.2 Probability of a photon being absorbed in the detector

Taking into account the probability of a photon being absorbed in the detector yields an impulse response  $h(t) = (1 - R)(1 - e^{-\alpha d})$ .  $\alpha$  is the absorption coefficient and  $d$  is the detector effective depth (length). The units of the impulse response are still dimensionless.

## 1.3 Amount of charge created by the absorbed photon

Considering the amount of charge created in the detector by the optical impulse yields an impulse response of  $h(t) = q(1 - R)(1 - e^{-\alpha d})$ , where  $q$  is the charge of an electron. The units of the impulse response are in Coulombs.

## 1.4 Get the charge moving, to create a current

The photogenerated charge won't produce a current until it starts moving. Taking this into account leads to an impulse response of  $h(t) = q(1 - R)(1 - e^{-\alpha d})v$ , where  $v$  is the average carrier velocity. The units of the impulse response are Coulomb-meter/second, or Amp-meter.

Note that a photoconductor requires an external voltage bias to create moving charge, as a photoconductor has no built-in electric field.

## 1.5 Normalize to account for using a single photon as the impulse driving function

We're eventually going to want to apply a pulse consisting of more than one photon to the detector. As a result, we need to normalize the impulse response of the previous step to account for the fact it's due to the energy of a single photon,  $\lambda/hc$ , where  $\lambda$  is the wavelength,  $h$  is Planck's constant and  $c$  is the speed of light. This yields an impulse response of  $h(t) = q \frac{\lambda}{hc} (1 - R)(1 - e^{-\alpha d})v = \mathfrak{R}v$ , where  $\mathfrak{R} \equiv \frac{q\lambda}{hc} (1 - R)(1 - e^{-\alpha d})$  is the responsivity. The units of the impulse response are Amp-meter/Joule.

## 1.6 Account for the effect of the contact spacing on the electric field

To create the moving charge, an external voltage bias has been assumed. Since the carrier velocity is proportional to the electric field, not the applied voltage bias, a  $(1/S)$  term, where  $S$  is the contact spacing, is required to convert the voltage bias to an electric field strength. This

leads to an impulse response of  $h(t) = q \frac{\lambda}{Shc} (1 - R)(1 - e^{-\alpha d}) \nu = \mathfrak{R} \frac{\nu}{S}$ . The units of the impulse response are Amps/Joule. While not used in this step, I'll also define  $\tau_{transit}$  as the time it takes a carrier to travel from the contact at  $x = 0$  to the contact at  $x = S$ . i.e.  $\tau_{transit} = \frac{S}{\nu}$ .

Using this, the impulse function is  $h(t) = \frac{\mathfrak{R}}{\tau_{transit}}$ .

### 1.7 Deal with the creation of the photogenerated charge

The photogenerated charge can't start moving until it's created, so add a unit step function to account for the creation of the carrier. This yields an impulse function of

$h(t) = q \frac{\lambda}{Shc} (1 - R)(1 - e^{-\alpha d}) \nu u(t) = \mathfrak{R} \frac{\nu}{S} u(t)$  The units of impulse function are still

Amps/Joule. (Carrying all the terms making up  $\mathfrak{R}$  is becoming annoying, so from now on the derivation will just use  $\mathfrak{R}$  by itself.)

### 1.8 Account for an exponential bulk recombination process

Since the moving charge in the previous sections consists of a photogenerated electron-hole pair that will recombine (due to the assumed presence of recombination centers in the bulk), it is necessary to include a term to account for this recombination. Assuming the standard

exponential-decay recombination process yields an impulse response of:  $h(t) = \mathfrak{R} \frac{\nu}{S} u(t) e^{-t/\tau_R}$ ,

where  $t$  is the time since the EHP was created and  $\tau_R$  is the recombination lifetime. Another way of thinking about  $\tau_R$  is that it is the time it takes for the photogenerated charge to drop to  $1/e$  of its original value. The units of the impulse function in this step are still Amps/Joule.

### 1.9 Should the polysilicon nature of the detectors be included?

Due to the polysilicon nature of the detector, I was initially going to include a term to account

for the polysilicon grain boundaries, similar to Korsh & Muller [1] eqn. 6:  $I = 2K \sinh\left(\frac{V_a}{\xi}\right)$ ,

where  $K = AA^*T^2 \exp\left(\frac{-qV_{B0}}{kT}\right)$  and  $\xi = \frac{2kTN}{q}$ . However, upon reflection, I've decided that

the sinh term only applies at low optical power levels and low applied voltage biases. For what I've been doing, the optical power levels are such that the potential barriers at the grain boundaries are either flat or so thin that tunneling through them is not a problem. In other words, there's no need for a sinh term since the current contribution from tunneling through the barrier is much larger than the current contribution from thermionic emission over the barrier.

### 1.10 Final impulse response

The end result of the previous sections is that the impulse response due to bulk recombination

$$\text{is given by } h_{\text{bulk\_recomb}}(t) = h_r(t) = \mathfrak{R} \frac{\nu}{S} u(t) e^{-t/\tau_R} .$$

## 2 Contact recombination impulse response

The bulk recombination center impulse response, found above, assumes that carriers recombine is at recombination centers. The case where recombination centers do not exist has to be treated separately. Fortunately, with appropriate modifications we can apply much of the work done for the bulk recombination center impulse response to the contact recombination impulse response.

First,  $\tau_R$  is effectively infinite, since recombination centers in the bulk are assumed not to exist. Second, the carrier lifetime is just the time it takes the carrier to reach the contact, as no photoconductive gain process can be present. As a result of the first point, the exponential decay term goes away. As a result of the second point, there is a “turn-off” step function at

$$\tau_{\text{life},c}, \text{ where } \tau_{\text{life},c} = \frac{S - x}{\nu} .$$

This leads to a contact recombination impulse response of

$$h_{\text{contact\_recomb}}(t) = \mathfrak{R} \frac{\nu}{S} [u(t) - u(t - \tau_{\text{life},c})] .$$

The following objection may be raised: “Why are you assuming a gain process which extends the effective lifetime of carriers in the case of bulk recombination, but not in the case of contact recombination?”

The answer is that the gain process observed in photodetectors with Schottky contacts relies on trapped photogenerated charge lowering the Schottky barrier at the contact junction. [2-4] In the case of bulk recombination, charge in recombination centers serves the role of trapped charge, at least until the charge in the recombination center recombines with charge of the opposite carrier type. In the case of contact recombination, there is no charge to serve in the role of trapped charge. In this context, note that the observed recombination lifetime is 2.5 ns, while the estimated transit time for a 2.64  $\mu\text{m}$  contact spacing device is 69 ps.

### 3 DC response

We can obtain the DC response of any system by convolving a DC signal with the impulse response of the system. If the system is linear, we can convolve a DC response with separate impulse responses independently and then add the responses together.

#### 3.1 DC system response due to the bulk recombination impulse response

Let  $f(t)$  = the DC signal, and let  $g(t)$  equal the bulk recombination center impulse response.

Note that I am using the “function of time” notation for a function which is independent of time. This is to keep the same formalism as is used in the AC response later, and the same formalism as is conventionally used in convolutions. Also, I’m defining  $f(t)$  to be the DC power, not the DC number of photons. This is because of how I defined the impulse response.

With these definitions, the convolution of  $f(t)$  and  $g(t)$  is:

$f(t) * g(t) = \int_{-\infty}^{\infty} P_{opt,\delta} \Re \frac{v}{S} u(\tau) e^{-\tau/\tau_R} d\tau$ , since  $f(t) = f(\tau) = f(t-\tau) = P_{opt,\delta}$ , the input optical power. Applying the unit step function and pulling constant terms out from the integral yields

$$\begin{aligned} \Re P_{opt,\delta} \frac{v}{S} \left\{ \int_0^{\infty} e^{-\tau/\tau_R} d\tau \right\} &= \Re P_{opt,\delta} \frac{v}{S} \left[ -\tau_R e^{-\tau/\tau_R} \right]_0^{\infty} \\ &= \Re P_{opt,\delta} \frac{v}{S} \tau_R = I_R \frac{v\tau_R}{S} = I_R \frac{\mu E \tau_R}{S} = I_R \frac{\mu \tau_R V}{S \times S} = I_R \frac{\mu \tau_R V}{S^2} \end{aligned}, \text{ where } I_R \equiv \Re P_{opt,\delta}.$$

Since  $\tau_{transit} = \frac{S}{v} = \frac{S}{\mu E} = \frac{S}{\mu(V/S)} = \frac{S^2}{\mu V}$ , an alternate way of expressing the above result

is  $I_R \frac{\mu \tau_R V}{S^2} = I_R \frac{\tau_R}{\tau_{transit}}$ . This formulation may provide more physical insight.

### 3.2 DC system response due to the contact recombination impulse response

Let  $f(t)$  = the DC signal, and let  $g(t)$  equal the contact recombination impulse response.

Again, note that I am using the “function of time” notation for a function which is independent of time, and for the same reasons as stated earlier.

Then the convolution of  $f(t)$  and  $g(t)$  is:

$$f(t) * g(t) = \int_{-\infty}^{\infty} \mathfrak{R}P_{opt} \frac{v}{S} [u(\tau) - u(\tau - \tau_{life,c})] d\tau, \text{ where the symbols are as defined earlier.}$$

$$\text{Pulling out the constant terms yields: } \mathfrak{R}P_{opt} \frac{v}{S} \int_{-\infty}^{\infty} [u(\tau) - u(\tau - \tau_{life,c})] d\tau$$

Applying the unit step functions to the limits of integration yields:

$$\mathfrak{R}P_{opt} \frac{v}{S} \left\{ \int_0^{\infty} d\tau - \int_{-\tau_{life,c}}^{\infty} d\tau \right\}$$

Evaluating the integrals yields:

$$\mathfrak{R}P_{opt} \frac{v}{S} \{ (\infty - 0) - (\infty + \tau_{life,c}) \} = \mathfrak{R}P_{opt} \frac{v}{S} \tau_{life,c} = \mathfrak{R}P_{opt} \frac{v \tau_{life,c}}{S} = I_c \frac{\tau_{life,c}}{\tau_{transit}}$$

where  $I_c \equiv \mathfrak{R}P_{opt}$  since, by definition,  $S = v \tau_{transit}$ . On average, however,  $\tau_{life,c} = \frac{1}{2} \tau_{transit}$  since

the average carrier is created halfway between the contacts. This means the integrals evaluate

to  $\frac{I_c}{2}$ . The factor of  $\frac{1}{2}$  here is indicative of the fact that I’m considering just one

photogenerated carrier type – electrons or holes. If both carrier types were considered, then the  $\frac{1}{2}$  will go away. For the sake of simplicity, further work will assume that both carrier types are considered.

### 3.3 Combine the bulk recombination and contact recombination responses

A certain amount of the input optical power goes into generating carriers that recombine at recombination centers in the bulk and the balance goes into generating carriers that recombine at the contacts. Let the ratio of bulk recombination carriers to contact recombination carriers be  $K_{DC}$ . Then the total DC photocurrent response  $I_P$  is

$$I_P = I_R \frac{\bar{\mu}\tau_R V}{S^2} + I_c = I_c + K_{DC} I_c \frac{\bar{\mu}\tau_R V}{S^2} = I_0 \left( 1 + K_{DC} \frac{\bar{\mu}\tau_R V}{S^2} \right), \quad \text{where } I_0 \equiv I_c \text{ and } K_{DC} \equiv \frac{I_R}{I_c}.$$

This formulation is defined purely for the convenience of matching the form of the equation used to fit the first-generation data in my IEEE PTL paper. [5] Note that  $K_{DC}$  may be less than or greater than 1. It may also vary with the optical input power level. At least, a variation with optical input power seems plausible, due to the above-discussed partition of carriers which recombine at recombination sites and carriers which recombine at contacts. If the optical power level gets high enough, it should be possible to have all of the recombination sites occupied, so that any additional carriers can't find an available recombination center.

## 4 AC response

In a manner similar to that used to obtain the DC response, we will convolve the AC input with the impulse response to obtain the AC response. This will be done by first convolving the AC response with the bulk recombination center impulse response, then with the contact recombination impulse response, and adding the two contributions together.

The AC response will be assumed to be a Gaussian pulse (i.e.  $E_{opt}(t) = \frac{E_{opt}}{\sqrt{2\pi\sigma^2}} e^{-t^2/2\sigma^2}$ ) with a

specified full-width half-max (FWHM) and optical energy per unit area  $E_{opt}$ . Note that for a Gaussian pulse, the FWHM and the variance are related by the equation

$$FWHM = 2\sqrt{2\ln(2)}\sigma \text{ or } \sigma = FWHM/2\sqrt{2\ln(2)}.$$

Also note that, unlike the DC case, in the AC case we are interested in the energy of the pulse rather than the power, as the energy is directly related to the number of photon in the pulse. Finally, note that the time dependence is a simple  $t^2$ , not a  $(t-t_{mean})^2$  one. This is because the unit step functions have  $t = 0$  when the electron-hole pair (EHP) is created, not at any arbitrary external time. (This is a somewhat subtle, but important, point, and one which initially escaped me.) The system response to the

value of the Gaussian pulse at  $t_{\text{system}} = t_1$  is determined by the number of photons in the Gaussian pulse at  $t_{\text{system}} = t_1$ , which means that  $t_{\text{unit step function}} = 0$  for those photons corresponds to  $t_{\text{system}} = t_1$ . i.e.  $u(t_{\text{unit step function}}) = u(t_{\text{system}} - t_1)$ . A little thought should convince you that one implication of this is that it doesn't matter when  $t_{\text{system}} = 0$  is defined, at least in terms of the system response. An exceptionally convenient choice for  $t_{\text{system}} = 0$  is at the peak of the Gaussian pulse, causing  $t_{\text{mean}}$  to be zero.

I have no intuition what the bulk recombination system response will look like, with one exception. Since the convolution involves integrating a Gaussian, the result should involve an error function. I wouldn't be shocked to see an exponential in the response, from the exponential time dependence of the recombination process.

I'd expect the contact recombination response to look similar to the bulk recombination response, but without the exponential time dependence.

#### 4.1 AC system response due to the bulk recombination impulse response

Let  $f(t)$  = the AC signal, and let  $g(t)$  equal the recombination center impulse response. Assume

$f(t)$  is a Gaussian pulse with FWHM =  $\tau_{\text{FWHM}}$ . i.e.  $f(t) = \frac{E_{\text{opt},W}}{\sqrt{2\pi\sigma^2}} e^{-t^2/2\sigma^2}$

$$g(t) = h_r(t) = \Re \frac{v}{S} u(t) e^{-t/\tau_R}$$

Then the convolution of  $f(t)$  and  $g(t)$  is:

$$f(t) * g(t) = \int_{-\infty}^{\infty} \frac{E_{\text{opt},W}}{\sqrt{2\pi\sigma^2}} e^{-\tau^2/2\sigma^2} \Re \frac{v}{S} u(t-\tau) e^{-(t-\tau)/\tau_R} d\tau .$$

Applying the unit step functions and pulling constant terms out from the integral yields:

$$\begin{aligned}
& \frac{1}{\sqrt{2\pi\sigma^2}} \Re E_{opt,W} \frac{v}{S} \left\{ \int_{-\infty}^t e^{-\tau^2/2\sigma^2} e^{-(t-\tau)/\tau_R} d\tau \right\} \\
&= \frac{1}{\sqrt{2\pi\sigma^2}} \Re E_{opt,W} \frac{v}{S} \left[ -\sigma e^{\sigma^2/2\tau_R^2} e^{-(t-\bar{t})/\tau_R} \sqrt{\frac{\pi}{2}} \left\{ \operatorname{erf} \left( \frac{\sigma^2 - \tau_R \tau}{\sqrt{2\sigma\tau_R}} \right) \right\}_{-\infty}^t \right] \\
&= \frac{1}{\sqrt{2\pi\sigma^2}} \Re E_{opt,W} \frac{v}{S} \left[ \sigma e^{\sigma^2/2\tau_R^2} e^{-t/\tau_R} \sqrt{\frac{\pi}{2}} \left\{ -\operatorname{erf} \left( \frac{\sigma^2 - \tau_R \tau}{\sqrt{2\sigma\tau_R}} \right) \right\}_t^{-\infty} \right]
\end{aligned}$$

Doing the evaluation yields:

$$\begin{aligned}
s(t) &= \frac{1}{2} \Re E_{opt,W} \frac{v}{S} e^{\sigma^2/2\tau_R^2} \left[ e^{-t/\tau_R} \operatorname{erf} \left( \frac{\sigma}{\sqrt{2\tau_R}} - \frac{\tau}{\sqrt{2\sigma}} \right) \right]_t^{-\infty} \\
&= \frac{1}{2} \Re E_{opt,W} \frac{v}{S} e^{\sigma^2/2\tau_R^2} e^{-t/\tau_R} \left[ 1 - \operatorname{erf} \left( \frac{\sigma}{\sqrt{2\tau_R}} - \frac{t}{\sqrt{2\sigma}} \right) \right] \\
&= \frac{1}{2} \Re E_{opt,W} \frac{v}{S} e^{\sigma^2/2\tau_R^2} \left[ 1 + \operatorname{erf} \left( \frac{t}{\sqrt{2\sigma}} - \frac{\sigma}{\sqrt{2\tau_R}} \right) \right] e^{-t/\tau_R}
\end{aligned}$$

In the evaluation, use has been made of the error function properties that  $\operatorname{erf}(\infty) = 1$  and  $\operatorname{erf}(-x) = -\operatorname{erf}(x)$ .

Since detected pulse starts when the carriers generated closest to the contact arrives and ends when the carriers generated furthest from the contact arrive, an integration across the waveguide is required. To cut down on the algebraic clutter, I am considering only the primary photocurrent here. Once that is found, the secondary photocurrent is easy to deduce.

However, given the complexity of the above result (the result of a convolution), it would probably be better to integrate the impulse response across the waveguide first and then convolve with the AC signal, instead of convolving the impulse response and the AC signal and then doing the integration across the waveguide.

As a reminder, the recombination center impulse response is:  $h_r(t) = \Re \frac{v}{S} u(t) e^{-t/\tau_R}$ .

Integrating  $h_i(t,x)$  across the waveguide across the waveguide yields: [Note that I am assuming a waveguide of width  $W$ , symmetrically placed between the contacts. Also note the use of the definition of  $\tau_{\text{transit}}$  (i.e.  $\tau_{\text{transit}} = \frac{S}{v}$ ) in the last equality.]

$$\begin{aligned} \int_{\frac{S-W}{2}}^{\frac{S+W}{2}} h(t,x) dx &= \int_{\frac{S-W}{2}}^{\frac{S+W}{2}} \Re \frac{v}{S} u(t) e^{-t/\tau_R} dx = \Re \frac{v}{S} e^{-t/\tau_R} \int_{\frac{S-W}{2}}^{\frac{S+W}{2}} u(t) dx = \Re \frac{v}{S} e^{-t/\tau_R} \left\{ \int_{\frac{S-W}{2}}^{\frac{S+W}{2}} u(t) dx \right\} \\ &= \Re \frac{v}{S} e^{-t/\tau_R} \left\{ u(t) x \Big|_{\frac{S-W}{2}}^{\frac{S+W}{2}} \right\} = \Re \frac{v}{S} e^{-t/\tau_R} \{u(t)W\} = \frac{\Re W}{\tau_{\text{transit}}} e^{-t/\tau_R} u(t) \end{aligned}$$

Now for the convolution. I'm going to temporarily drop the " $\Re W // \tau_{\text{transit}}$ " prefactor, for clarity. In all cases,  $f(t) = \frac{E_{\text{opt},W}}{\sqrt{2\pi\sigma^2}} e^{-t^2/2\sigma^2}$ , where  $E_{\text{opt},W}$  is the optical energy coupled from the waveguide to the detector per unit width, and is assumed uniform across the waveguide.

1.  $g(t) = \exp(-t/\tau_R)u(t)$

$$\begin{aligned} f(t) * g(t) &= \int_{-\infty}^{\infty} \frac{E_{\text{opt},W}}{\sqrt{2\pi\sigma^2}} e^{-\tau^2/2\sigma^2} e^{-(t-\tau)/\tau_R} u(t-\tau) d\tau \\ &= \frac{E_{\text{opt},W}}{\sqrt{2\pi\sigma^2}} e^{-t/\tau_R} \int_{-\infty}^t e^{-\tau^2/2\sigma^2} e^{\tau/\tau_R} d\tau \\ &= \frac{E_{\text{opt},W}}{\sqrt{2\pi\sigma^2}} e^{-t/\tau_R} \left[ -e^{\sigma^2/(2\tau_R^2)} \sigma \sqrt{\frac{\pi}{2}} \operatorname{erf} \left( \frac{\sigma^2 - \tau_R \tau}{\sqrt{2\tau_R} \sigma} \right) \right]_{-\infty}^t \\ &= \frac{E_{\text{opt},W}}{2} e^{-t/\tau_R} e^{\sigma^2/(2\tau_R^2)} \left[ \operatorname{erf} \left( \frac{\sigma}{\sqrt{2\tau_R}} - \frac{\tau}{\sqrt{2\sigma}} \right) \right]_{-t}^{\infty} \\ &= \frac{E_{\text{opt},W}}{2} e^{-t/\tau_R} e^{\sigma^2/(2\tau_R^2)} \left[ 1 - \operatorname{erf} \left( \frac{\sigma}{\sqrt{2\tau_R}} - \frac{t}{\sqrt{2\sigma}} \right) \right] \\ &= \frac{E_{\text{opt},W}}{2} e^{-t/\tau_R} e^{\sigma^2/(2\tau_R^2)} \left[ 1 + \operatorname{erf} \left( \frac{t}{\sqrt{2\sigma}} - \frac{\sigma}{\sqrt{2\tau_R}} \right) \right] \end{aligned}$$

where the third-to-last equality follows by reversing the limits of integration to

eliminate the negative sign, the next-to-last equality follows since  $\text{erf}(\infty) = 1$  and the last equality follows since  $\text{erf}(-x) = -\text{erf}(x)$ .

Reinserting the “ $\mathcal{R}W/\tau_{\text{transit}}$ ” prefactor yields:

$$\begin{aligned} & \frac{\mathcal{R}W}{\tau_{\text{transit}}} \frac{E_{\text{opt},W}}{2} e^{\sigma^2/2\tau_R^2} e^{-t/\tau_R} \left[ 1 + \text{erf}\left(\frac{t}{\sqrt{2}\sigma} - \frac{\sigma}{\sqrt{2}\tau_R}\right) \right] \\ &= \frac{\mathcal{R}E_{\text{opt}}}{2\tau_{\text{transit}}} e^{\sigma^2/2\tau_R^2} e^{-t/\tau_R} \left[ 1 + \text{erf}\left(\frac{t}{\sqrt{2}\sigma} - \frac{\sigma}{\sqrt{2}\tau_R}\right) \right] \end{aligned}$$

## 4.2 AC system response due to the contact recombination impulse response

As discussed earlier, the contact recombination impulse response is

$$h_c(t) = \mathcal{R} \frac{v}{S} [u(t) - u(t - \tau_{\text{life},c})].$$

Note that there is an implied  $x$  dependence in  $\tau_{\text{life},c}$ .

Integrating  $h_c(t,x)$  across the waveguide across the waveguide yields: [Note that I am assuming a waveguide of width  $W$ , symmetrically placed between the contacts. Also note the use of the definition of  $\tau_{\text{transit}}$  (i.e.  $\tau_{\text{transit}} = \frac{S}{v}$ ) in the last equality.]

$$\begin{aligned} i(t) &= \int_{\frac{S-W}{2}}^{\frac{S+W}{2}} h_c(t,x) dx = \int_{\frac{S-W}{2}}^{\frac{S+W}{2}} \mathcal{R} \frac{v}{S} [u(t) - u(t - \tau_{\text{life},c})] dx = \mathcal{R} \frac{v}{S} \int_{\frac{S-W}{2}}^{\frac{S+W}{2}} [u(t) - u(t - \tau_{\text{life},c})] dx \\ &= \mathcal{R} \frac{v}{S} \left\{ \int_{\frac{S-W}{2}}^{\frac{S+W}{2}} u(t) dx - \int_{\frac{S-W}{2}}^{\frac{S+W}{2}} u(t - \tau_{\text{life},c}) dx \right\} = \mathcal{R} \frac{v}{S} \left\{ u(t)x \Big|_{\frac{S-W}{2}}^{\frac{S+W}{2}} - \int_{\frac{S-W}{2}}^{\frac{S+W}{2}} u\left(t - \frac{S-x}{v}\right) dx \right\} \\ &= \mathcal{R} \frac{v}{S} \left\{ u(t)W - \int_{\frac{S-W}{2}}^{\frac{S+W}{2}} u\left(t - \frac{S-x}{v}\right) dx \right\} = \frac{\mathcal{R}}{\tau_{\text{transit}}} \left\{ u(t)W - \int_{\frac{S-W}{2}}^{\frac{S+W}{2}} u\left(t - \frac{S-x}{v}\right) dx \right\} \end{aligned}$$

To deal with the last integral, we want to know when the integrand is non-zero. I'll arbitrarily assume that the carrier in question is a hole, and that the bias is such that holes are moving from their creation point at  $x$  to the contact at  $S$ . Note that the current pulse will not terminate until the carriers generated furthest from the contact at  $S$  reach the contact at  $S$ .

These “travelled furthest” carriers are generated at  $x=(S-W)/2$ . The lifetime for these carriers is the distance they travel divided by their velocity. Thus,  $\tau_{life} = \frac{S - ((S-W)/2)}{v} = \frac{S+W}{2v}$ .

Taking this into account converts the unit step function in the last integral into

$u\left(t - \frac{S+W}{2v}\right)$ . Inserting this into the above yields:

$$\begin{aligned} i(t) &= \frac{\Re}{\tau_{transit}} \left\{ u(t)W - \int_{\frac{S-W}{2}}^{\frac{S+W}{2}} u\left(t - \frac{S+W}{2v}\right) dx \right\} = \frac{\Re}{\tau_{transit}} \left\{ u(t)W - u\left(t - \frac{S+W}{2v}\right) \int_{\frac{S-W}{2}}^{\frac{S+W}{2}} dx \right\} \\ &= \frac{\Re}{\tau_{transit}} \left[ u(t) - u\left(t - \frac{S+W}{2v}\right) \right] W = \frac{\Re W}{\tau_{transit}} \left[ u(t) - u\left(t - \frac{S+W}{2v}\right) \right] \end{aligned}$$

Now for the convolutions. I’ll do them one term at a time and, as before, I’ll drop the “ $RW/\tau_{transit}$ ” prefactor, for clarity.

1.  $g(t) = u(t)$

$$\begin{aligned} f(t) * g(t) &= \int_{-\infty}^{\infty} \frac{E_{opt,W}}{\sqrt{2\pi\sigma^2}} e^{-\tau^2/2\sigma^2} u(t-\tau) d\tau = \frac{E_{opt,W}}{\sqrt{2\pi\sigma^2}} \int_{-\infty}^t e^{-\tau^2/2\sigma^2} d\tau \\ &= \frac{E_{opt,W}}{\sqrt{2\pi\sigma^2}} \left[ \sigma \sqrt{\frac{\pi}{2}} \operatorname{erf}\left(\frac{\tau}{\sqrt{2}\sigma}\right) \right]_{-\infty}^t = \frac{E_{opt,W}}{2} \left[ \operatorname{erf}\left(\frac{\tau}{\sqrt{2}\sigma}\right) \right]_{-\infty}^t \\ &= \frac{E_{opt,W}}{2} \left[ \operatorname{erf}\left(\frac{t}{\sqrt{2}\sigma}\right) + 1 \right] \end{aligned}$$

2.  $g(t) = u(t - ((S+W)/2v))$

Evaluating the integral is simplified by noting that it is the same integrand as in part 1.

The only thing that has changed is the limits of integration. Therefore, the result is

$$f(t) * g(t) = \frac{E_{opt,W}}{2} \left[ \operatorname{erf}\left(\frac{t - \frac{S+W}{2v}}{\sqrt{2}\sigma}\right) + 1 \right]$$

Combining the two results and reinserting the prefactor yields

$$i_{cont}(t) = \frac{\Re W}{\tau_{transit}} \frac{E_{opt,W}}{2} \left[ erf\left(\frac{t}{\sqrt{2\sigma}}\right) - erf\left(\frac{t - \frac{S+W}{2\nu}}{\sqrt{2\sigma}}\right) \right]$$

$$= \frac{\Re E_{opt}}{2\tau_{transit}} \left[ erf\left(\frac{t}{\sqrt{2\sigma}}\right) - erf\left(\frac{t - \frac{S+W}{2\nu}}{\sqrt{2\sigma}}\right) \right]$$

### 4.3 Combine the bulk recombination and contact recombination responses

Repeating the AC system responses for the two mechanisms, for convenience:

$$i_{bulk}(t) = \frac{\Re E_{opt}}{2\tau_{transit}} e^{\sigma^2/2\tau_r^2} e^{-t/\tau_r} \left[ 1 + erf\left(\frac{t}{\sqrt{2\sigma}} - \frac{\sigma}{\sqrt{2\tau_r}}\right) \right]$$

$$i_{cont}(t) = \frac{\Re E_{opt}}{2\tau_{transit}} \left[ erf\left(\frac{t}{\sqrt{2\sigma}}\right) - erf\left(\frac{t - \frac{S+W}{2\nu}}{\sqrt{2\sigma}}\right) \right]$$

Paralleling the DC system response case, let the ratio of the optical energy creating carriers that recombine in the bulk to the optical energy creating carriers that recombine at the in the AC

case be  $K_{AC}$ . i.e.  $K_{AC} = \frac{E_{opt,bulk}}{E_{opt,cont}}$  Then the overall system response in the AC case is

$$\begin{aligned}
i(t) &= \frac{\Re E_{opt,bulk}}{2\tau_{transit}} e^{\sigma^2/2\tau_R^2} e^{-t/\tau_R} \left[ 1 + \operatorname{erf} \left( \frac{t}{\sqrt{2}\sigma} - \frac{\sigma}{\sqrt{2}\tau_R} \right) \right] \\
&+ \frac{\Re E_{opt,cont}}{2\tau_{transit}} \left[ \operatorname{erf} \left( \frac{t}{\sqrt{2}\sigma} \right) - \operatorname{erf} \left( \frac{t - \frac{S+W}{2v}}{\sqrt{2}\sigma} \right) \right] \\
&= \frac{\Re K_{AC} E_{opt,cont}}{2\tau_{transit}} e^{\sigma^2/2\tau_R^2} e^{-t/\tau_R} \left[ 1 + \operatorname{erf} \left( \frac{t}{\sqrt{2}\sigma} - \frac{\sigma}{\sqrt{2}\tau_R} \right) \right] \\
&+ \frac{\Re E_{opt,cont}}{2\tau_{transit}} \left[ \operatorname{erf} \left( \frac{t}{\sqrt{2}\sigma} \right) - \operatorname{erf} \left( \frac{t - \frac{S+W}{2v}}{\sqrt{2}\sigma} \right) \right] \\
&= \frac{\Re E_{opt,cont}}{2\tau_{transit}} \left\{ \left[ K_{AC} e^{\sigma^2/2\tau_R^2} e^{-t/\tau_R} \left[ 1 + \operatorname{erf} \left( \frac{t}{\sqrt{2}\sigma} - \frac{\sigma}{\sqrt{2}\tau_R} \right) \right] \right] \right. \\
&\quad \left. + \left[ \operatorname{erf} \left( \frac{t}{\sqrt{2}\sigma} \right) - \operatorname{erf} \left( \frac{t - \frac{S+W}{2v}}{\sqrt{2}\sigma} \right) \right] \right\}
\end{aligned}$$

I don't see any practical way to calculate the value of  $K_{AC}$  from first principles. I believe it will have to be extracted from fitting the data. I suspect that  $K_{AC}$  will vary with polysilicon grain size, and thus the deposition conditions.

## References

- [1] G. J. Korsh and R. S. Muller, "Conduction Properties of Lightly Doped, Polycrystalline Silicon," *Sol. St. Elect.*, vol. 21, pp. 1045-1051, 1978.
- [2] S. F. Soares, "Photoconductive Gain in a Schottky-Barrier Photodiode," *Jpn. J. Appl. Phys. Pt. 1*, vol. 31, pp. 210-216, 1992.
- [3] M. Klingenstein, J. Kuhl, J. Rosenzweig, C. Moglestue, A. Hulsmann, J. Schneider, et al., "Photocurrent Gain Mechanisms in Metal-Semiconductor-Metal Photodetectors," *Sol. St. Elect.*, vol. 37, pp. 333-340, 1994.
- [4] J. Burm and L. F. Eastman, "Low-Frequency Gain in MSM Photodiodes Due to Charge Accumulation and Image Force Lowering," *IEEE Phot. Tech. Lett.*, vol. 8, pp. 113-115, 1996.
- [5] R. Pownall, G. Yuan, T. W. Chen, P. Nikkel, and K. L. Lear, "Geometry dependence of CMOS-compatible, polysilicon, leaky-mode photodetectors," *IEEE Phot. Tech. Lett.*, vol. 19, pp. 513-515, 2007.

## *Appendix B*

### FIRST-GENERATION OPTICAL TEST CHIP DOCUMENTATION

This document was created from a combination of examination of the first-generation artwork and direct observation of the die. I would like to acknowledge Adrienne Iguchi for her assistance in creating this document.

There are two main types of detectors on this test die. The first type consists of detectors placed around the perimeter of the die, with waveguides leading from the edge of the die to the detector. The second type consists of vertical incidence interdigitated finger metal-semiconductor-metal detectors. For brevity, the first type is referred to as an “edge-coupled waveguide detector” while the second type is referred to as an “MSM detector”.

# 1 Edge-coupled waveguide detectors

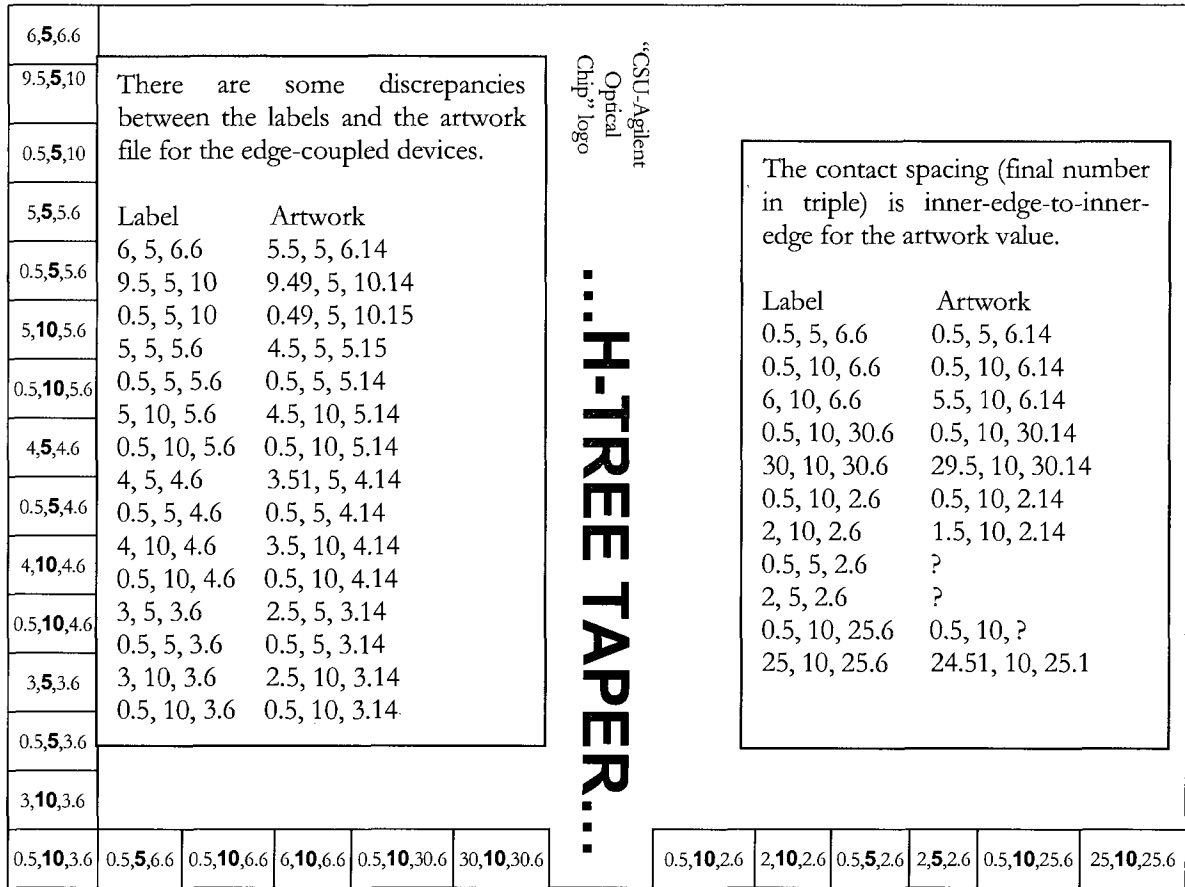


Figure 1: Location map for first-generation edge-coupled waveguide detectors. The waveguide for the 0.5,10,3.6 device goes left.. MSM detectors are in the area above this map, with more MSM detectors in the area to the right of this map and waveguide bend structures further to the right.

Note that the edge-coupled waveguide detector numeric values are in triples

- 1.The first number is the waveguide width.
- 2.The second number is the polysilicon length**
- 3.The third number is the contact spacing

The only reason the second (middle) number is in a different font is to make it easier to identify the individual numeric values in the triple. (A visual cue, if you will.) A typical layout of an edge-coupled waveguide detector is shown in Figure 2.

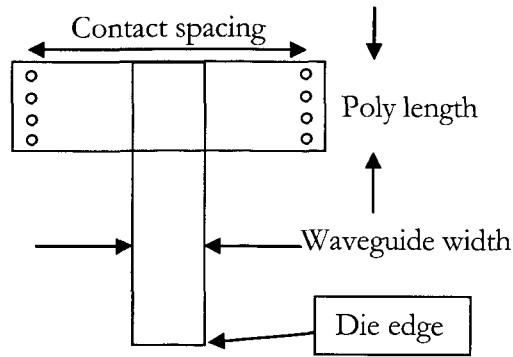


Figure 2: Top view of a typical edge-coupled waveguide detector, with waveguide width  $W$ , polysilicon length  $L$  and contact spacing  $S$  defined.

## 2 MSM detectors

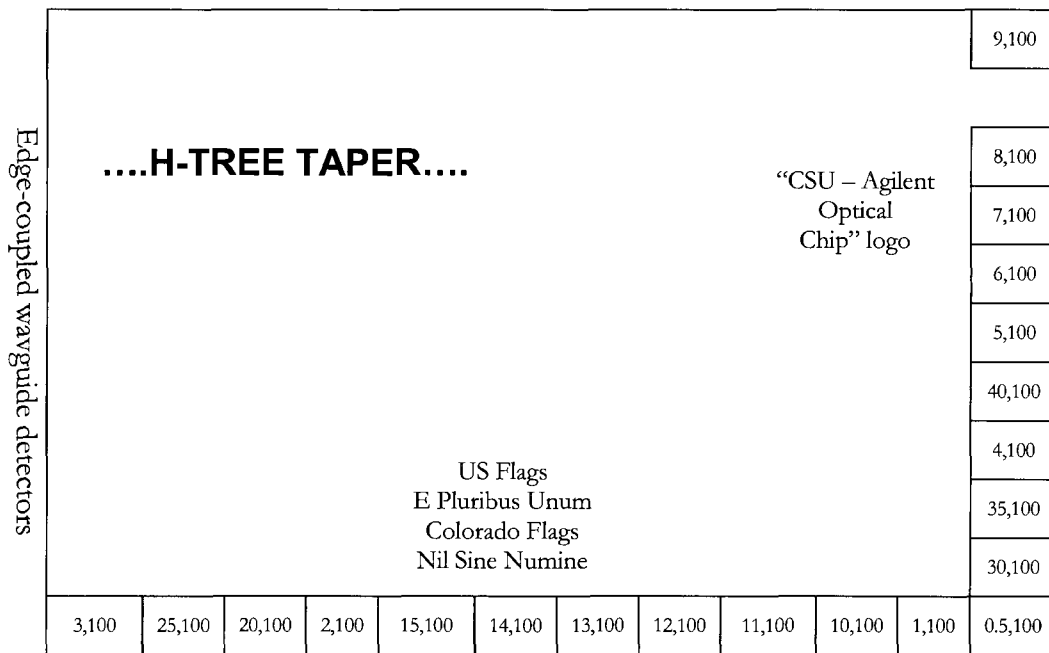


Figure 3: Location map for MSM detectors. Note that the orientation for this map is not the same as the orientation for Figure 1. The edge-coupled waveguide detectors are in the area above this map, with more MSM detectors in the area to the right of this map. Waveguide bend structures are in the areas below and to the right of the area shown in this map. Figure 4 is in the area to the right of this map.

Note that the MSM numeric values are in pairs. The first number is the finger spacing. The second number is the poly length.

### 3 More MSM and Edge-Coupled Waveguide Detectors

	..... Waveguides bend structures.....					0.5, <b>10</b> ,10.6
9,100						10, <b>10</b> ,10.6
						0.5, <b>5</b> ,10.6
8,100						10, <b>5</b> ,10.6
7,100						
6,100						
5,100						0.5, <b>10</b> ,15.6
40,100		2.5,100	5,100	20,100	40,100	15, <b>10</b> ,15.6
4,100		10,100	1,100	1,100	2,10	0.5, <b>10</b> ,20.6
35,100				0.5,10	1,10	20, <b>10</b> ,20.6
30,100						
0.5,100						

Figure 4: Location map for additional MSM and edge-coupled waveguide detectors. Note that the MSM devices shown on the right of Figure 3 are shown on the left of this map. The waveguide bend structures shown near the left of this map continue in the area below and to the left of the area shown in this map.

As before, numeric values in pairs indicate MSM detectors while numeric values in triples indicate edge-coupled waveguide detectors.

### 4 Waveguide bend structures

There are five sets of 90-degree bend structures, with nominal bend radii of 10  $\mu\text{m}$ , 20  $\mu\text{m}$ , 25  $\mu\text{m}$ , 50  $\mu\text{m}$  and 100  $\mu\text{m}$  as you go from the inner part of the die towards the outer part of the die. Each set of 90-degree bend structures consists of five waveguides, with nominal widths of 0.50  $\mu\text{m}$ , 1  $\mu\text{m}$ , 2  $\mu\text{m}$ , 4  $\mu\text{m}$  and 8  $\mu\text{m}$ , as you go from the inner part of the die towards the outer part of the die. Actual drawn bend radius and waveguide width may vary from the nominal width, however this was not checked.

SECOND-GENERATION OPTICAL TEST CHIP DOCUMENTATION

This document was created from a combination of examination of the second-generation artwork and direct observation of the die.

There are two main types of detectors on this test die. The first type consists of detectors placed around the perimeter of the die, with waveguides leading from the edge of the die to the detector. The second type consists of interdigitated finger metal-semiconductor-metal detectors. For brevity, the first type is referred to as an “edge-coupled waveguide detector” while the second type is referred to as an “MSM detector”.

1 Edge-Coupled Waveguide Detectors and MSM Detectors

1.1 Overview

		0.5,40,2.6	4,10,(1,10)	0.5,10,(1,10)	0.5,5,1.6	0.5,10,0.68	0.5,10,0.8	0.5,10,0.9	0.5,10,1.6	0.5,5,0.68	0.5,5,0.8
0.5,10,4.14				3,100			25,100				40,100
4,10,4.64	VDD D				20,100	6,100	5,100				VDD A
0.5,5,4.14					2,100						4,100
4,5,4.64			Small H-tree		15,100						
0.5,5,0.9		11,100	12,100	13,100	14,100	9,100					
		Large H-tree									
2,10,2.64					8,100						
0.5,5,2.14					VDP	35,100	30,100	10,100			
2,5,2.64	GND D		Small H-tree				7,100	GND A			
0.5,10,2.14					VDP		1,100	0.5,100			

Figure 1: Location map of edge-couple waveguide detectors and MSM detectors

The device locations in the interior of the die are approximate, as devices aren't laid out on a nice grid.

Note that the edge-coupled waveguide photodetector numeric values are in triples

1. The first number is the waveguide width.
2. **The second number is the poly detector length**
3. The third number is the contact spacing (inner-edge to inner-edge, not center-to-center)

The only reason the second (middle) number is in a different font is to make it easier to identify the individual numeric values in the triple. (A visual cue, if you will.)

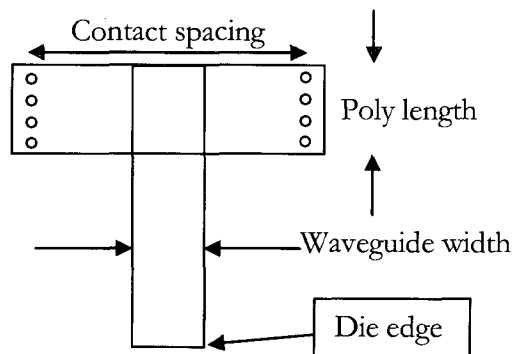


Figure 2: Top view of edge-coupled waveguide detector

The number pairs (e.g. 13,100) represent the vertical-incidence MSM photodetectors. The first number is the finger spacing; the second is the poly length.

In the location map, the letters “VDP” indicate a Van Der Pauw sheet resistance measurement structure. The letters “VDD A” and “GND A” indicate analog circuitry  $V_{DD}$  and ground pads, respectively. Similarly, the letters “VDD D” and “GND D” indicate digital circuitry  $V_{DD}$  and ground pads, respectively. The other labels are self-explanatory.

## 1.2 Specific edge-coupled waveguide detectors

The overall pad size for all pads is  $315\ \mu\text{m}$  in the direction perpendicular to the edge of the die and  $380\ \mu\text{m}$  in the direction parallel to the edge of the die. The center pad is  $215\ \mu\text{m}$  in the direction perpendicular to the edge of the die and  $80\ \mu\text{m}$  in the direction parallel to the edge of the die. The gap between the center pad and the outside pad on the long side of the center pad

is 20.5  $\mu\text{m}$  on one side and 20.0  $\mu\text{m}$  on the other. There is a 37.5  $\mu\text{m}$  gap on the short side of the center pad between the center pad and the outside pad. All pads are suitable for either needle probes or high-speed ground-signal-ground (GSG) probes.

If there are multiple repeated structures in the edge-coupled waveguide detectors which appear identical, I assume they are identical, and I've only measured one. In particular, I've only measured one pad.

In addition, many of the waveguides used with the edge-coupled waveguide detectors involve bends. It's a little difficult to decide exactly when a bend starts and stops, so the lengths of the waveguides leading to and from the bends may be off by a few microns.

Directions (north, south, east and west) on the chip are defined by a north arrow on the die near the 2,10,2.64 and 0.5,5,0.9 devices. However, from a naked-eye view, it's easier to orient the die by noting that the biosensor structures are on the east side of the die.

This device listing starts in the southwest corner of the die, heads north along the west edge, then east across the north edge. A summary table of all devices is at the end of the text descriptions.

### *1.2.1 0.5,10,2.14 device*

The input waveguide is 0.49  $\mu\text{m}$  wide at the start and comes in to the detector from behind. The input waveguide is 575  $\mu\text{m}$  long to the first bend. The first bend is a quarter-circle with a radius of curvature of 100  $\mu\text{m}$ . From the end of the first bend to the start of the second bend is 88  $\mu\text{m}$ . The second bend also is a quarter-circle with a radius of curvature of 100  $\mu\text{m}$ . From the end of the second bend to the start of the detector poly region is 46  $\mu\text{m}$ . Therefore, the total waveguide length to the detector is 1023  $\mu\text{m}$ , although this will vary some with edge polishing.

The detector itself has a 0.5  $\mu\text{m}$  wide waveguide, a 10  $\mu\text{m}$  long poly region, and contact spacing of 2.14  $\mu\text{m}$  edge-to-edge, matching the label. Metal-1 to metal-1 spacing is 1.82  $\mu\text{m}$ . The waveguide is centered between the contacts, with 0.66  $\mu\text{m}$  from the inner edge of the

contact to the edge of the waveguide. The waveguide ends at the edge of the polysilicon region.

### *1.2.2 2,5,2.64 device*

The input waveguide is 2  $\mu\text{m}$  wide and comes in to the detector from behind. The input waveguide is 571  $\mu\text{m}$  long to the first bend. The first bend is a quarter-circle with a radius of curvature of 100  $\mu\text{m}$ . From the end of the first bend to the start of the second bend is 82  $\mu\text{m}$ . The second bend also is a quarter-circle with a radius of curvature of 100  $\mu\text{m}$ . From the end of the second bend to the start of the detector poly region is 59  $\mu\text{m}$ . Therefore, the total waveguide length to the detector is 1026  $\mu\text{m}$ , although this will vary some with edge polishing.

The detector itself has a 2  $\mu\text{m}$  wide waveguide, a 5  $\mu\text{m}$  long poly region, and contact spacing of 2.64  $\mu\text{m}$  edge-to-edge, matching the label. Metal-1 to metal-1 spacing is 2.32  $\mu\text{m}$ . The waveguide is centered between the contacts, with 0.32  $\mu\text{m}$  from the inner edge of the contact to the edge of the waveguide. The waveguide ends at the edge of the polysilicon region.

The entrance waveguide to the lower small H-tree is just to the north of the 2,5,2.64 device.

### *1.2.3 0.5,5,2.14 device*

The input waveguide is 0.49  $\mu\text{m}$  wide at the start and comes in to the detector from behind. The input waveguide is 574  $\mu\text{m}$  long to the first bend. The first bend is a quarter-circle with a radius of curvature of 100  $\mu\text{m}$ . From the end of the first bend to the start of the second bend is 87  $\mu\text{m}$ . The second bend also is a quarter-circle with a radius of curvature of 100  $\mu\text{m}$ . From the end of the second bend to the start of the detector poly region is 46  $\mu\text{m}$ . Therefore, the total waveguide length to the detector is 1021  $\mu\text{m}$ , although this will vary some with edge polishing.

The detector itself has a 0.5  $\mu\text{m}$  wide waveguide, a 5  $\mu\text{m}$  long poly region, and contact spacing of 2.14  $\mu\text{m}$  edge-to-edge, matching the label. Metal-1 to metal-1 spacing is 1.82  $\mu\text{m}$ . The waveguide is centered between the contacts, with 0.82  $\mu\text{m}$  from the inner edge of the contact to the edge of the waveguide. The waveguide ends at the edge of the polysilicon region.

The entrance waveguide to the lower small H-tree is just to the south of the 0.5,5,2.14 device.

#### *1.2.4 2,10,2.64 device*

The input waveguide is 2  $\mu\text{m}$  wide and comes in to the detector from behind. The input waveguide is 562  $\mu\text{m}$  long to the first bend. The first bend is a quarter-circle with a radius of curvature of 100  $\mu\text{m}$ . From the end of the first bend to the start of the second bend is 82  $\mu\text{m}$ . The second bend also is a quarter-circle with a radius of curvature of 100  $\mu\text{m}$ . From the end of the second bend to the start of the detector poly region is 51  $\mu\text{m}$ . Therefore, the total waveguide length to the detector is 1009  $\mu\text{m}$ , although this will vary some with edge polishing.

The detector itself has a 2  $\mu\text{m}$  wide waveguide, a 10 $\mu\text{m}$  long poly region, and contact spacing of 2.64  $\mu\text{m}$  edge-to-edge, matching the label. Metal-1 to metal-1 spacing is 2.48  $\mu\text{m}$ . The waveguide is centered between the contacts, with 0.32  $\mu\text{m}$  from the inner edge of the contact to the edge of the waveguide. The waveguide ends at the edge of the polysilicon region.

For some reason, there are no contacts in the last 2.67  $\mu\text{m}$  of the device.

The entrance waveguide to the large H-tree is about 500  $\mu\text{m}$  north of the 2,10,2.64 device.

#### *1.2.5 0.5,5,0.9 device*

The input waveguide is 0.50  $\mu\text{m}$  wide at the start and comes straight in to the detector. From the start of the waveguide to the start of the detector poly region is 333  $\mu\text{m}$ .

The detector itself has a 0.5  $\mu\text{m}$  wide waveguide, a 5  $\mu\text{m}$  long poly region, and contact spacing of 0.9  $\mu\text{m}$  edge-to-edge, matching the label. Metal-1 to metal-1 spacing is 0.58  $\mu\text{m}$ . The waveguide is centered between the contacts, with 0.20  $\mu\text{m}$  from the inner edge of the contact to the edge of the waveguide. The waveguide ends at the edge of the polysilicon region.

The entrance waveguide to the large H-tree is about 67  $\mu\text{m}$  south of the 0.5,5,0.9 device.

### 1.2.6 4,5,4.64 device

The input waveguide is 4  $\mu\text{m}$  wide and comes in to the detector from behind. The input waveguide is 571  $\mu\text{m}$  long to the first bend. The first bend is a quarter-circle with a radius of curvature of 100  $\mu\text{m}$ . From the end of the first bend to the start of the second bend is 82  $\mu\text{m}$ . The second bend also is a quarter-circle with a radius of curvature of 100  $\mu\text{m}$ . From the end of the second bend to the start of the detector poly region is 44  $\mu\text{m}$ . Therefore, the total waveguide length to the detector is 1011  $\mu\text{m}$ , although this will vary some with edge polishing.

The detector itself has a 4.03  $\mu\text{m}$  wide waveguide, a 5  $\mu\text{m}$  long poly region, and contact spacing of 4.67  $\mu\text{m}$  edge-to-edge. Thus, **THIS DEVICE DOES NOT QUITE MATCH ITS LABEL!** (The difference probably is not significant, though.) Metal-1 to metal-1 spacing is 4.35  $\mu\text{m}$ . The waveguide is centered between the contacts, with 0.32  $\mu\text{m}$  from the inner edge of the contact to the edge of the waveguide. The waveguide ends at the edge of the polysilicon region.

### 1.2.7 0.5,5,4.14 device

The input waveguide is 0.49  $\mu\text{m}$  wide at the start and comes in to the detector from behind. The input waveguide is 574  $\mu\text{m}$  long to the first bend. The first bend is a quarter-circle with a radius of curvature of 100  $\mu\text{m}$ . From the end of the first bend to the start of the second bend is 87  $\mu\text{m}$ . The second bend also is a quarter-circle with a radius of curvature of 100  $\mu\text{m}$ . From the end of the second bend to the start of the detector poly region is 46  $\mu\text{m}$ . Therefore, the total waveguide length to the detector is 1021  $\mu\text{m}$ , although this will vary some with edge polishing.

The detector itself has a 0.5  $\mu\text{m}$  wide waveguide, a 5  $\mu\text{m}$  long poly region, and contact spacing of 4.14  $\mu\text{m}$  edge-to-edge, matching the label. Metal-1 to metal-1 spacing is 3.82  $\mu\text{m}$ . The waveguide is centered between the contacts, with 1.82  $\mu\text{m}$  from the inner edge of the contact to the edge of the waveguide. The waveguide ends at the edge of the polysilicon region.

The entrance to the upper small H-tree is approx. 124  $\mu\text{m}$  north of the pads for the 0.5,5,4.14 device.

#### *1.2.8 4,10,4.64 device*

The input waveguide is 4  $\mu\text{m}$  wide and comes in to the detector from behind. The input waveguide is 573  $\mu\text{m}$  long to the first bend. The first bend is a quarter-circle with a radius of curvature of 100  $\mu\text{m}$ . From the end of the first bend to the start of the second bend is 82  $\mu\text{m}$ . The second bend also is a quarter-circle with a radius of curvature of 100  $\mu\text{m}$ . From the end of the second bend to the start of the detector poly region is 46  $\mu\text{m}$ . Therefore, the total waveguide length to the detector is 1015  $\mu\text{m}$ , although this will vary some with edge polishing.

The detector itself has a 4  $\mu\text{m}$  wide waveguide, a 10  $\mu\text{m}$  long poly region, and contact spacing of 4.64  $\mu\text{m}$  edge-to-edge, matching the label. Metal-1 to metal-1 spacing is 4.32  $\mu\text{m}$ . The waveguide is centered between the contacts, with 0.32  $\mu\text{m}$  from the inner edge of the contact to the edge of the waveguide. The waveguide ends at the edge of the polysilicon region.

The entrance to the upper small H-tree is approximately 98  $\mu\text{m}$  south of the pads for the 4,10,4.64 device.

#### *1.2.9 0.5,10,4.14 device*

This is the northern-most device on the west side of the die.

The entrance waveguide is 0.49  $\mu\text{m}$  wide at the start and comes in to the detector from behind. The input waveguide is 572  $\mu\text{m}$  long to the first bend. The first bend is a quarter-circle with a radius of curvature of 100  $\mu\text{m}$ . From the end of the first bend to the start of the second bend is 87  $\mu\text{m}$ . The second bend also is a quarter-circle with a radius of curvature of 100  $\mu\text{m}$ . From the end of the second bend to the start of the detector poly region is 46  $\mu\text{m}$ . Therefore, the total waveguide length to the detector is 1019  $\mu\text{m}$ , although this will vary some with edge polishing.

The detector itself has a 0.50  $\mu\text{m}$  wide waveguide, a 10  $\mu\text{m}$  long poly region, and contact spacing of 4.14  $\mu\text{m}$  edge-to-edge, matching the label. Metal-1 to metal-1 spacing is 3.82  $\mu\text{m}$ . The waveguide is centered between the contacts, with 1.82  $\mu\text{m}$  from the inner edge of the contact to the edge of the waveguide. The waveguide ends at the edge of the polysilicon region.

#### *1.2.10 0.5,40,2.6 device*

This is the western-most device on the north side of the die.

The entrance waveguide is 0.50  $\mu\text{m}$  wide at the start and comes straight in to the detector. From the start of the waveguide to the start of the detector poly region is 328  $\mu\text{m}$ , although this will vary some with edge polishing.

The detector itself has a 0.50  $\mu\text{m}$  wide waveguide, a 40 $\mu\text{m}$  long poly region, and contact spacing of 2.60  $\mu\text{m}$  edge-to-edge, matching the label. Metal-1 to metal-1 spacing is 1.72  $\mu\text{m}$ . The waveguide is slightly asymmetrically placed between the contacts, with 1.07  $\mu\text{m}$  from the inner edge of the contact to the edge of the waveguide on the east side, and 1.03  $\mu\text{m}$  on the west side. The waveguide ends at the edge of the polysilicon region.

#### *1.2.11 4,10,[1,10] device*

The entrance waveguide is 4.0  $\mu\text{m}$  wide and comes straight in to the detector. From the start of the waveguide to the start of the detector poly region is 357  $\mu\text{m}$ , although this will vary some with edge polishing.

The detector itself has a 4.0  $\mu\text{m}$  wide waveguide, a 10.0  $\mu\text{m}$  long poly region, and asymmetric contact spacing of 10.0  $\mu\text{m}$  edge-to-waveguide on the east side and 1.0  $\mu\text{m}$  on the west side, matching the label. Metal-1 to metal-1 spacing is 14.68  $\mu\text{m}$ . Note that the waveguide is highly asymmetrically placed between the contacts. Contacts are enclosed by 0.18  $\mu\text{m}$  of metal on the west, and by 0.14  $\mu\text{m}$  on the east. The waveguide ends at the edge of the polysilicon region.

### *1.2.12 0.5,10,[1,10] device*

The entrance waveguide is 0.50  $\mu\text{m}$  wide and comes straight in to the detector. From the start of the waveguide to the start of the detector poly region is 355  $\mu\text{m}$ , although this will vary some with edge polishing.

The detector itself has a 0.5  $\mu\text{m}$  wide waveguide, a 10.0  $\mu\text{m}$  long poly region, and asymmetric contact spacing of 10.0  $\mu\text{m}$  edge-to-waveguide on the east side and 1.05  $\mu\text{m}$  on the west side, (essentially) matching the label. Metal-1 to metal-1 spacing is 11.23  $\mu\text{m}$ . Note that the waveguide is highly asymmetrically placed between the contacts. Contacts are enclosed by 0.21  $\mu\text{m}$  of metal on the west, and by 0.11  $\mu\text{m}$  on the east. The waveguide ends at the edge of the polysilicon region.

### *1.2.13 0.5,5,1.6 device*

The entrance waveguide is 0.5  $\mu\text{m}$  wide at the start and comes straight in to the detector. From the start of the waveguide to the start of the detector poly region is 356  $\mu\text{m}$ , although this will vary some with edge polishing.

The detector itself has a 0.50  $\mu\text{m}$  wide waveguide, a 5  $\mu\text{m}$  long poly region, and contact spacing of 1.60  $\mu\text{m}$  edge-to-edge, matching the label. Metal-1 to metal-1 spacing is 1.28  $\mu\text{m}$ . The waveguide is slightly asymmetrically placed between the contacts, with 0.57  $\mu\text{m}$  from the inner edge of the contact to the edge of the waveguide on the east side, and 0.53  $\mu\text{m}$  on the west side. The waveguide ends at the edge of the polysilicon region.

### *1.2.14 0.5,10,0.68 device*

The entrance waveguide is 0.50  $\mu\text{m}$  wide at the start and comes straight in to the detector. From the start of the waveguide to the start of the detector poly region is 360  $\mu\text{m}$ , although this will vary some with edge polishing.

The detector itself has a 0.50  $\mu\text{m}$  wide waveguide, a 10  $\mu\text{m}$  long poly region, and contact spacing of 0.68  $\mu\text{m}$  edge-to-edge, matching the label. Metal-1 to metal-1 spacing is 0.36  $\mu\text{m}$ . The waveguide is symmetrically placed between the contacts, with 0.09  $\mu\text{m}$  from the inner

edge of the contact to the edge of the waveguide on both sides. The waveguide ends at the edge of the polysilicon region.

#### *1.2.15 0.5,10,0.8 device*

The entrance waveguide is 0.50  $\mu\text{m}$  wide at the start and comes straight in to the detector. From the start of the waveguide to the start of the detector poly region is 360  $\mu\text{m}$ , although this will vary some with edge polishing.

The detector itself has a 0.50  $\mu\text{m}$  wide waveguide, a 10.0  $\mu\text{m}$  long poly region, and contact spacing of 0.80  $\mu\text{m}$  edge-to-edge, matching the label. Metal-1 to metal-1 spacing is 0.48  $\mu\text{m}$ . The waveguide is symmetrically placed between the contacts, with 0.15  $\mu\text{m}$  from the inner edge of the contact to the edge of the waveguide on both sides. The waveguide ends at the edge of the polysilicon region.

#### *1.2.16 0.5,10,0.9 device*

The entrance waveguide is 0.50  $\mu\text{m}$  wide at the start and comes straight in to the detector. From the start of the waveguide to the start of the detector poly region is 360  $\mu\text{m}$ , although this will vary some with edge polishing.

The detector itself has a 0.50  $\mu\text{m}$  wide waveguide, a 10.0  $\mu\text{m}$  long poly region, and contact spacing of 0.90  $\mu\text{m}$  edge-to-edge, matching the label. Metal-1 to metal-1 spacing is 0.58  $\mu\text{m}$ . The waveguide is symmetrically placed between the contacts, with 0.20  $\mu\text{m}$  from the inner edge of the contact to the edge of the waveguide on both sides. The waveguide ends at the edge of the polysilicon region.

#### *1.2.17 0.5,10,1.6 device*

The entrance waveguide is 0.50  $\mu\text{m}$  wide at the start and comes straight in to the detector. From the start of the waveguide to the start of the detector poly region is 362  $\mu\text{m}$ , although this will vary some with edge polishing.

The detector itself has a 0.50  $\mu\text{m}$  wide waveguide, a 10.0  $\mu\text{m}$  long poly region, and contact spacing of 1.60  $\mu\text{m}$  edge-to-edge, matching the label. Metal-1 to metal-1 spacing is 1.28  $\mu\text{m}$ . The waveguide is almost symmetrically placed between the contacts, with 0.56  $\mu\text{m}$  from the inner edge of the contact to the edge of the waveguide on one side and 0.54  $\mu\text{m}$  on the other. The waveguide ends at the edge of the polysilicon region.

#### *1.2.18 0.5,5,0.68 device*

The entrance waveguide is 0.50  $\mu\text{m}$  wide at the start and comes straight in to the detector. From the start of the waveguide to the start of the detector poly region is 362  $\mu\text{m}$ , although this will vary some with edge polishing.

The detector itself has a 0.50  $\mu\text{m}$  wide waveguide, a 5.0  $\mu\text{m}$  long poly region, and contact spacing of 0.68  $\mu\text{m}$  edge-to-edge, matching the label. Metal-1 to metal-1 spacing is 0.36  $\mu\text{m}$ . The waveguide is symmetrically placed between the contacts, with 0.09  $\mu\text{m}$  from the inner edge of the contact to the edge of the waveguide on both sides. The waveguide ends at the edge of the polysilicon region.

#### *1.2.19 0.5,5,0.8 device*

This is the easternmost device on the north side of the die.

The entrance waveguide is 0.50  $\mu\text{m}$  wide at the start and comes straight in to the detector. From the start of the waveguide to the start of the detector poly region is 354  $\mu\text{m}$ .

The detector itself has a 0.50  $\mu\text{m}$  wide waveguide, a 5.0  $\mu\text{m}$  long poly region, and contact spacing of 0.80  $\mu\text{m}$  edge-to-edge, matching the label. Metal-1 to metal-1 spacing is 0.48  $\mu\text{m}$ . The waveguide is symmetrically placed between the contacts, with 0.15  $\mu\text{m}$  from the inner edge of the contact to the edge of the waveguide on both sides. The waveguide ends at the edge of the polysilicon region.

#### *1.2.20 Summary of all edge-coupled waveguide devices*

Detector			Input waveguide		U-bend?	M1 to M1 spacing	WG to contact spacing
WG width	Poly length	Contact spacing	Width	Length			
0.5	10	2.14	0.49	1023	Y	1.82	0.66
2	5	2.64	2	1026	Y	2.32	0.32
0.5	5	2.14	0.49	1021	Y	1.82	0.82
2	10	2.64	2	1009	Y	2.48	0.32
0.5	5	0.9	0.50	333	N	0.58	0.20
4.03 [4]	5	4.67 [4.64]	4	1011	Y	4.35	0.32
0.5	5	4.14	0.49	1021	Y	3.82	1.82
4	10	4.64	4	1015	Y	4.32	0.32
0.5	10	4.14	0.49	1019	Y	3.82	1.82
0.5	40	2.60	0.5	328	N	1.72	1.07/1.03
4.0	10.0	15.0	4.0	357	N	14.68	1.0 / 10.0
0.5	10.0	11.55 [11.5]	0.50	355	N	11.23	1.05/10.0
0.50	5	1.60	0.5	356	N	1.28	0.57/0.53
0.5	10	0.68	0.5	360	N	0.36	0.09
0.50	10.0	0.80	0.50	360	N	0.48	0.15
0.50	10.0	0.90	0.50	360	N	0.58	0.20
0.50	10.0	1.60	0.50	362	N	1.28	0.56/0.54
0.50	5.0	0.68	0.50	362	N	0.36	0.09
0.50	5.0	0.80	0.50	354	N	0.48	0.15

### 1.3 Specific MSM detectors

#### 1.3.1 0.5,100 device

Pads are compatible with GSG probing, which should be done from the north or south. Overall pad size is 396.5  $\mu\text{m}$  (EW) x 328.5  $\mu\text{m}$  (NS). Center pad is 80  $\mu\text{m}$  (EW) by 98  $\mu\text{m}$  (NS). Poly region is 107.8  $\mu\text{m}$  (EW) by 100.2  $\mu\text{m}$  (NS). Contact spacing is 0.68  $\mu\text{m}$  (inside edge to inside edge). [Note that device label implies 0.50  $\mu\text{m}$  contact spacing.] Contacts are 0.32  $\mu\text{m}$  by 0.32  $\mu\text{m}$ . Finger width is 0.64  $\mu\text{m}$ . Fingers coming from the south extend  $\sim$ 0.35  $\mu\text{m}$  past the edge of the poly. Fingers coming from the north are  $\sim$ 0.09  $\mu\text{m}$  short of extending to the edge of the poly. These values imply finger lengths of 100.1 to 100.2  $\mu\text{m}$ .

An artwork error causes the fingers coming south from the outer, U-shaped pad to be  $\sim$ 0.65  $\mu\text{m}$  short of reaching the pad. See Figure 3. Oops. (Figure 3 is a screen capture from Visual Chip Inspector 2007 by Numerical Innovations.)

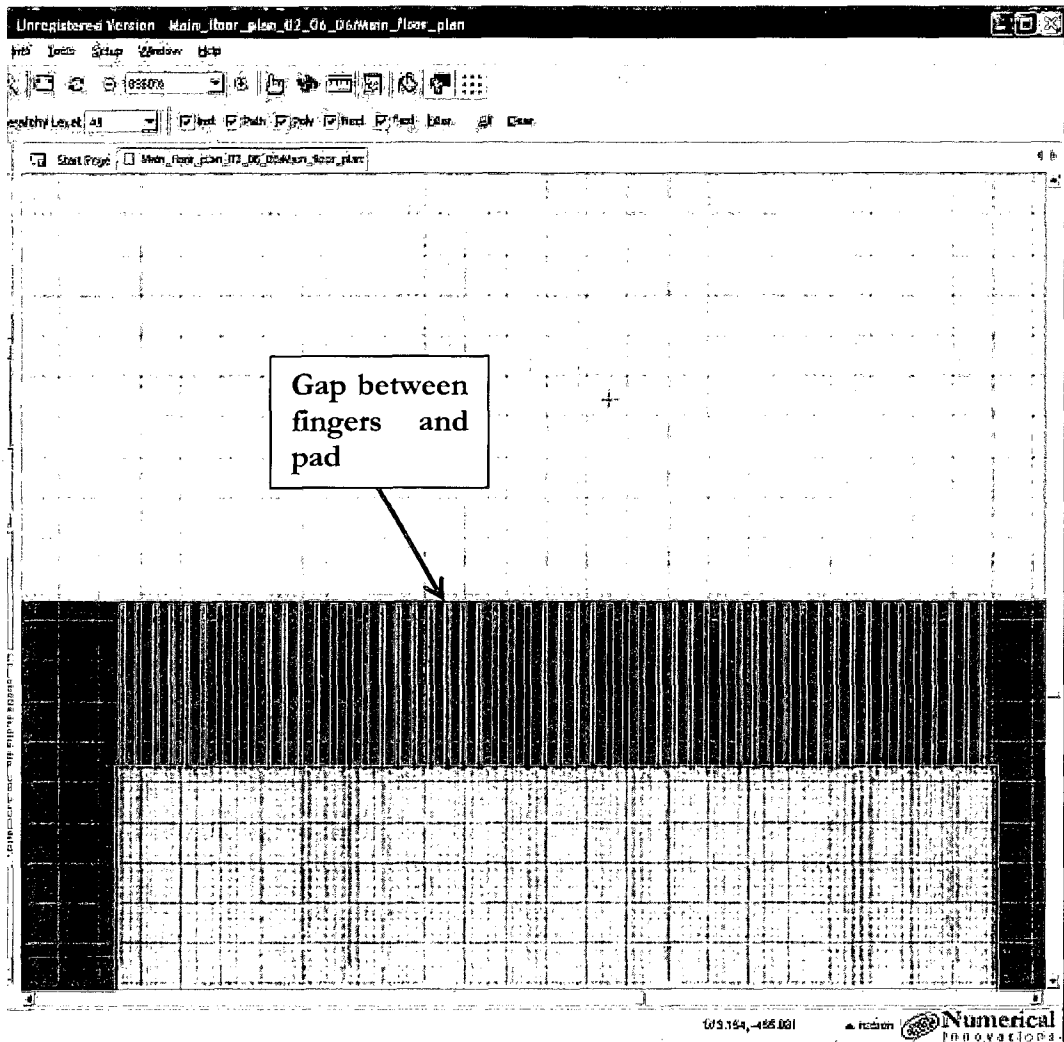


Figure 3: 0.5, 100 MSM device, showing that the fingers are not connected to the pad.

### 1.3.2 1,100 device

Pads are compatible with GSG probing, which should be done from the north or south. Overall pad size is  $396.5 \mu\text{m}$  (EW) x  $328.5 \mu\text{m}$  (NS). Center pad is  $80 \mu\text{m}$  (EW) by  $98 \mu\text{m}$  (NS). Poly region is  $107.8 \mu\text{m}$  (EW) by  $100.2 \mu\text{m}$  (NS). Contact spacing is  $1.00 \mu\text{m}$  (inside edge to inside edge). Contacts are  $0.32 \mu\text{m}$  by  $0.32 \mu\text{m}$ . Finger width is  $0.64 \mu\text{m}$ . Fingers coming from the south are  $\sim 0.06 \mu\text{m}$  short of extending to the edge of the poly. Fingers coming from the north are  $\sim 0.09 \mu\text{m}$  short of extending to the edge of the poly. These values imply finger lengths of  $100.1 \mu\text{m}$ .

### *1.3.3 2,100 device*

Pads are compatible with GSG probing, which should be done from the north or south. Overall pad size is 396.5  $\mu\text{m}$  (EW) x 328.5  $\mu\text{m}$  (NS). Center pad is 80  $\mu\text{m}$  (EW) by 98  $\mu\text{m}$  (NS). Poly region is 107.6  $\mu\text{m}$  (EW) by 100.2  $\mu\text{m}$  (NS). Contact spacing is 2.00  $\mu\text{m}$  (inside edge to inside edge). Contacts are 0.32  $\mu\text{m}$  by 0.32  $\mu\text{m}$ . Finger width is 0.64  $\mu\text{m}$ . Fingers coming from the south extend  $\sim$ 0.37  $\mu\text{m}$  past the edge of the poly. Fingers coming from the north are  $\sim$ 0.09  $\mu\text{m}$  short of extending to the edge of the poly. These values imply finger lengths of 100.1 to 100.2  $\mu\text{m}$ .

### *1.3.4 3,100 device*

Pads are compatible with GSG probing, which should be done from the north or south. Overall pad size is 396.5  $\mu\text{m}$  (EW) x 328.5  $\mu\text{m}$  (NS). Center pad is 80  $\mu\text{m}$  (EW) by 98  $\mu\text{m}$  (NS). Poly region is 110.4  $\mu\text{m}$  (EW) by 100.2  $\mu\text{m}$  (NS). Contact spacing is 3.00  $\mu\text{m}$  (inside edge to inside edge). Contacts are 0.32  $\mu\text{m}$  by 0.32  $\mu\text{m}$ . Finger width is 0.64  $\mu\text{m}$ . Fingers coming from the south extend  $\sim$ 0.37  $\mu\text{m}$  past the edge of the poly. Fingers coming from the north are  $\sim$ 0.09  $\mu\text{m}$  short of extending to the edge of the poly. These values imply finger lengths of 100.1 to 100.2  $\mu\text{m}$ .

### *1.3.5 4,100 device*

Pads are compatible with GSG probing, which should be done from the north or south. Overall pad size is 396.5  $\mu\text{m}$  (EW) x 328.5  $\mu\text{m}$  (NS). Center pad is 80  $\mu\text{m}$  (EW) by 98  $\mu\text{m}$  (NS). Poly region is 108.8  $\mu\text{m}$  (EW) by 100.2  $\mu\text{m}$  (NS). Contact spacing is 4.00  $\mu\text{m}$  (inside edge to inside edge). Contacts are 0.32  $\mu\text{m}$  by 0.32  $\mu\text{m}$ . Finger width is 0.64  $\mu\text{m}$ . Fingers coming from the south extend  $\sim$ 0.36  $\mu\text{m}$  past the edge of the poly. Fingers coming from the north are  $\sim$ 0.08  $\mu\text{m}$  short of extending to the edge of the poly. These values imply finger lengths of 100.1 to 100.2  $\mu\text{m}$ .

### *1.3.6 5,100 device*

Pads are compatible with GSG probing, which should be done from the north or south. Overall pad size is 396.5  $\mu\text{m}$  (EW) x 328.5  $\mu\text{m}$  (NS). Center pad is 80  $\mu\text{m}$  (EW) by 98  $\mu\text{m}$

(NS). Poly region is 112.6  $\mu\text{m}$  (EW) by 100.2  $\mu\text{m}$  (NS). Contact spacing is 5.00  $\mu\text{m}$  (inside edge to inside edge). Contacts are 0.32  $\mu\text{m}$  by 0.32  $\mu\text{m}$ . Finger width is 0.64  $\mu\text{m}$ . Fingers coming from the south are  $\sim 0.10$   $\mu\text{m}$  short of extending to the edge of the poly. Fingers coming from the north are  $\sim 0.09$   $\mu\text{m}$  short of extending to the edge of the poly. These values imply finger lengths of 100.1 to 100.2  $\mu\text{m}$ .

#### *1.3.7 6,100 device*

Pads are compatible with GSG probing, which should be done from the north or south. Overall pad size is 396.5  $\mu\text{m}$  (EW) x 328.5  $\mu\text{m}$  (NS). Center pad is 80  $\mu\text{m}$  (EW) by 98  $\mu\text{m}$  (NS). Poly region is 108.3  $\mu\text{m}$  (EW) by 100.2  $\mu\text{m}$  (NS). Contact spacing is 6.00  $\mu\text{m}$  (inside edge to inside edge). Contacts are 0.32  $\mu\text{m}$  by 0.32  $\mu\text{m}$ . Finger width is 0.64  $\mu\text{m}$ . Fingers coming from the south are  $\sim 0.06$   $\mu\text{m}$  short of extending to the edge of the poly. Fingers coming from the north are  $\sim 0.09$   $\mu\text{m}$  short of extending to the edge of the poly. These values imply finger lengths of 100.1 to 100.2  $\mu\text{m}$ .

#### *1.3.8 7,100 device*

Pads are compatible with GSG probing, which should be done from the north or south. Overall pad size is 396.5  $\mu\text{m}$  (EW) x 328.5  $\mu\text{m}$  (NS). Center pad is 80  $\mu\text{m}$  (EW) by 98  $\mu\text{m}$  (NS). Poly region is 110.6  $\mu\text{m}$  (EW) by 100.2  $\mu\text{m}$  (NS). Contact spacing is 7.00  $\mu\text{m}$  (inside edge to inside edge). Contacts are 0.32  $\mu\text{m}$  by 0.32  $\mu\text{m}$ . Finger width is 0.64  $\mu\text{m}$ . Fingers coming from the south are  $\sim 0.07$   $\mu\text{m}$  short of extending to the edge of the poly. Fingers coming from the north are  $\sim 0.09$   $\mu\text{m}$  short of extending to the edge of the poly. These values imply finger lengths of 100.1  $\mu\text{m}$ .

#### *1.3.9 8,100 device*

Pads are compatible with GSG probing, which should be done from the north or south. Overall pad size is 396.5  $\mu\text{m}$  (EW) x 328.5  $\mu\text{m}$  (NS). Center pad is 80  $\mu\text{m}$  (EW) by 98  $\mu\text{m}$  (NS). Poly region is 109.0  $\mu\text{m}$  (EW) by 100.2  $\mu\text{m}$  (NS). Contact spacing is 8.00  $\mu\text{m}$  (inside edge to inside edge). Contacts are 0.32  $\mu\text{m}$  by 0.32  $\mu\text{m}$ . Finger width is 0.64  $\mu\text{m}$ . Fingers coming from the south are  $\sim 0.07$   $\mu\text{m}$  short of extending to the edge of the poly. Fingers

coming from the north are  $\sim 0.09 \mu\text{m}$  short of extending to the edge of the poly. These values imply finger lengths of  $100.1 \mu\text{m}$ .

#### *1.3.10 9,100 device*

Pads are compatible with GSG probing, which should be done from the north or south. Overall pad size is  $396.5 \mu\text{m}$  (EW) x  $328.5 \mu\text{m}$  (NS). Center pad is  $80 \mu\text{m}$  (EW) by  $98 \mu\text{m}$  (NS). Poly region is  $103.4 \mu\text{m}$  (EW) by  $100.2 \mu\text{m}$  (NS). Contact spacing is  $9.00 \mu\text{m}$  (inside edge to inside edge). Contacts are  $0.32 \mu\text{m}$  by  $0.32 \mu\text{m}$ . Finger width is  $0.64 \mu\text{m}$ . Fingers coming from the south are  $\sim 0.05 \mu\text{m}$  short of extending to the edge of the poly. Fingers coming from the north are  $\sim 0.10 \mu\text{m}$  short of extending to the edge of the poly. These values imply finger lengths of  $100.1 \mu\text{m}$ .

#### *1.3.11 10,100 device*

Pads are compatible with GSG probing, which should be done from the north or south. Overall pad size is  $396.5 \mu\text{m}$  (EW) x  $328.5 \mu\text{m}$  (NS). Center pad is  $80 \mu\text{m}$  (EW) by  $98 \mu\text{m}$  (NS). Poly region is  $114.4 \mu\text{m}$  (EW) by  $100.2 \mu\text{m}$  (NS). Contact spacing is  $10.00 \mu\text{m}$  (inside edge to inside edge). Contacts are  $0.32 \mu\text{m}$  by  $0.32 \mu\text{m}$ . Finger width is  $0.64 \mu\text{m}$ . Fingers coming from the south are  $\sim 0.07 \mu\text{m}$  short of extending to the edge of the poly. Fingers coming from the north are  $\sim 0.09 \mu\text{m}$  short of extending to the edge of the poly. These values imply finger lengths of  $100.1 \mu\text{m}$ .

#### *1.3.12 11,100 device*

Pads are compatible with GSG probing, which should be done from the north or south. Overall pad size is  $396.5 \mu\text{m}$  (EW) x  $328.5 \mu\text{m}$  (NS). Center pad is  $80 \mu\text{m}$  (EW) by  $98 \mu\text{m}$  (NS). Poly region is  $102.7 \mu\text{m}$  (EW) by  $100.2 \mu\text{m}$  (NS). Contact spacing is  $11.00 \mu\text{m}$  (inside edge to inside edge). Contacts are  $0.32 \mu\text{m}$  by  $0.32 \mu\text{m}$ . Finger width is  $0.64 \mu\text{m}$ . Fingers coming from the south are  $\sim 0.06 \mu\text{m}$  short of extending to the edge of the poly. Fingers coming from the north are  $\sim 0.10 \mu\text{m}$  short of extending to the edge of the poly. These values imply finger lengths of  $100.1 \mu\text{m}$ .

### *1.3.13 12,100 device*

Pads are compatible with GSG probing, which should be done from the north or south. Overall pad size is 396.5  $\mu\text{m}$  (EW) x 328.5  $\mu\text{m}$  (NS). Center pad is 80  $\mu\text{m}$  (EW) by 98  $\mu\text{m}$  (NS). Poly region is 111.7  $\mu\text{m}$  (EW) by 100.2  $\mu\text{m}$  (NS). Contact spacing is 12.00  $\mu\text{m}$  (inside edge to inside edge). Contacts are 0.32  $\mu\text{m}$  by 0.32  $\mu\text{m}$ . Finger width is 0.64  $\mu\text{m}$ . Fingers coming from the south are  $\sim 0.06$   $\mu\text{m}$  short of extending to the edge of the poly. Fingers coming from the north are  $\sim 0.09$   $\mu\text{m}$  short of extending to the edge of the poly. These values imply finger lengths of 100.1  $\mu\text{m}$ .

An artwork error causes the fingers coming south from the outer, U-shaped pad to be  $\sim 1.42$   $\mu\text{m}$  short of reaching the pad. Oops. See the 0.5,100 device and Figure 3 for a picture of a similar situation.

### *1.3.14 13,100 device*

Pads are compatible with GSG probing, which should be done from the north or south. Overall pad size is 396.5  $\mu\text{m}$  (EW) x 328.5  $\mu\text{m}$  (NS). Center pad is 80  $\mu\text{m}$  (EW) by 98  $\mu\text{m}$  (NS). Poly region is 94.1  $\mu\text{m}$  (EW) by 100.2  $\mu\text{m}$  (NS). Contact spacing is 13.00  $\mu\text{m}$  (inside edge to inside edge). Contacts are 0.32  $\mu\text{m}$  by 0.32  $\mu\text{m}$ . Finger width is 0.64  $\mu\text{m}$ . Fingers coming from the south are  $\sim 0.07$   $\mu\text{m}$  short of extending to the edge of the poly. Fingers coming from the north are  $\sim 0.10$   $\mu\text{m}$  short of extending to the edge of the poly. These values imply finger lengths of 100.1  $\mu\text{m}$ .

### *1.3.15 14,100 device*

Pads are compatible with GSG probing, which should be done from the north or south. Overall pad size is 396.5  $\mu\text{m}$  (EW) x 328.5  $\mu\text{m}$  (NS). Center pad is 80  $\mu\text{m}$  (EW) by 98  $\mu\text{m}$  (NS). Poly region is 101.1  $\mu\text{m}$  (EW) by 100.2  $\mu\text{m}$  (NS). Contact spacing is 14.00  $\mu\text{m}$  (inside edge to inside edge). Contacts are 0.32  $\mu\text{m}$  by 0.32  $\mu\text{m}$ . Finger width is 0.64  $\mu\text{m}$ . Fingers coming from the south are  $\sim 0.05$   $\mu\text{m}$  short of extending to the edge of the poly. Fingers coming from the north are  $\sim 0.10$   $\mu\text{m}$  short of extending to the edge of the poly. These values imply finger lengths of 100.1  $\mu\text{m}$ .

#### *1.3.16 15,100 device*

Pads are compatible with GSG probing, which should be done from the north or south. Overall pad size is 396.5  $\mu\text{m}$  (EW) x 328.5  $\mu\text{m}$  (NS). Center pad is 80  $\mu\text{m}$  (EW) by 98  $\mu\text{m}$  (NS). Poly region is 108.1  $\mu\text{m}$  (EW) by 100.2  $\mu\text{m}$  (NS). Contact spacing is 15.00  $\mu\text{m}$  (inside edge to inside edge). Contacts are 0.32  $\mu\text{m}$  by 0.32  $\mu\text{m}$ . Finger width is 0.64  $\mu\text{m}$ . Fingers coming from the south are  $\sim 0.06$   $\mu\text{m}$  short of extending to the edge of the poly. Fingers coming from the north are  $\sim 0.10$   $\mu\text{m}$  short of extending to the edge of the poly. These values imply finger lengths of 100.1  $\mu\text{m}$ .

#### *1.3.17 20,100 device*

Pads are compatible with GSG probing, which should be done from the north or south. Overall pad size is 396.5  $\mu\text{m}$  (EW) x 328.5  $\mu\text{m}$  (NS). Center pad is 80  $\mu\text{m}$  (EW) by 98  $\mu\text{m}$  (NS). Poly region is 102.5  $\mu\text{m}$  (EW) by 100.2  $\mu\text{m}$  (NS). Contact spacing is 20.00  $\mu\text{m}$  (inside edge to inside edge). Contacts are 0.32  $\mu\text{m}$  by 0.32  $\mu\text{m}$ . Finger width is 0.64  $\mu\text{m}$ . Fingers coming from the south are  $\sim 0.07$   $\mu\text{m}$  short of extending to the edge of the poly. Fingers coming from the north are  $\sim 0.10$   $\mu\text{m}$  short of extending to the edge of the poly. These values imply finger lengths of 100.1  $\mu\text{m}$ .

An artwork error causes the fingers coming south from the outer, U-shaped pad to be  $\sim 0.07$   $\mu\text{m}$  short of reaching the pad. Oops. Since this is smaller than the process's minimum feature size, the gap may or may not result in an open circuit on the wafer. See the 0.5,100 device and Figure 3 for a picture of a similar situation.

#### *1.3.18 25,100 device*

Pads are compatible with GSG probing, which should be done from the north or south. Overall pad size is 396.5  $\mu\text{m}$  (EW) x 328.5  $\mu\text{m}$  (NS). Center pad is 80  $\mu\text{m}$  (EW) by 98  $\mu\text{m}$  (NS). Poly region is 102.2  $\mu\text{m}$  (EW) by 100.2  $\mu\text{m}$  (NS). Contact spacing is 25.00  $\mu\text{m}$  (inside edge to inside edge). Contacts are 0.32  $\mu\text{m}$  by 0.32  $\mu\text{m}$ . Finger width is 0.64  $\mu\text{m}$ . Fingers coming from the south are  $\sim 0.06$   $\mu\text{m}$  short of extending to the edge of the poly. Fingers

coming from the north are  $\sim 0.09 \mu\text{m}$  short of extending to the edge of the poly. These values imply finger lengths of  $100.1 \mu\text{m}$ .

An artwork error causes the fingers coming south from the outer, U-shaped pad to be  $\sim 0.18 \mu\text{m}$  short of reaching the pad. Oops. Since this is smaller than the process's minimum feature size, the gap may or may not result in an open circuit on the wafer. See the 0.5,100 device and Figure 3 for a picture of a similar situation.

#### *1.3.19 30,100 device*

Pads are compatible with GSG probing, which should be done from the north or south. Overall pad size is  $396.5 \mu\text{m}$  (EW) x  $328.5 \mu\text{m}$  (NS). Center pad is  $80 \mu\text{m}$  (EW) by  $98 \mu\text{m}$  (NS). Poly region is  $91.9 \mu\text{m}$  (EW) by  $100.2 \mu\text{m}$  (NS). Contact spacing is  $30.00 \mu\text{m}$  (inside edge to inside edge). Contacts are  $0.32 \mu\text{m}$  by  $0.32 \mu\text{m}$ . Finger width is  $0.64 \mu\text{m}$ . Fingers coming from the south are  $\sim 0.07 \mu\text{m}$  short of extending to the edge of the poly. Fingers coming from the north are  $\sim 0.10 \mu\text{m}$  short of extending to the edge of the poly. These values imply finger lengths of  $100.1 \mu\text{m}$ .

#### *1.3.20 35,100 device*

Pads are compatible with GSG probing, which should be done from the north or south. Overall pad size is  $396.5 \mu\text{m}$  (EW) x  $328.5 \mu\text{m}$  (NS). Center pad is  $80 \mu\text{m}$  (EW) by  $98 \mu\text{m}$  (NS). Poly region is  $106.8 \mu\text{m}$  (EW) by  $100.2 \mu\text{m}$  (NS). Contact spacing is  $35.00 \mu\text{m}$  (inside edge to inside edge). Contacts are  $0.32 \mu\text{m}$  by  $0.32 \mu\text{m}$ . Finger width is  $0.64 \mu\text{m}$ . Fingers coming from the south are  $\sim 0.09 \mu\text{m}$  short of extending to the edge of the poly. Fingers coming from the north are  $\sim 0.10 \mu\text{m}$  short of extending to the edge of the poly. These values imply finger lengths of  $100.1 \mu\text{m}$ .

#### *1.3.21 40,100 device*

Pads are compatible with GSG probing, which should be done from the north or south. Overall pad size is  $396.5 \mu\text{m}$  (EW) x  $328.5 \mu\text{m}$  (NS). Center pad is  $80 \mu\text{m}$  (EW) by  $98 \mu\text{m}$  (NS). Poly region is  $121.8 \mu\text{m}$  (EW) by  $100.2 \mu\text{m}$  (NS). Contact spacing is  $40.00 \mu\text{m}$  (inside

edge to inside edge). Contacts are  $0.32\ \mu\text{m}$  by  $0.32\ \mu\text{m}$ . Finger width is  $0.64\ \mu\text{m}$ . Fingers coming from the south are  $\sim 0.06\ \mu\text{m}$  short of extending to the edge of the poly. Fingers coming from the north are  $\sim 0.09\ \mu\text{m}$  short of extending to the edge of the poly. These values imply finger lengths of  $100.1\ \mu\text{m}$ .

## 2 H-tree Structures and Detectors

Many of the H-trees arms have two or more detectors in series which appear to be identical. If a quick inspection at a relatively high level indicated that all of the series detectors in an arm were identical, I assumed they were identical, and only examined one.

Device terminology for H-tree detectors matches that used for the edge-coupled waveguide detectors. Specifically, a device identified as X, Y, Z has a waveguide that is  $X\ \mu\text{m}$  wide, a polysilicon detector that is  $Y\ \mu\text{m}$  long, and a contact-edge-to-contact-edge spacing of  $Z\ \mu\text{m}$ .

“Oddities” about the detectors are noted where they have been observed in the artwork. However, it is almost certain that I missed some oddities.

Directions (e.g. NE) are defined by a “North” arrow that is on the die, about  $900\ \mu\text{m}$  in from the entrance to the large H-tree.

### 2.1 Small H-trees

#### 2.1.1 *Upper small H-tree*

This is the H-tree that is in the northwest corner of the die, as defined by the “North” arrow on the die.

The entrance waveguide is  $4\ \mu\text{m}$  at the start, tapering to  $2\ \mu\text{m}$  just before the first split. The waveguides after the split are also  $2\ \mu\text{m}$ , and remain  $2\ \mu\text{m}$  through the second split. After the second split, the waveguides taper down to  $0.5\ \mu\text{m}$ . (I’m assuming all four arms are like the one I examined. A quick check indicates that this is the case.)

The radius of curvature of the first bend appears to be  $50\mu\text{m}$ . The radius of curvature of the upper second bend appears to also be  $50\mu\text{m}$ , while the radius of curvature of the lower second bend appears to be  $25\mu\text{m}$ .

From the entrance to the start of the first bend is  $1264.5\mu\text{m}$ , although some of this will be removed during the edge-polish process. From the end of the first bend to the start of the second bend is  $468.1\mu\text{m}$ . From the end of the second bend to the start of the detector is  $242.0\mu\text{m}$ . (It's a little iffy deciding where a bend starts and stops, so these dimensions might be off by a micron or so.)

The H-tree has four sets of detectors, one at the end of each arm. The detector pads are not suitable for a high-speed GSG probe, only for two needle probes. Pads are  $100\mu\text{m}$  by  $100\mu\text{m}$ , and are probably best probed from the east or west.

The detector in the upper right corner is equivalent to eleven (11) 0.5, 2, 1.14 detectors in series along the waveguide. Metal-1 to metal-1 spacing over the waveguide is  $0.80\mu\text{m}$ .

The detector in the upper left corner is equivalent to eleven (11) 0.5, 5, 1.14 detectors in series along the waveguide. Metal-1 to metal-1 spacing over the waveguide is  $0.80\mu\text{m}$ .

The detector in the lower left corner is equivalent to eleven (11) 0.5, 3, 1.14 detectors in series along the waveguide. Metal-1 to metal-1 spacing over the waveguide is  $0.80\mu\text{m}$ .

The detector in the lower right corner is equivalent to eleven (11) 0.5, 4, 1.14 detectors in series along the waveguide. Metal-1 to metal-1 spacing over the waveguide is  $0.80\mu\text{m}$ .

There are no "scatter monitor" structures on this H-tree.

### 2.1.2 *Lower small H-tree*

This is the H-tree that is in the southwest corner of the region of the die enclosed by the waveguide bend structures.

The entrance waveguide is  $4\mu\text{m}$  at the start, and remains  $4\mu\text{m}$  until the first split. After the first split the waveguides are  $2\mu\text{m}$  wide, but begin tapering as soon as the split bend ends, eventually going to  $0.5\mu\text{m}$  wide. The waveguide then begins expanding, and reaches  $2\mu\text{m}$  at the entrance to the second split. The waveguides stay  $2\mu\text{m}$  through the split, but begin tapering again as soon as the second split bend ends, eventually down to  $0.5\mu\text{m}$  again. (I'm assuming all four arms are like the one I examined. A quick check indicates that this is the case.)

The radius of curvature of the first bend appears to be  $100\mu\text{m}$ . The radius of curvature of the both of the second bends also appears to be  $100\mu\text{m}$ .

From the entrance to the start of the first bend is  $1215.7\mu\text{m}$ , although some of this will be removed during the edge-polish process. From the end of the first bend to the start of the second bend is  $366.5\mu\text{m}$ . From the end of the second bend to the start of the detector is  $218.6\mu\text{m}$ . (It's a little iffy deciding where a bend starts and stops, so these dimensions might be off by a micron or so.)

The H-tree, like the upper small H-tree, has four sets of detectors. Again, the detector pads are not suitable for a high-speed GSG probe, only for two needle probes. Pads are  $100\mu\text{m}$  by  $100\mu\text{m}$ , and a probably best probed from the east or west.

The detector in the upper right corner is a single 0.5, 50, 1.14 detector. Note: The waveguide is  $0.50\mu\text{m}$  at the start, but  $0.49\mu\text{m}$  at the end. Metal-1 to metal-1 spacing over the waveguide is  $0.80\mu\text{m}$ .

The detector in the upper left corner is a single 0.5, 50, 1.14 detector. Note: The waveguide is  $0.50\mu\text{m}$  at the start, but  $0.49\mu\text{m}$  at the end. Metal-1 to metal-1 spacing over the waveguide is  $0.80\mu\text{m}$ . Note: This detector is identical to the upper right detector.

The detector in the lower left corner is a single 0.5, 50, 1.14 detector. Note: The waveguide is  $0.50\mu\text{m}$  at the start, but  $0.49\mu\text{m}$  at the end. Metal-1 to metal-1 spacing over the waveguide is  $0.80\mu\text{m}$ . Note: This detector is identical to the upper right detector.

The detector in the lower right corner is effectively dead, due to what appears to be a layout error. There is a  $4.24\mu\text{m}$  gap in the waveguide  $2.65\mu\text{m}$  after the waveguide crosses the poly detector region. Except for this, the detector appears identical to the other three detectors in the H-tree.

There are no “scatter monitor” structures on this H-tree.

### *2.1.3 Bottom left small H-tree*

This is the H-tree that is at the far southern edge of the die, on the left side of the die's centerline.

The entrance waveguide is  $4\mu\text{m}$  at the start, and remains  $4\mu\text{m}$  until the first split. After the first split the waveguides are  $2\mu\text{m}$  wide, but begin tapering as soon as the split bend ends, eventually going to  $0.5\mu\text{m}$  wide. The waveguide then begins expanding, and reaches  $2\mu\text{m}$  at the entrance to the second split. The waveguide behavior varies from left half to right half after the second split. On the left side, the arms stay  $2\mu\text{m}$  through the split, but begin tapering again as soon as the second split bend ends, eventually down to  $0.5\mu\text{m}$  again. On the right side, the arms stay  $2\mu\text{m}$  through the split, but do not taper, remaining  $2\mu\text{m}$  wide all the way to the detector.

The radius of curvature of the first bend appears to be  $100\mu\text{m}$ . The radius of curvature of the both of the second bends also appears to be  $100\mu\text{m}$ .

From the entrance to the start of the first bend is  $835.9\mu\text{m}$ , although some of this will be removed during the edge-polish process. From the end of the first bend to the start of the second bend is  $366.1\mu\text{m}$ . From the end of the second bend to the start of the detector is

218.6 $\mu\text{m}$ . (It's a little iffy deciding where a bend starts and stops, so these dimensions might be off by a micron or so.)

The H-tree, like the upper and lower small H-trees, has four sets of detectors. Again, the detector pads are not suitable for a high-speed GSG probe, only for two needle probes. Pads are 100 $\mu\text{m}$  by 100 $\mu\text{m}$ , and are probably best probed from the north or south.

The detector in the upper right corner is labeled as a single 2,50,2.97 detector, and this appears to be accurate. Metal-1 to metal-1 spacing over the waveguide is 2.63 $\mu\text{m}$ .

The detector in the lower right corner is labeled as a single 2,50,3.44 detector, and this appears to be accurate. Metal-1 to metal-1 spacing over the waveguide is 3.10 $\mu\text{m}$ .

The detector in the upper left corner is labeled as a single 0.5,50,1.64 detector, and this appears to be accurate. Metal-1 to metal-1 spacing over the waveguide is 1.30 $\mu\text{m}$ .

The detector in the lower left corner is labeled as a single 0.5,50,1.14 detector, and this appears to be accurate. Metal-1 to metal-1 spacing over the waveguide is 0.80 $\mu\text{m}$ .

There are no "scatter monitor" structures on this H-tree.

#### *2.1.4 Bottom right small H-tree*

This is the H-tree that is at the far southern edge of the die, on the right side of the die's centerline.

The entrance waveguide is 2 $\mu\text{m}$  at the start, and tapers to 1 $\mu\text{m}$  at the first split. After the first split the waveguides are 0.5 $\mu\text{m}$  wide, and remain 0.5 $\mu\text{m}$  wide to the second split. After the second split, the waveguides are 0.25 $\mu\text{m}$  wide, and remain 0.25 $\mu\text{m}$  through the split bend and all the way to the detector. Note that 0.35 $\mu\text{m}$  is the minimum feature size in the process, so 0.25 $\mu\text{m}$  is sub-minimum geometry.

The radius of curvature of the first split is labeled as  $10\mu\text{m}$ , but it appears to be closer to  $13\mu\text{m}$  on the outside of the bend. The second split is also labeled as  $10\mu\text{m}$ , but also appears to be closer to  $13\mu\text{m}$  on the outside of the bend.

From the entrance to the start of the first bend is  $877.9\mu\text{m}$ , although some of this will be removed during the edge-polish process. From the end of the first bend to the start of the second bend is  $517.6\mu\text{m}$ . From the end of the second bend to the start of the detector is  $329.9\mu\text{m}$ . (It's a little iffy deciding where a bend starts and stops, so these dimensions might be off by a micron or so.)

This H-tree, like the other three H-trees, has four sets of detectors. As with the other small H-trees, the detector pads are not suitable for a high-speed GSG probe, only for two needle probes. Pads are  $100\mu\text{m}$  by  $100\mu\text{m}$ , and are probably best probed from the north or south.

All four detectors in this H-tree are identical, a single 0.25,50,0.89 device. Note: The waveguide is  $0.25\mu\text{m}$  at the start, but  $0.24\mu\text{m}$  at the end. Metal-1 to metal-1 spacing over the waveguide is  $0.55\mu\text{m}$ .

There are no "scatter monitor" structures on this H-tree.

#### 2.1.5 *Southwest small H-tree*

This is the H-tree that is in the southwest corner of the die, facing west.

The entrance waveguide is  $4\mu\text{m}$  at the start, and remains  $4\mu\text{m}$  until the first split. After the first split, the waveguides are  $2\mu\text{m}$  wide through the second split. After the second split, the waveguides tapers to  $0.50\mu\text{m}$  at the detector.

The radius of curvature of the first split appears to be  $100\mu\text{m}$ . The radius of curvature of the second split also appears to be  $100\mu\text{m}$ .

From the entrance to the start of the first bend is  $947.2\mu\text{m}$ , although some of this will be removed during the edge-polish process. From the end of the first bend to the start of the

second bend is  $366.7\mu\text{m}$ . From the end of the second bend to the start of the detector is  $218.6\mu\text{m}$ . (It's a little iffy deciding where a bend starts and stops, so these dimensions might be off by a micron or so.)

There is a single detector in each corner of the H-tree. All four detectors are identical: a single 0.5,50,1.14 device. (Note: The waveguide is  $0.50\mu\text{m}$  at the start and in the middle, but  $0.49\mu\text{m}$  at the end.) Metal-1 to metal-1 spacing is  $0.80\mu\text{m}$ . The single detector pad is  $100\mu\text{m}$  by  $100\mu\text{m}$ , and is not suitable for probing with a high-speed GSG probe. It's also not obvious how to probe the device with needle probes, as there is only the one pad, in metal-1. The other side of the detector appears to go through some FETs and other circuitry.

The upper right and lower left detectors are labeled REPLICA BAIS (sic).

The upper left and lower right detectors are labeled BIG L. Unfortunately, the lower right detector is effectively dead, due to a  $4.24\mu\text{m}$  break in the waveguide  $2.65\mu\text{m}$  after the waveguide crosses the poly

There are no "scatter monitor" structures on this H-tree.

## 2.2 Large H-tree

The large H-tree is divided into quadrants (NE, NW, SW, SE), and then each quadrant is further subdivided into quadrants (A, B, C, D). (There is a "North" arrow about  $900\mu\text{m}$  from the start of the large H-tree.)

- The A sub-quadrant is in the NE corner of the quadrant.
- The B sub-quadrant is in the NW corner of the quadrant.
- The C sub-quadrant is in the SW corner of the quadrant.
- The D sub-quadrant is in the SE corner of the quadrant.

Some of the sub-quadrants are not labeled. (NE C, NW B, SW C, SE D)

Again, if repeated detectors appear identical at first glance, I assume they are identical and only examine and measure one.

The entrance to the large waveguide is  $7.97\mu\text{m}$  wide, and gradually expands to  $8.0\mu\text{m}$  at the first split. After the split, the waveguide is  $4\mu\text{m}$  wide, and stays  $4\mu\text{m}$  wide until the second split. After the second split, the waveguide is  $2\mu\text{m}$  wide, and remain  $2\mu\text{m}$  wide until the third split. After the third split, the waveguide is  $1\mu\text{m}$  wide. (Note: The straight waveguide is very slightly,  $\sim 0.001\mu\text{m}$ , offset from the waveguide bend coming out of the third split. As a practical matter, this will have no effect.) The waveguide remains  $1\mu\text{m}$  wide until the fourth split. After the fourth split, the waveguide is  $0.5\mu\text{m}$  wide, and remains  $0.5\mu\text{m}$  wide until the detector.

The radius of curvature of all the bends in the large H-tree appears to be  $100\mu\text{m}$ .

From the entrance to the start of the first bend is  $3449.1\mu\text{m}$ , although some of this will be removed during the edge-polish process. From the end of the first bend to the start of the second bend is  $1501.3\mu\text{m}$ . From the end of the second bend to the start of the third bend is  $1500.6\mu\text{m}$ . From the end of the third bend to the start of the fourth bend is  $670.6\mu\text{m}$ . From the end of the fourth bend to the detector is  $585.1\mu\text{m}$ . (It's a little iffy deciding where a bend starts and stops, so these dimensions might be off by a micron or so.)

“Scatter monitor” structures exist at the first split and all subsequent splits of the large H-tree. “Scatter monitor” structures also exist along all large H-tree arms except the input arm. On the second arm of the H-tree (between the first and second split), two “scatter monitor” structures are place at roughly  $1/3$  and  $2/3$  of the arm length. On the two southern third arms of the H-tree (between the second and third splits), a single “scatter monitor” structure is placed slightly more than half-way along the arm. On the north-eastern third arm of the H-tree, two “scatter monitor” structures are placed at roughly  $1/3$  and  $2/3$  of the arm length. On the north-western third arm, a single “scatter monitor” structure is placed roughly half-way down the arm. The “scatter monitor” detectors up to the second split are tested with GSG

probes. From the second split and up to the third split, the “scatter monitors” in the south are tested with GSG probes while in the north they’re tested with needle probes.

In the table below, the scatter monitor’s detector’s perpendicular direction is that which is perpendicular to the adjacent (or incoming, in the case of detectors at splits) waveguide, while the parallel direction is that which is parallel to the adjacent waveguide. “E / W” and “EW” mean “East / West”, while “N / S” and “NS” mean “North / South”. “GSG” means Ground-Signal-Ground type probe pads, while “needle” means needle-style probe pads. GSG pads can be probed with needle-style probes, but needle-style pads cannot be probed with GSG probes. GSG pads, when probed with GSG probes, must be tested from the indicated direction. When probing either GSG pads or needle pads with needle probes, testing can generally be done from any direction. (“D / C” = “Don’t Care”) This includes both needle probes coming from the same direction, if care is taken. When appropriate, typically for “parallel” and “closest” values, dimensions are measured from the inside edge of the contacts. For detectors at splits, the closest part of the detector is that reached by proceeding straight from the split. For detectors not at splits, the distance from the waveguide is the perpendicular distance from the polysilicon detector region to the waveguide. Some detectors are interdigitated finger structures, and some of those have the fingers parallel to the adjacent waveguide while others have the fingers perpendicular to the adjacent waveguide. Reference numbers in the table are to Figure 4. The scatter monitor detectors with the bias voltage running perpendicular to the waveguide are unlike to be useful, as any photons scattered out of the waveguide will probably be absorbed in a region which has little or no field. A lack of a field to separate the electron and hole once the EHP is created will probably lead to their quick recombination.

ID	Pad probe style	Test from?	Detector size ( $\mu\text{m}$ )		Comment
			Perp.	Parall.	
1	GSG	E / W	21.1 (NS)	10.0 (EW)	Contacts are $0.32 \mu\text{m}$ by $0.32 \mu\text{m}$ and are at NS. Center of detector is offset $\sim 9.1 \mu\text{m}$ north of the center of the 1 <sup>st</sup> split. Closest part of detector is $93.4 \mu\text{m}$ from 1 <sup>st</sup> split. Closest part of waveguide is $24.0 \mu\text{m}$ from detector. Polysi region is $10.0 \mu\text{m}$ (EW) by $22.3 \mu\text{m}$ (NS). Long axis of detector is perpendicular to incoming waveguide.
2	GSG	E / W	10.0 (EW)	21.1 (NS)	Contacts are $0.32 \mu\text{m}$ by $0.32 \mu\text{m}$ and are at NS. Detector is $8.7 \mu\text{m}$ from waveguide and starts $625 \mu\text{m}$ south of 1 <sup>st</sup> split. Polysi region is $10.0 \mu\text{m}$ (EW) by $22.3 \mu\text{m}$ (NS). Long axis of detector is parallel to waveguide.
3	GSG	E / W	10.0 (EW)	21.1 (NS)	Contacts are $0.32 \mu\text{m}$ by $0.32 \mu\text{m}$ and are at NS. Detector is $8.7 \mu\text{m}$ from waveguide and starts $1241 \mu\text{m}$ south of 1 <sup>st</sup> split. Polysi region is $10.0 \mu\text{m}$ (EW) by $22.3 \mu\text{m}$ (NS). Long axis of detector is parallel to waveguide.
4	GSG	E / W	10.0 (EW)	21.1 (NS)	Contacts are $0.32 \mu\text{m}$ by $0.32 \mu\text{m}$ and are at NS. Detector is $8.7 \mu\text{m}$ from waveguide and starts $664 \mu\text{m}$ north of 1 <sup>st</sup> split. Polysi region is $10.0 \mu\text{m}$ (EW) by $22.3 \mu\text{m}$ (NS). Long axis of detector is parallel to waveguide.
5	GSG	E / W	10.0 (EW)	21.1 (NS)	Contacts are $0.32 \mu\text{m}$ by $0.32 \mu\text{m}$ and are at NS. Detector is $8.7 \mu\text{m}$ from waveguide and starts $1297 \mu\text{m}$ north of 1 <sup>st</sup> split. Polysi region is $10.0 \mu\text{m}$ (EW) by $22.3 \mu\text{m}$ (NS). Long axis of detector is parallel to waveguide.
6	GSG	N / S	21.1 (EW)	10.0 (NS)	Contacts are $0.32 \mu\text{m}$ by $0.32 \mu\text{m}$ and are at EW. Center of detector is offset $\sim 4.0 \text{ mm}$ west of the center of the 2 <sup>nd</sup> split. Closest part of detector is $77.3 \mu\text{m}$ from 2 <sup>nd</sup> split. Closest part of waveguide is $15.8 \mu\text{m}$ from detector. Polysi region is $10.0 \mu\text{m}$ (NS) by $22.3 \mu\text{m}$ (EW). Long axis of detector is perpendicular to incoming waveguide.

ID	Pad probe style	Test from?	Detector size ( $\mu\text{m}$ )		Comment
			Perp.	Parall.	
7	GSG	N / S	10.0 (NS)	21.1 (EW)	Contacts are $0.32 \mu\text{m}$ by $0.32 \mu\text{m}$ and are at EW. Detector is $5.6 \mu\text{m}$ from waveguide and starts $1003 \mu\text{m}$ east of 2 <sup>nd</sup> split. Polysi region is $10.0 \mu\text{m}$ (NS) by $22.3 \mu\text{m}$ (EW). Long axis of detector is parallel to waveguide.
8	GSG	N / S	10.0 (NS)	21.1 (EW)	Contacts are $0.32 \mu\text{m}$ by $0.32 \mu\text{m}$ and are at EW. Detector is $5.6 \mu\text{m}$ from waveguide and starts $1141 \mu\text{m}$ west of 2 <sup>nd</sup> split. Polysi region is $10.0 \mu\text{m}$ (NS) by $22.3 \mu\text{m}$ (EW). Long axis of detector is parallel to waveguide.
9	needle	D / C	1.14 (EW)	10.0 (NS)	Contacts are $0.32 \mu\text{m}$ by $0.32 \mu\text{m}$ and are at EW. Center of detector is offset $\sim 4.5 \mu\text{m}$ east of the center of the 2 <sup>nd</sup> split. Closest part of detector is $\sim 85.4 \mu\text{m}$ from 2 <sup>nd</sup> split. Closest part of waveguide is $\sim 28.2 \mu\text{m}$ from detector. Polysi region is $10.0 \mu\text{m}$ (NS) by $2.32 \mu\text{m}$ (EW). Short axis of detector is perpendicular to incoming waveguide.
10	needle	D / C	10.0 (NS)	1.14 (EW)	Contacts are $0.32 \mu\text{m}$ by $0.32 \mu\text{m}$ and are at EW. Detector is $13.2 \mu\text{m}$ from waveguide and starts $597 \mu\text{m}$ east of 2 <sup>nd</sup> split. Polysi region is $10.0 \mu\text{m}$ (NS) by $2.32 \mu\text{m}$ (EW). Short axis of detector is parallel to waveguide.
11	needle	D / C	10.0 (NS)	1.14 (EW)	Contacts are $0.32 \mu\text{m}$ by $0.32 \mu\text{m}$ and are at EW. Detector is $13.2 \mu\text{m}$ from waveguide and starts $1045 \mu\text{m}$ east of 2 <sup>nd</sup> split. Polysi region is $10.0 \mu\text{m}$ (NS) by $2.32 \mu\text{m}$ (EW). Short axis of detector is parallel to waveguide.
12	needle	D / C	10.0 (NS)	1.14 (EW)	Contacts are $0.32 \mu\text{m}$ by $0.32 \mu\text{m}$ and are at EW. Detector is $13.2 \mu\text{m}$ from waveguide and starts $1006 \mu\text{m}$ west of 2 <sup>nd</sup> split. Polysi region is $10.0 \mu\text{m}$ (NS) by $2.32 \mu\text{m}$ (EW). Short axis of detector is parallel to waveguide.
13	needle	D / C	1.14 (NS)	10.0 (EW)	Contacts are $0.32 \mu\text{m}$ by $0.32 \mu\text{m}$ and are at NS. Center of detector is offset $\sim 2.8 \mu\text{m}$ north of center of 3 <sup>rd</sup> split. Closest part of detector is $\sim 84.0 \mu\text{m}$ from 3 <sup>rd</sup> split. Closest part of waveguide is $\sim 28.5 \mu\text{m}$ from detector. Polysi region is $10.0 \mu\text{m}$ (EW) by $2.32 \mu\text{m}$ (NS). Short axis of detector is perpendicular to incoming waveguide.

ID	Pad probe style	Test from?	Detector size ( $\mu\text{m}$ )		Comment
			Perp.	Parall.	
14	needle	D / C	10.0 (NS)	1.14 (NS)	Contacts are $0.32 \mu\text{m}$ by $0.32 \mu\text{m}$ and are at NS. Detector is $6.0 \mu\text{m}$ from waveguide and starts $449 \mu\text{m}$ south of 3 <sup>rd</sup> split. Polysi region is $10.0 \mu\text{m}$ (EW) by $2.32 \mu\text{m}$ (NS). Short axis of detector is parallel to waveguide.
15	needle	D / C	10.0 (NS)	1.14 (NS)	Contacts are $0.32 \mu\text{m}$ by $0.32 \mu\text{m}$ and are at NS. Detector is $6.0 \mu\text{m}$ from waveguide and starts $485 \mu\text{m}$ north of 3 <sup>rd</sup> split. Polysi region is $10.0 \mu\text{m}$ (EW) by $2.32 \mu\text{m}$ (NS). Short axis of detector is parallel to waveguide.
16	needle	D / C	1.14 (EW)	10.0 (NS)	Contacts are $0.32 \mu\text{m}$ by $0.32 \mu\text{m}$ and are at EW. Center of detector is offset $\sim 3.6 \mu\text{m}$ east of center of 4 <sup>th</sup> split. Closest part of detector is $\sim 83.8 \mu\text{m}$ from 4 <sup>th</sup> split. Closest part of waveguide is $\sim 27.7 \mu\text{m}$ from detector. Polysi region is $2.32 \mu\text{m}$ (EW) by $10.0 \mu\text{m}$ (NS). Short axis of detector is perpendicular to incoming waveguide.
17	needle	D / C	10.0 (NS)	1.14 (EW)	Contacts are $0.32 \mu\text{m}$ by $0.32 \mu\text{m}$ and are at EW. Detector is $3.9 \mu\text{m}$ from waveguide and starts $448 \mu\text{m}$ east of 4 <sup>th</sup> split. Polysi region is $2.32 \mu\text{m}$ (EW) by $10.0 \mu\text{m}$ (NS). Short axis of detector is parallel to waveguide.
18	needle	D / C	10.0 (NS)	1.14 (EW)	Contacts are $0.32 \mu\text{m}$ by $0.32 \mu\text{m}$ and are at EW. Detector is $3.9 \mu\text{m}$ from waveguide and starts $474 \mu\text{m}$ west of 4 <sup>th</sup> split. Polysi region is $2.32 \mu\text{m}$ (EW) by $10.0 \mu\text{m}$ (NS). Short axis of detector is parallel to waveguide.
19	needle	D / C	1.14 (EW)	10.0 (NS)	Contacts are $0.32 \mu\text{m}$ by $0.32 \mu\text{m}$ and are at EW. Center of detector is offset $\sim 4.2 \mu\text{m}$ east of center of 4 <sup>th</sup> split. Closest part of detector is $\sim 79.4 \mu\text{m}$ from 4 <sup>th</sup> split. Closest part of waveguide is $\sim 24.5 \mu\text{m}$ from detector. Polysi region is $2.32 \mu\text{m}$ (EW) by $10.0 \mu\text{m}$ (NS). Short axis of detector is perpendicular to incoming waveguide.
20	needle	D / C	10.0 (NS)	1.14 (EW)	Contacts are $0.32 \mu\text{m}$ by $0.32 \mu\text{m}$ and are at EW. Detector is $3.4 \mu\text{m}$ from waveguide and starts $448 \mu\text{m}$ east of 4 <sup>th</sup> split. Polysi region is $2.32 \mu\text{m}$ (EW) by $10.0 \mu\text{m}$ (NS). Short axis of detector is parallel to waveguide.

ID	Pad probe style	Test from?	Detector size ( $\mu\text{m}$ )		Comment
			Perp.	Parall.	
21	needle	D / C	10.0 (NS)	1.14 (EW)	Contacts are $0.32 \mu\text{m}$ by $0.32 \mu\text{m}$ and are at EW. Detector is $3.4 \mu\text{m}$ from waveguide and starts $366 \mu\text{m}$ west of 4 <sup>th</sup> split. Polysi region is $2.32 \mu\text{m}$ (EW) by $10.0 \mu\text{m}$ (NS). Short axis of detector is parallel to waveguide.
22	needle	D / C	12.3 (NS)	12.8 (EW)	Interdigitated finger structure contacts running NS. (Four fingers running N, four running S.) Contacts are $0.32 \mu\text{m}$ by $0.32 \mu\text{m}$ . Finger spacing $1.00$ to $1.05 \mu\text{m}$ (contact edge to contact edge), finger width $0.81$ to $0.90 \mu\text{m}$ , finger length over detector $12.0 \mu\text{m}$ . Center of detector is offset $\sim 7.0 \mu\text{m}$ north of center of 3 <sup>rd</sup> split. Closest part of detector is $\sim 76.1 \mu\text{m}$ from split. Polysi region is $12.8 \mu\text{m}$ (EW) by $12.3 \mu\text{m}$ (NS). Long axis of detector is perpendicular to incoming waveguide. Poly edge to closest contact edge is $1.56 \mu\text{m}$ (EW).
23	needle	D / C	12.8 (EW)	12.3 (NS)	Interdigitated finger structure contacts running NS. (Four fingers running N, four running S.) Contacts are $0.32 \mu\text{m}$ by $0.32 \mu\text{m}$ . Finger spacing $1.00$ to $1.05 \mu\text{m}$ (contact edge to contact edge), finger width $0.81$ to $0.90 \mu\text{m}$ , finger length over detector $12.0 \mu\text{m}$ . Detector is $9.7 \mu\text{m}$ from waveguide and starts $273 \mu\text{m}$ south of 3 <sup>rd</sup> split. Polysi region is $12.8 \mu\text{m}$ (EW) by $12.3 \mu\text{m}$ (NS). Short axis of detector is parallel to waveguide. Poly edge to closest contact edge is $1.58 \mu\text{m}$ (EW).
24	needle	D / C	12.8 (EW)	12.3 (NS)	Interdigitated finger structure contacts running NS. (Four fingers running N, four running S.) Contacts are $0.32 \mu\text{m}$ by $0.32 \mu\text{m}$ . Finger spacing $1.00$ to $1.05 \mu\text{m}$ (contact edge to contact edge), finger width $0.81$ to $0.90 \mu\text{m}$ , finger length over detector $12.0 \mu\text{m}$ . Detector is $9.7 \mu\text{m}$ from waveguide and starts $585 \mu\text{m}$ south of 3 <sup>rd</sup> split. Polysi region is $12.8 \mu\text{m}$ (EW) by $12.3 \mu\text{m}$ (NS). Short axis of detector is parallel to waveguide. Poly edge to closest contact edge is $1.58 \mu\text{m}$ (EW).

ID	Pad probe style	Test from?	Detector size ( $\mu\text{m}$ )		Comment
			Perp.	Parall.	
25	needle	D / C	12.8 (EW)	12.3 (NS)	Interdigitated finger structure contacts running NS. (Four fingers running N, four running S.) Contacts are $0.32 \mu\text{m}$ by $0.32 \mu\text{m}$ . Finger spacing 1.00 to $1.05 \mu\text{m}$ (contact edge to contact edge), finger width $0.81$ to $0.90 \mu\text{m}$ , finger length over detector $12.0 \mu\text{m}$ . Detector is $9.7 \mu\text{m}$ from waveguide and starts $271 \mu\text{m}$ north of 3 <sup>rd</sup> split. Polysi region is $12.8 \mu\text{m}$ (EW) by $12.3 \mu\text{m}$ (NS). Short axis of detector is parallel to waveguide. Poly edge to closest contact edge is $1.58 \mu\text{m}$ (EW).
26	needle	D / C	12.8 (EW)	12.3 (NS)	Interdigitated finger structure contacts running NS. (Four fingers running N, four running S.) Contacts are $0.32 \mu\text{m}$ by $0.32 \mu\text{m}$ . Finger spacing 1.00 to $1.05 \mu\text{m}$ (contact edge to contact edge), finger width $0.81$ to $0.90 \mu\text{m}$ , finger length over detector $12.0 \mu\text{m}$ . Detector is $9.7 \mu\text{m}$ from waveguide and starts $637 \mu\text{m}$ north of 3 <sup>rd</sup> split. Polysi region is $12.8 \mu\text{m}$ (EW) by $12.3 \mu\text{m}$ (NS). Short axis of detector is parallel to waveguide. Poly edge to closest contact edge is $1.58 \mu\text{m}$ (EW).
27	needle	D / C	12.3 (EW)	12.8 (NS)	Interdigitated finger structure contacts running EW. (Four fingers running E, four running W.) Contacts are $0.32 \mu\text{m}$ by $0.32 \mu\text{m}$ . Finger spacing 1.00 to $1.05 \mu\text{m}$ (contact edge to contact edge), finger width $0.81$ to $0.90 \mu\text{m}$ , finger length over detector $12.0 \mu\text{m}$ . Center of detector is offset $\sim 4.5 \mu\text{m}$ east of center of 4 <sup>th</sup> split. Closest part of detector is $\sim 80.6 \mu\text{m}$ from split. Polysi region is $12.3 \mu\text{m}$ (EW) by $12.8 \mu\text{m}$ (NS). Short axis of detector is perpendicular to incoming waveguide. Poly edge to closest contact edge is $1.58 \mu\text{m}$ (NS).

ID	Pad probe style	Test from?	Detector size ( $\mu\text{m}$ )		Comment
			Perp.	Parall.	
28	needle	D / C	12.8 (NS)	12.3 (EW)	Interdigitated finger structure contacts running EW. (Four fingers running E, four running W.) Contacts are $0.32 \mu\text{m}$ by $0.32 \mu\text{m}$ . Finger spacing $1.00$ to $1.05 \mu\text{m}$ (contact edge to contact edge), finger width $0.81$ to $0.90 \mu\text{m}$ , finger length over detector $12.0 \mu\text{m}$ . Detector is $6.7 \mu\text{m}$ from waveguide and starts $320 \mu\text{m}$ east of 4 <sup>th</sup> split. Polysi region is $12.3 \mu\text{m}$ (EW) by $12.8 \mu\text{m}$ (NS). Short axis of detector is parallel to waveguide. Poly edge to closest contact edge is $1.58 \mu\text{m}$ (NS).
29	needle	D / C	12.8 (NS)	12.3 (EW)	Interdigitated finger structure contacts running EW. (Four fingers running E, four running W.) Contacts are $0.32 \mu\text{m}$ by $0.32 \mu\text{m}$ . Finger spacing $1.00$ to $1.05 \mu\text{m}$ (contact edge to contact edge), finger width $0.81$ to $0.90 \mu\text{m}$ , finger length over detector $12.0 \mu\text{m}$ . Detector is $6.7 \mu\text{m}$ from waveguide and starts $620 \mu\text{m}$ east of 4 <sup>th</sup> split. Polysi region is $12.3 \mu\text{m}$ (EW) by $12.8 \mu\text{m}$ (NS). Short axis of detector is parallel to waveguide. Poly edge to closest contact edge is $1.58 \mu\text{m}$ (NS).
30	needle	D / C	12.8 (NS)	12.3 (EW)	Interdigitated finger structure contacts running EW. (Four fingers running E, four running W.) Contacts are $0.32 \mu\text{m}$ by $0.32 \mu\text{m}$ . Finger spacing $1.00$ to $1.05 \mu\text{m}$ (contact edge to contact edge), finger width $0.81$ to $0.90 \mu\text{m}$ , finger length over detector $12.0 \mu\text{m}$ . Detector is $6.6 \mu\text{m}$ from waveguide and starts $367 \mu\text{m}$ west of 4 <sup>th</sup> split. Polysi region is $12.3 \mu\text{m}$ (EW) by $12.8 \mu\text{m}$ (NS). Short axis of detector is parallel to waveguide. Poly edge to closest contact edge is $1.58 \mu\text{m}$ (NS).
31	needle	D / C	12.3 (EW)	12.8 (NS)	Interdigitated finger structure contacts running EW. (Four fingers running E, four running W.) Contacts are $0.32 \mu\text{m}$ by $0.32 \mu\text{m}$ . Finger spacing $1.00$ to $1.05 \mu\text{m}$ (contact edge to contact edge), finger width $0.81$ to $0.90 \mu\text{m}$ , finger length over detector $12.0 \mu\text{m}$ . Center of detector is offset $\sim 0.5 \mu\text{m}$ W of center of 4 <sup>th</sup> split. Closest part of detector is $\sim 83.6 \mu\text{m}$ from split. Polysi region is $12.3 \mu\text{m}$ (EW) by $12.8 \mu\text{m}$ (NS). Short axis of detector is perp. to incoming waveguide. Poly edge to closest contact edge is $1.58 \mu\text{m}$ (NS).

ID	Pad probe style	Test from?	Detector size ( $\mu\text{m}$ )		Comment
			Perp.	Parall.	
32	needle	D / C	12.8 (NS)	12.3 (EW)	Interdigitated finger structure contacts running EW. (Four fingers running E, four running W.) Contacts are $0.32 \mu\text{m}$ by $0.32 \mu\text{m}$ . Finger spacing 1.00 to $1.05 \mu\text{m}$ (contact edge to contact edge), finger width $0.81$ to $0.90 \mu\text{m}$ , finger length over detector $12.0 \mu\text{m}$ . Detector is $3.5 \mu\text{m}$ from waveguide and starts $463 \mu\text{m}$ east of 4 <sup>th</sup> split. Polysi region is $12.3 \mu\text{m}$ (EW) by $12.8 \mu\text{m}$ (NS). Short axis of detector is parallel to waveguide. Poly edge to closest contact edge is $1.58 \mu\text{m}$ (NS).
33	needle	D / C	12.8 (NS)	12.3 (EW)	Interdigitated finger structure contacts running EW. (Four fingers running E, four running W.) Contacts are $0.32 \mu\text{m}$ by $0.32 \mu\text{m}$ . Finger spacing 1.00 to $1.05 \mu\text{m}$ (contact edge to contact edge), finger width $0.81$ to $0.90 \mu\text{m}$ , finger length over detector $12.0 \mu\text{m}$ . Detector is $3.5 \mu\text{m}$ from waveguide and starts $389 \mu\text{m}$ west of 4 <sup>th</sup> split. Polysi region is $12.3 \mu\text{m}$ (EW) by $12.8 \mu\text{m}$ (NS). Short axis of detector is parallel to waveguide. Poly edge to closest contact edge is $1.58 \mu\text{m}$ (NS).
34	needle	D / C	12.8 (NS)	12.3 (EW)	Interdigitated finger structure contacts running EW. (Four fingers running E, four running W.) Contacts are $0.32 \mu\text{m}$ by $0.32 \mu\text{m}$ . Finger spacing 1.00 to $1.05 \mu\text{m}$ (contact edge to contact edge), finger width $0.64 \mu\text{m}$ , finger length over detector $12.0 \mu\text{m}$ . Center of detector is offset $\sim 4.4 \mu\text{m}$ north of center of 3 <sup>rd</sup> split. Closest part of detector is $\sim 111 \mu\text{m}$ from split. Polysi region is $12.3 \mu\text{m}$ (EW) by $12.8 \mu\text{m}$ (NS). Long axis of detector is perpendicular to incoming waveguide. Poly edge to closest contact edge is $1.03 \mu\text{m}$ (NS).
35	needle	D / C	12.3 (EW)	12.8 (NS)	Interdigitated finger structure contacts running EW. (Four fingers running E, four running W.) Contacts are $0.32 \mu\text{m}$ by $0.32 \mu\text{m}$ . Finger spacing 1.00 to $1.05 \mu\text{m}$ (contact edge to contact edge), finger width $0.64 \mu\text{m}$ , finger length over detector $12.0 \mu\text{m}$ . Detector is $11.2 \mu\text{m}$ from waveguide and starts $417 \mu\text{m}$ south of 3 <sup>rd</sup> split. Polysi region is $12.3 \mu\text{m}$ (EW) by $12.8 \mu\text{m}$ (NS). Long axis of detector is parallel to waveguide. Poly edge to closest contact edge is $1.03 \mu\text{m}$ (EW).

ID	Pad probe style	Test from?	Detector size ( $\mu\text{m}$ )		Comment
			Perp.	Parall.	
36	needle	D / C	12.3 (EW)	12.8 (NS)	Interdigitated finger structure contacts running EW. (Four fingers running E, four running W.) Contacts are $0.32 \mu\text{m}$ by $0.32 \mu\text{m}$ . Finger spacing 1.00 to $1.05 \mu\text{m}$ (contact edge to contact edge), finger width $0.64 \mu\text{m}$ , finger length over detector $12.0 \mu\text{m}$ . Detector is $11.2 \mu\text{m}$ from waveguide and starts $526 \mu\text{m}$ north of 3 <sup>rd</sup> split. Polysi region is $12.3 \mu\text{m}$ (EW) by $12.8 \mu\text{m}$ (NS). Long axis of detector is parallel to waveguide. Poly edge to closest contact edge is $1.03 \mu\text{m}$ (EW).
37	needle	D / C	12.8 (EW)	12.3 (NS)	Interdigitated finger structure contacts running NS. (Four fingers running N, four running S.) Contacts are $0.32 \mu\text{m}$ by $0.32 \mu\text{m}$ . Finger spacing 1.00 to $1.05 \mu\text{m}$ (contact edge to contact edge), finger width $0.64 \mu\text{m}$ , finger length over detector $12.0 \mu\text{m}$ . Center of detector is offset $\sim 3.9 \mu\text{m}$ east of center of 4 <sup>th</sup> split. Closest part of detector is $\sim 111 \mu\text{m}$ from split. Polysi region is $12.8 \mu\text{m}$ (EW) by $12.3 \mu\text{m}$ (NS). Long axis of detector is perpendicular to incoming waveguide. Poly edge to closest contact edge is $1.03 \mu\text{m}$ (NS).
38	needle	D / C	12.3 (NS)	12.8 (EW)	Interdigitated finger structure contacts running NS. (Four fingers running N, four running S.) Contacts are $0.32 \mu\text{m}$ by $0.32 \mu\text{m}$ . Finger spacing 1.00 to $1.05 \mu\text{m}$ (contact edge to contact edge), finger width $0.64 \mu\text{m}$ , finger length over detector $12.0 \mu\text{m}$ . Detector is $11.1 \mu\text{m}$ from waveguide and starts $512 \mu\text{m}$ east of 4 <sup>th</sup> split. Polysi region is $12.8 \mu\text{m}$ (EW) by $12.3 \mu\text{m}$ (NS). Long axis of detector is parallel to waveguide. Poly edge to closest contact edge is $1.03 \mu\text{m}$ (EW).
39	needle	D / C	12.3 (NS)	12.8 (EW)	Interdigitated finger structure contacts running NS. (Four fingers running N, four running S.) Contacts are $0.32 \mu\text{m}$ by $0.32 \mu\text{m}$ . Finger spacing 1.00 to $1.05 \mu\text{m}$ (contact edge to contact edge), finger width $0.64 \mu\text{m}$ , finger length over detector $12.0 \mu\text{m}$ . Detector is $11.1 \mu\text{m}$ from waveguide and starts $361 \mu\text{m}$ west of 4 <sup>th</sup> split. Polysi region is $12.8 \mu\text{m}$ (EW) by $12.3 \mu\text{m}$ (NS). Long axis of detector is parallel to waveguide. Poly edge to closest contact edge is $1.03 \mu\text{m}$ (NS).

ID	Pad probe style	Test from?	Detector size ( $\mu\text{m}$ )		Comment
			Perp.	Parall.	
40	needle	D / C	12.8 (EW)	12.3 (NS)	Interdigitated finger structure contacts running NS. (Four fingers running N, four running S.) Contacts are $0.32 \mu\text{m}$ by $0.32 \mu\text{m}$ . Finger spacing $1.00$ to $1.05 \mu\text{m}$ (contact edge to contact edge), finger width $0.64 \mu\text{m}$ , finger length over detector $12.0 \mu\text{m}$ . Center of detector is offset $\sim 2.5 \mu\text{m}$ east of center of 4 <sup>th</sup> split. Closest part of detector is $\sim 112 \mu\text{m}$ from split. Polysi region is $12.8 \mu\text{m}$ (EW) by $12.3 \mu\text{m}$ (NS). Long axis of detector is perpendicular to incoming waveguide. Poly edge to closest contact edge is $1.03 \mu\text{m}$ (NS).
41	needle	D / C	12.3 (NS)	12.8 (EW)	Interdigitated finger structure contacts running NS. (Four fingers running N, four running S.) Contacts are $0.32 \mu\text{m}$ by $0.32 \mu\text{m}$ . Finger spacing $1.00$ to $1.05 \mu\text{m}$ (contact edge to contact edge), finger width $0.64 \mu\text{m}$ , finger length over detector $12.0 \mu\text{m}$ . Detector is $11.7 \mu\text{m}$ from waveguide and starts $422 \mu\text{m}$ west of 4 <sup>th</sup> split. Polysi region is $12.8 \mu\text{m}$ (EW) by $12.3 \mu\text{m}$ (NS). Long axis of detector is parallel to waveguide. Poly edge to closest contact edge is $1.03 \mu\text{m}$ (NS).
42	GSG	E / W	12.3 (NS)	12.8 (EW)	Interdigitated finger structure contacts running NS. (Four fingers running N, four running S.) Contacts are $0.32 \mu\text{m}$ by $0.32 \mu\text{m}$ . Finger spacing $1.00$ to $1.05 \mu\text{m}$ (contact edge to contact edge), finger width $0.84$ to $0.94 \mu\text{m}$ , finger length over detector $12.0 \mu\text{m}$ . Center of detector is offset $\sim 3.0 \mu\text{m}$ north of center of 3 <sup>rd</sup> split. Closest part of detector is $\sim 89.5 \mu\text{m}$ from split. Polysi region is $12.8 \mu\text{m}$ (EW) by $12.3 \mu\text{m}$ (NS). Short axis of detector is perpendicular to incoming waveguide. Poly edge to closest contact edge is $1.58 \mu\text{m}$ (EW)

ID	Pad probe style	Test from?	Detector size ( $\mu\text{m}$ )		Comment
			Perp.	Parall.	
43	GSG	E / W	12.8 (EW)	12.3 (NS)	Interdigitated finger structure contacts running NS. (Four fingers running N, four running S.) Contacts are $0.32 \mu\text{m}$ by $0.32 \mu\text{m}$ . Finger spacing $1.00$ to $1.05 \mu\text{m}$ (contact edge to contact edge), finger width $0.84$ to $0.94 \mu\text{m}$ , finger length over detector $12.0 \mu\text{m}$ . Detector is $11.3 \mu\text{m}$ from waveguide and starts $545 \mu\text{m}$ south of 3 <sup>rd</sup> split. Polysi region is $12.8 \mu\text{m}$ (EW) by $12.3 \mu\text{m}$ (NS). Short axis of detector is parallel to waveguide. Poly edge to closest contact edge is $1.58 \mu\text{m}$ (EW)
44	GSG	E / W	12.8 (EW)	12.3 (NS)	Interdigitated finger structure contacts running NS. (Four fingers running N, four running S.) Contacts are $0.32 \mu\text{m}$ by $0.32 \mu\text{m}$ . Finger spacing $1.00$ to $1.05 \mu\text{m}$ (contact edge to contact edge), finger width $0.84$ to $0.94 \mu\text{m}$ , finger length over detector $12.0 \mu\text{m}$ . Detector is $11.3 \mu\text{m}$ from waveguide and starts $403 \mu\text{m}$ north of 3 <sup>rd</sup> split. Polysi region is $12.8 \mu\text{m}$ (EW) by $12.3 \mu\text{m}$ (NS). Short axis of detector is parallel to waveguide. Poly edge to closest contact edge is $1.58 \mu\text{m}$ (EW)
45	GSG	N / S	12.3 (EW)	12.8 (NS)	Interdigitated finger structure contacts running EW. (Four fingers running E, four running W.) Contacts are $0.32 \mu\text{m}$ by $0.32 \mu\text{m}$ . Finger spacing $1.00$ to $1.05 \mu\text{m}$ (contact edge to contact edge), finger width $0.84$ to $0.94 \mu\text{m}$ , finger length over detector $12.0 \mu\text{m}$ . Center of detector is offset $\sim 2.0 \mu\text{m}$ east of center of 4 <sup>th</sup> split. Closest part of detector is $\sim 84.5 \mu\text{m}$ from split. Polysi region is $12.3 \mu\text{m}$ (EW) by $12.8 \mu\text{m}$ (NS). Short axis of detector is perpendicular to incoming waveguide. Poly edge to closest contact edge is $1.58 \mu\text{m}$ (NS).
46	GSG	N / S	12.8 (NS)	12.3 (EW)	Interdigitated finger structure contacts running EW. (Four fingers running E, four running W.) Contacts are $0.32 \mu\text{m}$ by $0.32 \mu\text{m}$ . Finger spacing $1.00$ to $1.05 \mu\text{m}$ (contact edge to contact edge), finger width $0.84$ to $0.94 \mu\text{m}$ , finger length over detector $12.0 \mu\text{m}$ . Detector is $16.1 \mu\text{m}$ from waveguide and starts $470 \mu\text{m}$ east of 4 <sup>th</sup> split. Polysi region is $12.3 \mu\text{m}$ (EW) by $12.8 \mu\text{m}$ (NS). Short axis of detector is parallel to waveguide. Poly edge to closest contact edge is $1.58 \mu\text{m}$ (NS).

ID	Pad probe style	Test from?	Detector size ( $\mu\text{m}$ )		Comment
			Perp.	Parall.	
47	GSG	N / S	12.8 (NS)	12.3 (EW)	Interdigitated finger structure contacts running EW. (Four fingers running E, four running W.) Contacts are $0.32 \mu\text{m}$ by $0.32 \mu\text{m}$ . Finger spacing 1.00 to $1.05 \mu\text{m}$ (contact edge to contact edge), finger width $0.84$ to $0.94 \mu\text{m}$ , finger length over detector $12.0 \mu\text{m}$ . Detector is $16.1 \mu\text{m}$ from waveguide and starts $507 \mu\text{m}$ west of 4 <sup>th</sup> split. Polysi region is $12.3 \mu\text{m}$ (EW) by $12.8 \mu\text{m}$ (NS). Short axis of detector is parallel to waveguide. Poly edge to closest contact edge is $1.58 \mu\text{m}$ (NS).
48	GSG	N / S	12.3 (EW)	12.8 (NS)	Interdigitated finger structure contacts running EW. (Four fingers running E, four running W.) Contacts are $0.32 \mu\text{m}$ by $0.32 \mu\text{m}$ . Finger spacing 1.00 to $1.05 \mu\text{m}$ (contact edge to contact edge), finger width $0.84$ to $0.94 \mu\text{m}$ , finger length over detector $12.0 \mu\text{m}$ . Center of detector is offset $\sim 3.1 \mu\text{m}$ east of center of 4 <sup>th</sup> split. Closest part of detector is $\sim 86.1 \mu\text{m}$ from split. Polysi region is $12.3 \mu\text{m}$ (EW) by $12.8 \mu\text{m}$ (NS). Short axis of detector is perpendicular to incoming waveguide. Poly edge to closest contact edge is $1.58 \mu\text{m}$ (NS).
49	GSG	N / S	12.8 (NS)	12.3 (EW)	Interdigitated finger structure contacts running EW. (Four fingers running E, four running W.) Contacts are $0.32 \mu\text{m}$ by $0.32 \mu\text{m}$ . Finger spacing 1.00 to $1.05 \mu\text{m}$ (contact edge to contact edge), finger width $0.84$ to $0.94 \mu\text{m}$ , finger length over detector $12.0 \mu\text{m}$ . Detector is $13.3 \mu\text{m}$ from waveguide and starts $480 \mu\text{m}$ east of 4 <sup>th</sup> split. Polysi region is $12.3 \mu\text{m}$ (EW) by $12.8 \mu\text{m}$ (NS). Short axis of detector is parallel to waveguide. Poly edge to closest contact edge is $1.58 \mu\text{m}$ (NS).
50	GSG	N / S	12.8 (NS)	12.3 (EW)	Interdigitated finger structure contacts running EW. (Four fingers running E, four running W.) Contacts are $0.32 \mu\text{m}$ by $0.32 \mu\text{m}$ . Finger spacing 1.00 to $1.05 \mu\text{m}$ (contact edge to contact edge), finger width $0.84$ to $0.94 \mu\text{m}$ , finger length over detector $12.0 \mu\text{m}$ . Detector is $13.3 \mu\text{m}$ from waveguide and starts $436 \mu\text{m}$ west of 4 <sup>th</sup> split. Polysi region is $12.3 \mu\text{m}$ (EW) by $12.8 \mu\text{m}$ (NS). Short axis of detector is parallel to waveguide. Poly edge to closest contact edge is $1.58 \mu\text{m}$ (NS).

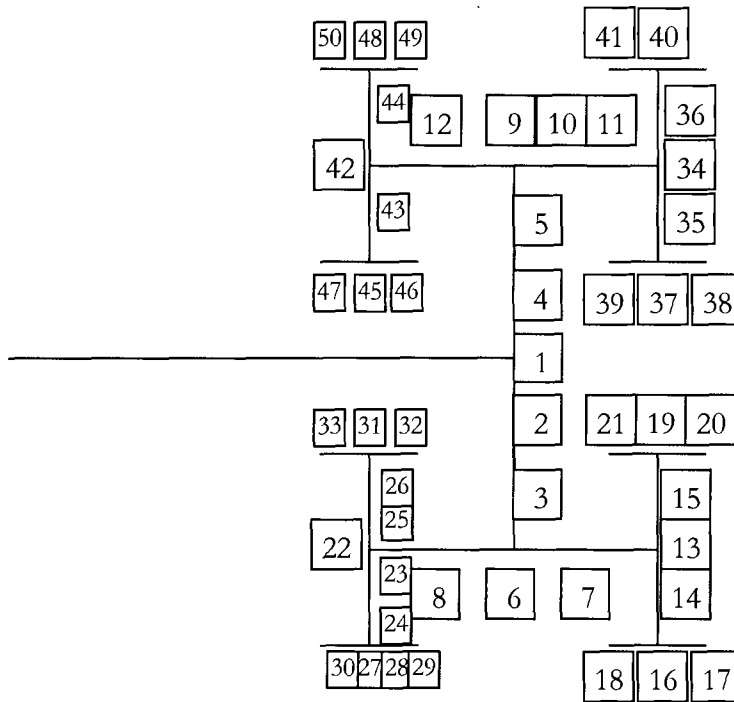


Figure 4: Location map for large H-tree scatter monitor detectors

In the NE quadrant, “scatter monitor” detectors exist at the 3<sup>rd</sup> and 4<sup>th</sup> splits and (except for the A sub-quadrant) at roughly the mid-points of the arms. All “scatter monitor” detectors from the second split to the end are tested with needle probes.

In the NW quadrant, “scatter monitor” detectors exist at the 3<sup>rd</sup> and 4<sup>th</sup> splits and at roughly the mid-points of the arms. All scatter monitors from the third split to the end are tested with GSG probes. (The “scatter monitor” detector between the second and third splits is tested with needle probes, as mentioned above.)

In the SE quadrant, “scatter monitor” detectors exist at the 3<sup>rd</sup> and 4<sup>th</sup> splits and at roughly the mid-points of the arms. All “scatter monitor” detectors from the third split to the end are probed with needle probes. (The “scatter monitor” detector between the second and third splits is tested with a GSG probe, as mentioned above.)

In the SW quadrant, “scatter monitor” detectors exist at the 3<sup>rd</sup> and 4<sup>th</sup> splits. They also exist at roughly 1/3 and 2/3 of the distance between the 3<sup>rd</sup> and 4<sup>th</sup> splits, as well as at roughly half-way between the fourth split and the end. An exception is in the D sub-quadrant, where two “scatter monitor” detectors are placed at roughly 1/3 and 2/3 of the distance from the fourth split to the end. All “scatter monitor” from the 3<sup>rd</sup> split to the end are probed with needle probes. (The “scatter monitor” detector between the second and third splits is probed with a GSG probe, as noted above.)

Probing orientation is as you would expect. The H-tree arms from the first to the second split and from the third to the fourth split run north-south, so the “scatter monitor” detectors along these arms are best probed from the east or west. The H-tree arms from the second to the third split and from the fourth split to the end run east-west, so the “scatter monitor” detectors along these arms are best probed from the north or south.

### **2.3 Large H-tree end-node detectors**

A detector structure exists at every end-node of the large H-tree. This section describes those end-node detectors. When a label is associated with the end-node detector structure, it is noted.

#### *2.3.1 NE A detector (REPLICA, 1)*

Three (3) repetitions of:

- Waveguide width: 0.50 $\mu$ m in, 0.50 $\mu$ m out
- Detector length: 50 $\mu$ m
- Contacts spacing: 1.14 $\mu$ m
- Metal-1 to metal-1 spacing: 0.79 $\mu$ m on left and right, 0.80 $\mu$ m in center

The single detector pad is 100 $\mu$ m by 100 $\mu$ m, and is not suitable for probing with a high-speed GSG probe. It's also not obvious how to probe the device with needle probes, as there is only the one pad. The other side of the detector appears to go through some FETs and other circuitry.

#### *2.3.2 NE B detector (BIG L,2)*

Three (3) repetitions of:

- Waveguide width: 0.50 $\mu\text{m}$  in, 0.51 $\mu\text{m}$  in middle, 0.50 $\mu\text{m}$  out
- Detector length: 50 $\mu\text{m}$
- Contacts spacing: 1.14 $\mu\text{m}$
- Metal-1 to metal-1 spacing: 0.80 $\mu\text{m}$  on left and right, 0.81 $\mu\text{m}$  in center

The single detector pad is 100 $\mu\text{m}$  by 100 $\mu\text{m}$ , and is not suitable for probing with a high-speed GSG probe. It's also not obvious how to probe the device with needle probes, as there is only the one pad. The other side of the detector appears to go through some FETs and other circuitry.

### 2.3.3 *NE C detector (unlabeld)*

Three (3) repetitions of:

- Waveguide width: 0.50 $\mu\text{m}$  in, 0.51 $\mu\text{m}$  in middle, 0.50 $\mu\text{m}$  out
- Detector length: 50 $\mu\text{m}$
- Contacts spacing: 1.14 $\mu\text{m}$
- Metal-1 to metal-1 spacing: 0.82 $\mu\text{m}$  on right, 0.81 $\mu\text{m}$  in center, 0.78 $\mu\text{m}$  on left

The detector is not suitable for probing with a high-speed GSG probe, but it can be probed with needle probes. Pad size is 100 $\mu\text{m}$  by 100 $\mu\text{m}$ .

### 2.3.4 *NE D detector (BIG L, 1)*

Three (3) repetitions of:

- Waveguide width: 0.50 $\mu\text{m}$  in, 0.51 $\mu\text{m}$  in middle, 0.50 $\mu\text{m}$  out
- Detector length: 50 $\mu\text{m}$
- Contacts spacing: 1.14 $\mu\text{m}$
- Metal-1 to metal-1 spacing: 0.80 $\mu\text{m}$  on left and right, 0.82 $\mu\text{m}$  in center

The single detector pad is 100 $\mu\text{m}$  by 100 $\mu\text{m}$ , and is not suitable for probing with a high-speed GSG probe. It's also not obvious how to probe the device with needle probes, as there is only the one pad. The other side of the detector appears to go through some FETs and other circuitry.

### 2.3.5 *NW A detector (REPLICA, 1)*

One (1) repetition of:

- Waveguide width: 0.50 $\mu\text{m}$  in, 0.50 $\mu\text{m}$  in middle, 0.50 $\mu\text{m}$  out
- Detector length: 50 $\mu\text{m}$
- Contacts spacing: 1.14 $\mu\text{m}$
- Metal-1 to metal-1 spacing: 0.80 $\mu\text{m}$  on left and right, 0.79 $\mu\text{m}$  in center

The single detector pad is 100 $\mu\text{m}$  by 100 $\mu\text{m}$ , and is not suitable for probing with a high-speed GSG probe. It's also not obvious how to probe the device with needle probes, as there is only the one pad. The other side of the detector appears to go through some FETs and other circuitry.

### 2.3.6 *NW B detector (unlabeled)*

One (1) repetition of:

- Waveguide width: 0.485 $\mu\text{m}$  in, 0.50 $\mu\text{m}$  in middle, 0.485 $\mu\text{m}$  out
- Detector length: 50 $\mu\text{m}$
- Contacts spacing: 1.14 $\mu\text{m}$
- Metal-1 to metal-1 spacing: 0.81 $\mu\text{m}$  on right, 0.78 $\mu\text{m}$  and 0.81 $\mu\text{m}$  in center, 0.80 $\mu\text{m}$  on right

The detector has pads suitable for probing with a high-speed GSG probe, or with needle probes. Probing with a GSG probe must be done from the north or south. The center pad is 80 $\mu\text{m}$  east-west by 100 $\mu\text{m}$  north-south. The overall pad side is 380 $\mu\text{m}$  east-west and 140 $\mu\text{m}$  north-south.

### 2.3.7 *NW C detector (REPLICA, 2)*

One (1) repetition of

- Waveguide width: 0.485 $\mu\text{m}$  in, 0.50 $\mu\text{m}$  in center, 0.485 $\mu\text{m}$  out
- Detector length: 50 $\mu\text{m}$
- Contact spacing: 1.14 $\mu\text{m}$
- Metal-1 to metal-1 spacing: 0.81 $\mu\text{m}$  on right, 0.78 $\mu\text{m}$  and 0.81 $\mu\text{m}$  in center, 0.80 $\mu\text{m}$  on left.

The single detector pad is 100 $\mu\text{m}$  by 100 $\mu\text{m}$ , and is not suitable for probing with a high-speed GSG probe. It's also not obvious how to probe the device with needle probes, as there is only the one pad. The other side of the detector appears to go through some FETs and other circuitry.

### 2.3.8 *NW D detector (BIG L, 1)*

One (1) repetition of

- Waveguide width: 0.50 $\mu\text{m}$  in, 0.50 $\mu\text{m}$  in center, 0.50 $\mu\text{m}$  out
- Detector length: 50 $\mu\text{m}$
- Contact spacing: 1.14 $\mu\text{m}$
- Metal-1 to metal-1 spacing: 0.77 $\mu\text{m}$  on right, 0.75 $\mu\text{m}$  and 0.76 $\mu\text{m}$  in center, 0.77 $\mu\text{m}$  on left.

The single detector pad is 100 $\mu\text{m}$  by 100 $\mu\text{m}$ , and is not suitable for probing with a high-speed GSG probe. It's also not obvious how to probe the device with needle probes, as there is only the one pad. The other side of the detector appears to go through some FETs and other circuitry.

### 2.3.9 *SW A detector (REPLICA, 1)*

One (1) repetition of

- Waveguide width: 0.50 $\mu\text{m}$  in, 0.50 $\mu\text{m}$  in center, 0.50 $\mu\text{m}$  out
- Detector length: 50 $\mu\text{m}$
- Contact spacing: 1.14 $\mu\text{m}$
- Metal-1 to metal-1 spacing: 0.78 $\mu\text{m}$  on left, 0.76 $\mu\text{m}$  and 0.78 $\mu\text{m}$  in center, 0.78 $\mu\text{m}$  on right.

The single detector pad is 100 $\mu\text{m}$  by 100 $\mu\text{m}$ , and is not suitable for probing with a high-speed GSG probe. It's also not obvious how to probe the device with needle probes, as there is only the one pad. The other side of the detector appears to go through some FETs and other circuitry.

Unfortunately, the single pad is missing the pad opening, apparently due to a design / layout error.

### 2.3.10 *SW B detector (BIG L, 2)*

One (1) repetition of

- Waveguide width: 0.50 $\mu\text{m}$  in, 0.50 $\mu\text{m}$  in center, 0.49 $\mu\text{m}$  out
- Detector length: 50 $\mu\text{m}$
- Contact spacing: 1.14 $\mu\text{m}$
- Metal-1 to metal-1 spacing: 0.80 $\mu\text{m}$  on right, 0.87 $\mu\text{m}$  in center, 0.80 $\mu\text{m}$  on left.

The single detector pad is 100 $\mu\text{m}$  by 100 $\mu\text{m}$ , and is not suitable for probing with a high-speed GSG probe. It's also not obvious how to probe the device with needle probes, as there is only the one pad. The other side of the detector appears to go through some FETs and other circuitry.

### 2.3.11 *SW C detector (unlabeled)*

One (1) repetition of

- Waveguide width: 0.49 $\mu\text{m}$  in, 0.50 $\mu\text{m}$  in center, 0.49 $\mu\text{m}$  out
- Detector length: 50 $\mu\text{m}$
- Contact spacing: 1.14 $\mu\text{m}$
- Metal-1 to metal-1 spacing: 0.79 $\mu\text{m}$  on right, 0.86 $\mu\text{m}$  in center, 0.79 $\mu\text{m}$  on left.

The detector has pads suitable for probing with a high-speed GSG probe or with needle probes. Probing with a GSG probe must be done from the north or south. The center pad is 80 $\mu\text{m}$  east-west by 100 $\mu\text{m}$  north-south. The overall pad side is 380 $\mu\text{m}$  east-west and 140 $\mu\text{m}$  north-south.

### 2.3.12 *SW D detector (BIG L, 1)*

One (1) repetition of

- Waveguide width: 0.50 $\mu\text{m}$  in, 0.50 $\mu\text{m}$  in center, 0.50 $\mu\text{m}$  out
- Detector length: 50 $\mu\text{m}$
- Contact spacing: 1.14 $\mu\text{m}$
- Metal-1 to metal-1 spacing: 0.79 $\mu\text{m}$  on right, 0.80 $\mu\text{m}$  in center, 0.79 $\mu\text{m}$  on left.

The single detector pad is 100 $\mu\text{m}$  by 100 $\mu\text{m}$ , and is not suitable for probing with a high-speed GSG probe. It's also not obvious how to probe the device with needle probes, as there is only the one pad. The other side of the detector appears to go through some FETs and other circuitry.

### 2.3.13 SE A detector (REPLICA, 1)

One (1) repetition of

- Waveguide width: 0.50 $\mu\text{m}$  in, 0.50 $\mu\text{m}$  in center, 0.50 $\mu\text{m}$  out
- Detector length: 50 $\mu\text{m}$
- Contact spacing: 1.14 $\mu\text{m}$
- Metal-1 to metal-1 spacing: 0.78 $\mu\text{m}$  on left, 0.79 $\mu\text{m}$  in center, 0.78 $\mu\text{m}$  on right.

The single detector pad is 100 $\mu\text{m}$  by 100 $\mu\text{m}$ , and is not suitable for probing with a high-speed GSG probe. It's also not obvious how to probe the device with needle probes, as there is only the one pad. The other side of the detector appears to go through some FETs and other circuitry.

### 2.3.14 SE B detector (BIG L, 1)

One (1) repetition of

- Waveguide width: 0.50 $\mu\text{m}$  in, 0.50 $\mu\text{m}$  in center, 0.50 $\mu\text{m}$  out
- Detector length: 50 $\mu\text{m}$
- Contact spacing: 1.14 $\mu\text{m}$

The single detector pad is 100 $\mu\text{m}$  by 100 $\mu\text{m}$ , and is not suitable for probing with a high-speed GSG probe. It's also not obvious how to probe the device with needle probes, as there is only the one pad. The other side of the detector appears to go through some FETs and other circuitry.

### 2.3.15 SE C detector (REPLICA, 2)

One (1) repetition of

- Waveguide width: 0.49 $\mu\text{m}$  in, 0.50 $\mu\text{m}$  in center, 0.49 $\mu\text{m}$  out
- Detector length: 50 $\mu\text{m}$
- Contact spacing: 1.14 $\mu\text{m}$
- Metal-1 to metal-1 spacing: 0.79 $\mu\text{m}$  on right, 0.80 $\mu\text{m}$  in center, 0.79 $\mu\text{m}$  on left.

The single detector pad is 100 $\mu\text{m}$  by 100 $\mu\text{m}$ , and is not suitable for probing with a high-speed GSG probe. It's also not obvious how to probe the device with needle probes, as there is only

the one pad. The other side of the detector appears to go through some FETs and other circuitry.

Unfortunately, the single pad is missing the pad opening, apparently due to a design / layout error.

#### 2.3.16 *SE D detector (unlabeled)*

One (1) repetition of

- Waveguide width: 0.50 $\mu\text{m}$  in, 0.50 $\mu\text{m}$  in center, 0.50 $\mu\text{m}$  out
- Detector length: 50 $\mu\text{m}$
- Contact spacing: 1.14 $\mu\text{m}$
- Metal-1 to metal-1 spacing: 0.79 $\mu\text{m}$  on left, 0.77 $\mu\text{m}$  in center, 0.79 $\mu\text{m}$  on right.

The detector is not suitable for probing with a high-speed GSG probe, but it is suitable for probing with two needle probes. Pads are 100 $\mu\text{m}$  by 100 $\mu\text{m}$ , and are probably best probed from the east or west.

### 3 Waveguide bend structures

Most of the waveguide bend structures start on the west side of the die and end on the north side. (Or vice-versa, depending on how you want to think about it.) There's also one set that starts on the west side and ends on the east side. (Or vice-versa.) (OK, this one, technically, isn't a "waveguide bend structure".)

Directions (e.g. north) are defined by a "North" arrow that is on the die, about 900 $\mu\text{m}$  in from the entrance to the large H-tree. However, from a naked-eye view, it's easier to orient the die by noting that the biosensor structures are on the east side of the die.

There are five sets of 90-degree bend structures, and one straight-through structure. Each set of 90-degree bend structures consists of five (5) waveguides: 0.50  $\mu\text{m}$ , 1  $\mu\text{m}$ , 2  $\mu\text{m}$ , 4  $\mu\text{m}$  and 8  $\mu\text{m}$  nominal widths, as you go from the inner part of the die towards the outer part of the die. (Actual drawn width may vary from the nominal width, as noted below.)

Each set of waveguides has its own bend radius, with the bend radius increasing as you move to waveguide sets further and further from the center of the die. (The bends don't appear to be perfect sections of a circle, so it's hard to define a unique bend radius.) In addition, the bend radius for each waveguide in a set will vary slightly, again increasing as you move further from the center of the die. (i.e. Go to larger waveguides.) For this reason, the bend radii listed below should be treated as rough estimates of the average bend radius for a set.

When scanning down the waveguide (e.g. for waveguide loss measurements), you are pretty much limited to doing the north-south segment. The east-west segment has four metal-2 bridges across the waveguide. These bridges would almost certainly interfere with any kind of waveguide loss measurements made on the waveguide.

The metal-2 bridges are approximately:

1. 569  $\mu\text{m}$  to 620  $\mu\text{m}$  or 468  $\mu\text{m}$  to 507  $\mu\text{m}$  from the west edge of the die (The bridge jogs to the east as it goes south, so the distance depends on the waveguide set)
2. 800  $\mu\text{m}$  to 804  $\mu\text{m}$  from the west edge of the die
3. 1980  $\mu\text{m}$  to 2161  $\mu\text{m}$  from the west edge of the die
4. 6287  $\mu\text{m}$  to 6403  $\mu\text{m}$  from the west edge of the die.

### 3.1 90-degree bend waveguides

#### 3.1.1 10 $\mu\text{m}$ bend radius waveguides

All dimensions in $\mu\text{m}$		Nominal width				
		0.5 $\mu\text{m}$	1 $\mu\text{m}$	2 $\mu\text{m}$	4 $\mu\text{m}$	8 $\mu\text{m}$
West edge to bend		6403	6415	6428	6442	6459
North edge to bend		6564	6576	6588	6602	6620
Total length (approx.)		12982	13006	13031	13059	13094
Width	West edge	0.50	1.00	2.01	3.99	8.00
	West side of bend	0.52	1.03	2.04	4.02	8.00
	North side of bend	0.50	1.00	2.00	4.00	8.00
	North edge	0.50	1.00	2.00	4.00	8.01
Gap	West side, to previous	n/a	11.96	11.82	12.17	13.19
	West side, to next	11.96	11.82	12.17	13.19	10.54
	North side, to previous	n/a	11.94	11.50	12.09	12.89
	North side, to next	11.94	11.50	12.09	12.89	10.99

The “previous” waveguide is the waveguide closer to the center of the die. The “next” waveguide is the waveguide further from the center of the die.

##### 3.1.1.1 0.5 $\mu\text{m}$ waveguide

6403  $\mu\text{m}$  from west edge of the die to the start of the bend, 6564  $\mu\text{m}$  from the end of the bend to the north edge of the die. Total waveguide length is approximately 12982  $\mu\text{m}$ . (This will change after edge polishing.) The waveguide is 0.50  $\mu\text{m}$  wide on the west side of the die and 0.50  $\mu\text{m}$  wide on the north side, tapering to 0.52  $\mu\text{m}$  on the west side of the bend and 0.50  $\mu\text{m}$  on the north side of the bend.

##### 3.1.1.2 1 $\mu\text{m}$ waveguide

6415  $\mu\text{m}$  from west edge of the die to the start of the bend, 6576  $\mu\text{m}$  from the end of the bend to the north edge of the die. Total waveguide length is approximately 13006  $\mu\text{m}$ . (This will change after edge polishing.) The gap between the 0.5  $\mu\text{m}$  waveguide and the 1  $\mu\text{m}$  wide waveguide is 11.96  $\mu\text{m}$  on the west side of the die and 11.94  $\mu\text{m}$  on the north side. The

waveguide is 1.00  $\mu\text{m}$  wide on the west side of the die and 1.00  $\mu\text{m}$  wide on the north side, tapering to 1.03  $\mu\text{m}$  on the west side of the bend and 1.00  $\mu\text{m}$  on the north side of the bend.

#### *3.1.1.3 2 $\mu\text{m}$ waveguide*

6428  $\mu\text{m}$  from west edge of the die to the start of the bend, 6588  $\mu\text{m}$  from the end of the bend to the north edge of the die. Total waveguide length is approximately 13031  $\mu\text{m}$ . (This will change after edge polishing.) The gap between the 1  $\mu\text{m}$  waveguide and the 2  $\mu\text{m}$  wide waveguide is 11.82  $\mu\text{m}$  on the west side of the die and 11.50  $\mu\text{m}$  on the north side. The waveguide is 2.01  $\mu\text{m}$  wide on the west side of the die and 2.00  $\mu\text{m}$  wide on the north side, tapering to 2.04  $\mu\text{m}$  on the west side of the bend and 2.00  $\mu\text{m}$  on the north side of the bend.

#### *3.1.1.4 4 $\mu\text{m}$ waveguide*

6442  $\mu\text{m}$  from west edge of the die to the start of the bend, 6602  $\mu\text{m}$  from the end of the bend to the north edge of the die. Total waveguide length is approximately 13059  $\mu\text{m}$ . (This will change after edge polishing.) The gap between the 2  $\mu\text{m}$  waveguide and the 4  $\mu\text{m}$  wide waveguide is 12.17  $\mu\text{m}$  on the west side of the die and 12.09  $\mu\text{m}$  on the north side. The waveguide is 3.99  $\mu\text{m}$  wide on the west side of the die and 4.00  $\mu\text{m}$  wide on the north side, tapering to 4.02  $\mu\text{m}$  on the west side of the bend and 4.00  $\mu\text{m}$  on the north side of the bend.

#### *3.1.1.5 8 $\mu\text{m}$ waveguide*

6459  $\mu\text{m}$  from west edge of the die to the start of the bend, 6620  $\mu\text{m}$  from the end of the bend to the north edge of the die. Total waveguide length is approximately 13094  $\mu\text{m}$ . (This will change after edge polishing.) The gap between the 4  $\mu\text{m}$  waveguide and the 8  $\mu\text{m}$  wide waveguide is 13.19  $\mu\text{m}$  on the west side of the die and 12.89  $\mu\text{m}$  on the north side. The waveguide is 8.00  $\mu\text{m}$  wide on the west side of the die and 8.01  $\mu\text{m}$  wide on the north side, tapering to 8.00  $\mu\text{m}$  on the west side of the bend and 8.00  $\mu\text{m}$  on the north side of the bend.

The “previous” waveguide is the waveguide closer to the center of the die. The “next” waveguide is the waveguide further from the center of the die.

### 3.1.2 20 $\mu\text{m}$ bend radius waveguides

All dimensions in $\mu\text{m}$		Nominal width				
		0.5 $\mu\text{m}$	1 $\mu\text{m}$	2 $\mu\text{m}$	4 $\mu\text{m}$	8 $\mu\text{m}$
West edge to bend		6469	6482	6493	6507	6525
North edge to bend		6629	6641	6654	6668	6684
Total length (approx.)		13129	13154	13178	13206	13240
Width	West edge	0.53	1.00	2.01	4.01	8.00
	West side of bend	0.51	1.02	2.02	4.02	7.99
	North side of bend	0.50	1.00	2.00	4.00	8.00
	North edge	0.53	1.00	2.00	3.95	8.01
Gap	West side, to previous	10.54	12.17	11.64	12.14	12.28
	West side, to next	12.17	11.64	12.14	12.28	11.16
	North side, to previous	10.99	12.17	10.29	12.56	13.16
	North side, to next	12.17	10.29	12.56	13.16	11.67

#### 3.1.2.1 0.5 $\mu\text{m}$ waveguide

6469  $\mu\text{m}$  from west edge of the die to the start of the bend, 6629  $\mu\text{m}$  from the end of the bend to the north edge of the die. Total waveguide length is approximately 13129  $\mu\text{m}$ . (This will change after edge polishing.) The gap between the 8  $\mu\text{m}$  wide, 10  $\mu\text{m}$  bend radius waveguide and the 0.5  $\mu\text{m}$  wide, 20  $\mu\text{m}$  bend radius waveguide is 10.54  $\mu\text{m}$  on the west side of the die and 10.99  $\mu\text{m}$  on the north side. The waveguide is 0.53  $\mu\text{m}$  wide on the west side of the die, 0.51  $\mu\text{m}$  on the west side of the bend, 0.50  $\mu\text{m}$  on the north side of the bend, and 0.53  $\mu\text{m}$  wide on the north side.

#### 3.1.2.2 1 $\mu\text{m}$ waveguide

6482  $\mu\text{m}$  from west edge of the die to the start of the bend, 6641  $\mu\text{m}$  from the end of the bend to the north edge of the die. Total waveguide length is approximately 13154  $\mu\text{m}$ . (This will change after edge polishing.) The gap between the 0.5  $\mu\text{m}$  waveguide and the 1  $\mu\text{m}$  wide waveguide is 12.17  $\mu\text{m}$  on the west side of the die and 12.17  $\mu\text{m}$  on the north side. The

waveguide is 1.00  $\mu\text{m}$  wide on the west side of the die, 1.02  $\mu\text{m}$  on the west side of the bend, 1.00  $\mu\text{m}$  on the north side of the bend, and 1.00  $\mu\text{m}$  wide on the north side.

#### *3.1.2.3 2 $\mu\text{m}$ waveguide*

6493  $\mu\text{m}$  from west edge of the die to the start of the bend, 6654  $\mu\text{m}$  from the end of the bend to the north edge of the die. Total waveguide length is approximately 13178  $\mu\text{m}$ . (This will change after edge polishing.) The gap between the 1  $\mu\text{m}$  waveguide and the 2  $\mu\text{m}$  wide waveguide is 11.64  $\mu\text{m}$  on the west side of the die and 10.29  $\mu\text{m}$  on the north side. The waveguide is 2.01  $\mu\text{m}$  wide on the west side of the die, 2.02  $\mu\text{m}$  on the west side of the bend, 2.00  $\mu\text{m}$  on the north side of the bend, and 2.00  $\mu\text{m}$  wide on the north side.

#### *3.1.2.4 4 $\mu\text{m}$ waveguide*

6507  $\mu\text{m}$  from west edge of the die to the start of the bend, 6668  $\mu\text{m}$  from the end of the bend to the north edge of the die. Total waveguide length is approximately 13206  $\mu\text{m}$ . (This will change after edge polishing.) The gap between the 2  $\mu\text{m}$  waveguide and the 4  $\mu\text{m}$  wide waveguide is 12.14  $\mu\text{m}$  on the west side of the die and 12.56  $\mu\text{m}$  on the north side. The waveguide is 4.01  $\mu\text{m}$  wide on the west side of the die, 4.02  $\mu\text{m}$  on the west side of the bend, 4.00  $\mu\text{m}$  on the north side of the bend, and 3.95  $\mu\text{m}$  wide on the north side of the die.

#### *3.1.2.5 8 $\mu\text{m}$ waveguide*

6525  $\mu\text{m}$  from west edge of the die to the start of the bend, 6684  $\mu\text{m}$  from the end of the bend to the north edge of the die. Total waveguide length is approximately 13240  $\mu\text{m}$ . (This will change after edge polishing.) The gap between the 4  $\mu\text{m}$  waveguide and the 8  $\mu\text{m}$  wide waveguide is 12.28  $\mu\text{m}$  on the west side of the die and 13.16  $\mu\text{m}$  on the north side. The waveguide is 8.00  $\mu\text{m}$  wide on the west side of the die and 8.01  $\mu\text{m}$  wide on the north side, tapering to 7.99  $\mu\text{m}$  on the west side of the bend and 8.00  $\mu\text{m}$  on the north side of the bend.

### 3.1.3 25 $\mu\text{m}$ bend radius waveguides

All dimensions in $\mu\text{m}$		Nominal width				
		0.5 $\mu\text{m}$	1 $\mu\text{m}$	2 $\mu\text{m}$	4 $\mu\text{m}$	8 $\mu\text{m}$
West edge to bend		6538	6550	6563	6576	6592
North edge to bend		6698	6710	6723	6737	6754
Total length (approx.)		13275	13299	13325	13352	13385
Width	West edge	0.50	1.00	2.00	4.00	7.02
	West side of bend	0.50	1.00	2.00	4.00	8.00
	North side of bend	0.50	1.00	2.00	4.00	8.00
	North edge	0.50	1.00	2.00	4.00	6.99
Gap	West side, to previous	11.16	11.54	11.77	11.56	12.71
	West side, to next	11.54	11.77	11.56	12.71	19.02
	North side, to previous	11.67	11.43	11.67	11.48	12.50
	North side, to next	11.43	11.67	11.48	12.50	18.22

#### 3.1.3.1 0.5 $\mu\text{m}$ waveguide

6538  $\mu\text{m}$  from west edge of the die to the start of the bend, 6698  $\mu\text{m}$  from the end of the bend to the north edge of the die. Total waveguide length is approximately 13275  $\mu\text{m}$ . (This will change after edge polishing.) The gap between the 8  $\mu\text{m}$  wide, 20  $\mu\text{m}$  bend radius waveguide and the 0.5  $\mu\text{m}$  wide, 25  $\mu\text{m}$  bend radius waveguide is 11.16  $\mu\text{m}$  on the west side of the die and 11.67  $\mu\text{m}$  on the north side. The waveguide is 0.50  $\mu\text{m}$  wide on the west side of the die and on both sides of the bend and also 0.50  $\mu\text{m}$  on the north side.

#### 3.1.3.2 1 $\mu\text{m}$ waveguide

6550  $\mu\text{m}$  from west edge of the die to the start of the bend, 6710  $\mu\text{m}$  from the end of the bend to the north edge of the die. Total waveguide length is approximately 13299  $\mu\text{m}$ . (This will change after edge polishing.) The gap between the 0.5  $\mu\text{m}$  waveguide and the 1  $\mu\text{m}$  wide waveguide is 11.54  $\mu\text{m}$  on the west side of the die and 11.43  $\mu\text{m}$  on the north side. The

waveguide is 1.00  $\mu\text{m}$  wide on the west side of the die and on both sides of the bend, and also 1.00  $\mu\text{m}$  wide on the north side.

#### *3.1.3.3 2 $\mu\text{m}$ waveguide*

6563  $\mu\text{m}$  from west edge of the die to the start of the bend, 6723  $\mu\text{m}$  from the end of the bend to the north edge of the die. Total waveguide length is approximately 13325  $\mu\text{m}$ . (This will change after edge polishing.) The gap between the 1  $\mu\text{m}$  waveguide and the 2  $\mu\text{m}$  wide waveguide is 11.77  $\mu\text{m}$  on the west side of the die and 11.67  $\mu\text{m}$  on the north side. The waveguide is 2.00  $\mu\text{m}$  wide on the west side of the die and on both sides of the bend, and also 2.00  $\mu\text{m}$  wide on the north side.

#### *3.1.3.4 4 $\mu\text{m}$ waveguide*

6576  $\mu\text{m}$  from west edge of the die to the start of the bend, 6737  $\mu\text{m}$  from the end of the bend to the north edge of the die. Total waveguide length is approximately 13352  $\mu\text{m}$ . (This will change after edge polishing.) The gap between the 2  $\mu\text{m}$  waveguide and the 4  $\mu\text{m}$  wide waveguide is 11.56  $\mu\text{m}$  on the west side of the die and 11.48  $\mu\text{m}$  on the north side. The waveguide is 4.00  $\mu\text{m}$  wide on the west side of the die and on both sides of the bend, and also 4.00  $\mu\text{m}$  wide on the north side.

#### *3.1.3.5 8 $\mu\text{m}$ waveguide*

6592  $\mu\text{m}$  from west edge of the die to the start of the bend, 6754  $\mu\text{m}$  from the end of the bend to the north edge of the die. Total waveguide length is approximately 13385  $\mu\text{m}$ . (This will change after edge polishing.) The gap between the 4  $\mu\text{m}$  waveguide and the 8  $\mu\text{m}$  wide waveguide is 12.71  $\mu\text{m}$  on the west side of the die and 12.50  $\mu\text{m}$  on the north side. The waveguide is 7.02  $\mu\text{m}$  wide on the west side of the die and 6.99  $\mu\text{m}$  wide on the north side, tapering to 8.00  $\mu\text{m}$  on both sides of the bend.

### 3.1.4 50 $\mu\text{m}$ bend radius waveguides

All dimensions in $\mu\text{m}$		Nominal width				
		0.5 $\mu\text{m}$	1 $\mu\text{m}$	2 $\mu\text{m}$	4 $\mu\text{m}$	8 $\mu\text{m}$
West edge to bend		6593	6605	6618	6633	6650
North edge to bend		6755	6768	6782	6799	6818
Total length (approx.)		13426	13451	13478	13510	13546
Width	West edge	0.50	1.00	2.00	4.00	7.00
	West side of bend	0.50	1.00	2.00	4.00	8.00
	North side of bend	0.50	1.00	2.00	4.00	8.00
	North edge	0.50	1.00	2.00	4.00	8.09
Gap	West side, to previous	19.02	13.00	12.41	13.10	13.01
	West side, to next	13.00	12.41	13.10	13.01	26.55
	North side, to previous	18.22	11.39	11.97	13.07	12.91
	North side, to next	11.39	11.97	13.07	12.91	24.70

#### 3.1.4.1 0.5 $\mu\text{m}$ waveguide

6593  $\mu\text{m}$  from west edge of the die to the start of the bend, 6755  $\mu\text{m}$  from the end of the bend to the north edge of the die. Total waveguide length is approximately 13426  $\mu\text{m}$ . (This will change after edge polishing.) The gap between the 8  $\mu\text{m}$  wide, 25  $\mu\text{m}$  bend radius waveguide and the 0.5  $\mu\text{m}$  wide, 50  $\mu\text{m}$  bend radius waveguide is 19.02  $\mu\text{m}$  on the west side of the die and 18.22  $\mu\text{m}$  on the north side. The waveguide is 0.50  $\mu\text{m}$  wide on the west side of the die and on both sides of the bend and also 0.50  $\mu\text{m}$  on the north side

#### 3.1.4.2 1 $\mu\text{m}$ waveguide

6605  $\mu\text{m}$  from west edge of the die to the start of the bend, 6768  $\mu\text{m}$  from the end of the bend to the north edge of the die. Total waveguide length is approximately 13451  $\mu\text{m}$ . (This will change after edge polishing.) The gap between the 0.5  $\mu\text{m}$  wide waveguide and the 1  $\mu\text{m}$  wide waveguide is 13.00  $\mu\text{m}$  on the west side of the die and 11.39  $\mu\text{m}$  on the north side. The

waveguide is 1.00  $\mu\text{m}$  on the west side of the die and both sides of the bend and also 1.00  $\mu\text{m}$  on the north side.

#### *3.1.4.3 2 $\mu\text{m}$ waveguide*

6618  $\mu\text{m}$  from west edge of the die to the start of the bend, 6782  $\mu\text{m}$  from the end of the bend to the north edge of the die. Total waveguide length is approximately 13478  $\mu\text{m}$ . (This will change after edge polishing.) The gap between the 1  $\mu\text{m}$  wide waveguide and the 2  $\mu\text{m}$  wide waveguide is 12.41  $\mu\text{m}$  on the west side of the die and 11.97  $\mu\text{m}$  on the north side.. The waveguide is 2.00  $\mu\text{m}$  wide on the west side of the die and on both sides of the bend and also 2.00  $\mu\text{m}$  on the north side.

#### *3.1.4.4 4 $\mu\text{m}$ waveguide*

6633  $\mu\text{m}$  from west edge of the die to the start of the bend, 6799  $\mu\text{m}$  from the end of the bend to the north edge of the die. Total waveguide length is approximately 13510  $\mu\text{m}$ . (This will change after edge polishing.) The gap between the 2  $\mu\text{m}$  wide waveguide and the 4  $\mu\text{m}$  wide waveguide is 13.1  $\mu\text{m}$  on the west side of the die and 13.07  $\mu\text{m}$  on the north side. The waveguide is 4.00  $\mu\text{m}$  wide on the west side of the die and on both sides of the bend, and also 4.00  $\mu\text{m}$  on the north side.

#### *3.1.4.5 8 $\mu\text{m}$ waveguide*

6650  $\mu\text{m}$  from west edge of the die to the start of the bend, 6818  $\mu\text{m}$  from the end of the bend to the north edge of the die. Total waveguide length is approximately 13546  $\mu\text{m}$ . (This will change after edge polishing.) The gap between the 4  $\mu\text{m}$  waveguide and the 8  $\mu\text{m}$  wide waveguide is 13.01  $\mu\text{m}$  on the west side of the die and 12.91  $\mu\text{m}$  on the north side. The waveguide is 7.00  $\mu\text{m}$  wide on the west side of the die and 8.09  $\mu\text{m}$  wide on the north side, tapering to 8.00  $\mu\text{m}$  on both sides of the bend.

### 3.1.5 100 $\mu\text{m}$ bend radius waveguides

All dimensions in $\mu\text{m}$		Nominal width				
		0.5 $\mu\text{m}$	1 $\mu\text{m}$	2 $\mu\text{m}$	4 $\mu\text{m}$	8 $\mu\text{m}$
West edge to bend		6633	6643	6658	6672	6689
North edge to bend		6798	6809	6822	6838	6855
Total length (approx.)		13588	13609	13637	13667	13701
Width	West edge	0.46	0.93	2.12	4.14	8.07
	West side of bend	0.50	1.00	2.00	4.00	8.00
	North side of bend	0.50	1.00	2.00	4.00	8.00
	North edge	0.46	1.07	2.14	4.87	8.00
Gap	West side, to previous	26.55	9.04	11.95	11.68	12.12
	West side, to next	9.04	11.95	11.68	12.12	25.06 (to straight WG)
	North side, to previous	24.70	9.78	13.06	11.78	12.36
	North side, to next	9.78	13.06	11.78	12.36	n/a

#### 3.1.5.1 0.5 $\mu\text{m}$ waveguide

6633  $\mu\text{m}$  from west edge of the die to the start of the bend, 6798  $\mu\text{m}$  from the end of the bend to the north edge of the die. Total waveguide length is approximately 13588  $\mu\text{m}$ . (This will change after edge polishing.) The gap between the 8  $\mu\text{m}$  wide, 50  $\mu\text{m}$  bend waveguide and 0.5  $\mu\text{m}$  wide, 100  $\mu\text{m}$  bend radius waveguide is 24.70  $\mu\text{m}$  on the north side of the die and 26.55  $\mu\text{m}$  on the west side. The waveguide is 0.46  $\mu\text{m}$  wide on both the north and west sides of the die and tapers to 0.50  $\mu\text{m}$  on both sides of the bend.

#### 3.1.5.2 1 $\mu\text{m}$ waveguide

6643  $\mu\text{m}$  from west edge of the die to the start of the bend, 6809  $\mu\text{m}$  from the end of the bend to the north edge of the die. Total waveguide length is approximately 13609  $\mu\text{m}$ . (This will change after edge polishing.) The gap between the 0.5  $\mu\text{m}$  waveguide and the 1  $\mu\text{m}$  waveguide is 9.78  $\mu\text{m}$  on the north side of the die and 9.04  $\mu\text{m}$  on the west side. The

waveguide is 1.07  $\mu\text{m}$  wide on the north side of the die and 0.93  $\mu\text{m}$  wide on the west side, tapering to 1.00  $\mu\text{m}$  on both sides of the bend.

#### *3.1.5.3 2 $\mu\text{m}$ waveguide*

6658  $\mu\text{m}$  from west edge of the die to the start of the bend, 6822  $\mu\text{m}$  from the end of the bend to the north edge of the die. Total waveguide length is approximately 13637  $\mu\text{m}$ . (This will change after edge polishing.) The gap between the 1 $\mu\text{m}$  waveguide and the 2 $\mu\text{m}$  waveguide is 13.06  $\mu\text{m}$  on the north edge of the die and 11.95  $\mu\text{m}$  on the east edge. This waveguide is 2.14  $\mu\text{m}$  wide on the north side of the die and 2.12  $\mu\text{m}$  wide on the west side, tapering to 2.00  $\mu\text{m}$  wide on both sides of the bend.

#### *3.1.5.4 4 $\mu\text{m}$ waveguide*

6672  $\mu\text{m}$  from west edge of the die to the start of the bend, 6838  $\mu\text{m}$  from the end of the bend to the north edge of the die. Total waveguide length is approximately 13667  $\mu\text{m}$ . (This will change after edge polishing.) The gap between the 2  $\mu\text{m}$  waveguide and the 4  $\mu\text{m}$  waveguide is 11.78  $\mu\text{m}$  on the north edge of the die and 11.68  $\mu\text{m}$  on the east edge. This waveguide is 4.87  $\mu\text{m}$  wide on the north side of the die and 4.14  $\mu\text{m}$  wide on the west side. Both directions taper to 4.00  $\mu\text{m}$  at the bend.

#### *3.1.5.5 8 $\mu\text{m}$ waveguide*

6689  $\mu\text{m}$  from west edge of the die to the start of the bend, 6855  $\mu\text{m}$  from the end of the bend to the north edge of the die. Total waveguide length is approximately 13701  $\mu\text{m}$ . (This will change after edge polishing.) The gap between the 4  $\mu\text{m}$  waveguide and the 8  $\mu\text{m}$  waveguide is 12.36  $\mu\text{m}$  on the north edge of the die and 12.12  $\mu\text{m}$  on the west edge. This waveguide is 8.00  $\mu\text{m}$  wide on the north side of the die and on both sides of the bend, and tapers to 8.07  $\mu\text{m}$  wide on the west side.

### 3.2 Straight-through waveguides

As with the waveguide bend structures, the “straight-through” waveguides consist of a group of five (5) waveguides, 0.5  $\mu\text{m}$ , 1  $\mu\text{m}$ , 2  $\mu\text{m}$ , 4  $\mu\text{m}$  and 8  $\mu\text{m}$  in width. Lacking a bend, all of the “straight-through” waveguides are 9415  $\mu\text{m}$  in length.

Note that the waveguide prior to the 0.5  $\mu\text{m}$  straight-through waveguide is the 8  $\mu\text{m}$  wide, 100  $\mu\text{m}$  bend radius waveguide, but only on the west edge. On the east side, there is no waveguide prior to the 0.5  $\mu\text{m}$  straight-through waveguide.. Note also that there is no waveguide after the 8  $\mu\text{m}$  straight-through waveguide, on either the west or east sides.

All dimensions in $\mu\text{m}$		Nominal width				
		0.5 $\mu\text{m}$	1 $\mu\text{m}$	2 $\mu\text{m}$	4 $\mu\text{m}$	8 $\mu\text{m}$
West edge to east edge		9415	9415	9415	9415	9415
Width	West edge	0.50	1.00	2.00	4.00	8.00
	East edge	0.50	1.00	2.00	4.00	8.00
Gap	West side, to previous	25.06	10.20	10.09	10.10	10.00
	West side, to next	10.20	10.09	10.10	10.00	n/a
	East side, to previous	n/a	10.20	10.09	10.10	10.00
	East side, to next	10.20	10.09	10.10	10.00	n/a

Appendix D

PROCESS FLOWS FOR THE FIRST AND SECOND-GENERATION OPTICAL TEST CHIPS

1 First generation process flow

This process flow, done at what is now Avago Technologies, Fort Collins, CO, had the minimum processing to establish the basic feasibility of the concepts behind the optical interconnect technology examined in this work. At Avago, this process flow was known as EXPCSUXX. Measurement holds were placed after steps 4302, 4308, 4312, 4548, 4550 and 4580.

4005	RUN MAKE UP	0010	4005S	RUN MAKE UP
4140	GROW FIELD OXIDE	0010	4140S	GROW FIELD OXIDE
4290	DEP POLY	0010	4290S	DEP POLY
4302	MASK 6 POLY GATE	0010	4302S	MASK 6 POLY
4308	POLYSILICON ETCH	0010	4308S	POLYSILICON
4311	SECOND SULFURIC CLN	0010	4311S	SECOND SULFURIC CLEAN
4312	MEASURE GATE	0010	4312S	MEASURE GATE
4390	DEP NITRIDE SPACER	0010	4390S	DEP NITRIDE SPACER
4400	ETCH NITRIDE SPACER	0010	4400S	ETCH NITRIDE SPACER
4405	CLEAN NITRIDE SPACER	0010	4405S	CLEAN NITRIDE SPACER
4435	CLEAN N+ RTA	0010	4435S	CLEAN N+ RTA
4440	RTA N+ S/D	0010	4440S	RTA N+ S/D
4480	ANNEAL P+ S/D	0010	4480S	ANNEAL P+ S/D
4490	DEP RESISTOR NIT	0010	4490S	DEP RESISTOR NIT
4530	DEP 7% PSG	0010	4530S	DEP 7% PSG
4534	DENS PSG	0010	4534S	DENS PSG
4541	DEP DIEL .5	0010	4541S	DEP DIEL .5
4542	POLISH DIEL .5	0010	4542S	POLISH DIEL .5
4543	DEP WAVEGUIDE NIT	0010	4543S	DEP WAVEGUIDE NIT
4544	MASK 71 WAVEGUIDE	0010	4544S	MASK 71 WAVEGUIDE
4546	WAVEGUIDE ETCH	0010	4546S	WAVEGUIDE ETCH
4547	DEP DIEL 1	0010	4547S	DEP DIEL 1
4548	POLISH DIEL 1	0010	4548S	POLISH DIEL 1
4550	MASK 12 CONTACT 1	0010	4550S	MASK 12 CONTACT
4560	ETCH CONTACT 1	0010	4560S	ETCH CONTACT 1
4561	STRIP CONTACT 1	0010	4561S	STRIP CONTACT 1
4563	DEP TIN SEED LAYER 1	0010	4563S	DEP TIN SEED LAYER 1
4565	DEP W PLUG 1	0010	4565S	DEP W PLUG 1
4567	POLISH W PLUG 1	0010	4567S	POLISH W PLUG 1
4570	DEP METAL 1	0010	4570S	DEP METAL 1
4580	MASK 13 METAL 1	0010	4580S	MASK 13 METAL
4590	ETCH METAL 1	0010	4590S	ETCH METAL 1
4980	ANNEAL PASSIVATION	0010	4980S	ANNEAL PASSIVATION

## 2 Second generation process flow

The second generation process flow was also done at Avago Technologies in Fort Collins, CO. In contrast to the first generation process flow, this process flow was a full process up through the second layer of metal, and included working MOSFETs. This process flow was based on Avago's A07 QLAPX process, with some steps added, primarily to make the detectors and optical waveguides. This also involved moving step 4540 to step 4547. The steps added to create the detectors and optical waveguides can be identified by a lack of any entry in the "PROCESS" field below. In addition, some steps removed. This was primarily because they involved metal layers after the second. Measurement holds were placed after steps 4302, 4308, 4312, 4548, 4550 and 4580.

PROCESS	LOCATION	OPERATION	LOCATION_DESCRIPTION
A07QLAPX	4030	4030S	RUN_MAKE_UP
A07QLAPX	4040	4040SX	MASK_01_ACTIVE_AREA
A07QLAPX	4050	4050SL	ETCH_ACTIVE_AREA_NIT
A07QLAPX	4070	4070S	MASK_92_N-WELL
A07QLAPX	4080	4080S	IMPLANT_N_WELL
A07QLAPX	4090	4090S	STRIP_RESIST_N_WELL
A07QLAPX	4100	4100S	DRIVE_N_WELL
A07QLAPX	4110	4110S	GROW_LOCOS_OXIDE
A07QLAPX	4121	4121S	DEP_LOCOS_NITRIDE_2
A07QLAPX	4131	4131S	ETCH_LOCOS_NITRIDE_2
A07QLAPX	4140	4140S	GROW_FIELD_OXIDE
A07QLAPX	4151	4151S	ETCH_NITRIDE
A07QLAPX	4160	4160S	GROW_SAC_OXIDE
A07QLAPX	4180	4180SX	MASK_02_P_CHANNEL
A07QLAPX	4195	4195S	IMPLANT_PCHAN_MIDDLE
A07QLAPX	4205	4205S	IMPLANT_PCHAN_SHALLO
A07QLAPX	4220	4220S	STRIP_RESIST_P_CHAN
A07QLAPX	4230	4230SX	MASK_03_N_CHANNEL
A07QLAPX	4242	4242S	IMPLANT_NCHAN_DEEP
A07QLAPX	4247	4247S	IMPLANT_NCHAN_MIDDLE
A07QLAPX	4255	4255S	IMPLANT_NCHAN_SHALLO
A07QLAPX	4260	4260S	STRIP_RESIST_N_CHAN
A07QLAPX	4272	4272SX	MASK_04_CAPACITOR
A07QLAPX	4273	4273S	IMPLANT_CAPACITOR
A07QLAPX	4275	4275S	STRIP_CAPACITOR_IMPL
A07QLAPX	4276	4276S	MASK_45_PNP_BASE
A07QLAPX	4277	4277S	PNP_BASE_IMPLANT
A07QLAPX	4278	4278S	PNP_BASE_IMPLANT_STR
A07QLAPX	4280	4280SL	GROW_GATE_OXIDE
A07QLAPX	4290	4290S	DEP_POLY
A07QLAPX	4292	4292S	MASK_05_POLY_IMPLANT
A07QLAPX	4294	4294S	IMPLANT_POLY
A07QLAPX	4296	4296S	STRIP_RESIST
A07QLAPX	4297	4297S	CLEAN_POLY_IMPLANT
A07QLAPX	4302	4302S	MASK_6_POLY_GATE

A07QLAPX	4308	4308S	POLYSILICON_ETCH
A07QLAPX	4311	4311S	SECOND_SULFURIC_CLN
	4312	4312S	MEASURE_GATE
A07QLAPX	4320	4320SX	MASK_07_NLDD
A07QLAPX	4330	4330S	IMPLANT_NLDD
A07QLAPX	4340	4340S	STRIP_RESIST_NLDD
A07QLAPX	4350	4350S	GROW_POLY_OXIDE_80A
A07QLAPX	4360	4360SX	MASK_08_PLDD
A07QLAPX	4375	4375S	IMPLANT_PLDD
A07QLAPX	4380	4380S	STRIP_RESIST_PLDD
A07QLAPX	4390	4390S	DEP_NITRIDE_SPACER
A07QLAPX	4400	4400S	ETCH_NITRIDE_SPACER
A07QLAPX	4405	4405S	CLEAN_NITRIDE_SPACER
A07QLAPX	4410	4410SX	MASK_09_N+_S/D
A07QLAPX	4420	4420S	IMPLANT_N+_S/D
A07QLAPX	4430	4430S	STRIP_RESIST_N+_S/D
A07QLAPX	4435	4435S	CLEAN_N+_RTA
A07QLAPX	4440	4440S	RTA_N+_S/D
A07QLAPX	4450	4450SX	MASK_10_P+_S/D
A07QLAPX	4465	4465S	IMPLANT_P+_S/D
A07QLAPX	4470	4470S	STRIP_RESIST_P+_S/D
A07QLAPX	4475	4475S	CLEAN_P+_RTA
A07QLAPX	4480	4480S	ANNEAL_P+_S/D
A07QLAPX	4490	4490S	DEP_RESISTOR_NIT
A07QLAPX	4495	4495S	MASK_11_RESISTOR
A07QLAPX	4497	4497S	ETCH_RESISTOR_NIT
A07QLAPX	4498	4498S	PRE-TI-DEP_CLEAN
A07QLAPX	4500	4500S	DEP_TITANIUM
A07QLAPX	4510	4510S	IMPLANT_SI
A07QLAPX	4520	4520S	ANNEAL_TISI2
A07QLAPX	4530	4530S	DEP_7%_PSG
A07QLAPX	4534	4534S	DENS_PSG
	4541	4541S	DEP_DIEL .5
	4542	4542S	POLISH_DIEL .5
	4543	4543S	DEP_WAVEGUIDE_NIT
	4544	4544S	MASK_71_WAVEGUIDE
	4546	4546S	WAVEGUIDE_ETCH
A07QLAPX	4547	4547S	DEP_DIEL_1 (Moved from 4540 to 4547)
A07QLAPX	4548	4548S	POLISH_DIEL_1
A07QLAPX	4550	4550S	MASK_12_CONTACT_1
A07QLAPX	4560	4560S	ETCH_CONTACT_1
A07QLAPX	4561	4561S	STRIP_CONTACT_1
A07QLAPX	4563	4563S	DEP_TIN_SEED_LAYER_1
A07QLAPX	4565	4565S	DEP_W_PLUG_1
A07QLAPX	4567	4567S	POLISH_W_PLUG_1
A07QLAPX	4570	4570S	DEP_METAL_1
A07QLAPX	4580	4580S	MASK_13_METAL_1
A07QLAPX	4590	4590S	ETCH_METAL_1
A07QLAPX	4600	4600S	DEP_DIEL_2
A07QLAPX	4648	4648S	POLISH_DIEL_2
A07QLAPX	4650	4650S	MASK_14_CONTACT_2
A07QLAPX	4660	4660S	ETCH_CONTACT_2
A07QLAPX	4663	4663S	DEP_TIN_SEED_2
A07QLAPX	4665	4665S	DEP_W_PLUG_2
A07QLAPX	4667	4667S	POLISH_W_PLUG_2
A07QLAPX	4680	4680S	DEP_METAL_2

A07QLAPX	4685	4685S	MASK_15_METAL_2
A07QLAPX	4690	4690S	ETCH_METAL_2
A07QLAPX	4892	4892S	DEP_PASSIVATION
A07QLAPX	4976	4976S	MASK_20_PASSIVATION
A07QLAPX	4977	4977S	ETCH_PASSIVATION
A07QLAPX	4980	4980S	ANNEAL_PASSIVATION
A07QLAPX	4993	4993XFER	TRANSFER_TO_BLDG_1
A07QLAPX	4995	4995S.M4	TEST_APT

### 3 Explanation of terms and acronyms.

The mask numbers are for the full A07QLAPX process. In general, mask numbers increase with each mask step, however there are exceptions. The exceptions are generally based on historic reasons connected with other processes.

“LOCOS” stands for Local Oxidation of Silicon. “SAC OXIDE” is sacrificial oxide. “NLDD” and “PLDD” stand for N and P Lightly Doped Drain, respectively. “S/D” is source / drain. “RTA” is rapid thermal anneal. “NIT” is nitride”. “PSG” is phosphosilicate glass, basically phosphorous-doped silicon dioxide. “DIEL .5” stands for dielectric-0.5, and is called this because it was inserted before dielectric-1, or what is normally the first dielectric layer. “W\_PLUG” is tungsten plug – W is the chemical symbol for tungsten.

## *Appendix E*

### DIE EDGE POLISHING PROCEDURE

Polishing the die edge to an optical-quality finish is a crucial step in the sample preparation process. Without an optical-quality finish on the die edge, it will be difficult or impossible to couple light into waveguides on the chip.

These instructions are written for use with the Allied MultiPrep tool in the Physical Analysis lab at Avago Technologies. With the agreement of Ron Kee, manager of Avago's Physical Analysis Lab, I was allowed to use their MultiPrep tool to do sample preparation. This permission was largely due to the fact that Ron and I knew each other from my time at Avago, and Ron knew I could be trusted with the equipment. This ability to use their MultiPrep tool was a great help to me, as I was able to get much better edge polish results with it than I could with the Buehler Ecomet polisher in our CSU lab.

While these instructions are written with the MultiPrep in mind, the basic principle also apply to the Ecomet tool as well.

1. When preparing to put the cover slip on the sample, spray the surface of the sample with some isopropyl, to clean it, before applying the cover slip.
2. After applying the cover slip to the sample, move it around over the sample, to ensure good coverage of CrystalBond across the sample. This allows the CrystalBond to form a "gasket" on top of the sample. Gaps or bubbles in the CrystalBond could result in surface damage to the sample while polishing. While doing moving the cover slip around on the sample, try to ensure the CrystalBond is uniform in thickness across the sample.
3. When placing the cover slip on the sample, try to have the top edge of the cover slip away from the top edge of the stub (i.e. sample holder). If the cover slip is past the top of the stub, the cover slip will have to be ground down or you won't be able to properly mount the stub in the polisher mount. It's impossible to have the cover slip well away from both the left and right sides of the stubs, so have the overhang on the left side. You can polish down the left side; you can't polish the right side, due to the stub handle.
4. When trying to decide if the sample is square to start with (i.e. before grinding down the cover slip), check the edge of the sample relative to the **top** of the stub, not the

bottom. The top will be flush against the holder, and will be fixed. The bottom of the stub could have been ground down at some previous time.

5. Use the grinder to take the cover slip down close to the edge of the sample, maybe 0.5mm to 1mm away from the edge. As noted above, any part of the cover slip sticking out past the edge of the stub (except on the sample edge side) will have to be polished down so that the cover slip is even with the stub.
  - a. The grinder does not have a stub holder; you have to manually hold the stub in place.
  - b. Recommended rotational speed for the grinder is 250 to 300 RPM
  - c. Grinding seems to work best if the sample is nearly parallel to the rotational direction of the grinding wheel. The cover slip has a tendency to pop off if the sample is perpendicular to the rotational direction. Best guess is that this is a vibration issue. However, make sure the grinding wheel hits the cover slip before the sample. (i.e. Don't come in from the "back side" of the sample.)
6. As with the grinder, polishing samples with a cover slip on them seems to go better if the sample is nearly parallel to the rotational direction of the grinder or polisher wheel. Use the polisher's "Rotation – Full" button to change the angle of the sample with respect to the polishing wheel. You can control the rotational speed of the sample head by holding the "Rotation – Full" button down for a few seconds until the polisher beeps and the timer display changes to indicate the rotation speed. Use the up and down arrows on the numeric keypad to change the rotational speed up or down. Slowing the rotational speed of the head can make it easier to get the angle you want.
  - a. As with grinding, polishing samples with the sample perpendicular to the rotational direction seems to cause the cover slip to pop off the sample.
  - b. Don't rotate the sample head with the raising cam engaged. The head will slip off the cam and fall down.
  - c. Recommended rotational speed for the polisher is 200RPM.
  - d. You can roughly control how much material is removed by using the Mitutoyo gauge on the polisher. Turn the gauge on, then make sure it is reading millimeters, not inches, by checking for a little "mm" in the lower right corner of the display. Note that 0.001mm is 1 micron. Set the gauge to zero by pressing the yellow "Zero/Abs" button while the sample is suspended in mid-air. (You may wind up getting -0.001 instead of zero.) Lower the cam, then use the "RAISE/LOWER" knob at the back of the polisher to lower the head until the amount of material you want to remove is displayed on the Mitutoyo gauge's display. Due to "wobble" in the polish disk, this value isn't exact, so use it with some caution. (The wobble in the disk means that you might be at a low spot on the disk, so you'll remove more than you think, or at a high spot on the disk, so you'll remove less than you think.)
  - e. When you first move from the grinder to the polisher, use the Mitutoyo gauge to take off only 25µm or so for the first couple of passes. This is in case the cover slip is slightly angled, and will help you avoid digging into the

polishing paper and accidentally ruining it. Taking off 25 to 50 $\mu$ m should smooth off any edges in the cover slip, without going deep enough into the polishing paper to damage it.

7. During polishing, regularly check the “squareness” of the polishing relative to the sample edge.
  - a. To increase the polish rate on the right side of the sample, adjust the micrometer screw at the back of the sample mount (with the release lever on the right side) clockwise while looking down at it.
  - b. Similarly, to increase the polish rate on the left side of the sample, adjust the micrometer screw counter-clockwise.
8. If you have to, or want to, stop polishing at some point (say to eat lunch or go to the restroom), I recommend leaving the sample under the inspection scope. That way, it’s easy to re-inspect the sample and see what needs to be done. I find that if I leave the stub on the stub holder, or if I put the stub back on the stub holder after inspecting it, when I resume polishing I have trouble remembering if I was getting ready to take the stub off and inspect it, or if I had put the stub back on and was getting ready to resume polishing.
9. When applying the final polishing:
  - a. Use the red fiber polishing pad.
  - b. Use the red Buehler Masterpolish 2 polishing liquid in the cabinet above and to the right of the polisher.
  - c. Wet down the polishing pad first.
  - d. Do not pour the liquid from the bottle on to the polishing pad. Instead, use two pipettes worth of the liquid, taking care not to get any of the dried crud around the mouth of the bottle either on the polishing pad, in the pipette or in the liquid itself. (Pipettes are available in the cabinet to the left of the sliding doors into the electrical analysis lab.)
  - e. After squirting the liquid on to the polishing pad, smear it around with your finger.
  - f. Do not use cooling water during the polishing step.
  - g. Final polishing should take only about 10 to, at most, 30 seconds.
  - h. Don’t bother trying to use the Mitutoyo height gauge on the final polish step – it won’t work the red fiber pad. You can determine when the sample is in contact with the pad by looking for the fluid flow that pushes up against the cover slip.
  - i. When you think you’ve got the final polish as good as it’s going to get, rinse the sample off in tap water from the sink next to the polisher and blow the sample dry using an air gun. If any of the liquid polish dries on the edge of the sample, you can remove it with a little organic soap (from the bottle at the sink) and water on a cotton-tipped swab.

- j. Once you're done, it may look like the waveguides are completely gone. This is an optical illusion caused by the polishing of the edge of the cover slip.
- k. In addition, once you're done with the final polish, rinse the red fiber pad off in tap water from the sink next to the polisher. You don't want the polishing liquid to dry on the pad.

*Appendix F*

FIRST AND SECOND GENERATION DIE NUMBERING SCHEME

**First generation die numbering scheme**

The first generation die numbering scheme is shown in Figure 1.

	1	2	3	4	5	6	7	8	9	10	11	12	13	14	15
A						A6	A7	A8	A9						
B				B4	B5	B6	B7	B8	B9	B10	B11				
C			C3	C4	C5	C6	C7	C8	C9	C10	C11	C12			
D		D2	D3	D4	D5	D6	D7	D8	D9	D10	D11	D12	D13	D14	D15
E		E1	E2	E3	E4	E5	E6	E7	E8	E9	E10	E11	E12	E13	E14
F		F1	F2	F3	F4	F5	F6	F7	F8	F9	F10	F11	F12	F13	F14
G		G1	G2	G3	G4	G5	G6	G7	G8	G9	G10	G11	G12	G13	G14
H		H1	H2	H3	H4	H5	H6	H7	H8	H9	H10	H11	H12	H13	H14
I		I1	I2	I3	I4	I5	I6	I7	I8	I9	I10	I11	I12	I13	I14
J		J1	J2	J3	J4	J5	J6	J7	J8	J9	J10	J11	J12	J13	J14
K		K1	K2	K3	K4	K5	K6	K7	K8	K9	K10	K11	K12	K13	K14
L		L1	L2	L3	L4	L5	L6	L7	L8	L9	L10	L11	L12	L13	L14
M		M1	M2	M3	M4	M5	M6	M7	M8	M9	M10	M11	M12	M13	M14
N															

Figure 1: First generation die numbering scheme, full-size

## **Second generation die numbering scheme**

The second generation die numbering scheme is shown in Figure 2. Some general information about second generation wafers is as follows:

- 15 rows from top to bottom, plus a blank half-column at the bottom.
- 14 columns from left to right, plus printed half-columns on both the left and right.
- 60mm major flat.
- 38mm minor flat.
- Columns end at left and right of major flat, with six columns across major flat.
- Rows end at top and bottom of minor flat, with four rows along minor flat.

A1	A2	A3	A4	A5	A6	A7	A8	A9	A10	A11	A12	A13	A14
B1	B2	B3	B4	B5	B6	B7	B8	B9	B10	B11	B12	B13	B14
C1	C2	C3	C4	C5	C6	C7	C8	C9	C10	C11	C12	C13	C14
D1	D2	D3	D4	D5	D6	D7	D8	D9	D10	D11	D12	D13	D14
E1	E2	E3	E4	E5	E6	E7	E8	E9	E10	E11	E12	E13	E14
F1	F2	F3	F4	F5	F6	F7	F8	F9	F10	F11	F12	F13	F14
G1	G2	G3	G4	G5	G6	G7	G8	G9	G10	G11	G12	G13	G14
H1	H2	H3	H4	H5	H6	H7	H8	H9	H10	H11	H12	H13	H14
I1	I2	I3	I4	I5	I6	I7	I8	I9	I10	I11	I12	I13	I14
J1	J2	J3	J4	J5	J6	J7	J8	J9	J10	J11	J12	J13	J14
K1	K2	K3	K4	K5	K6	K7	K8	K9	K10	K11	K12	K13	K14
L1	L2	L3	L4	L5	L6	L7	L8	L9	L10	L11	L12	L13	L14
M1	M2	M3	M4	M5	M6	M7	M8	M9	M10	M11	M12	M13	M14
N1	N2	N3	N4	N5	N6	N7	N8	N9	N10	N11	N12	N13	N14
O1	O2	O3	O4	O5	O6	O7	O8	O9	O10	O11	O12	O13	O14

Figure 2: Second generation die numbering scheme, full-size

## MEASUREMENT INSTRUCTIONS

### **1 Performing DC and AC measurements on edge-coupled waveguide detectors**

#### **1.1 Align the fiber to the waveguide**

1. Position the sample so that it is reasonably square to the sample holder and fiber.
2. Make sure the Keithley output is disabled, and then attach test leads from the Keithley to the bias tee's DC input.
3. Connect the AC output of the bias tee to the input of the Miteq AM-1646 amp. Note: You don't need the Miteq amp in the part but you will in the next, and you don't want to be making connections to things connected to the probe card once you've finished the fiber alignment that is done in this step.
4. Manually retract the fiber so that it is in no danger of hitting the sample during the next few steps.
5. Roughly align the fiber to the waveguide for the detector of interest. You don't have to be very close at this step, within 50 to 100  $\mu\text{m}$  will do for now. (For reference, the pads for the edge-coupled waveguide detectors are 315  $\mu\text{m}$  by 380  $\mu\text{m}$ .)
6. Lower the probe card on to the pads of the device to be tested. Don't raise the probes until done will all measurements, DC and AC, on the device.
7. Set the ThorLabs piezostage to X=75, Y=75, Z=150
8. Manually move the fiber in so that it is as close as possible to the sample without actually touching the sample. Move the fiber left/right and up/down a little, to be sure that it is clear in all four directions.
9. Turn the microscope light off.

10. Set the Keithley to force a voltage and measure a current. Set the Keithley bias voltage to 10V and the current compliance to 1  $\mu$ A, and then enable the Keithley output.
11. Connect the laser diode to the ILX Lightwave and set the current to an appropriate level. (75 mA for the Hitachi HL6738MG laser diode, 40 mA for the Sharp GH06510B2A laser diode.) Note: Before taking the current all the way up, stop just above threshold ( $\sim$ 42 mA for the Hitachi,  $\sim$ 30 mA for the Sharp) and use the microscope to check that the laser spot from the fiber is near the waveguide entrance. Adjust appropriately if not, then continue increasing the drive current.
12. Manually align the fiber to the detector waveguide so that you obtain close to the maximum current response from the detector. Note: This is a rough alignment, so you don't have to hit the exact maximum. You just want to have the fiber "reasonably" close to the maximum response point.
13. Reset the piezostage to X=0, Y=0, Z=0.
14. Enter the run conditions for the LabVIEW program "ThorLabs MDT693xyz Keithley 2400.vi". As of 11 Sept 2008, this LabVIEW VI only exists on the C921 computer and is located in the C:\Program Files\ThorLabs\LabVIEW folder. This isn't the best place for the program, so it may move. If it does, you'll have to search for it. You may want to create a Windows Desktop shortcut to the program, if you haven't already. See Appendix H for screen captures of this LabVIEW program.
  - a. Use COM Port 1 and "Fast Y" unless you're sure you don't want to.
  - b. Set Y-axis V start to 0, Y-axis V stop to 150, Y-axis V step to 5. (These are recommended settings. You can change them if you want, but be sure you know what you are doing.)
  - c. Set X-axis V start to 10, X-axis V stop to 140, X-axis V step to 5. (Again, these are only recommended settings.)

- d. Set Z-axis V start to 150, Z-axis backup voltage amount to 0.1 and Z-axis backup V step to 0.1. (Again, these are only recommended settings.)
  - e. Set “2<sup>nd</sup> pass” to “Scan about max”.
  - f. Set 2<sup>nd</sup> pass Y range to 30 and 2<sup>nd</sup> pass Y V step to 1.
  - g. Set 2<sup>nd</sup> pass X range to 25 and 2<sup>nd</sup> pass X V step to 1.
  - h. Set the output file name. Make sure it’s in a folder you can write to. I use ThorLabs\_Keithley\_YYYYMMDD\_HHMM.txt, where YYYYMMDD\_HHMM is the time when the run starts.
15. Record all the important data about this run: Start time, finish time (when finished), wafer, die, device, laser diode, drive current, Vbias, compliance limit, measurement speed setting, “ThorLabs MDT693xyz Keithley 2400” settings, initial dark current (you’ll need to turn the laser diode off briefly for this), first pass max and location, second pass max and location, end-of-run values, and anything else you think worth recording. An example of this kind of record is at the end of this section. I record this data, along with the name of the output file, in a file called “metadata.txt”. “metadata”, because it’s data about data.
16. Place a blackout cloth over the probe stage.
17. Start the ThorLabs Keithley LabVIEW program.
18. When using the recommended settings listed above, the program will take about 1 ¾ hours to run. (About 25 minutes for the first pass and about 80 minutes for the second pass.) When it finished, you should have a fiber nicely aligned to the waveguide.

The following is an example of the data recorded for an alignment run. This kind of information is often called “metadata” – data about data – and is often kept in a file called “metadata.txt”.

- \* Started at 0838 15 Jun 2008, finished at 1025.
- \* Wfr 0443B150 (2nd gen), die J9, 4,10,4.64 device (NEW DEVICE!)
- \* NOTE: Hitachi HL638MG LD
- \* Idrive set to 75.0mA nominal (ILX Lightwave LDX-3525) (No HP DMM hooked up at present.)
- \* Detector Vbias set to +10V, compliance set to 1.05 mA on Keithley 2400.
- \* Measurement speed set to "Hi-Accuracy".
- \* Data obtained using "ThorLabs MDT693xyz Keithley 2400" LabVIEW VI, with Y-axis (parallel to long axis of edge of die) running from 0V to 150V in 5V steps, X-axis (perpendicular to long axis of edge of die) running from 10V to 140V in 5V steps and Z axis (along optical propagation axis) running from 150V to 149.9V in 0.1V steps.
- \* Running in "Y fast" mode.
- \* Post-first-pass scans are +/-30V around max in 1V steps on Y, +/-25V around max in 1V steps in X.
- \* Initial rough alignment, as always, was done with piezocontroller set to 75V on both X and Y stages, then reset to 0V on both before starting the VI. In addition, Z axis was set to 150V, then also reset to 0V before starting. The fiber was placed so that that edge appeared to be just barely off the edge of the die. (As close as possible without touching.) Free travel was verified by moving the fiber in the Y and X axes while the top of the fiber and the waveguide were in focus simultaneously.
  - Initial dark current: 0.28 uA
  - First pass max: (missed)
  - Second pass max: 66.809uA at Y=92, X=79
  - End-of-run display on Keithley: 57.8 uA (REM), 57.1 uA (LOC)

“REM” stands for REMote mode, while “LOC” stands for “LOCal” mode.

After both the first and second passes, evaluate the appearance of the measurement results. The resulting peak should be symmetric. If it is not, you may have a measurement problem. Possibly the fiber was too close to sample die (i.e. touching), perhaps something changed during the alignment run without you doing anything to cause it. In combination with the magnitude and location of the first and second pass peaks, decide whether it is necessary to re-run the alignment.

## 1.2 If desired, perform your DC measurement

1. If you want to perform an AC measurement, not a DC measurement, skip to Section 1.3.

2. For a DC measurement, decide if you want to do a voltage sweep (OK, technically a voltage sweep isn't a DC measurement, but it's commonly considered a DC measurement) or a measurement at a single bias voltage.
  - a. If you want to do a voltage sweep measurement, see the documentation on performing dark current voltage sweep measurements in Section 2. If you want to do a voltage sweep, you're probably going to want to do sweeps of both dark current and photocurrent. The only difference in the procedure for the two measurements is that for a dark current measurement, the source laser diode is off, while for a photocurrent measurement the laser diode is on at whatever drive current bias point you want to use. Remember to record the laser diode drive current with the other information about the measurement in a metadata file, as was done in the alignment example in Section 1.1. Note: Use different metadata files for the alignment data and for the DC response data. For dark current measurements, it's obviously not important how well the input fiber is aligned to the waveguide. On the other hand, it doesn't hurt dark current measurements if the input fiber is well aligned, and the input fiber must be well-aligned in order to perform accurate photocurrent measurements.
  - b. If you want to do a single bias voltage measurement, you're already set up once you've finished the alignment process. Just pick the bias voltage you want to use on the Keithley and make your measurement.

### **1.3 Apply an AC pulse to the laser diode to create an optical pulse, then measure the resulting electrical output from the detector**

1. Disable the output of the HP 8116A function generator before proceeding.
2. Put on a grounding strap, then disconnect the Hitachi laser diode from the ILX Lightwave laser diode driver (a DC source) and connect it to the function generator (an AC source). Be sure to run the output of the function generator through the adaptor card (which contains a 47  $\Omega$  resistor and a laser diode socket) before connecting to the connectorized Hitachi laser diode. **NOTE: Failure to use the**

**adaptor card, with its 47  $\Omega$  current-limiting resistor, may result in failure of the connectorized laser diode.**

3. Connect a power supply capable of outputting at least 15 V and at least 125 mA to the Miteq AM-1646 amp. Set the power supply to 15V.
4. Connect the output of the Miteq amp to the electrical channel input of the Agilent 86100 DCA. Note that the Miteq amp is an inverting amplifier. This means that the pulse on the DCA will be upside down from what you might expect.
5. Set the initial voltage pulse conditions on the function generator (typically  $V_{OL} = 0.0V$ ,  $V_{OH} = 0.1V$ , pulse width = 8 nsec, frequency = 20 MHz) then enable the function generator output.
6. Set the Agilent 86100 DCA appropriately. Since this procedure is covered in Section 3, it will not be repeated here. An exception will be made to remind the reader of the necessity of wearing a grounding strap when using the 86100A DCA.
7. Turn on the Keithley, to bias the photodetector. Use a 10 V bias, unless otherwise specified.
8. Begin increasing the  $V_{OH}$  level. As  $V_{OH}$  goes past 3.60 V, you should start seeing a pulse on the 86100A's screen. **NOTE: Under no circumstances should you increase  $V_{OH}$  above 4.70 V when using the Hitachi laser diode. Failure to observe this limitation may result in damage or failure of the Hitachi laser diode.** Note that you may have to play around some with the voltage/division, voltage offset, time/division and time offset settings in order to see the pulse. You might need to find the pulse at the 4.70 V setting and then reduce  $V_{OH}$  until you're at the level you actually want to use.
9. When you reach the desired  $V_{OH}$  level, record the trace data to the DCA's internal hard drive, then copy the data to a floppy. **NOTE: Attempting to record the trace data to the floppy directly, without first saving data to the internal hard**

**drive, is not recommended, due to potential loss of data.** Record all the pertinent measurement information in a file. As with the fiber alignment step, I store this kind of information in a file called “metadata.txt”. An example of the kind of data stored in the file is at the end of this section.

The following is an example of the kind of information stored in the AC pulse measurement’s “metadata.txt” file. Note that this the “metadata.txt” file for AC pulse data, not the “metadata.txt” file for alignment data or the “metadata.txt” for the DC response data.

```
waveform_20080528_1705.txt
* Wfr 0443B150 (2nd gen), die J9, device 0.5,10,2.14 (NEW DEVICE!)
* 86100A DCA settings:
  - 5.0 mV/div, offset -18.7 mV, 2.0 nsec/div, delay 66.6121 nsec, ave
    256, two 10 dB attenuators in the signal path, front panel trigger
    from FG
* HP8116A function generator: 8 nsec pulse width, 20 MHz rep rate, Vol
  = 0.0 V, Voh = 4.00 V
* Keithley: 5.169V (equivalent to 10V on a 4.14um contact spacing
  device), 1.05 mA compliance, Iphoto = 2.8 uA
* Miteq amp: 15.03 V indicated, 120 mA indicated
* 90% to 10% fall time of trace (rise time of detector response, due to
  inverting amp) - bouncing around too much
  - My eye doesn't believe the 90% and 10% levels.
* FWHM 2.727 ns
```

You may notice the pulse suddenly shrinking while you are doing the measurement. I’m not sure what causes this, but don’t freak out. Sometimes the pulse comes back on its own in a few minutes. If this doesn’t happen, my suggestion is to take the VOH level back down to 0.1 V, then disable the Keithley output (so the detector is no longer biased, then take the Miteq amplifier power supply back down to 0 V. Wait 30 minutes to an hour, and then try again. I’m not sure if this helps, but it can’t hurt. The reason behind the changes is that the pulse change might be due to some sort of thermal effect. If still no luck, try re-aligning the fiber to the waveguide.

If you can’t get a decent pulse at  $V_{OH} = 3.60$  V, increase  $V_{OH}$  until you do, then just note that fact in the “metadata.txt” file. i.e. “Couldn’t get a measureable pulse until  $V_{oh} = 3.90V$ .”

## 2 General procedure for dark current and photocurrent voltage sweep measurements

These instructions provide an overview of the sequence of events to do the dark current voltage sweep measurements. They are not necessarily detailed at any given step.

It is assumed that prior to these steps the probe card has been connected to the 4145 through the triaxial cables. (The red alligator clip on the triaxial cables is connector to the center conductor on the cable.) Further, these instructions assume the triaxial cables are connected to the rear-panel jacks for SMU3 and SMU4.

When using the 4145, it is not practical to verify electrical connectivity between the probe card and the pads by turning the microscope light up and down, as was done when using the Keithley 2400 SourceMeter. You need to verify good probe contact in other ways, possibly by examining the scrub marks on the pads, possibly by making sure your results make sense.

These same basic instructions will also work for photocurrent voltage sweep measurements.

The only two differences are:

1. You must align the input fiber from the laser diode source to detector you want to measure before the measurement. For normal incidence MSM detectors, this means placing the input fiber above the detector. For waveguide-coupled MSM detectors, this means aligning the input fiber to the waveguide for the detector. For details on the process of aligning the fiber to the waveguide, see Section 1.1.
2. The laser diode is on. (Duh.)

With those preliminaries out of the way, we can now move on to the measurement procedure itself.

1. Set up the 4145 for a voltage sweep measurement.
  - a. Channel Definition
    - i. SMU3: V3, I3, V mode, VAR1

- ii. SMU4: V4, I4, COM mode, CONST
        - iii. Press the “NEXT” button
      - b. Source Setup
        - i. VAR1 setup: Linear sweep, Start: -20V, Stop: +20V, Step: 0.1V, current compliance: 10 $\mu$ A
        - ii. Press the “NEXT” button
      - c. Measure & Display Mode Setup
        - i. X: V3, Linear, -20V, +20V
        - ii. Y: I3, Linear, -10 $\mu$ A, +10 $\mu$ A
        - iii. Press the “NEXT” button
      - d. Integration time: Long
2. Turn on the microscope light, to the lowest-possible setting. The remaining steps, up to “Turn off the light and start the voltage sweep” should be done in 60 seconds, for consistency.
3. Place the probes on the device to be tested.
4. Place the blackout cloth over the system.
5. Wait the remainder of the 60 seconds, then turn off the microscope light, wait 15 seconds (for the microscope light to be completely off) and start the voltage sweep by pressing the SINGLE button in the MEASUREMENT section of the front panel.
  - a. When the voltage sweep finishes, you may want to press the AUTO SCALE softkey button, to better display the results.



- ii. SMU4:V4 COM, 0, 105mA compliance (Can't change these)
    - iii. Press the "NEXT" button
  - c. Measurement Mode:
    - i. Time Domain Setup: Time delay = 1.00sec, time interval = 1.00 second, # readings = 300
    - ii. Display Mode Setup
      - 1. X: Time, Linear, 0, 300
      - 2. Y: I3, Linear, 0uA, 1uA
    - iii. Press the "NEXT" button
- 8. Turn the microscope light on for one minute, on the lowest possible setting, just past the "On" click.
- 9. Turn the microscope light off.
- 10. Start the time-domain sweep by pressing the SINGLE button in the MEASUREMENT section of the front panel.
  - a. Again, you may want to press the AUTO-SCALE softkey button, to better display the results.
  - b. Again, check for signs of flat-lining and hitting the current compliance. If so, go back to step 7.b.i and increase the current compliance limit. Again, you must be smart if you increase the current compliance.
- 11. Use the "HP4145 Data Output2" program to save the time domain measurement data to a file.

- a. Name of measurement: I3, Start: 1, Step: 1
  - b. Again, you will need to press the LOCAL button to return the instrument to local mode after running the “Data Output2” program.
  - c. When you save this data, call it the “time domain1” data.
12. Repeat the time domain measurement, but this time allow at least 15 seconds from the time you turn off the light to the time you start the measurement. This will allow the microscope light to turn off and cool down.
  13. When you save this data, call it the “time domain2” data.
  14. Remove the blackout cover, move to the next device and repeat. Note that a time-domain measurement forces the integration time to “Short”, so you will have to change the integration time to “Long” before running the voltage sweep.

### **3 Using the Agilent 86100A DCA to measure optical and electrical pulses**

1. The 86100A DCA (a.k.a. DCA) has two input channels. Channel1 is the optical input channel, while Channel 2 is the electrical input channel, like a regular oscilloscope.
2. Both channels have a maximum input signal level. The optical channel is easily overloaded by the output of one of the connectorized laser diodes, especially the high-power Hitachi laser diode. For that reason, when using the optical channel, start with low drive currents. In addition, you probably won't be able to insert the end of the fiber all the way into the optical channel's input socket.
3. When measuring electrical signals using Channel 2, start by connecting two 10 dB attenuators to the DCA's input connector. If you can't detect a signal, remove one attenuator. If you still can't detect a signal, remove the other attenuator.
4. When attaching and removing cables and attenuators, only rotate the hexagonal nut. Don't rotate the entire connector. This will avoid damaging the threads.

5. When using the 10 dB attenuators on the electrical channel, protect the DCA's connector by leaving the attenuators attached as much as possible. Disconnect the cable by removing it from the attenuators; don't disconnect the cable by removing the attenuators and cable from the DCA. If you are going to be doing measurements without any attenuators, talk to Dr. Lear about using a "Connector Saver" with the DCA.
6. The DCA has multiple input modes, set by buttons a little to the right of the display. For essentially everything you're going to want to do, you'll want to make sure you're in "Oscilloscope" mode.
7. To maintain equipment accuracy, you need to calibrate the DCA at least every 10 hours. Do this by selecting "Calibrate" → "Calibrate All" → "Vertical Left"
8. You're probably going to want to be in "Averaging" mode, especially when taking electrical measurements on the detectors. To set averaging mode, go "Setup" → "Acquisition". A new window will appear on the display. Select a value for the number of periods to be averaged. You can either select a predefined value (powers of 2) or enter your own. 256 is a good choice to start with, if you don't have any better ideas. Note that for some reason, it appears that you can't manually enter a 0 into an averaging value. i.e. You can average 111 samples, but not 100 samples.
9. The Hitachi HL6738MG laser diode is rated for 35 mW. Threshold is about 41 mA. Operating current is 75 mA. When using a function generator in pulse or square wave mode, an operating current of 75 mA corresponds to a low voltage level of 0.00 V and a high voltage level of approximately 4.70 V. Threshold corresponds to a high voltage level of approximately 3.60 V. Note that these voltage level correspondences are only valid for the Hitachi HL6738MG laser diode, not for the Sharp GH06510B2A.
10. When using the function generator in pulse mode to drive a laser diode (currently the most common technique for performing AC measurements), make sure the pulse width is set to 8 nsec, the minimum possible pulse width.

11. **Use a grounding strap when handling a laser diode or any test leads connected to the laser diode.** Failure to follow this rule may result in you personally buying a new connectorized laser diode.
12. **Use a grounding strap when connecting or disconnecting cables from the DCA.** Failure to follow this rule may result in you personally paying for repairs to the DCA. In the interests of caution, I use a grounding strap even when pushing front panel buttons on the DCA.
13. Ordinary oscilloscopes have vertical and horizontal divisions which are limited to certain fixed values. e.g. 10 nsec/div or 25 mV/div. This is not the case with the DCA. You can have, say, 2.3 nsec/div or 14.1 mV/div. This is neither a good thing nor a bad thing. It is, however, something to be aware of.
14. Ordinary oscilloscopes can trigger off the displayed signal. This is not the case with the DCA. You must use a trigger signal. This would typically be from the trigger output of the function generator, and would be sent to the trigger input of the DCA.
15. When you display a detector trace, a good time unit to start with is so the horizontal axis is 10 ns and so the peak of the response is about 2 ns in. These are just guidelines to get you started, not hard and fast rules that must always be obeyed.
16. It is possible to save DCA trace data. Be sure to save the data to the internal hard drive first. Only after the data is on the hard drive should you try copying the data to a floppy in the DCA's floppy drive. Sometimes the process of copying data to the floppy drive doesn't work. If the data is on the hard drive, you can just try copying later, possibly with a different floppy disk. If you try to copy the data to the floppy first, before copying the data to the hard drive, and the transfer doesn't work, you've just created a problem for yourself.
  - a. To save the data, select "File" → "Save As" → "Waveform" → "Verbose (text)"

- b. When entering the filename, you must also include the “.txt” extension.
  - c. The saved file will only have the Y-axis data. You can reconstruct the X-axis data from the X-origin and X-increment values that are included when you specify “Verbose”. (“Verbose” mode also gives you some other useful information.)
17. When saving or copying data, make sure you’re using the correct channel – electrical (Channel 1) or optical (Channel 2), as the case may be. Also make sure you’re not accidentally set to use one of the memories instead of an active channel.
18. When you save data, use a unique filename. I like to use the timestamp when I save the file. e.g. 20080716\_1530. And, of course, be sure to record what the test conditions were for the measurement.
- a. Wafer, die and device
  - b. DCA settings: voltage offset; volts/division; time offset; time/division; averaging settings; presence of attenuators, if any; trigger conditions, and anything else that you think would be useful to replicate or understand the results.
  - c. Function generator: model, pulse width (if applicable), repetition rate (if applicable), low voltage level, high voltage level, and anything else that you think would be useful to replicate or understand the results.
  - d. Bias conditions: bias source, bias voltage
  - e. Amplifier conditions: amp model, source voltage, source current
  - f. You may also find it useful to measure and record the pulse fall time (since we’re using an inverting amp) and pulse full-width half-max (FWHM).

## *Appendix H*

### LABVIEW SCREEN CAPTURES

Two LabVIEW programs were written to aid in the measurement process. “ThorLabs MDT693xyz Keithley 2400.vi” performed the alignment of the input optical fiber to the waveguide leading to the edge-coupled waveguide detectors, while “MultiAbsoluteMoveAndRead.vi” performed the waveguide scans for the waveguide loss measurements. Front panel and block diagram screen captures from both LabVIEW VIs are shown below.

# 1 ThorLabs MDT693xyz Keithley 2400

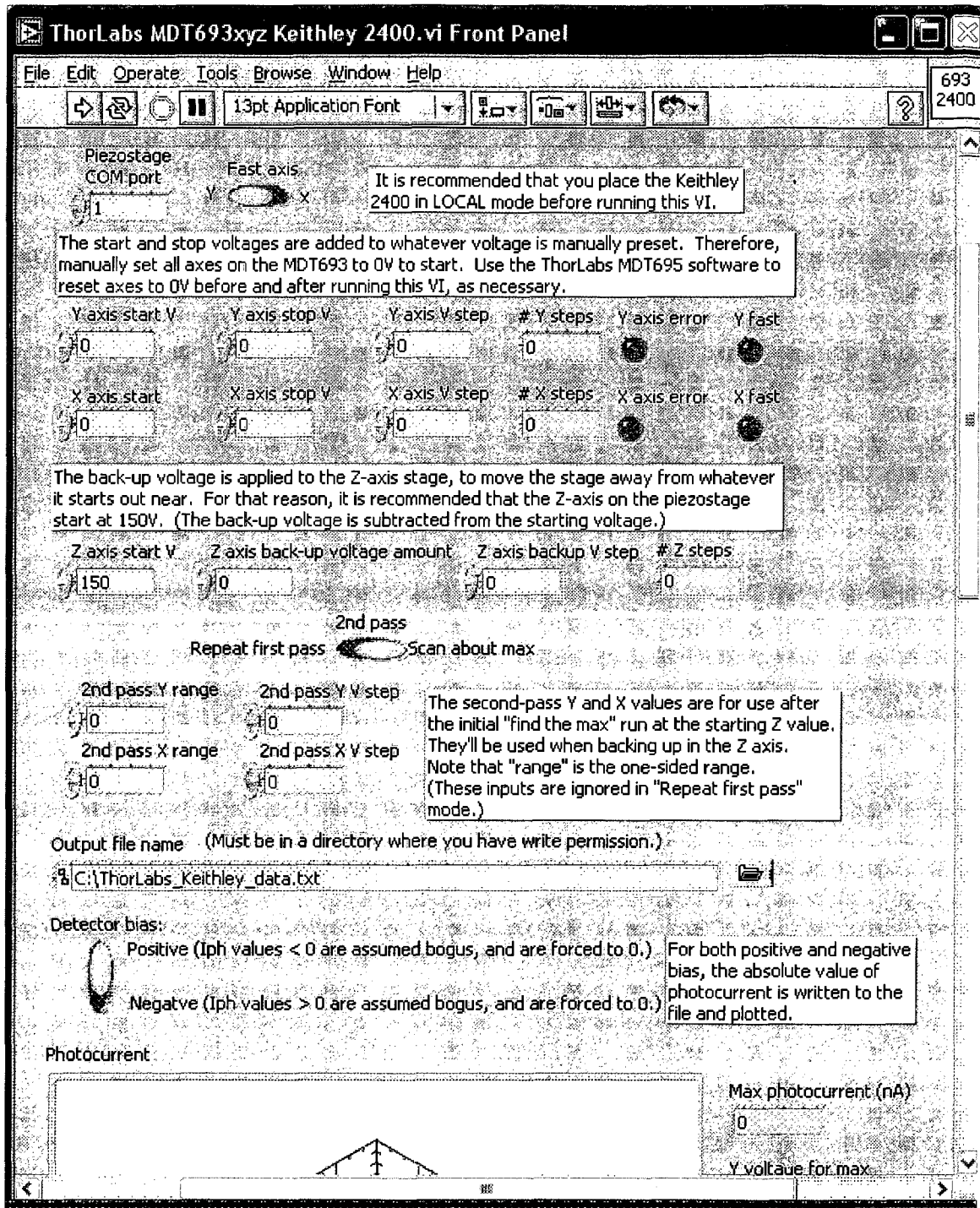


Figure 1: Front panel, top third

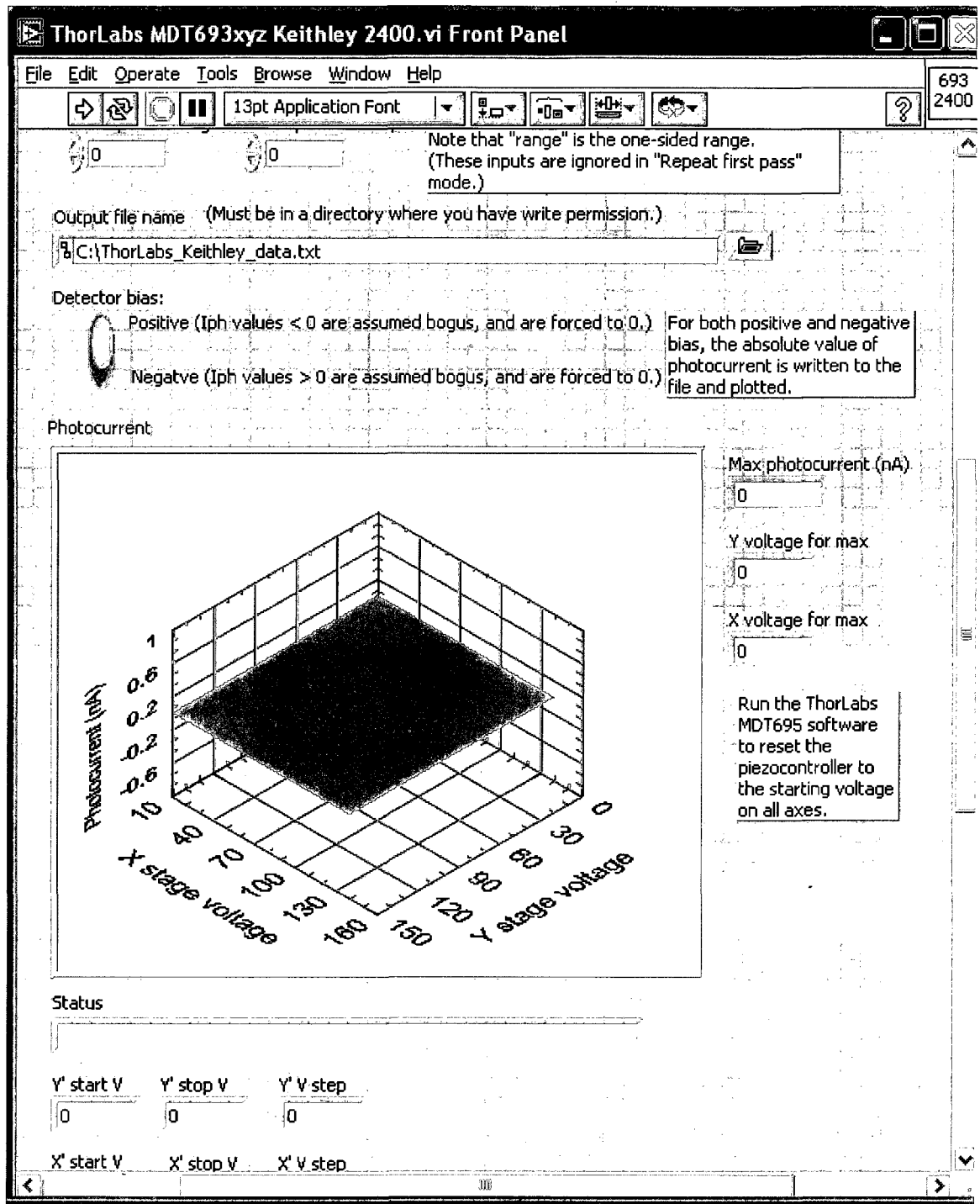


Figure 2: Front panel, middle third

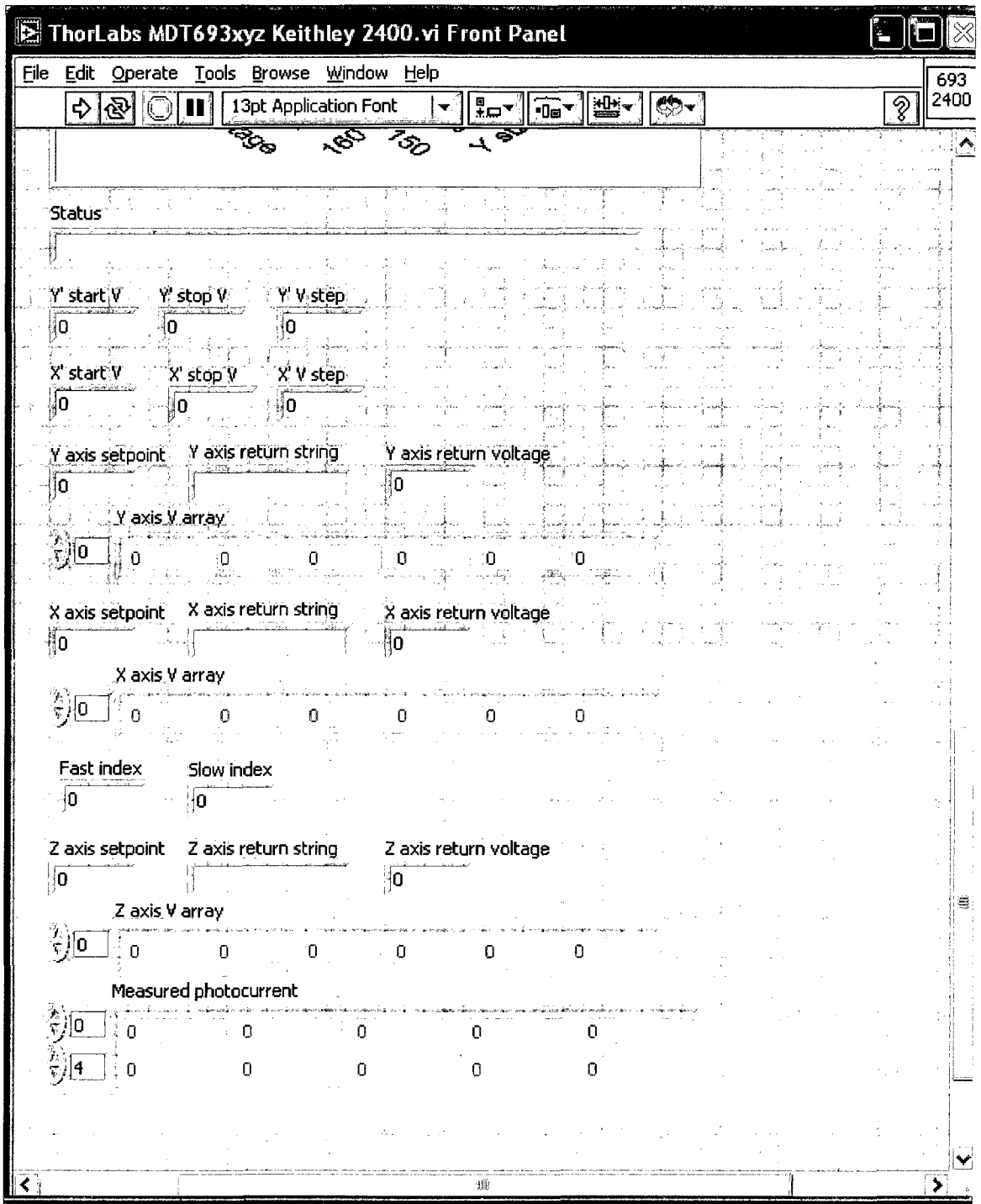


Figure 3: Front panel, bottom third

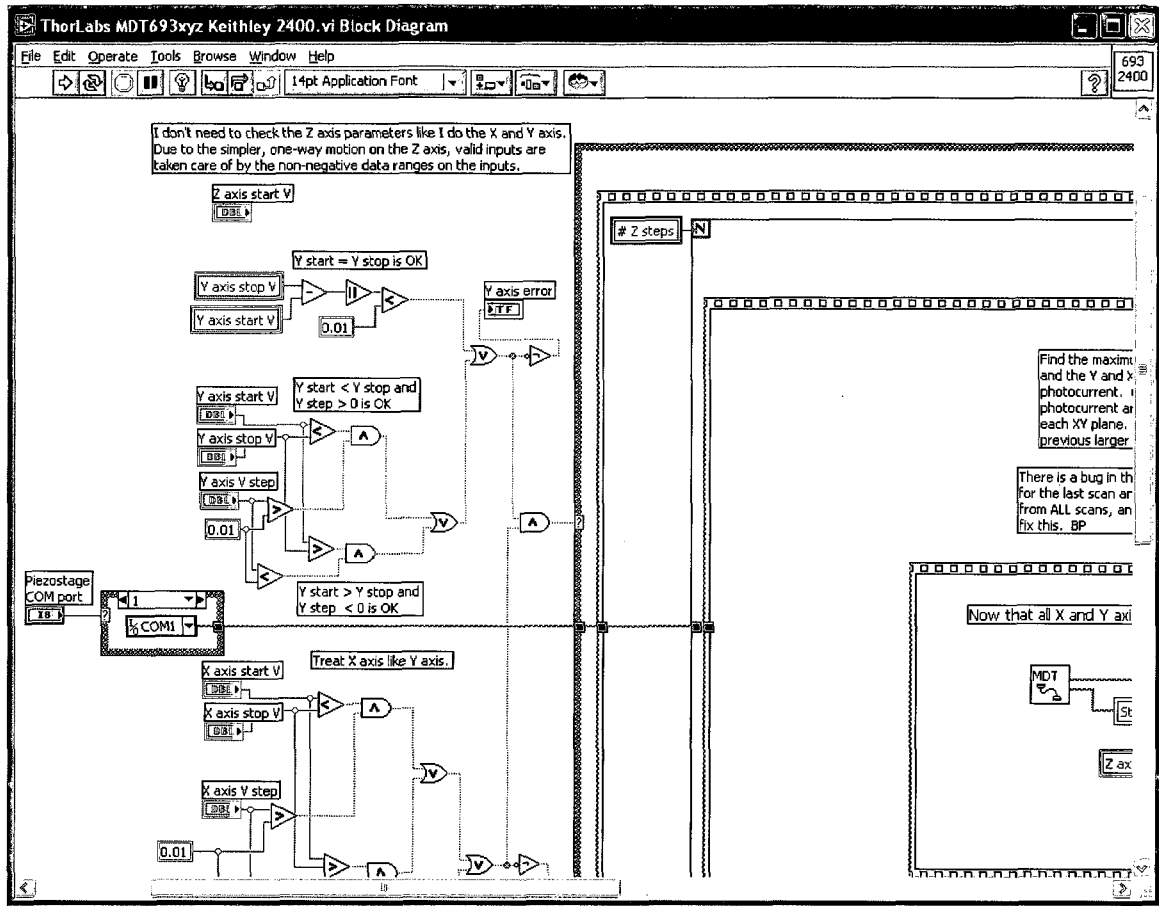


Figure 4: Block diagram, upper left

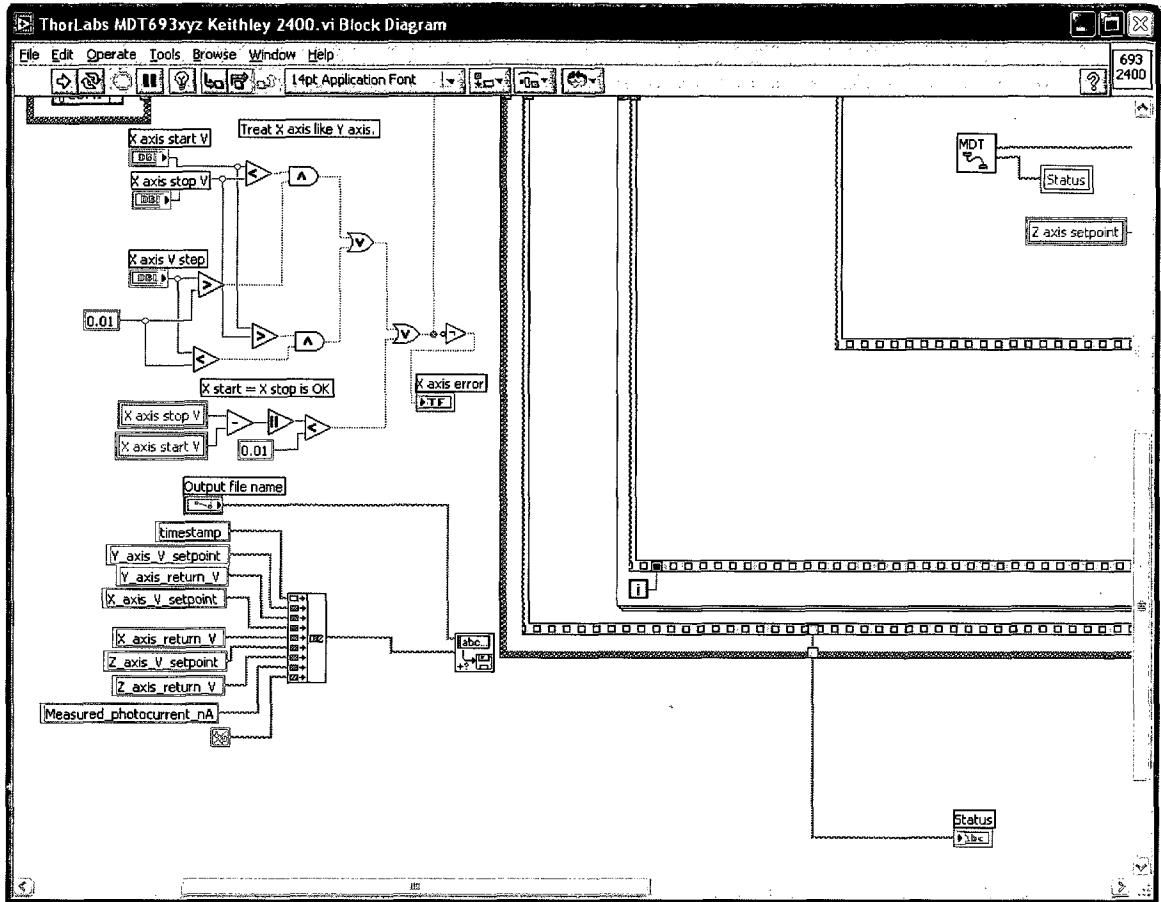


Figure 5: Block diagram, lower left

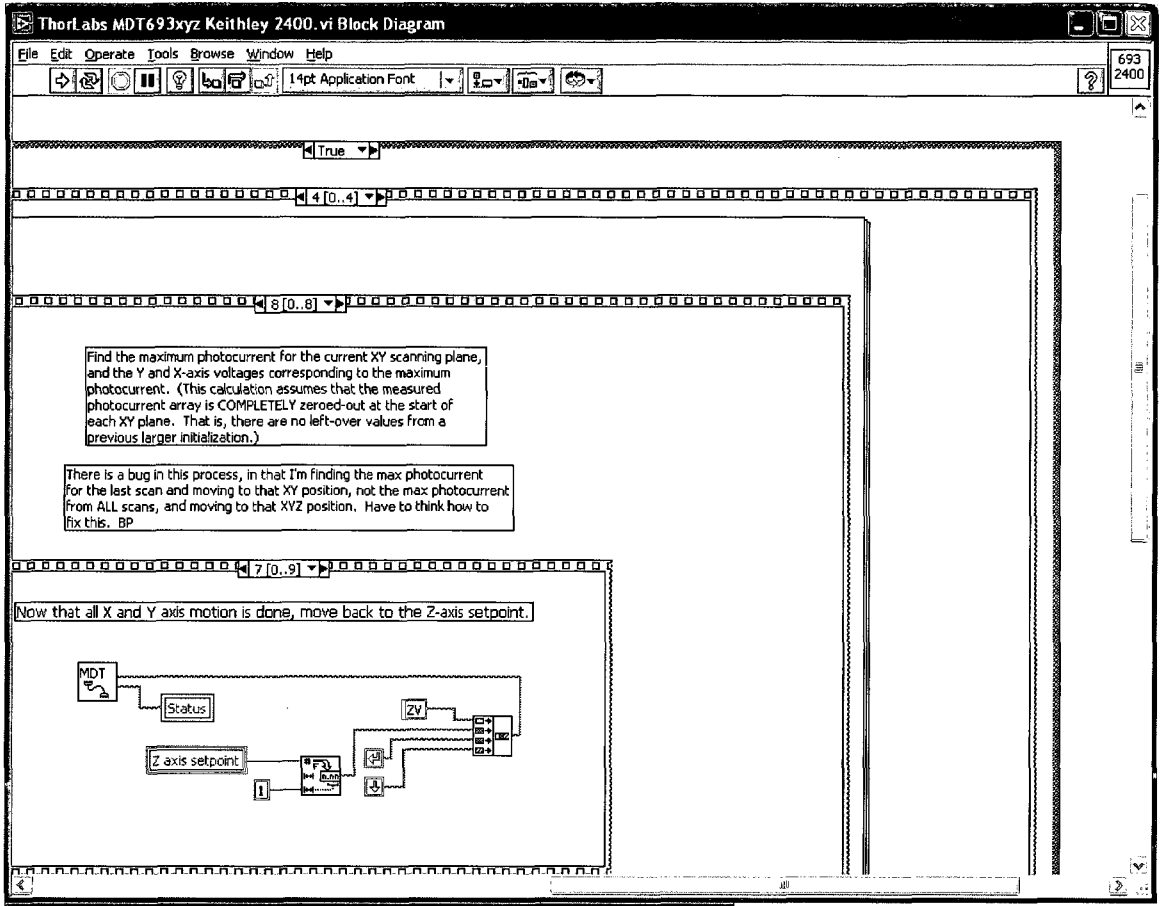


Figure 6: Block diagram, upper right

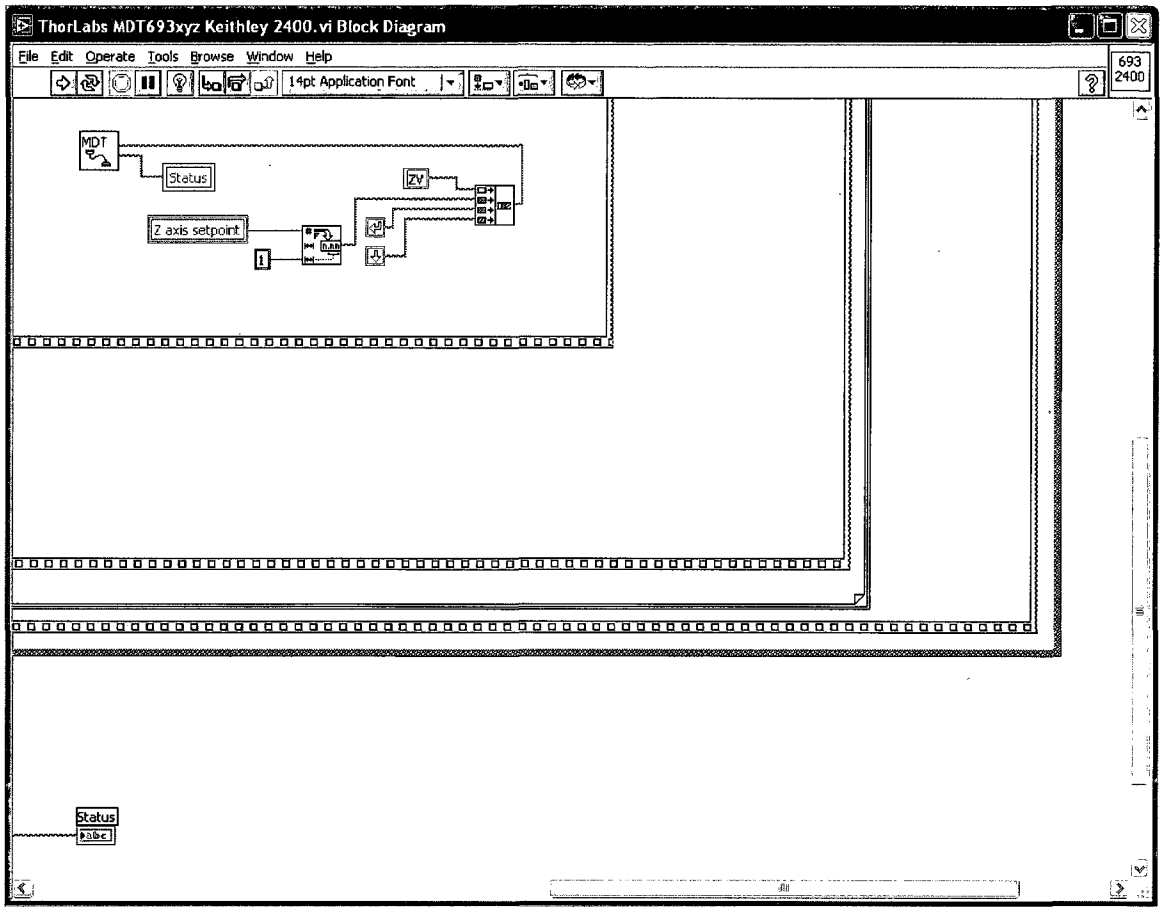


Figure 7: Block diagram, lower right

## 2 MultiAbsoluteMoveAndRead

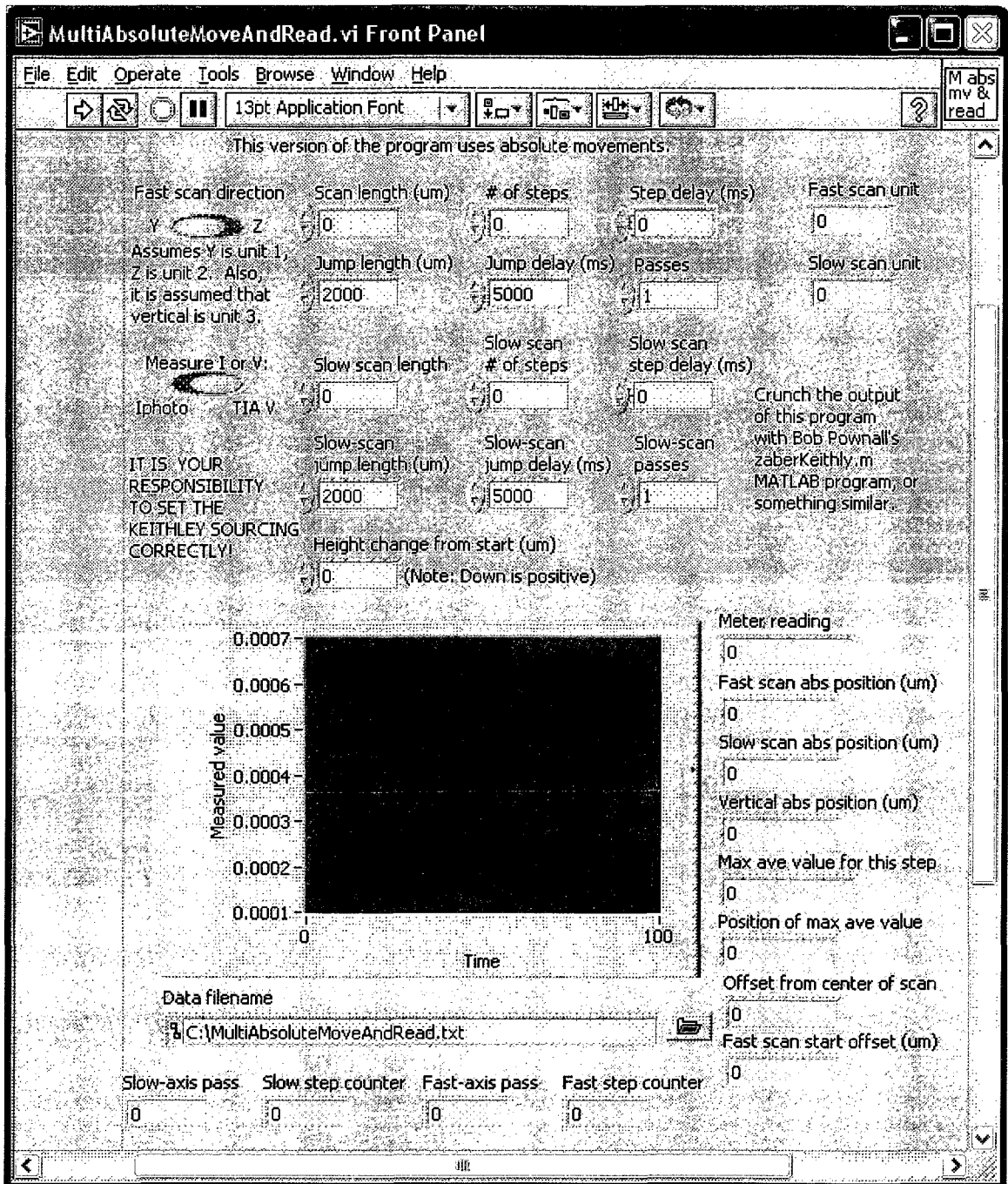


Figure 8: Front panel, top part

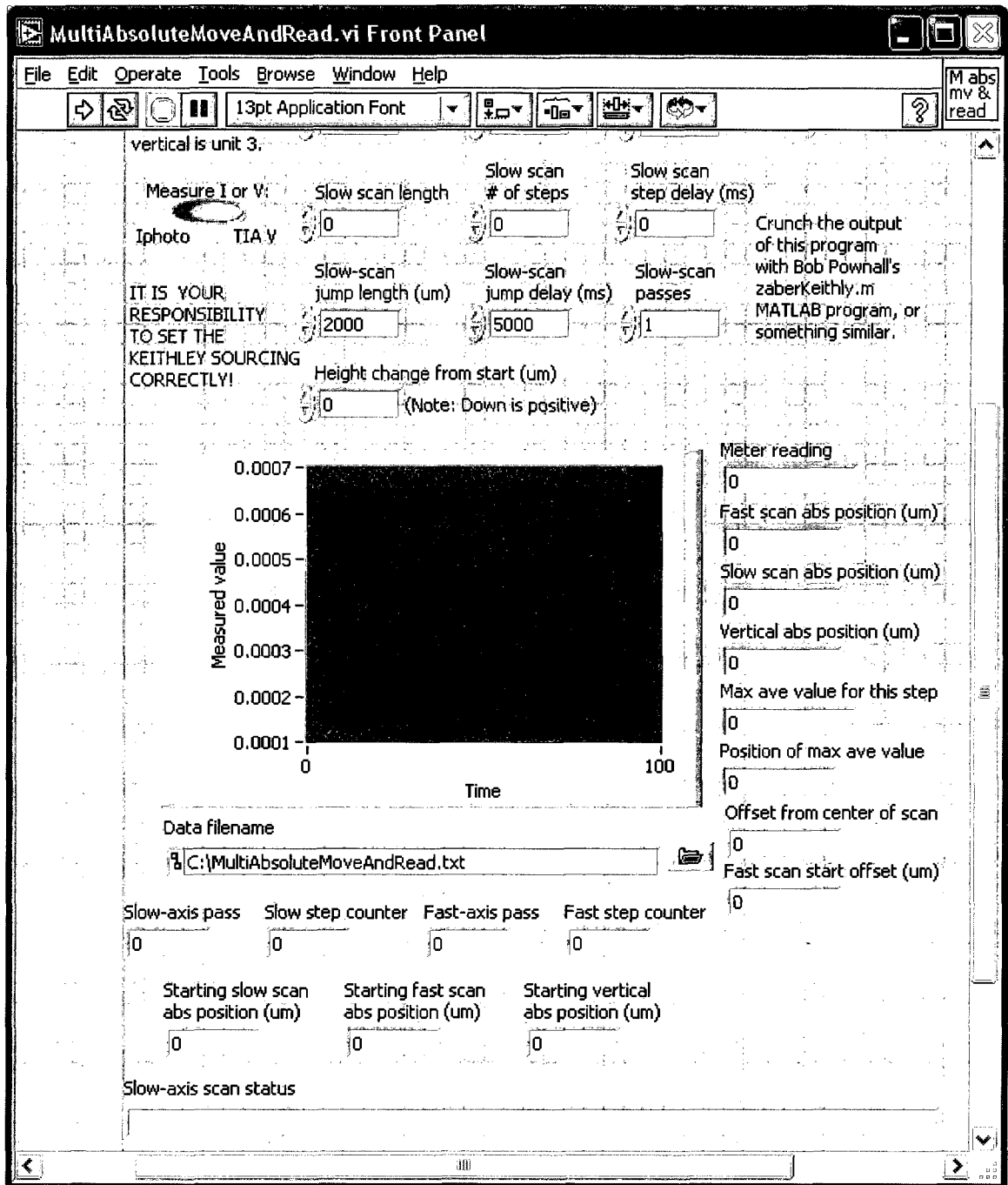


Figure 9: Front panel, bottom part

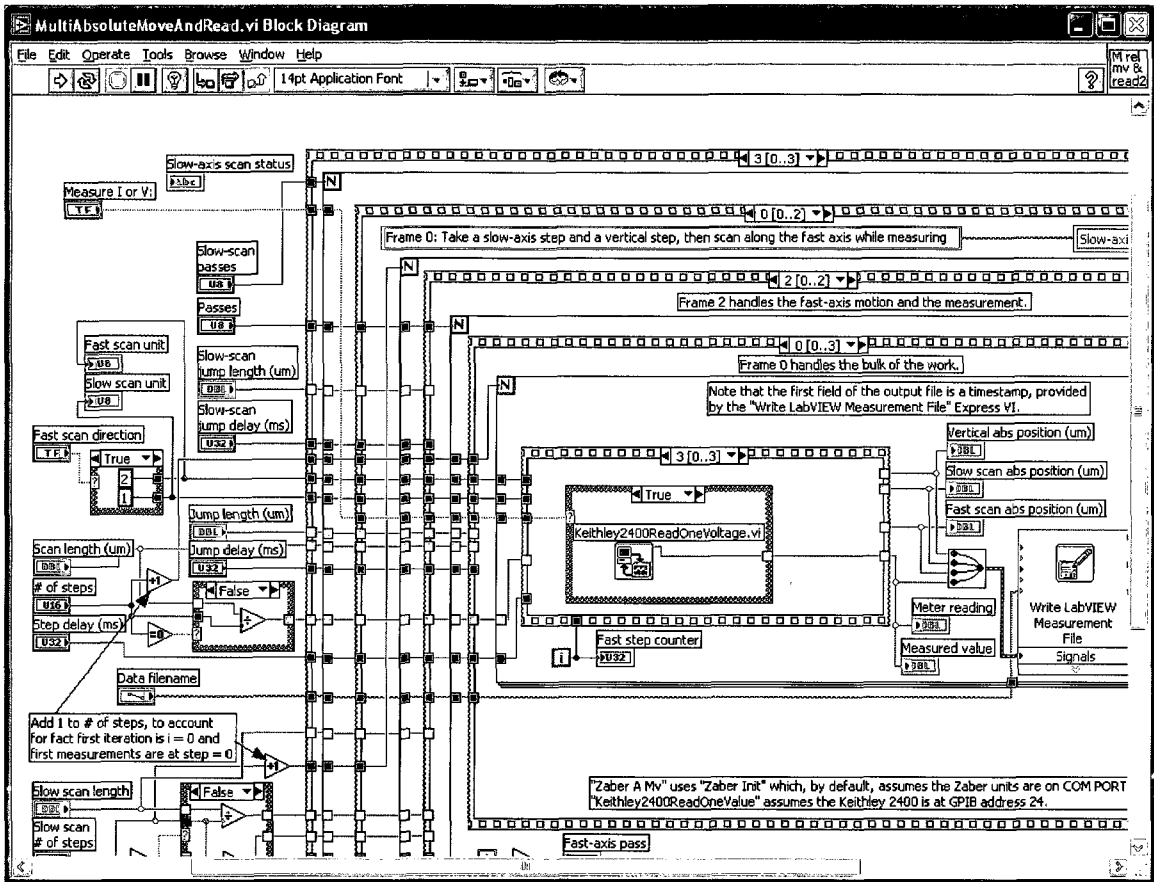


Figure 10: Block diagram, upper left



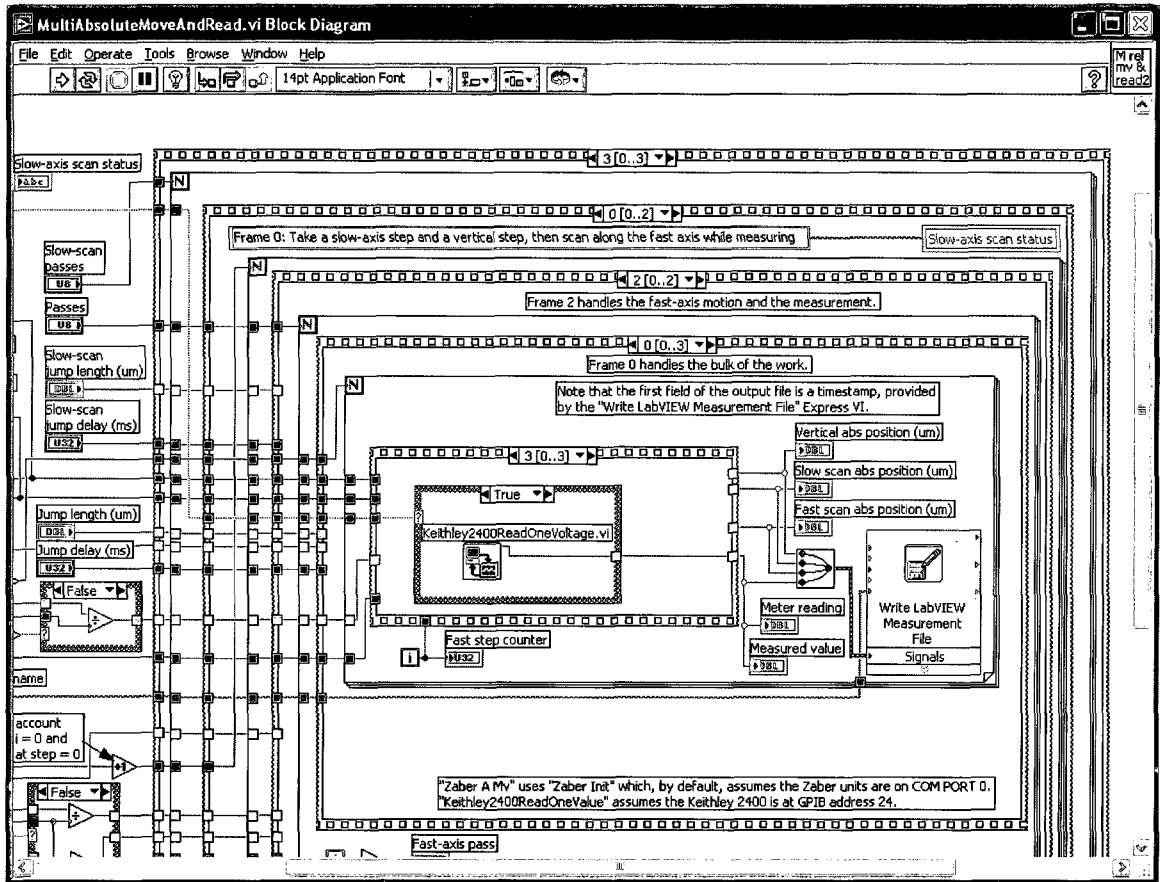


Figure 12: Block diagram, upper right

